1984

Structure-property relationships in dual phase steels.

Mukesh. Jain
University of Windsor

CANADIAN THESES

THÈSES CANADIENNES

NOTICE

The quality of this microfiche is heavily dependent upon the quality of the original thesis submitted for microfilming. Every effort has been made to ensure the highest quality of reproduction possible.

If pages are missing, contact the university which granted the degree.

Some pages may have indistinct print especially if the original pages were typed with a poor typewriter ribbon or if the university sent us an inferior photocopy.

Previously copyrighted materials (journal articles, published tests, etc.) are not filmed.

Reproduction in full or in part of this film is governed by the Canadian Copyright Act, R.S.C. 1970, c. C-30. Please read the authorization forms which accompany this thesis.

AVIS

La qualité de cette microfiche dépend grandement de la qualité de la thèse soumise au microfilmage. Nous avons tout fait pour assurer une qualité supérieure de reproduction.

S'il manque des pages, veuillez communiquer avec l'université qui a conféré le grade.

La qualité d'impression de certaines pages peut laisser à désirer, surtout si les pages originales ont été dactylographiées à l'aide d'un ruban usé ou si l'université nous a fait parvenir une photocopie de qualité inférieure.

Les documents qui font déjà l'objet d'un droit d'auteur (articles de revue, examens publiés, etc.) ne sont pas microfilmés.

La reproduction, même partielle, de ce microfilm est soumise à la Loi canadienne sur le droit d'auteur, SRC 1970, c. C-30. Veuillez prendre connaissance des formules d'autorisation qui accompagnent cette thèse.

THIS DISSERTATION
HAS BEEN MICROFILMED
EXACTLY AS RECEIVED

LA THÈSE A ÉTÉ
MICROFILMÉE TELLE QUE
NOUS L'AVONS REÇUE

NL 339 (r. 86/01)

Canada

STRUCTURE-PROPERTY RELATIONSHIPS IN DUAL PHASE STEELS

by

Mukesh Jain

A Thesis
Submitted to the Faculty of Graduate Studies
Through the Department of Engineering Materials
In Partial Fulfillment of the Requirements
For the Degree of Master of Applied Science
at the University of Windsor

Windsor, Ontario

C Mukesh Jain

ABSTRACT

A modified approach for producing dual phase steels, based on the TTT curve, has been examined. Dual phase steels have been studied in terms of this modified method of production (referred to as isothermal reaction treatment) to correlate their microstructure and mechanical properties. A comparison with the conventional intercritical annealing treatment has been done.

The Bauschinger test has been utilized as a method of measuring the permanent softening (or back stress) generated by the incompatibility of plastic deformation between ferritic and martensitic phases in dual phase steels.

A strength-differential has been observed between the tensile and compressive flow curves of dual phase steels, the magnitude of which has been measured for different microstructures and heat treatments.

The permanent softening has been studied as a function of tensile and compressive prestrain to compare compressive and tensile prestrained dual phase specimens with banded, unbanded, aged, unaged, intercritically annealed and isothermally reacted microstructures.

An equation for accurate representation of stress-strain behaviour of dual phase steels has been developed and its application was found to be in good agreement with experimental data. This equation has also been utilised for extrapolation of the prestrain part of Bauschinger curves for a more accurate measurement of the permanent softening parameter.

ACKNOWLEDGEMENTS

I would like to express my thanks to Professor D.F. Watt for his advice, direction and interest during the course of this work.

I would also like to thank Professor W.V. Youdelis for his interest, encouragement as well as for arranging financial assistance from the University during my stay at Windsor.

Thanks are also due to Dr. H. Yamauchi for his interest in my education and help in many ways.

I am indebted to Dr. J.D. Embury of McMaster University for the generous use of their equipment, for suggesting the use of the Bauschinger effect as a means of measuring the internal stress fields, and also for his general interest and (indirect) advice. Thanks also to Dr. R. Sowerby for the long term loan of his Bauschinger tester and literature, and also to Dr. Li Cheng Ji for examining the microstructures of dual phase specimens on the McMaster SEM.

I would like to thank Rick Dumala of the Geography Department for his help in digitizing experimental graphs and to Ed Klinard for his help with the Bauschinger tests.

I would also like to thank John Robinson for his help with the electron microscopy.

Particular appreciation is expressed to Michiteru Ayukawa, Douglas Ivey, Josef Karov, Nuri Zreiba, Ramesh Sharma, Mohammad Malik, Arvind Sethi, Robert Pearson and all other people I have met at the University of Windsor

for their encouragement, friendship and comraderie during studies in the Engineering Materials Department.

Special thanks are due to my parents for their continuing confidence and optimism throughout my education.

TABLE OF CONTENTS

LIST OF FIGURES

LIST OF TABLES

ABBREVIATIONS

D.P.	Dual Phase
H/T	Heat Treatment
MEF	Martensite Enclosed Ferrite
FEM	Ferrize Enclosed Martensite
F-M	Ferrite-Martensite
FGS	Ferrite Grain Size
V_m	Volume fraction of martensite
A_{Temp}	Austenitizing temperature
A_{Time}	Austenitizing time
R_{Temp}	Reaction temperature
R_{Time}	Reaction time
σ	True Stress
ε	True Strain
$\frac{d\sigma}{d\varepsilon}$	Work hardening rate
ε_y	Uniform strain
B.E.	Bauschinger Effect
BIR	Banded, isothermally reacted
S-D	Strength-Differential
IA	Intercritical Annealing
IR	Isothermal Reaction
PS	Permanent Softening
UBIR	Unbanded, isothermally reacted
SBIA	Strongly banded, intercritically annealed
HSLA	High Strength Low Alloy
UTS	Ultimate Tensile Strength

YS	Yield Strength
D_o	Initial diameter
L_o	Initial length
ω_o	Initial width
t_o	Initial thickness
A_o	Initial area of cross-section
ϵ_f	Elongation at fracture

CHAPTER 1

1.1 Introduction to Dual Phase Steels

Recently much attention has been focussed on a two phase steel with a microstructure comprising mainly martensite islands embedded in a ferrite matrix.

Most dual phase steels are produced by annealing in the ferrite plus austenite intercritical region of the iron-carbon phase diagram, then cooling rapidly enough to transform the austenite to martensite. The merits of this new class of steel called dual phase steel lie in its unusual ability to work harden, its high strength-to-weight ratio, and its high ductility and formability. The properties favour the manufacture of cold worked structural components formed with large strains (see Figure 1.1).

The first papers to effectively demonstrate the advantages of dual phase steels over other steels were published in 1977 by Rashid (1) and Hayami and Furukawa (2) but earlier discussion of the processing and properties are also in the literature (3,4,5). The 1977 papers generated intense practical and theoretical study of the dual-phase steels, much of which is recorded in proceedings of three symposia devoted to dual phase steels in 1977, 1979 and 1981 (6,7,8). In this period, a number of papers have been published to establish different structure-property relationships in dual phase steels.

The strength of dual phase steels is raised by an increase in the volume fraction of martensite as shown in

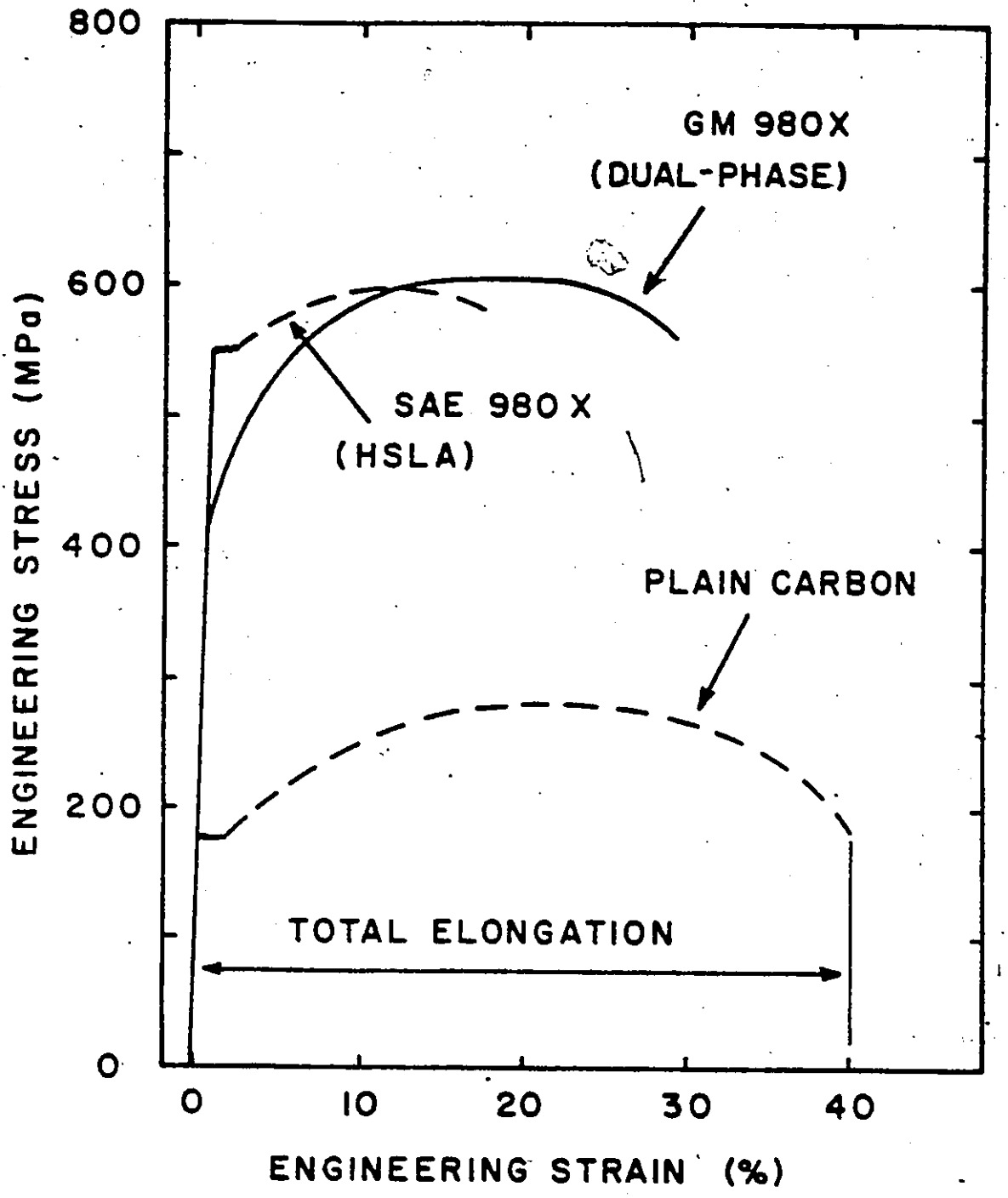

Figure1.1 Comparison of the stress-strain curve of a dual-phase steel with those of a plain carbon steel and an HSLA steel(1).

Figure 1.2 which is taken from the work of Davies (9) on Fe-1.5Mn-C dual phase steels. More detailed analysis of the strength of dual phase steels have shown that the composition, strength, size and distribution of the martensitic phase may cause variations in the strength. It is therefore not surprising that a range of experimental scatter larger than 200 MPa has been reported by Davies (9). Figure 1.3 from Speich and Miller (10) shows that an increase in the actual annealing temperature, which results in a lower carbon content of the martensite, reduces the strength of dual phase steels of comparable martensitic content.

Figure 1.4 shows a minimum in 0.2% offset yield strength at low volume fractions of martensite as reported by Lawson et al (11). The minimum in yield strength has also been reported by other investigators, who changed the volume fraction of martensite by applying various intercritical annealing temperatures (12) and cooling rates (13). The volume fraction of martensite at which the minimum yield strength is achieved appears to be related to the disappearance of discontinuous yielding caused by an insufficient number of mobile dislocations (13). Continuous yielding is caused by the production of a high dislocation density in the ferrite due to the expansion which occurs during the austenite-to-martensite transformation.

Another parameter influencing the strength of dual phase steels is the strength of the ferrite matrix which can be increased by refining grain size, precipitation and solid

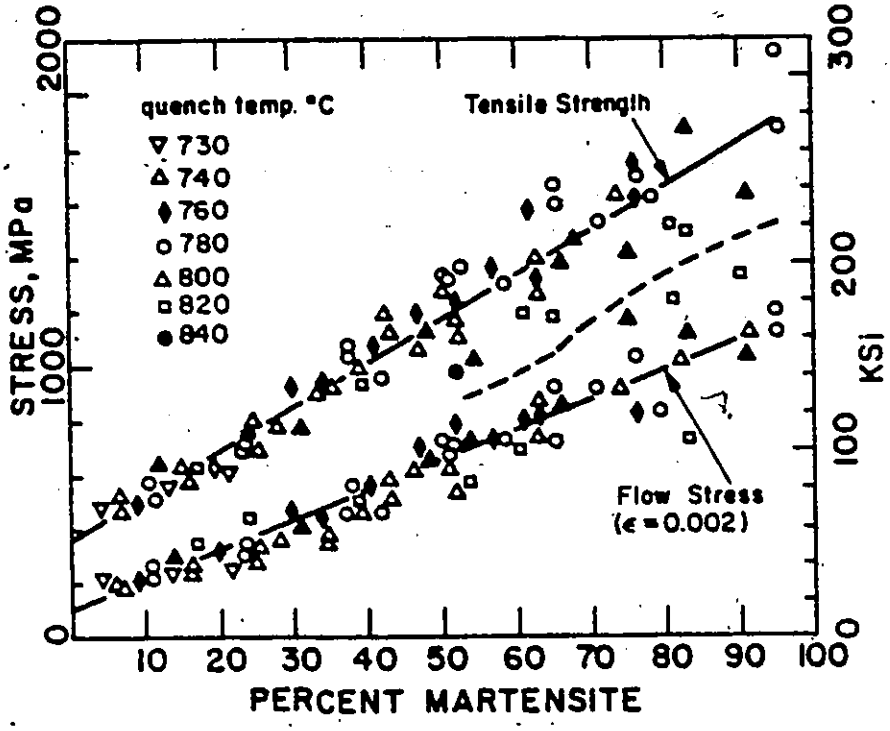

Figure L2 Flow stress (0.2 pct) and tensile strength as a function of percent martensite for Fe-Mn-C alloys(9).

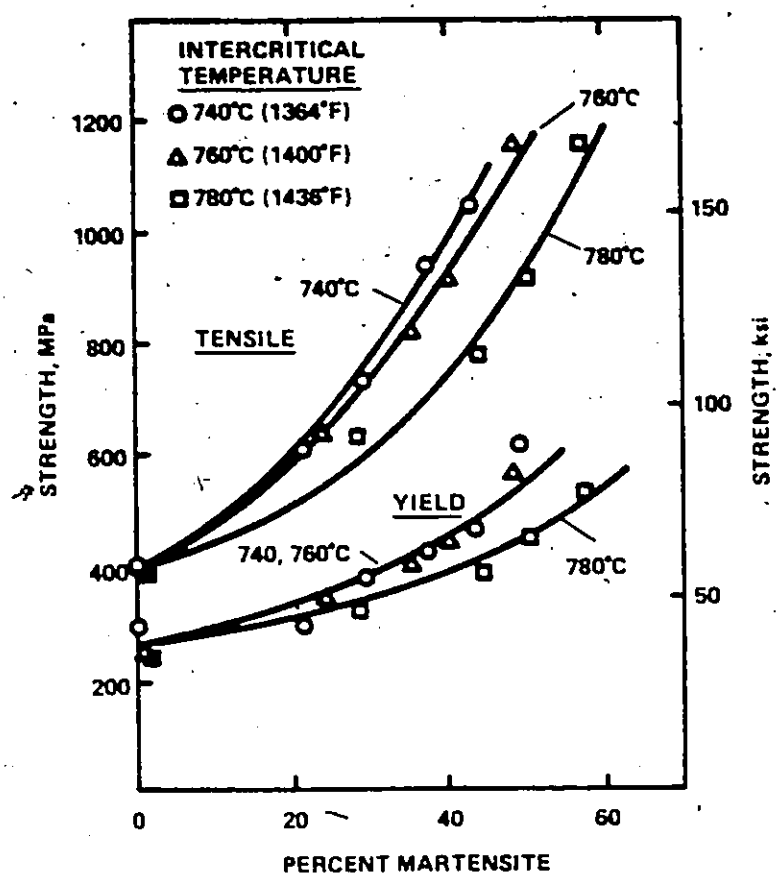

Figure 13 Flow stress (0.2 pct) and tensile strength as a function of percent martensite for Fe-1.5 Mn-0.5 Si-0.15 Mo alloys(10).

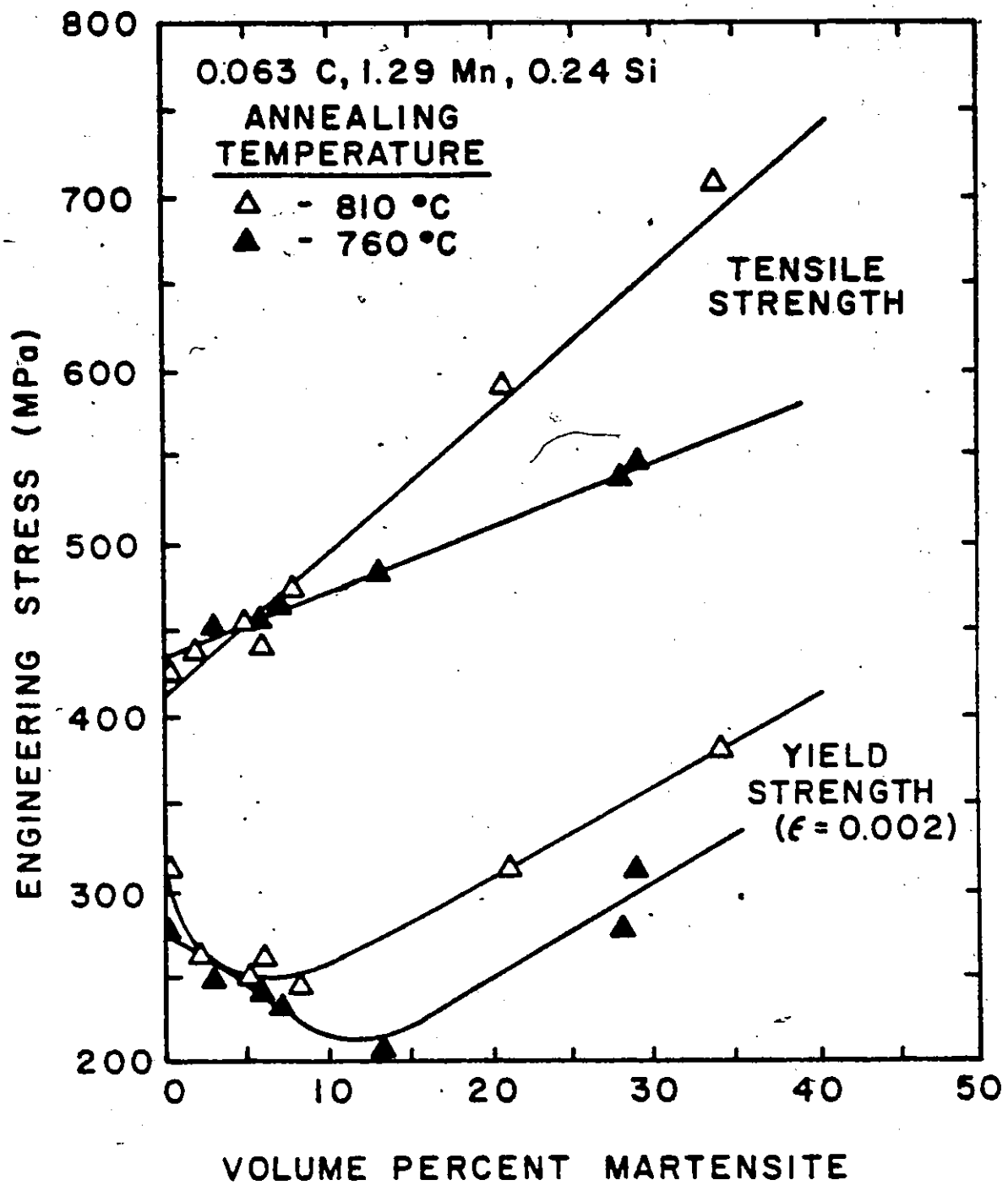

Figure 1.4 Flow stress (0.2 pct) and tensile strength as a function of percent martensite for an Fe-0.063 C-1.29 Mn-0.24 Si steel annealed 10 minutes at 810°C and 760°C (11).

solution hardening. Smaller ferrite grain size can be achieved by a finer initial microstructure. Figure 1.5 shows the effect of grain size on the 0.2% flow stress of dual phase steels with a constant volume fraction of martensite and silicon content. This dependency of strength of dual phase steels on the inverse square root of grain diameter (Hall-Petch relation) has been reported by several investigators (14,15).

The primary commercial interest in dual phase steels has been as a means of weight reduction in the automobile. The high formability of dual phase steels in sheet metal form holds the promise of large tonnage production as strip. As a result, virtually all of the data quoted in the preceding review and in Chapter III is for sheet metal samples. Thus there is a lot of tensile data, but very little testing has been done in compression.

The present study can be broadly classified into three categories. Firstly, an investigation was made of the effect of heat treatment schedule on the martensite morphology and its effect on mechanical properties. Secondly, a new empirical equation for representing tensile and compressive flow curves has been proposed. Finally, the Bauschinger properties of banded, unbanded and aged dual phase steels have been studied. The objectives of the present work are outlined in more detail in the next chapter.

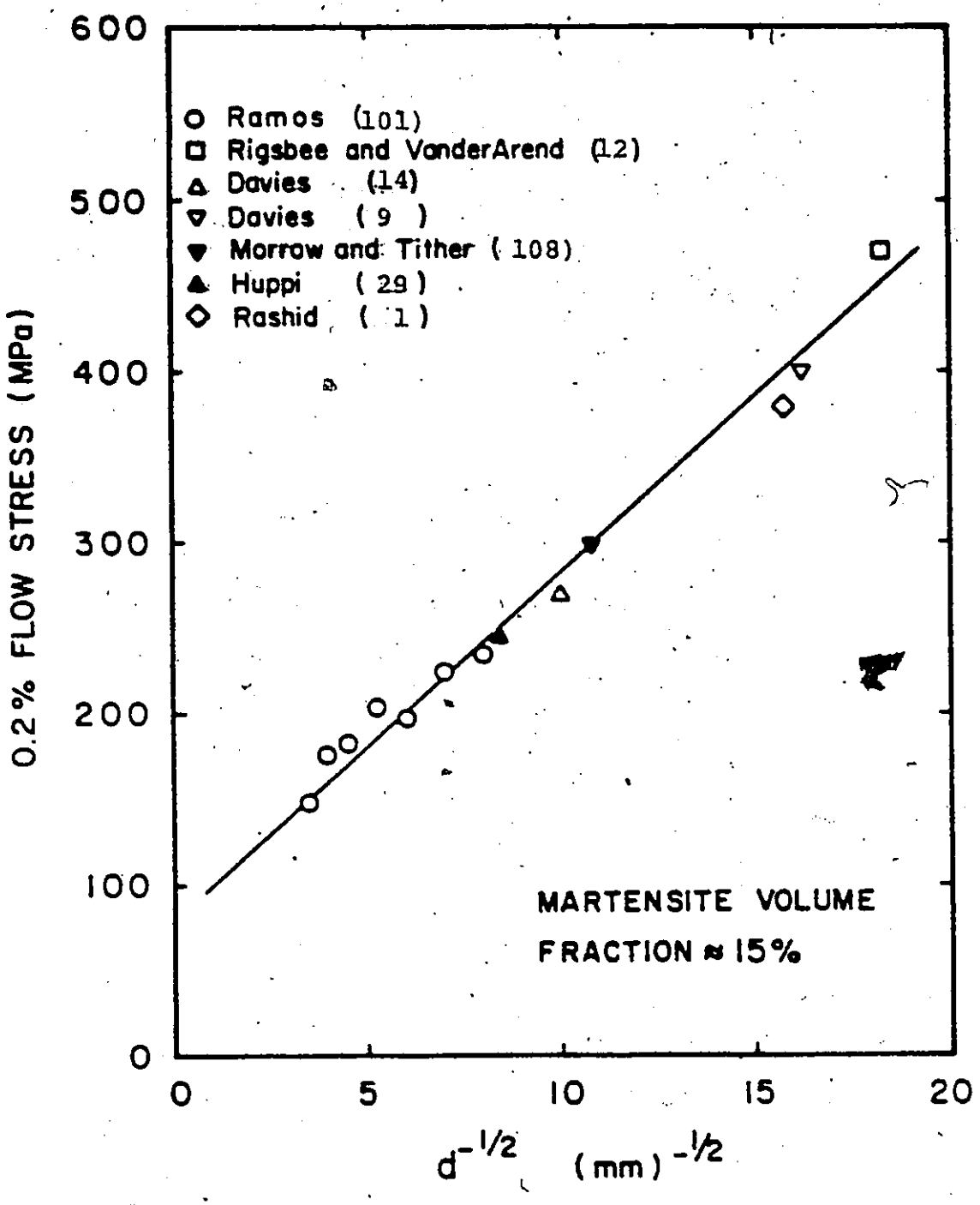

Figure 15 Flow stress (0.2 pct) as a function of $d^{-\frac{1}{2}}$ for dual-phase steels with a martensite volume fraction of 15 pct.

CHAPTER 2

OBJECTIVE OF THE PRESENT WORK

The aim of this work, in general, was to understand the relationship between structure and mechanical properties of dual phase steels. This objective was fulfilled in terms of three other objectives.

2.1 Effect of Heat Treatment Schedule on Microstructure

There are two ways of obtaining dual phase microstructures namely, intercritical annealing or by isothermal reaction. These treatments, in reference to Fe-C equilibrium diagram, have been used to obtain different martensite morphologies by a number of workers, as mentioned in more detail in the next chapter.

In the present work, an approach similar in essence to the isothermal reaction treatment, based on the TTT curve, has been studied for obtaining dual phase structures in nominally 1020 plain C steel bars. This method offers a rapid and useful way of obtaining dual phase structures. The microstructures obtained by this heat treatment have been studied in relation to the mechanical properties and a comparison has been made with the microstructure and mechanical properties obtained by an intercritical annealing treatment.

2.2 Mathematical Modelling of Stress-Strain Data

Modelling of stress-strain curves was attempted in order to relate the stress-strain and work hardening behaviour of dual phase steels to their microstructure. This was done by obtaining accurate digitized data from experimental curves and expressing these in terms of well established models of stress-strain and work hardening. This has been attempted by other workers in the case of their dual phase steels and conclusions have been drawn about the strain mechanisms. Finally, the applicability of the above-mentioned empirical equations has been discussed along with the results of other workers.

The extrapolation of data in the present work required a more suitable empirical equation to express the deformation behaviour of dual phase steels. A new equation was developed and was found to be valid over a larger strain interval. This proposed equation, was then utilized for extrapolating Bauschinger prestrain curves for the measurement of Bauschinger effect in dual phase structures.

2.3 Compressive Compared with Tensile Loading

A strength differential effect not previously reported for this material has been observed in the present work. As well, the Bauschinger effect and its relationship to different dual phase microstructures was studied. The Bauschinger effect can be described as a lowering of the elastic limit in compression (or tension) subsequent to a previous straining in tension (or compression) beyond the elastic limit.

A large Bauschinger effect has been observed by other workers in two phase systems including dual phase steels. Brown and Stobbs (42-46), in their models of dispersion hardened systems, have illustrated the usefulness of Bauschinger tests in rationalizing the mechanical behaviour of these materials. They and others (72-74) have used the Bauschinger effect as a measure of the internal stresses that develop due to inhomogeneity of plastic deformation and have drawn conclusions about the initial work hardening behaviour of materials. To date, very limited data have been available to evaluate this effect on a quantitative basis, for different morphologies in dual phase steels.

In the present work, an effort is made to establish the relationship between different microstructures and the Bauschinger effect in dual phase steels. Different specimen microstructures such as banded, unbanded, aged, unaged, intercritically annealed and isothermally reacted microstructures were tested to draw conclusions about the effect of prestrain on the Bauschinger effect.

A detailed literature review, pertinent to each of the above objectives is presented in the next chapter.

CHAPTER 3

LITERATURE REVIEW

3.1 Introduction

Structure-property relationships in dual phase steels, in general, have been recently reviewed by Speich and Miller (16). A brief review for the case of C-Mn dual phase steels, pertinent only to our objectives is therefore presented here.

3.1.1 Methods of Producing Dual Phase Steels

Dual phase ferrite-martensite structures have been developed by two different routes which are normally referred to as intercritical annealing and isothermal reaction treatments (1). These two schemes of heat treatment are shown in Figure 3.1. Intercritical annealing is the most common method of producing dual phase steels in the laboratory as well as on a commercial scale. In this method, the normalized ferritic-pearlitic steel is heated into the ferrite-austenite region and held for long periods to obtain an equilibrium ferrite-austenite mixture. The steel is subsequently cooled at an appropriate rate, based on the hardenability of the steel, to transform the austenite into martensite. In the isothermal reaction treatment (5), however the normalized steel is heated into the single phase austenite field and subsequently reacted at a lower temperature in the two phase ferrite-austenite field at temperatures above the eutectoid temperature. This allows the formation of ferrite from austenite. The steel is held in the two phase

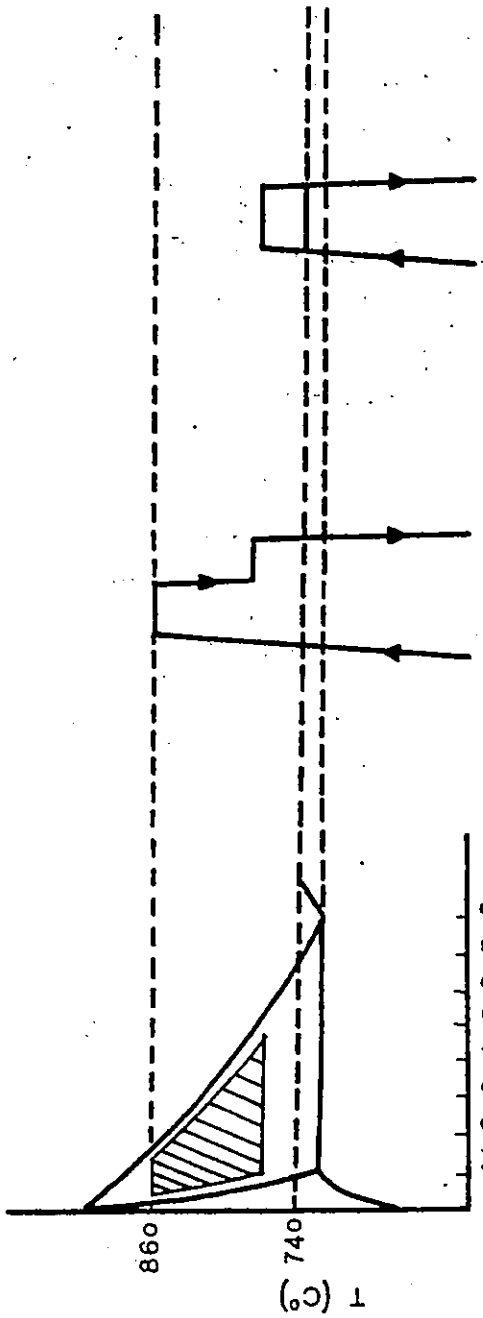

Figure 3.1 Two methods of producing dual phase steels.

field until an equilibrium ferrite and austenite mixture is obtained. The steel is subsequently appropriately cooled to produce a ferrite-martensite structure. In both cases, the temperature, and the time that the steel is held in the two phase field, are the main determinants of the resulting microstructure.

In these two approaches to obtain dual phase structures, the Fe-C equilibrium diagram has been consistently used to obtain the necessary dual phase microstructure and to predict the volume fraction of the constituent phases. This has been possible, because the specimens have been held in the two phase alpha-gamma field for long times to obtain equilibrium amounts of ferrite and austenite without the formation of low temperature transformation products such as bainite or pearlite.

In the present work, a different approach, based on TTT curve, has been attempted to obtain dual phase structures. This can be described as follows:

1) Heating of as-rolled steel specimens in the austenite range slightly above the A_3 line, for a few minutes to obtain small and uniform austenite grains. The temperature of austenitizing was primarily fixed by the carbon content of the steel and was about 860^{o}C for the present 1020 carbon steel bars.

2) The specimens were then rapidly quenched to a temperature below the eutectoid reaction temperature as shown in Figure 3.2. The specimens were held at this

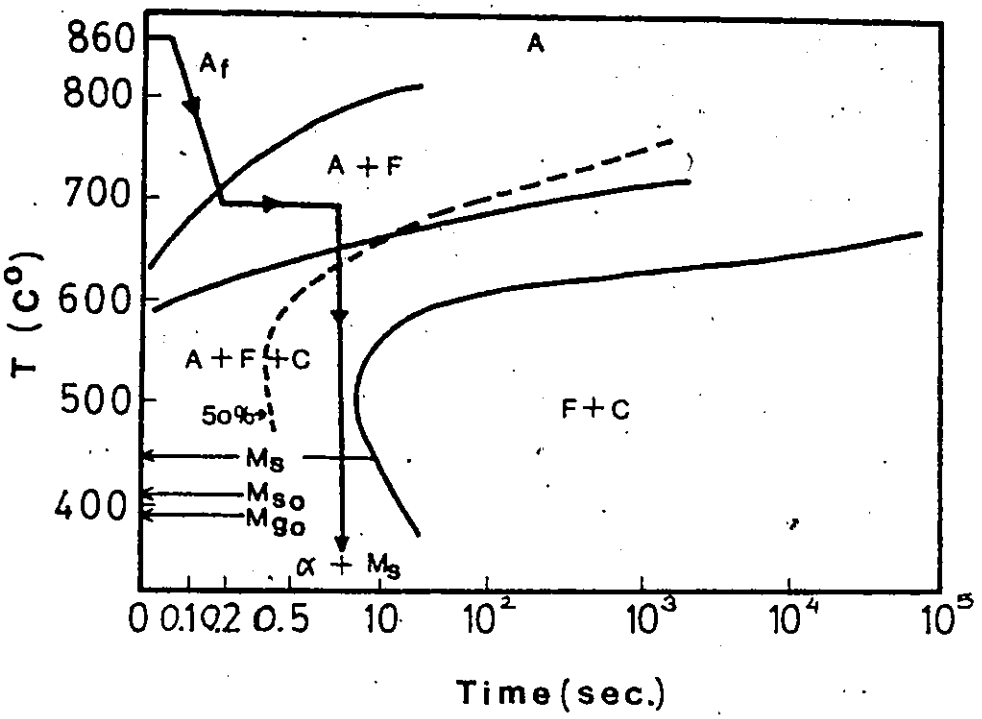

Figure 3.2 Isothermal transformation diagram of a 1019 plain C steel containing 0.69%Mn.

temperature for a few minutes during which ferrite nucleates and grows. The amount of ferrite increases with time but the equilibrium amount of ferrite is never allowed to form.

3) The steel was then water quenched to transform the remaining austenite to martensite.

3.1.2 The Kinetics of the Formation of Austenite

A large body of information is available on the austenitizing reaction, but this review will be restricted to some fairly recent work (16,18,19) on the formation of austenite in low alloy steels from Fe_3C-ferrite aggregates. The reaction is undoubtedly one of nucleation and growth. In any type of Fe_3C-ferrite aggregate, growth consists in the conversion of the aggregate to the gamma phase at the interface of the growing austenite nodule; the converstion to the nodule does not necessarily mean the dissolution of all carbides, nor the full dissipation of C concentration gradients.

The kinetic variables are the state variables of time and temperature and structural variables of form and degree of dispersion of the Fe_3C and ferrite phases. The nucleation rate, N, has been found to increase with the increase in the Fe_3-C ferrite interfacial area (17). Since diffusion must occur in converting this aggregate to a single solid solution phase, it would be expected that the growth rate G would be greater the smaller the distance between the carbide particles or the smaller the interlamellar spacing in pearlite. Both N and G are thus structure sensitive in this reaction. Since the diffusion coefficient increases

with temperature, G has also been found to increase with temperature.

In the case of dual phase steels produced by intercritical annealing the austenitization process has been recently studied by a number of workers (17,18,19) and the results of Garcia et al (17) are shown in Figure 3.3. The increase in volume fraction of austenite takes place as follows:

1) Austenite is nucleated at Fe_3C particles situated in the ferrite grain boundaries and nucleation occurs throughout the isothermal holding period.

2) The austenite grain grows into the ferrite matrix and along the ferrite grain boundaries. The rate of the austenite growth into the ferrite is much smaller than that along the grain boundaries.

This difference in austenite grain growth is presumably caused by the difference in diffusion coefficient in the ferrite grain boundaries compared with the bulk diffusion rate.

3.1.3 Kinetics of Nucleation and Growth of Ferrite From Austenite

In this section, a general review of the present knowledge of the kinetics of the austenite-ferrite reaction in hypoeutectoid plain C steels will be presented. Experimental observations as well as the theory of nucleation and diffusional growth of ferrite crystals from austenite will also be briefly presented.

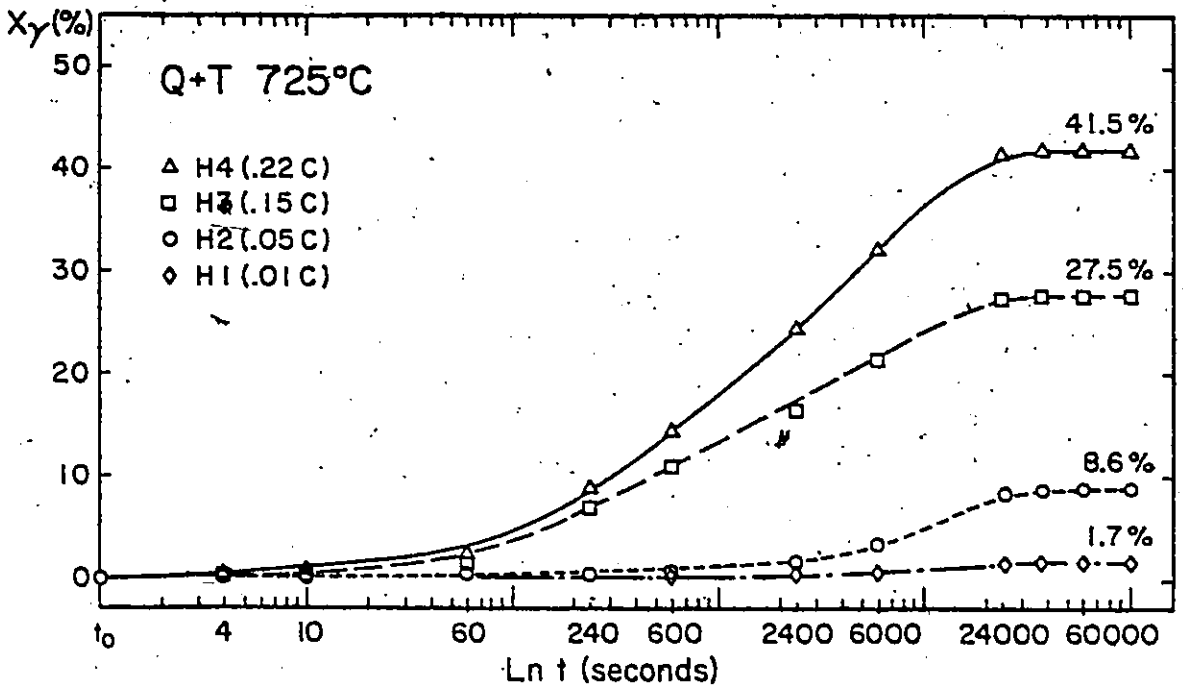

Figure 3.3 Kinetics of austenite formation in 1.5Mn steels at 725°C (from Garcia et al (17)). X_γ(%) indicates the volume % of austenite formed.

3.1.3.1 Nucleation of Ferrite

Ferrite precipitates from the austenite phase below the A3 line. Figure 3.4 shows the approximate temperature-composition regions in which ferrite and cementite are present first in readily observable amounts in partially reacted plain carbon steels. As shown in the figure, at temperatures below the eutectoid, pearlite can become an effective competitor for the now entirely unstable austenite matrix only at low temperatures or higher carbon contents.

a) Effect of Austenitizing Temperature -A number of workers (20,21,22) have studied the effect of austenitizing temperature on the nucleation rate of proeutectoid ferrite during isothermal holding. Hull et al (20) first showed that the nucleation rate of proeutectoid ferrite* decreases with increasing austenitizing temperature. Two factors (21) may contribute to this effect: (i) residual concentration gradients from the solution of ferrite or carbide in the austenite may be dissipated by raising the austenitizing temperature, and (ii) the increase in grain size of the austenite may reduce the number of preferred nucleation sites at grain boundaries. Mazanec and Cadek (22) have also ascertained the effects of austenitizing temperature upon the nucleation rate of ferrite, N_s. Using commercial type 0.4 % C steels containing 0.5 and 1.6 % W, they found about three-fold increases at a reaction temperature of 745°C and smaller rises in the nucleation rate at 675°C. Their results are shown in Table 3.1

---

* ferrite formed in the two-phase ferrite-austenite region.

TABLE 3.1

Influence of Austentizing Temperature Upon the Rate of Nucleation(Ns) of Ferrite for a 0.41%C 0.16% Mn, 0.20% Si and 1.56%W Steel(22)

Austentizing temp., C	Reaction temp., C	Ns x 10^{-4} nuclei/cm^2/sec.
950	745	0.29
1100	745	0.09
950	675	0.89
1100	675	0.70

b) Effect of Isothermal Reaction Temperature - Mazanec and Cadek (22) have also examined the influence of isothermal reaction temperature on the nucleation rate of ferrite, N_S, by comparing values of N_S at the times when 2% of the austenite had transformed to ferrite. As shown in Figure 3.5, N_S increases rapidly with decreasing temperature.

Krahe et al (23) have more recently observed that austenitizing a high-purity Fe-0.11 pct C alloy at 1300°C to set the austenite grain size and then further austenitizing at a lower temperature prior to isothermal reaction markedly increased the overall kinetics of the proeutectoid ferrite reaction. When the second austenitizing treatment was sufficiently close the AC_3, the transformation kinetics became so rapid that isothermal reaction studies were no longer feasible.

c) Ferrite Nucleation Rates - The data which have been recounted on the nucleation kinetics of ferrite can be qualitatively rationalized on the basis of the following simple arguments. Sufficient prolonged holding of a hypoeutectoid steel at a given temperature in the austenite-ferrite region is taken to establish a steady state distribution of ferrite embryos. The number of embryos of radius, r, per mole, n_r, can be expressed as (21):

$$n_r = n_o \, e^{-\Delta Fo/RT} \qquad (1)$$

where n_o is the number of lattice sites per mole and ΔF_o is the free energy of activation for the formation of a mole of embryos of radius r. Assuming the embryos to be hemi-

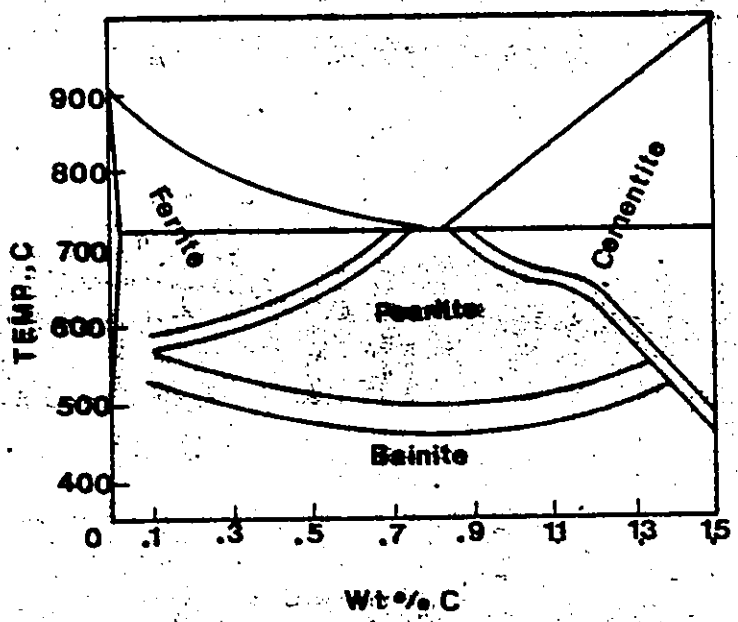

Figure 3.4 Temperature-composition regions in which the ferrite, cementite, pearlite, and bainite are dominant in plain-carbon steels.

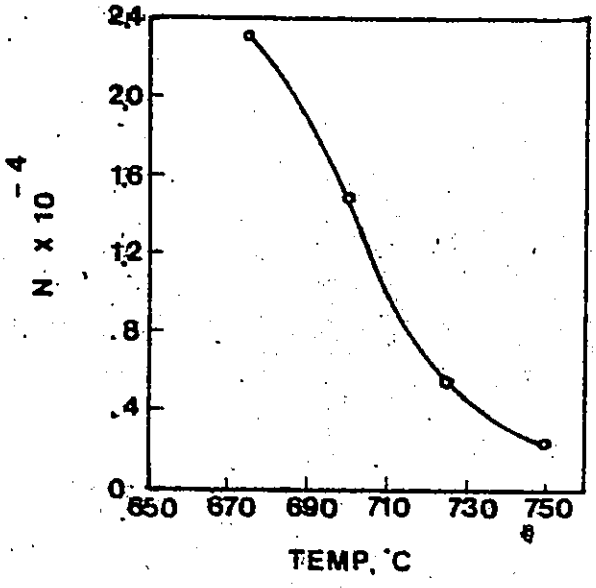

Figure 3.5 Effect of temperature upon nucleation rate of ferrite at reaction times at which 2% ferrite is formed in an 0.42%C, 0.54%W, 0.16%Mn steel (Mazanec and Cadek (19)).

spheres, formed heterogeneously against a planar austenite grain boundary (21):

$$\Delta F_o = 2\pi r^2 \sigma_{v\alpha} + \pi r^2 \nu(\sigma_{r\alpha} - \sigma_{rr}) + \frac{2}{3}\pi r^3(\Delta F_v + W) \qquad (2)$$

where ν is a number less than unity to account for varying area of cross-section of the ferrite embryo at the austenite grain boundary, $\sigma_{r\alpha}$ is the specific interfacial free energy of an austenite-ferrite boundary, σ_{rr} is the specific interfacial free energy of an austenite grain boundary. The volume free energy change F_v per unit volume accompanies the formation of a mole of embryos and W is the volume strain energy attending the appearance of the embryos. When the steel is quenched to a temperature below the austenite field, the volume free energy change associated with the formation of an embryo of radius r becomes negative. According to Equation (1) the number of these embryos is thus considerably increased.

The influence of austenitizing temperature upon the rate of nucleation at a given reaction temperature can be explained in the following manner.

The higher the austenitizing temperature and time the larger will be the grain growth of austenite and the smaller will be the grain boundary area of the austenite grains. This will lead to a decreased nucleation rate.

3.1.3.2 Growth of Ferrite

a) Theoretical Predictions - The rate of growth of

ferrite perpendicular to the boundary, G_p, can be treated simply as a problem in the mass transport of carbon to or from the boundary by volume diffusion through austenite. A number of workers have solved this growth problem by assuming growth faces of ferrite of a certain defined nature. Dubé (24), for simplicity, has obtained a solution to the planar growth problem, and Frank (25) has solved the spherical case; Zener (26) has generalized the Dubé analysis, making it applicable to one-, two- or three-dimensional growth in the form of a plate, a cylinder or a sphere, respectively. The mathematics of all these analyses are complex. Results of the rigorous analysis by Zener for the planar and spherical cases (26) yields:

i) For planar growth (Figure 3.6):

$$x = \alpha_1 (Dt)^{\frac{1}{2}}$$

$$\text{where } \alpha_1 = k_1 \alpha_1^*, \quad \alpha_1^* = \frac{(C_\gamma^\alpha - C_\gamma)}{(C_\gamma^{\gamma\alpha} - C_\alpha)^{\frac{1}{2}} (C_\gamma - C_\alpha)^{\frac{1}{2}}} \qquad (3)$$

and k_1 varies from 1.13 to 1.41 as C_γ decreases from $C_\gamma^{\gamma\alpha}$ to C_α. $C_\gamma^{\gamma\alpha}$, C_α and C_γ are the carbon concentrations in austenite at the austenite:ferrite boundary, in ferrite, and in austenite, respectively. D is the diffusivity of carbon in austenite at the carbon content of the austenite in contact with the boundary.

ii) For spherical growth:

$$x = r = \frac{K_2 (C_\gamma^{\gamma\alpha} - C_\gamma)^{\frac{1}{2}}}{(C_\gamma - C\alpha)^{\frac{1}{2}}} (Dt)^{\frac{1}{2}} \qquad (4)$$

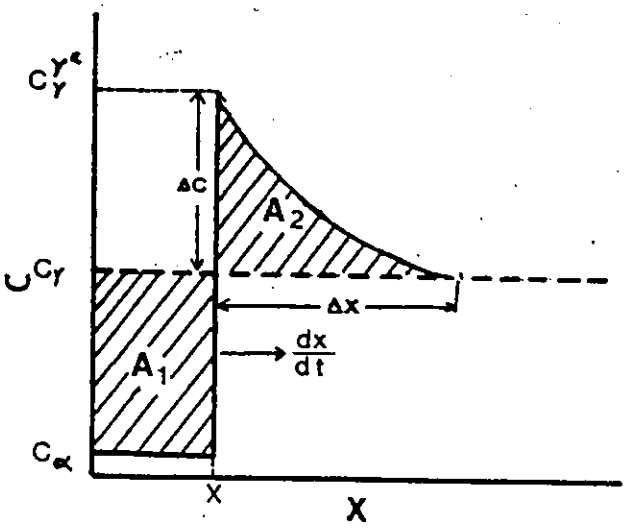

Figure 3.6 Approximate carbon concentration profile in the region of an advancing austenite:ferrite boundary (Zener (26)).

where K_2 ranges from 1.4 to 2.4 as C_v varies from $C_v^{\nu\alpha}$ to C_α.

b) Experimental Observations - Values of Gp as a function of $t^{-\frac{1}{2}}$, obtained by Mazanec and Cadek (22) are plotted in Figure 3.7. Differentiating Equation (3) with respect to time and grouping the constant terms into a new constant, c,

$$Gp = \frac{dx}{dt} = ct^{-\frac{1}{2}} \qquad (5)$$

Thus the linear dependence of Gp upon $t^{-\frac{1}{2}}$ in Figure 3.7 indicates that ferrite grain growth is controlled by a rate of diffusional mass transport.

Ascertaining the species whose transport rate controls the rate of growth is conventionally done by determining the activation energy of the growth process. Mazanec and Cedek (22) performed this determination by means of an equation for the rate of growth due to Danilov and Kristal (27).

$$G = k_1 \exp\{(-k_2/\Delta T)\cdot T\}\exp\{-Q/RT\} \qquad (6)$$

where k_1 and k_2 are constants and Q is the enthalpy of activation for diffusion. When degree of supercooling, ΔT, is appreciable,

$$\exp\{(-k_2/\Delta T)\cdot T\} \simeq 1 \qquad (7)$$

Therefore,

$$G = k_1 \exp\{-Q/RT\} \qquad (8)$$

Mazanec and Cadek (22) applied the above equation to growth rate data obtained from specimen of an 0.42%C, 1.58%W steel which has been transformed to 2, 5 and 10% ferrite respectively at temperatures from 675 to 730°C (Figure 3.8). The

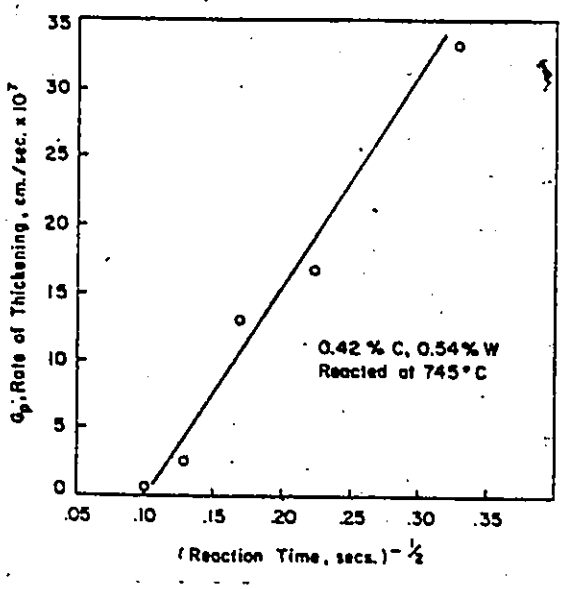

Figure 3.7 Growth rate of ferrite as a function of time$^{-\frac{1}{2}}$ from the data of Mazanec and Cadek (22).

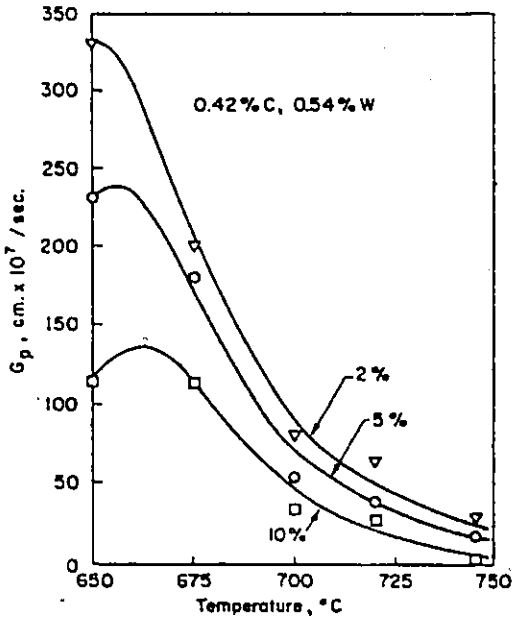

Figure 3.8 Growth rate of ferrite vs. reaction temperature at three levels of transformation in a 0.42%C, 0.54%W steel (Mazanec and Cadek (22)).

activation energies for growth at these levels of transformation were 33200; 33800; and 34000 cal/mole, in acceptable agreement with the energy of activation for the diffusion of carbon in austenite containing a similar amount of tungsten. The rate of growth of ferrite, it was thus concluded, is controlled by the volume diffusion of carbon in austenite. This result is pertinent to the present work because it implies that the carbon distribution in the martensite could be different in isothermally reacted dual phase steels compared to intercritically annealed steels. This point is discussed further in Chapter 5.

As evident from Figure 3.8, the growth rate of ferrite increases with decreasing temperature and decreases with increasing volume fraction of ferrite.

3.1.4 Effect of Heat Treatment on the Mechanical Properties of Ferrite-Martensite Structures

The ferrite-martensite mixture formed by the isothermally reacted path is different from that formed by the intercritically annealed method. In the case of the isothermally transformed specimens, all the ferrite that is formed is essentially new ferrite, transformed from austenite. In the case of intercritically annealed heat treatment there are two types of ferrite which have been termed 'retained ferrite' and 'epitaxial ferrite'. The retained ferrite is that ferrite of the original room temperature ferrite-pearlite microstructure. The epitaxial ferrite is the ferrite that grows from the austenite epitaxially onto the retained ferrite

during cooling (28,29). Mn and Si may partition between the austenite and ferrite during intercritical annealing and thus the epitaxial ferrite has been found to inherit a higher Mn and/or lower Si from the parent austenite. For low alloy steels, the retained ferrite may contain precipitates which are absent in the epitaxial ferrite. These compositional differences and the relative amounts of epitaxial and retained ferrite have been found to affect the susceptibility of dual phase steels to room temperature ageing (30). The relative importance of the roles of epitaxial and retained ferrite on the general mechanical properties has not been properly elucidated.

Kunio et al (31) were first to study the mechanical property differences between isothermally transformed and intercritically annealed ferrite-martensite microstructures. In their studies in 1975 (before the term 'dual phase steel' was coined to represent these microstructures) they obtained 'ferrite enclosed martensite' and 'martensite enclosed ferrite' type structures from isothermally reacted and intercritical annealed treatments respectively. The results were analyzed in terms of tensile and fracture behaviour of the two martensitic morphologies. They reported a higher tensile strength, a lower ductility and a brittle mode of fracture in the case of intercritically annealed, MEF, structures.

Recently, Suzuki et al (32) have also studied these structures for their tensile and fatigue crack growth properties. They have reported, in agreement with the work of

Kunio et al (31), that a continuous martensite network (MEF), results in an increase in strength as compared to a continuous ferrite network. In addition, a continuous ferrite network (FEM) has been found to possess better ductility and an improved resistance to fatigue crack growth, probably due to a smaller plastic zone size.

Thomas and Koo (33), in their studies on duplex ferrite-martensite steels (1010), have conducted a similar work on morphology and structure-property relationships. They state that an isothermal reaction brings about a coarser and more connected martensite geometry compared to that obtained after intercritically annealing. The latter treatment gives improved ductility. They report that strength, on the other hand, is less sensitive to morphology and depends to a good approximation on the "law of mixtures" (Figure 3.9). These results are clearly in conflict with the work of Kunio et al (31) and Suzuki and McEvily (32). In the case of Thomas and Koo (33), the details of heat treatment, especially, intercritical annealing and isothermal holding times, are not available. This is important since a banded and connected martensite morphology has been obtained by Garcia and DeArdo (17) for long intercritical annealing times.

In the present work, therefore, dual phase structures were produced by both isothermal and intercritical annealing heat treatments to establish a definite relationship between martensite morphology and the heat treatment procedure as

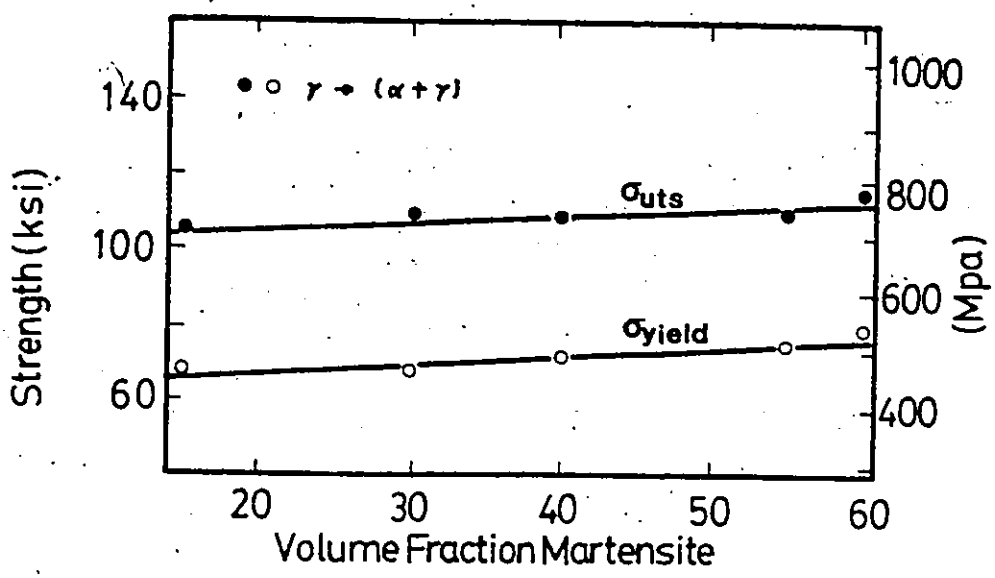

Figure 3.9 Strength as a function of volume fraction of martensite (Thomas & Koo (32)).

well as to study the effect of heat treatment procedure on structure-property relationships in dual phase steels.

3.1.5 Effect of Tempering on the Mechanical Properties of Dual Phase Steels

The mechanical properties of dual phase steels can be altered by low temperature heating or tempering which produces various microstructural changes in the steel. Recently, a few papers (34,35,36) have been published on the effect of tempering on intercritically annealed DP steels. The relationship between mechanical properties and tempering treatments as a function of steel composition and processing parameters and on the phase transformations and other microstructural changes that are produced by tempering have been investigated. This section deals with a brief review of the existing literature on mechanical property changes in these intercritically annealed and tempered dual phase steels.

Figure 3.10, taken from the results of Rashid and Rao (34), represents in general the effect of tempering on mechanical properties of a vanadium bearing dual phase steel (.1%C, 1.5%Mn and .1%V) for tempering times of 1 hour.

The yield strength increased slightly and the ultimate tensile strength, total and uniform elongation decreased slightly on heating the steel at 200°C. However, on heating above 200°C, the yield strength increased rapidly with increasing tempering temperature and reached a maximum value. A return of the yield point (discontinuous yielding) is observed above 200°C in low martensite dual phase steels.

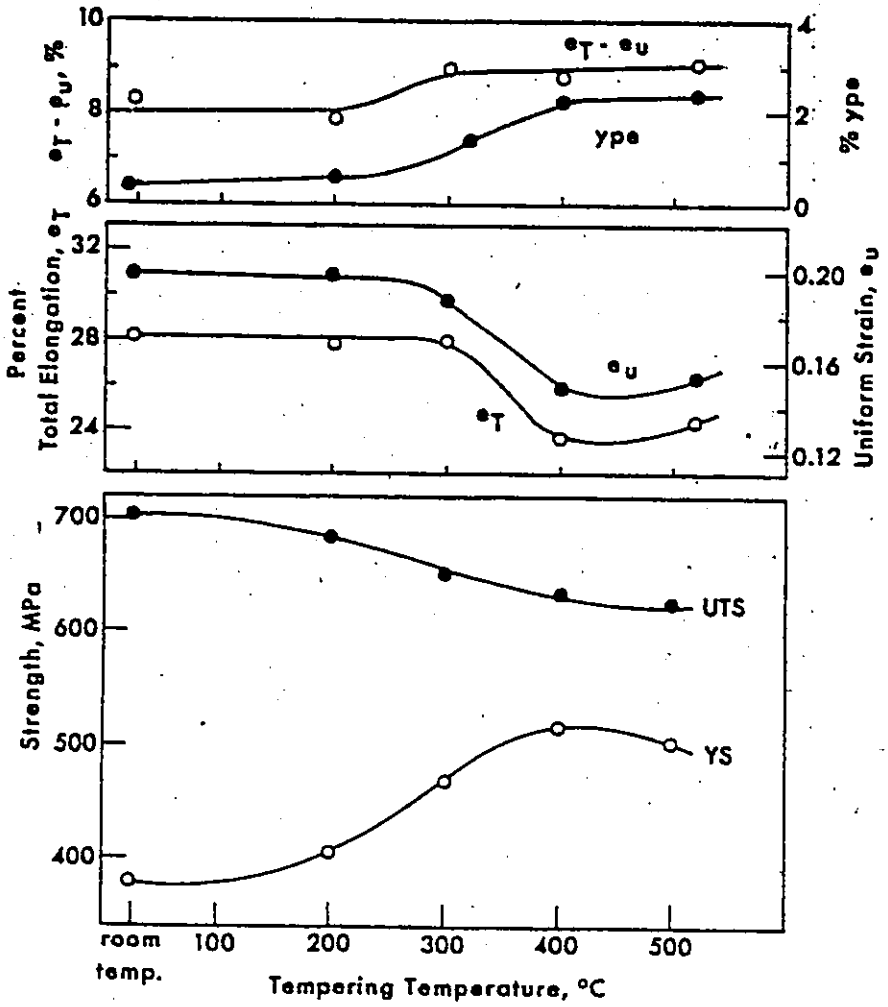

Figure 3.10 Effect of tempering temperature on the mechanical properties of inter-critically annealed dual phase steels(34).

The UTS decreased continually with increasing heating temperature and tended to level off at the higher temperatures. A higher tempering temperature (~650°C) leads to a return of yield point for high martensite content dual phase steels. The total and uniform elongation decrease rapidly with increasing tempering temperatures.

These changes, in mechanical properties on tempering, have been explained in terms of microstructural changes in ferrite, martensite and retained austenite observed by TEM (34,35). The yield strength increase is believed to be caused by the observed relaxation of residual stresses at the ferrite martensite interfaces, the rearrangement of dislocations in the ferrite, and the precipitation of carbides in the retained austenite. The decrease in tensile strength has been attributed to the twin boundary precipitation of cementite particles in the martensite. A slight increase in yield point was observed due to an increase of dislocation-interstitial coupling (36). The decrease in ductility has been ascribed to the observed decomposition of retained austenite to upper bainite and to the morphology of the bainite.

Figures 3.11-12, taken from the work of Davies (35), show a marked reduction in tensile strength of an intercritically annealed, water quenched low alloy dual phase steel, on tempering, compared to high alloy dual phase steels. This has been explained in terms of a higher carbon content of high alloyed steels and consequently a higher

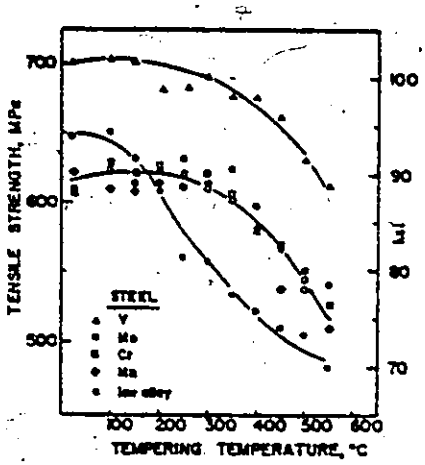

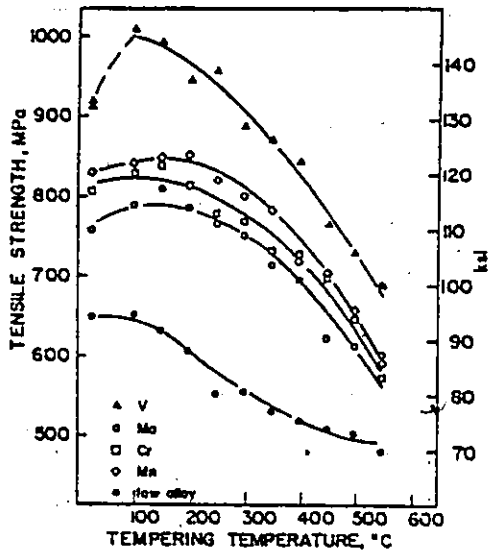

Figure 3.11(top) Tensile strength as a function of tempering temperature for the air cooled high alloy steels. The data for the low alloy steel is added for comparision(35).

Figure 3.12(bottom) Tensile strength as a function of tempering temperature for the high alloy and low alloy water quenched steels(35).

volume fraction of martensite which retains the tensile strength during tempering. The difference in the tempering behaviour of air-cooled and water quenched high alloyed dual phase steels could be due to (35):

1. Auto-tempering of the martensite during the air cooling operation.
2. Higher carbon martensite in the air-cooled dual phase steels arising from some of the austenite transforming to ferrite during cooling and so increasing the carbon content of the remaining austenite, which eventually transforms to martensite.
3. Precipitation in the ferrite during air cooling.

Low alloy steels have to be water quenched in order to transform austenite to martensite due to hardenability considerations.

Water quenched dual phase steels have been found to have a poor strength-ductility combination on tempering, compared to air cooled dual phase steels. The overall effect of tempering of any dual phase steel is to result in an inferior strength - ductility combination (34-36). It has been suggested (34) that the ductility of a dual-phase steel is essentially determined by the initial structure and the percentage of ferrite in the structure is the dominant factor controlling the ductility of dual phase steels; the greater the amount of ferrite the greater is the ductility. The strength of dual phase steels is very strongly dependent upon the strength of the martensite. Thus, softening

the martensite by tempering will reduce the strength of the dual-phase steel, but not necessarily increase the ductility.

3.2 Bauschinger Effect

Since Bauschinger discovered the phenomenon in 1881 (37), a number of investigators have studied the Bauschinger effect in various single crystal and polycrystalline metals and alloys. A review of Bauschinger effect in different metals will not be attempted here since a rather comprehensive review on Bauschinger effect has been recently published by Sowerby et al (38). It would, however, be useful to briefly review the Bauschinger effect in two phase systems and in particular dual phase steels.

The Bauschinger effect illustrates the anisotropy of work hardening. Materials showing no Bauschinger effect would be mechanically isotropic after unloading and would possess a compressive flow stress closely equal to that achieved in tension before unloading. The Bauschinger effect can be described as a lowering of the elastic limit in compression subsequent to a previous stressing in tension beyond the elastic limit. Conversely, the elastic limit in tension would be reduced for a material strained beyond the elastic limit in compression (Figure 3.13).

Cyclic torsion tests and cyclic tension-compression tests where prestraining in tension is followed by reverse straining in compression (or vice versa) are commonly used to study Bauschinger effect in materials.

The shape of the stress-strain curve for reverse

loading in compression following prestraining in tension is shown schematically in Figure 3.13. The reduction in the elastic limit (compare σ_y with σ_{yc}) and the well-rounded nature of the initial portion of the reverse flow curve is not untypical of real materials.

A pronounced Bauschinger effect has been observed in two phase materials and in particular, the systems containing non-deforming particles in a soft matrix. Theoretical proposals to explain the B.E. in two phase systems can be broadly classified as being either macroscopic or microscopic in nature.

The macroscopic approach is based on the continuum theory of plasticity. It attempts to describe the work hardening behaviour of materials for complex loading histories. Two rules of work hardening that have been widely employed are those of isotropic and kinematic work hardening (38). Isotropic work hardening occurs when the initial yield surface expands uniformly during plastic flow. The initial yield surface may define an isotropic or an anisotropic material but it remains centred on the hydrostatic stress axis. In contrast the kinematic hardening yield surface does not change in its initial form and orientation, but it translates in stress space as a rigid body. The theoretical extension to combinations of these rather basic concepts has resulted in models which in principle, allow for continuous expansion, distortion and translation of the yield surface in order to describe the work hardening behaviour.

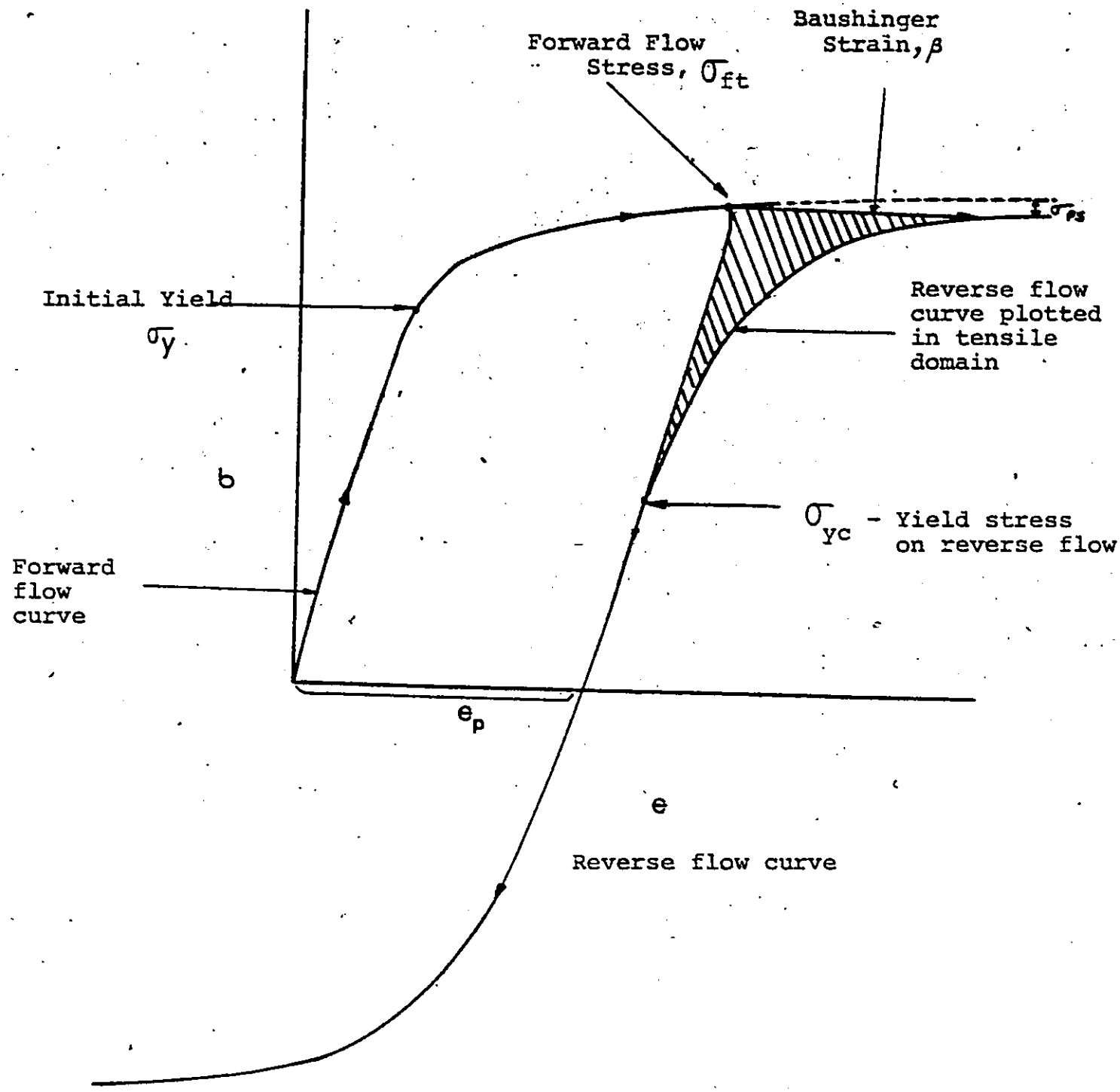

Figure 3.13 Schematic representation of the uniaxial stress-strain behaviour of many real metals during forward and reverse flow tests.

A detailed review of macroscopic models such as Masing model based on elastic-plastic elements, residual stress models, Mroz model and other work hardening models based on the translation, expansion and distortion of an initial yield surface are presented in the review by Sowerby et al (38). It is important, however, to mention here that these models still provide a drastically oversimplified version of the real events.

The microscopic approach is based on the inhomogeneity of the plastic flow. This inhomogeneity could be viewed in terms of dislocation motion at second phase inclusions, the macroscopic scale of grains, etc. The inhomogeniety gives rise to material incompatibility and the generation of internal stresses. These internal stresses can be classified as being "short range" or "long range" in nature. In a plastically deformed matrix, containing strong particles which remain elastic while the matrix deforms plastically, the particles act as a barrier to dislocations. During deformation, dislocation loops are built up around the particles which suffer purely elastic strain and a "long range" stress field will arise. The effect of removing the applied stress is to leave the material in a state in which there is a non zero back stress within the matrix. This stress is, of course, in a sense to help the plastic deformation of the matrix when a reverse stress is externally applied.

Short range internal stresses are more a function of local dislocation arrangements, interparticle spacing, and

solute atom interactions.

It is to be noted that in general a certain amount of plastic relaxation will occur around the embedded particles or other barriers during plastic straining. Partial relaxation still leaves some incompatability between the matrix and inclusions. An average measure of the incompatibility is the unrelaxed strain (defined as ϵ_p^*) which in turn is related to the back stress as mentioned later.

3.2.1 Microscopic Models of The Bauschinger Effect (B.E.)

3.2.1.1 Orowan's Approach

Orowan (39) invoked his loop hardening theory in which a rather specific obstacle distribution with regions of both high and low obstacle density will accumulate dislocation loops on stressing in one direction. On removing the stress local adjustment takes place, so that on reapplying the stress in the reversed direction segments are propelled under both the back stress of the loop accumulations, and the applied stress, which will therefore be lower than in the forward direction. This implies that part of the initial work hardening is permanently removed by reverse straining.

Orowan has also discussed the problem of back stress in terms of the effects of two generalized types of obstacles. The build-up of loops around permeable obstacles results in continued hardening but at a much lower rate than for strong barrier hardening. Grain boundaries and cell walls may be

considered as weak obstacles in single-phase metals, compared to strong particles in two-phase alloys. It is generally true that the permanent softening effects observed in most single-phase metals are much smaller than those observed in dispersion hardening alloys.

3.2.1.2 Fisher et al's Model

Fisher et al (40) have treated the work-hardening problem for a simple case, that of a random distribution of rigid obstacles of circular section in two dimensions. The passage of each dislocation leaves behind an Orowan dislocation loop round each particle intersecting the glide plane. Fisher et al have pointed out that such loops will exert a shear stress on the matrix opposing further slip. Assuming the spacing of dislocation sources to be large compared to the spacing of accumulated loops, a uniform distribution of particles was shown to give rise to a hardening stress increment ($\Delta\tau_H$) so that,

$$\Delta\tau_H = 3\mu\frac{n}{R} f^{3/2}$$

where, n = number of loops per particle;

R = particle radius;

f = volume fraction of particles.

This stress field is reversible and is considered as a back stress which assists deformation in the reversed direction. Fisher et al's model neglects the possibility of cross-slip and therefore the relaxation of highly developed back stresses around particles. Thus, it overestimates the B.E.

in the two-phase alloys.

3.2.1.3 Model of Tanaka and Mori

Tanaka and Mori (41) have developed a theory to explain the work hardening behaviour of crystals with non-deforming particles or fibers. The theory is based on the stability of a material considering the effect of the applied stress on the Gibbs free energy. Internal stresses are built up around the particles because of the constraining effect on them by the uniformly deformed matrix. The theory predicts a linear hardening in the form:

$$\sigma = \sigma_o + \frac{2\gamma f \mu \varepsilon_p}{1-f}$$

where, σ = applied stress;

σ_o = initial yield stress;

μ = shear modulus;

ε_p = the plastic strain in the composite;

γ = a geometrical term, $7-5\nu/15(1-\nu)$ for spherical particles where ν is the Poisson's ratio.

The theory predicts an elastic back stress of $2\gamma f \mu \varepsilon_p / (1-f)$ which acts to help deformation in the reverse direction. Brown and Stobbs (42-46) have indicated that Tanaka and Mori's theory provides a lower bound for the strength because any additional heat production will increase the flow stress.

3.2.1.4 Brown and Stobb's Models

Brown and Stobb (42-46) have developed two models to

account for work-hardening behaviour in copper-containing spherical particles of silica. The first model (elastic model) assumes no plastic relaxation around the particles while the second one takes into account the role of plastic relaxation at the particles.

In the elastic model, plastic relaxation does not occur, so every Orowan loop remains as a shear loop around the particles. Brown and Stobb showed that, if a volume fraction f of the material is only elastically strained then a uniform back stress of magnitude $\sim\mu\varepsilon_p f$ exists together with locally fluctuating, inhomogeneous stresses of both signs. In the linear hardening region, the flow stress is given as:

$$\sigma = \mu\varepsilon_p f + \sqrt{\frac{6}{\pi}}\,\mu\varepsilon_p f^{3/2} + 2\sigma_o$$

which shows that for small volume fractions, the image stress is primarily responsible for the hardening. Brown and Stobbs showed that the work-hardening predicted by this model is about three times larger than that experimentally observed because of the hypothetical assumption of no plastic relaxation. They have also emphasized that the work hardening described by the model is unstable with respect to unloading, and that reverse plastic flow will occur as long as the image stress is greater than the Orowan stress, so that a very large proportion of plastic strain would be reversible. In the model accounting for plastic relaxation (45) the Orowan loops around the particles act together to produce large stresses in the neighbourhood of the particles. In order to lower these elastic stresses, plastic relaxation may take

place by local climb of dislocation loops, or the screw segments can cross slip, to produce prismatic loops. Also various processes involving secondary slip can occur as proposed by Ashby (47). All these processes of plastic relaxation lower the work-hardening rate by lowering the local stresses at the barriers.

Brown and Stobbs have emphasized that at small strains and small particles only primary dislocations are involved in the stress-relief process. They invoke Hirsch's mechanism (48-49) which proposes that when the cross-slip occurs, a shear loop is converted into two equal and opposite prismatic loops, and the line length of dislocation is increased.

Brown and Stobbs also showed that at large particles and large strains the stress-relief mechanism involves the generation of secondary dislocations and a plastic zone containing a high density of forest dislocations builds up in the neighbourhood of particles. The plastic zones have two effects: they harden the matrix directly and they inhibit the local slip which is required to relieve the elastic stresses. Thus, the presence of plastic zone prevents full plastic relaxation, and gives rise to a localized elastic stress field with its accompanying image stress which acts as a back stress.

With the simple assumption that the flow stress consists of three additive components: an Orowan stress (σ_o), a Forest hardening, and a back stress. Brown and Stobb's treatment predicts a back stress in the form:

$$\sigma = \sigma_o + \sqrt{3}\alpha\mu f^{\frac{1}{2}} \frac{\sqrt{8b\varepsilon_p}}{\pi R} + \alpha\mu f \left(\frac{8\pi b}{\alpha^2 \varepsilon_p R}\right)^{1/8} \frac{\sqrt{8b\varepsilon_p}}{\pi R}$$

where α is a constant $(\frac{1}{3} \sim \frac{1}{5})$.

This model provides the most quantitative treatment to the problem of work hardening in two-phase alloys. It predicts a strength in one direction of about $2f^{\frac{1}{2}}$ that in the opposite direction. The theory treats the problem of spherical hard particles in a soft matrix and does not account for the effect of particle shape.

In the case of all the models mentioned here, the degree of correspondence between experimental data and theoretical predictions has been mixed. Even the sophisticated model of Brown and Stobbs does not provide an a priori account of the actual behaviour[6]; invariably, some measurements are made on the material in its deformed state in order to assign numerical quantities to coefficients in the theoretical expressions. It is also to be noted that problems exist with the experimentation since it is not easy to devise controlled laboratory tests which permit complex loading paths.

3.2.2 Methods of Measuring the Bauschinger Effect

There have been several proposals in the literature to define a parameter which can be used as a quantitative measure of the Bauschinger effect. Among these are, the difference between forward and reverse flow stress (Bauschinger stress), the Bauschinger strain, the Bauschinger effect

factor, the Bauschinger effect parameter, the average Bauschinger strain, the Bauschinger strain parameter, the Bauschinger stress parameter, the Bauschinger energy parameter and the permanent softening stress. These are individually discussed below.

3.2.2.1 Bauschinger Stress

The simplest and, from a theoretical standpoint, the most easily interpreted measure of the B.E. is the difference between the forward and reverse flow stresses (Bauschinger stress). Assuming that the same mobile dislocations which contributed the last portion of forward flow are the first to move on reversal, then the difference between the forward and reverse flow stress is a direct measure of the value of the back stress. Unfortunately, the stress-strain curve for unloading and stress reversal is almost always one of continuous curvature which makes it impossible to accurately measure the onset of reverse plastic deformation. In general, it is difficult to accurately measure the elastic modulus or even to roughly estimate (<15%) the reverse flow stress.

The Bauschinger effect is thus more than just a stress lowering effect.

3.2.2.2 Bauschinger Strain

Woolley (50) and Buckley and Entwistle (51) have presented their results on B.E. of pure metals in terms of Bauschinger strain, β_μ, as defined in Figure 3.14. According to them, an annealed specimen is stressed in tension

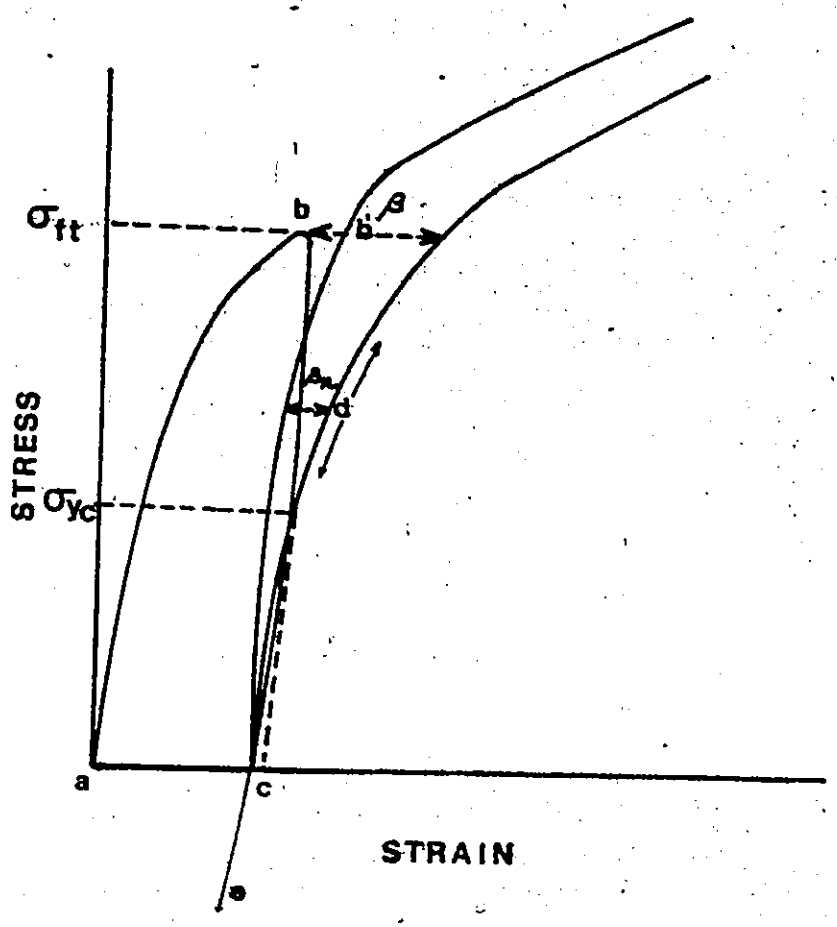

Bauschinger Strain, β_μ (Woolley and Buckley and Entwistle (51)).

Bauschinger strain, β (Abel and Muir (56)).

Figure 3.14 Schematic diagram showing Bauschinger strain as measured by different workers.

along ab and then unloaded to c and the tensile stress is reapplied to the same value b, giving the curve cb'. After unloading, the specimen is now stressed in compression along ce, the reverse strain curve, which is plotted in the same direction as cb'. Then the Bauschinger strain, β_μ, can be expressed as the strain difference between cd and cb' at an arbitrarily chosen stress of n times the prestress value where n is either 3/4 or unity.

This method has been criticized by a number of workers (54,55,56), because the shape of cd varies in a complex manner and the Bauschinger behaviour depends upon the value of n selected.

Abel and Muir (56) have modified this definition of Bauschinger strain, β, to "the amount of strain required to raise the stress level in the reverse direction to that of the forward direction." This is also shown in Figure 3.14. This is similar to the Woolley definition with n=1 except that Woolley measures the strain from the tensile re-load curve whereas Muir and Abel measure it from the unloading curve.

3.2.2.3 Bauschinger Effect Factor

Juniche et al (53) proposed this parameter as a measure of the B.E. in the form,

$$\text{Bauschinger Effect Factor, BEF} = \frac{\sigma_{ft} - \sigma_{yc}}{\sigma_{yc}}$$

where, σ_{ft} = the forward flow stress just before

reversal;

σ_{yc} = the yield stress in compression corresponding to 0.2% offset in the reverse direction (Figure 3.15).

The 0.2% offset stress is easier to measure than the true reverse stress, but is somewhat arbitrary.

Milligan et al (68) have defined Bauschinger effect factor in a slightly different manner as follows:

$$BEF = \frac{\text{Flow stress in compression (0.2 pct offset)}}{\text{Maximum flow stress in tensile prestraining}}$$

or,

$BEF = \sigma_{yc}/\sigma_{ft}$, this is shown in Figure 3.15.

Thus, the Bauschinger effect factors suggested by Juniche et al (53) and Milligan et al (68) are opposite. In the former case, the BEF increases with increasing B.E. whereas in the latter case, it decreases with increasing B.E. In addition, in both these approaches, due to yield stress difference in different materials, difficulty arises in comparing the Bauschinger effect of different materials as a function of prestrain.

3.2.2.4 Bauschinger Effect Parameter

The Bauschinger effect parameter, proposed by Ibrahim and Embury (54), takes into account the yield stress of the material, that is:

$$\text{Bauschinger Effect Parameter, BEP} = \frac{\sigma_{ft}-\sigma_{yc}}{\sigma_{ft}-\sigma_{o}}$$

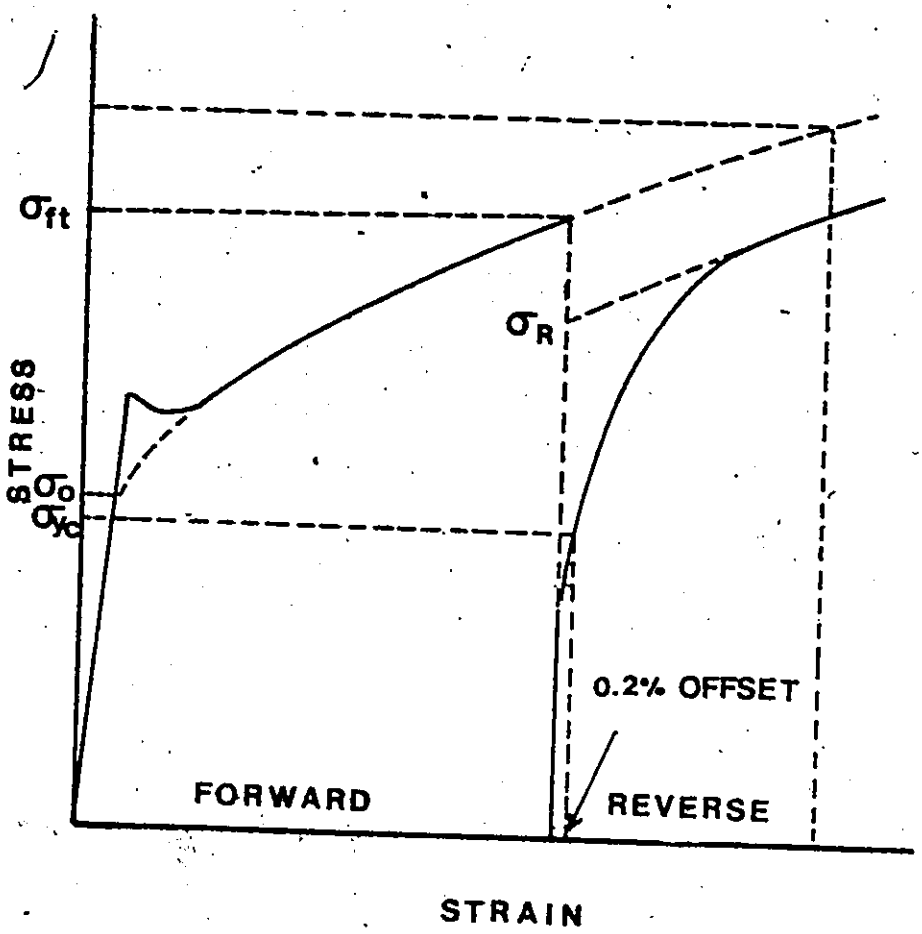

Bauschinger Effect Factor;

1) Juniche et al (53) = $(\sigma_{ft}-\sigma_{yc})/\sigma_{yc}$

2) Milligan et al (68) = σ_{yc}/σ_{ft}

Bauschinger Effect Parameter, BEP = $\dfrac{\sigma_{ft}-\sigma_R}{\sigma_{ft}-\sigma_o}$

Figure 3.15 Schematic diagram showing Bauschinger effect factors and the Bauschinger effect parameter.

where $\sigma_{ft}-\sigma_{yc}$ is equal to twice the back stress σ_B. Since σ_o is the initial yield stress (or friction stress) of the material, $\sigma_{ft}-\sigma_o$ is the work hardening accumulated in the forward direction. The BEP has been described as "the reversible fraction of work hardening", i.e., twice the backstress stated as a fraction of forward work hardening.

In this method, σ_R , is determined by extrapolating the part of the reverse curve, which is parallel to the forward curve, back to zero strain as shown in Figure 3.15. σ_o is estimated by extrapolating the part of the stress-strain curve corresponding to homogeneous deformation back to zero plastic strain using a log-log plot.

3.2.2.5 Bauschinger Strain Parameter

The Bauschinger strain parameter, B_ε has been defined by Abel and Muir (56) as:

$$B_\varepsilon = \frac{\text{Bauschinger Strain}}{\text{Plastic Prestrain}}$$

or,

$$B_\varepsilon = \frac{B}{\varepsilon_p}$$

According to them, when $B_\varepsilon = 1.0$ the prestrain is fully reversed and no strain hardening can have taken place. The value of B_ε generally lies below 1.0 although values larger than 1.0 are possible for some materials. They predict a maximum value of 2.0 when all the mobile dislocations are involved in reverse flow and when all are displaced by twice the distance covered during prestrain. This parameter

is shown in figure 3.16.

3.2.2.6 Bauschinger Stress Parameter

The original Bauschinger effect was described as a yield stress lowering effect. This parameter, also proposed by Abel and Muir (56) relates yield reduction to the pre-stress as follows (Figure 3.16):

$$\beta_\sigma = \frac{\Delta\sigma}{\sigma_{ft}}$$

where the yield reduction $\Delta\sigma = \sigma_{ft} + \sigma_{yc}$ in which σ_{ft} is the prestress and σ_{yc} is the reverse yield stress as described earlier. When plastic flow takes place during unloading σ_{yc} is positive so that β_σ will be larger than 1.0, with a theoretical maximum of 2.0 when plastic flow starts on reversal of the load σ_{yc} will be negative and β_σ less than 1.0.

3.2.2.7 Bauschinger Energy Parameter

This parameter has also been proposed by Abel and Muir (56). They conclude on the basis of their results that neither stress nor strain, can independently provide an adequate measure of the Bauschinger effect. They suggest an approach based on the areas on the stress-strain plot, having dimensions of work per unit volume. The shaded area in Figure 3.16 can be taken to represent the energy saved in achieving a certain amount of deformation in reverse loading, as compared with the energy which would have been required to achieve the same increment of deformation in the absence of a Bauschinger effect, assuming isotropic work

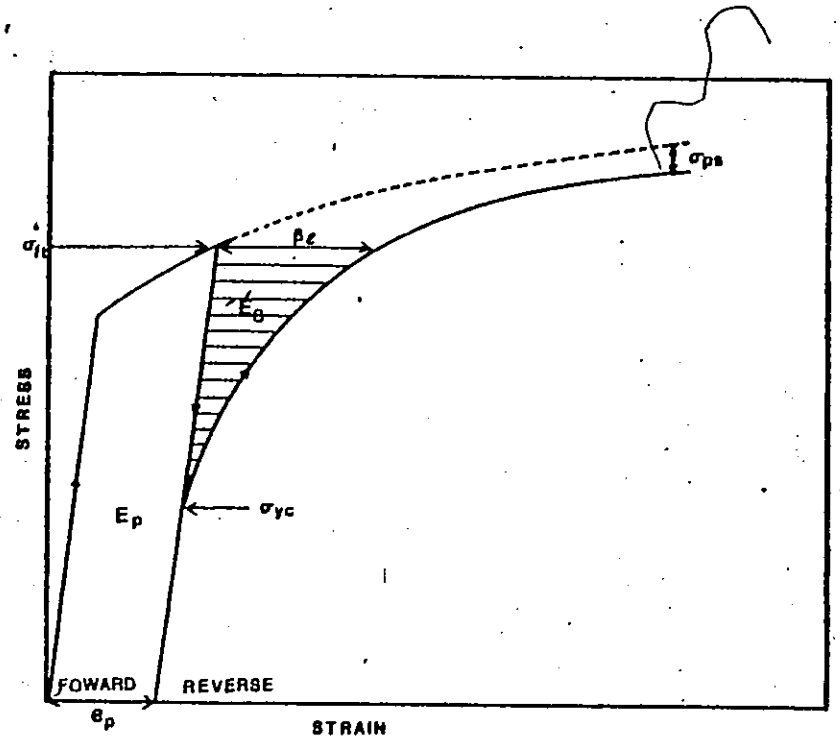

Bauschinger Strain Parameter, $\beta_\varepsilon = \beta/\varepsilon_p$

Bauschinger Stress Parameter, $\beta_\sigma = \frac{\sigma_{ft}+\sigma_{yc}}{\sigma_{ft}}$

Bauschinger Energy Parameter, $\beta_E = E_\beta/E_p$

Average Bauschinger Strain, ABS $= E_\beta/\sigma_{ft}$

Figure 3.16 Schematic diagram showing Bauschinger strain parameter, Bauschinger stress parameter, Bauschinger energy parameter and the average Bauschinger strain.

hardening . The Bauschinger energy (energy saved) is defined as E_s and the energy expended during the prestrain as E_p. The ratio of these, $\beta_E = E_s/E_p$, has been taken as a measure of Bauschinger effect.

3.2.2.7 Average Bauschinger Strain

The Average Bauschinger Strain, ABS, has been defined as the area between the elastic unloading curve and the reverse curve up to a stress equal to the forward stress, E_s divided by the maximum forward prestress σ_{ft}.

$$ABS = \frac{E_s}{\sigma_{ft}}$$

ABS is set equal to the shaded area in Figure 3.16, divided by maximum prestress and hence it gives an average width (ϵ) during the reverse flow. E_s was described earlier in the previous section as the energy saved in achieving a certain amount of reverse deformation. ABS has units of strain as it is a ratio of energy and stress. This method is an attempt to define a parameter which allows comparison of widely different reverse curve shapes. This method has been utilised by Tseng et al (73) for measuring the B.E. in dual phase steels.

The different proposals for measuring the B.E. have resulted in considerable confusion in comparing different results, and there is disagreement with respect to the merits of any particular method over the others. As a result, a number of workers have expressed their results in terms of more than one method (56,74).

In the next section the permanent softening stress as a measure of Bauschinger effect is described. This approach has been widely accepted and has been used to characterize the back stress as a function of prestrain in a wide range of metals and alloys.

3.2.2.9 Permanent Softening Stress

McClintock and Argon (57) have defined a 'permanent softening parameter' as the difference in the (absolute) values of flow strength, for continued forward and for reverse straining, measured at the same total strain and beyond the point at which the two flow stress curves become approximately parallel (Figure 3.16). This parameter gained credence when the x-ray work of Wilson (58) and Wilson and Konnan (59) found the back stress to be about half the amount of permanent softening. This relationship between σ_B and σ_{ps} has also been theoretically supported by an approximate 'shake down' model consisting of microscopic parallel elastic-plastic elements (60).

A difficulty with this method is that the prestrain curve must be accurately extrapolated to obtain meaningful results. Very few authors discuss how this extrapolation was performed. Most of them simply drew curves parallel to other similar specimens pulled at higher prestrains in tension. In materials with the sample-to-sample variability of steels, this practice is quite questionable.

In the present work, the permanent softening parameter, σ_{ps}, was used as a measure of the Bauschinger effect

but a better extrapolation technique has been devised.

3.2.3 Simple Empirical Representation of The Back Stress as a Function of Prestrain

A number of recent papers (62-64) have attempted to establish a relationship between the prestrain and the magnitude of the Bauschinger effect. Kishi and Gokyu (62) have expressed their results in terms of a power relation:

$$\tau_B = k\nu_p^m$$

where τ_B is the difference between maximum applied shear stress and reverse shear stress at a plastic shear strain ν_p, and k and m are constants. In their investigations, a number of materials including spherodized and normalised plain carbon steels were found to obey this relationship. Kishi and Tanabe (63) have confirmed the above relationship for the case of both torsion and tension-compression samples.

Gupta and Kodali (64) have expressed their experimental results in disagreement with the above relationship and have proposed the following expression:

$$\sigma_B = m\ell n\varepsilon_p + k$$

where σ_B is the Bauschinger stress defined as the difference between the forward flow stress, σ_F, after some forward prestrain, ε_p, and the yield stress, σ_R in the reverse direction. It is not clear from their paper how σ_R was measured, whether at zero strain or 0.1% reverse offset, or by some other method.

Recently Moan and Embury (65) have presented arguments which suggest that the relationship between the

Bauschinger stress and the prestrain in two phase alloys cannot be valid over a large strain range. At small strains, the deformation is unrelaxed and the Bauschinger stress (or the long range back stress, or the mean stress in the matrix) shows a linear dependence on the prestrain. As the prestrain increases some of the subsequent deformation becomes relaxed and the linear dependence on prestrain is no longer valid. The onset of relaxation is shown in Figure 8 of the paper by Atkinson et al (45).

Since the character of the deformation process changes during the strain history, it is unlikely that a single equation will suffice to describe the relationship between the Bauschinger effect and the prestrain.

3.2.4 The Bauschinger Effect in Steels

Several workers (50,51,52) have found that the magnitude of the back stress and hence the Bauschinger effect increases with increasing volume fraction of rigid particles for a given size and shape of the particles. Brown and Stobb's theory predicts such proportionality. Junische et al (53) measured the B.E. in terms of Bauschinger Effect Factor, BEF and found a larger B.E. in steels with high pearlitic content than those with low pearlitic content, but the effect was not sensitive to lamellar spacing. Kamakura (52) measured the B.E. in terms of Bauschinger strain and found a reduced B.E. in carbon steel of spherodized pearlite compared with the same carbon steel with lamellar pearlite.

The effect of grain size on the Bauschinger effect in steels has been investigated by a number of workers (66, 67). Harrison et al (66) observed an independence of Bauschinger effect on the grain size in C-Mn steels. A similar observation was made by Jamieson and Hood (67) in the case of HSLA steels.

3.2.4.1 Effect of Prestrain on the B.E.

There have been a few attempts towards establishing a general relationship between the Bauschinger stress and prestrains in addition to those discussed in 3.2.3. Jamieson and Hood (67) studying the B.E. in HSLA steels found an increased Bauschinger stress with increasing prestrain. The Bauschinger effect factor, BEF, was reported to saturate after a prestrain of 4%, for pearlitic contents ranging from 21 to 40%. Similar proportionality of the B.E. and torsional prestrain was earlier observed by Kamakura (52) in spherodised steels for prestrains less than 5%. Milligan et al (68) also observed a nonlinear increase in Bauschinger effect with prestrain until saturation was reached at a prestrain of about 3.5% for pearlitic, bainitic and martensitic structures obtained from the heat treatment of a 4340 steel.

3.2.5 Bauschinger Effect in Dual Phase Steels

The Bauschinger effect in dual phase is of interest for two reasons. Firstly, dual phase steels consist of a mixture of a soft ferrite matrix and hard non-deforming martensitic particles. A large Bauschinger effect has been observed in similar two phase alloys with a strong non-

shearable second phase (52,55,56). Secondly, the transformation of the austenite phase into martensite in dual phase steels occurs such that the ferrite phase must plastically deform to accommodate the accompanying volume expansion (~2 to 4 percent) (69,70). As a result, both a high dislocation density and residual stresses are generated in the ferrite phase immediately surrounding the martensite particles. The residual stress patterns are on too small a scale to be directly measured, but a theoretical analysis indicates that their value would be of the order of the yield strength of the ferrite out to the edge of the plastic zone and would decay exponentially (71) beyond that region.

Gerbase et al (72), Tseng and Vitovec (73) and Goel et al (74), have recently attempted to study the Bauschinger effect and deformation behaviour of dual phase steels. Gerbase et al (72) have utilized the Bauschinger effect as a method of measuring the back stresses generated by the incompatibility of plastic deformation between ferrite and martensite. The volume fraction of martensite in their steels varied from 0.10 to 0.17. Their results, presented in Figure 3.17, indicate that in the range of very small plastic strains (~0.3%), the permanent softening parameter, σ^{ps}, increases rapidly with imposed plastic strain until a saturation in back stress (or σ^{ps}) is reached at a prestrain of about 1%. This saturation presumably arises due to the onset of some alternative processes, such as, plastic relaxation around the martensite or plastic yielding of martensite. They have

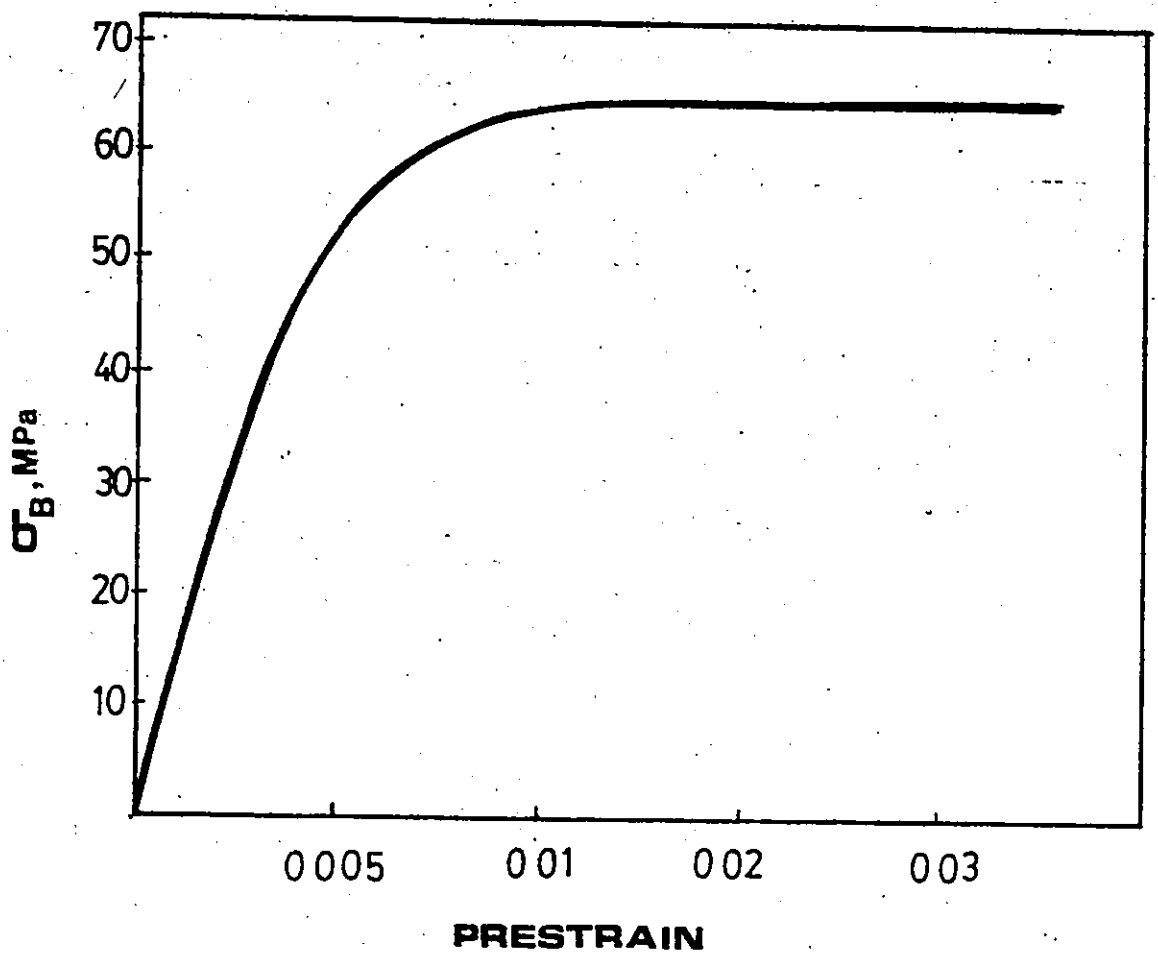

Figure 3.17 The back stress and unrelaxed plastic strain for a dual phase steel containing 10% martensite (72).

also developed a model for the work hardening of dual phase steels and its application has been shown to be in agreement with their experimental data.

Tseng and Vitovec (73), on the other hand, have observed no permanent softening (see Figure 3.18). The reverse curves become tangent to the extrapolation of the prestrain. According to them, however, a strong Bauschinger effect still persists as measured by an average Bauschinger strain, ABS. They have expressed their experimental results in terms of Mroz-Sowerby model for combined kinematic hardening and isotropic hardening. Their results indicate that the initiation of plasticity is governed by kinematic hardening and can be described by a simple parallel element model. Deviations from kinematic hardening become important as the deformation progresses. This deviation between experimental and theoretical reverse curves is less for specimens with low C martensites, i.e., with high intercritical annealing temperatures and vice versa as shown in Figure 3.18. They have plotted their experimental data in terms of reverse strain and average Bauschinger strain (ABS) as a function of prestrain. From these plots, (Figure 3.19) which seem to show a considerable scatter, they have concluded an increase of Bauschinger strain (or back stress) with increasing prestrain for low C martensite specimens (high intercritical annealing temperatures). In high C martensite structures, however, the values of reverse strain and ABS increases only slightly up to ~5% prestrain and then a saturation is observed.

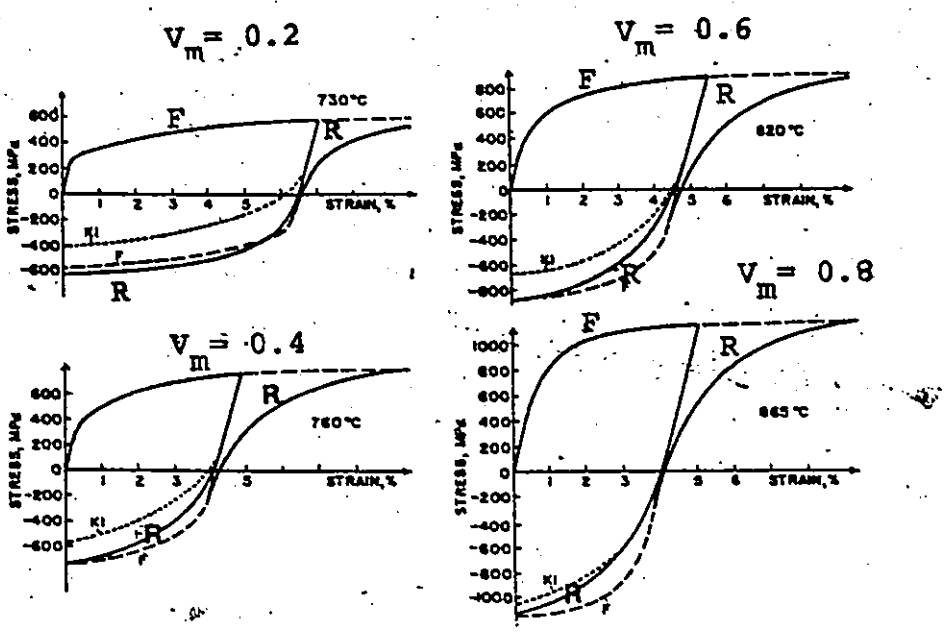

Figure 3.18 Tension-compression stress-strain curves for different intercritical annealing temperatures (and martensitic contents); KI-theoretical kinematic hardening curves, R-compression curves and F-tensile curves, V_M-volume fraction of martensite.

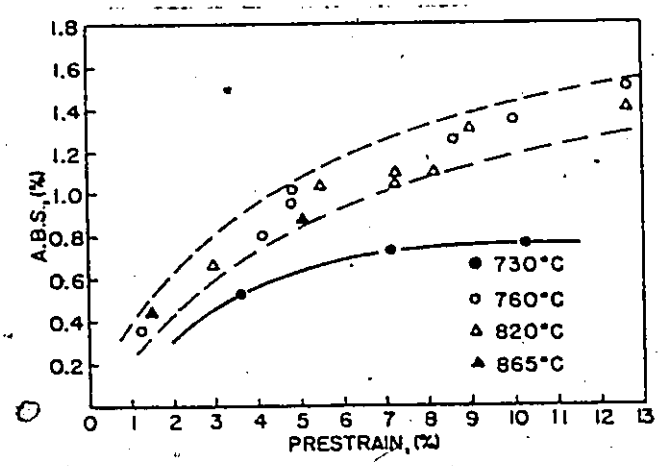

Figure 3.19 Average Bauschinger strain as a function of tensile prestrain.

Embury and Duncan (75) have discussed these results and re-emphasized that the initial hardening rate reflects the volume fraction of the second phase via the back stresses σ_B and also that the contribution of σ_B is fixed by the local strength of the martensite.

Goel et al (74) in their studies on the Bauschinger effect on dual phase steels have measured a number of different parameters described earlier as the Bauschinger strain β; the Bauschinger strain parameter, β_ε; the Bauschinger energy parameter, BEP; the Bauschinger effect factor, BEF and back stress, σ_B, as a function of volume fraction of martensite (15-35%) and the tensile prestrain. Their results indicate an increase of σ_B, β, β_ε, β_{EP} with an increase in martensite content up to about 20 volume percent, and then a decrease with further increase in the martensite content. The long range back stress σ_B and Bauschinger strain β are both found to increase with increasing tensile prestrain. The details of the measurement of different parameters or the explanation of their results is extremely limited. They make no mention of permanent softening.

In all the investigations dealing with the relationship between the permanent softening parameter and prestrain, no mention has been made of the way in which 'permanent softening, σ_{ps}, was measured. Accurate measurements will be possible only if the forward flow curve is clearly established beyond the prestrain interval as indicated in Figure 3.13. Such predictions of the forward flow curve, for accurate

measurement of σ_{ps}, have not been carried out previously.

In the present work, a number of empirical equations were studied for representing the forward flow curves of Bauschinger tests beyond prestrain region so that an accurate value of σ_{ps} could be measured.

3.3 Strength Differential Effect

It has previously been noted that the flow stresses of certain high strength steels are greater in uniaxial compression than in uniaxial tension. This phenomenon, known as strength-differential or S-D effect, has been studied by a number of workers (76-84). As a result of these studies it has been shown that the S-D effect exists in steels with martensitic, bainitic or Widmanstatten ferrite microstructures. A common feature of all these studies is a high density of dislocations. No S-D effect appears in annealed ferrite nor ferrite-pearlite mixtures nor in HSLA steels. This effect has not been reported, and apparently has not been previously investigated for dual phase steels. Figure 3.-20 shows the S-D effect in 4310 martensitic steel. As shown in the figure, the S-D phenomenon is manifested not merely in the initial yielding range, but also along stress-strain curve up to the maximum strain (~4%)(82).

The magnitude of the fractional strength differential, $2[(|\sigma_c|-|\sigma_T|)/(|\sigma_c|+|\sigma_T|)]$, has been estimated to be in the range 0.10-0.15 (79). The absolute magnitude of S-D effect in martensitic steels decreases by tempering as shown

in Figure 3.21 . The differential, however, persists to at least a true strain of 0.7 (79) and is substantially constant over this range. In addition, the magnitude of S-D effect is observed to increase with decreasing test temperatures below room temperature and to remain relatively constant with increasing plastic strain.

3.3.1 Theories of the S-D Effect

Hirth and Cohen (78) have discussed a variety of tentative explanations of the S-D effect. These include microcracks, residual stresses of both long-range and short-range types, deformation-induced transformation of retained austenite , Bauschinger effects arising from martensitic transformation and solid solution interaction. Several of the tentative hypotheses advanced by Hirth and Cohen (78) have been eliminated by experimental results. Among these are frictional effects during compression, deformation induced transformation of the retained austenite and microcracking. Hirth and Cohen (78) have also suggested a theory based upon the nonlinear elastic interaction between dislocations and interstitial carbon atoms. An effective modulus interpretation has been offered by Pampillo et al (85). An explanation for the observed temperature dependence of the S-D effect, based on a thermally activated double kink mechanism of dislocation motion, has been proposed by Fletcher et al (86).

Radcliffe and Leslie (87), based on their experimental results, have suggested that a relatively large volume expansion during deformation of martensite could lead to the

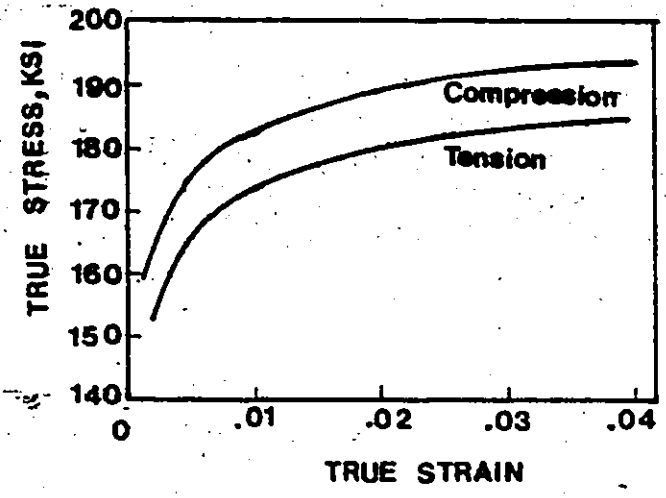

Figure 3.20 Stress-strain curve in tension and compression for 4310 steel (82).

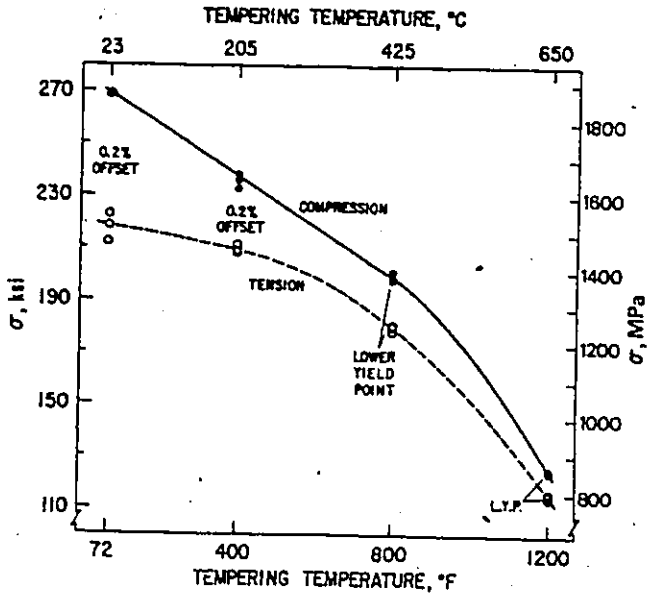

Figure 3.21 The effect of tempering on the yield strength of AISI 4330, quenched from 900°C. Time at 204, 425 or 650°C, 1 hr.; time at room temperature, 4 days (79).

S-D effect. This has been further investigated by Rauch et al (84) and Spitzig et al (82,83) Measurements of the pressure dependence of yielding and flow, and of the volume changes occurring during plastic deformation, have been made on as-quenched martensite (82), and maraging steels (83). The magnitude of S-D effect has been found to be independent of hydrostatic pressure or strain.

A complete review of the strength-differential phenomenon would require a comprehensive description of each of the tentative explanations of S-D effect, a detailed description of experimental results on different mechanisms as well as a review of various theories advanced to explain S-D effect. Such a detailed review covering different aspects of S-D phenomenon is beyond the scope of the present work and will not be attempted. It is, however, important to point out that no attempt has been made by any of the workers to correlate the strength-differential effect with any of the Bauschinger effect parameters. A discussion of strength-differential effect, pertinent to our results on Bauschinger tests will be attempted in Chapter 7.

CHAPTER 4

Experimental Methods

4.1 Materials

The chemical composition of the steel used in the present study was determined by x-ray spectroscopy (at Dominion Forge Ltd.) and the results are shown in Table 4.1

Table 4.1

Steel	Composition (wt%)									
	C	Mn	Si	S	Ni	P	Cr	Cu	V	Al
1020	0.14	1.08	0.20	0.045	0.06	0.02	0.08	0.17	Nil	Nil
1018	0.15	0.72	0.15	0.024	0.01	0.03	0.04	0.14	Nil	Nil

The steels used in the present study were nominally 1020 and 1018 commercial plain carbon steel rods of 0.5 inch diameter. The 1020 steel fortuitously had a Mn content of 1.08%, well above the 0.3 to 0.6% specified by the AISI. This made the production of dual phase steels much easier.

4.2 Heat Treatment

Isothermal and intercritical annealing heat treatments were done to obtain the dual phase structures. The sequence of heat treatment was shown earlier in Figure 3.1. These schemes illustrate the path by which the two phase ferrite-martensite final microstructures were obtained for isothermal and intercritical annealing methods. Commercial salt mixtures of NaCl, KCl and $BaCl_2$ in two different compositions (known as NUSAL and No. 800 Neutral salt, manufactured by

Park Thermal Ltd.) were utilized for the austenitizing and reaction salt baths respectively.

4.2.1 Procedure for Isothermal Reaction

Two salt pot furnaces were utilized for isothermal heat treatment. The specimens were heated in the austenite range (860-980°C) in one furnace and subsequently reacted in another furnace maintained at reaction temperatures which ranged from 650°C to 720°C. Nucleation and growth of ferrite takes place at this temperature.

Chromel-Alumel thermocouples, 102 cm long enclosed in Inconel 600 tubing and attached to a digital temperature readout were used for temperature measurement. The temperatures were maintained within ±3°C. Immediately after the isothermal reaction, the specimens were water quenched in a cold water tub, placed beside reaction bath, to transform the remaining austenite to martensite and thus obtain a dual phase microstructure of ferrite and martensite.

4.2.2 Intercritical Annealing

Intercritical annealing was also done in the salt bath. Specimens were held in the two phase ferrite-austenite temperatures region for about 15-20 minutes. During this period, the pearlite was transformed to austenite and an equilibrium amount of ferrite and austenite was formed. Subsequent water quenching resulted in a mixture of ferrite and martensite as in the case of isothermal reaction. The two microstructural features of primary interest were the ferrite grain size and volume fraction of

martensite.

4.2.3 Control of Ferrite Grain Size

The ferrite grain size primarily depends on the prior austenite grain size and the reaction temperature. The austenite grain size was generally kept small by heating the steel slightly above the AC_3 temperature and holding for a short time. Since the starting ferrite grain size was fairly small, no attempt was made to refine the austenite grain size by cyclic austenitizing treatment. The effect of reaction time and temperature on the ferrite grain size was studied. Small ferrite grain sizes were obtained by using a short soak at a low austenitizing temperature and a low reaction temperature.

4.2.4 Control of Volume Fraction of Martensite:

4.2.4.1 Isothermal Transformation

As mentioned earlier, the volume fraction of martensite formed depended mainly on the isothermal reaction temperature and holding time. A range of isothermal reaction temperatures and times were selected to obtain varying amounts of martensite. The isothermal reaction temperatures, in general, were below the eutectoid transformation line. No isothermal transformation diagram was available for either of the 1018 and 1020 steels used in the present study. The isothermal transformation diagram of a 1019 steel containing 0.79 Mn was thus used as a guideline for isothermal holding times (Figure 3.2). Reaction times in the range from 10 seconds to 60 minutes were tried in the early experiments

to determine the rate of austenite decomposition. It was found that holding times from 1 to 8 minutes produced the best structures, at reaction temperatures in the range of 660 to 700°C.

A similar experimental procedure was also adopted for establishing the time required for complete austenization at different temperatures in the austenite phase field. The specimens were heated in a salt bath for austenitizing temperatures in the range of 850°C to 970°C for 30 seconds to 60 minutes and then water quenched. The microstructures were examined and it was found that austenitizing time in excess of 1 minute was enough to obtain a complete austenization of the ferritic-pearlitic structure.

4.2.4.2 Intercritical Annealing

Specimens for intercritical annealing were held in the vicinity of 735°C for about 20 minutes to obtain about 25% austenite. The specimens were then quenched in water to obtain the required ferrite-martensite microstructure. Unfortunately, in some of the Bauschinger specimens, a ferrite plus martensite structure was not obtained. Instead a ferrite-spherodized pearlite structure was produced. This was not discovered until after the specimens were sectioned for metallography after testing. The probable cause of this was that the Inconel tubing shielding the thermocouple was found to be corroded and hot salt leaking into contact with the thermocouple appears to have given erroneous temperature readings.

4.3 Quantitative Metallography

4.3.1 Measurement of the Ferrite Grain Size

The linear analysis technique was utilized for its convenience and accuracy. In its simplest form, random lines of known length are superimposed over the micrograph and the number of intercepts are counted. Then, dividing the total length by the total number of intercepts and the magnification, the average grain size is obtained.

The situation becomes more complex when a second phase is introduced because the second phase (martensite in the present case) may have a different size distribution from the phase in which it is dispersed. In such a situation if an average grain diameter is obtained, irrespective of the phases present, then the value of the grain size obtained will not be a true value.

In the present work, the microstructure was traversed by random lines and the ferrite grain diameter was obtained by dividing the total length of the line in the ferrite by the number of ferrite grains traversed and by the magnification (88). Micrographs 20 x 25 cm were made up for ferrite grain size measurement. A transparent grid containing seven random lines (Figure 4.1) was superimposed on the micrograph and individual lengths of random lines traversed in the ferrite regions were digitized using an ALTEK digitizer fitted to a microcomputer. A simple computer program was then used to calculate the ferrite grain size (Appendix (III)).

Figure 4.1 Measurement of the ferrite grain size by linear intercept method (Mag. 100X)

4.3.2 Measurement of the Volume Fraction of Martensite

A point counting method was utilized for measuring the volume fractions of martensite because of its simplicity, accuracy and wide acceptability. In this method a regular grid is superimposed on the microstructure and the number of grid intersections that lie in the dispersed phase (martensite in the present case) is determined. The volume fraction of the dispersed phase is equivalent to the ratio of the number of grid intersections lying in the dispersed phase to the total number of grid intersections.

In the present work, a fine grid containing 33 x 26 points was superimposed on 20 x 25 cm magnified micrographs for accurate point counting.

4.4 Electron Metallography

4.4.1 Scanning Electron Microscopy

Scanning electron microscopy was used for the observation of fracture surfaces of specimens and for observing cracking of the second phase particles, and decohesion of the matrix-second phase interface. The use of SEM for these studies is desirable due to the greater depth of field and resolution of the SEM relative to the optical microscope. This work was done at the McMaster Medical Center.

The polishing technique applied was the same as for the optical microscopy, and the etching method was Picral for 20 to 30 seconds, followed by Nital at 2% for 5 to 10 seconds.

4.4.2 Transmission Electron Microscopy

TEM was utilized to observe the microstructure of dual phase steels at high magnifications. Samples for TEM were cut from the ends of tensile specimens. Disk shaped foils were cut and mechanically polished to a thickness of 0.15 mm. They were next chemically polished in a solution of 5 ml H_2O_2 and 95 ml of HF. Foils were finally electro-polished in a jet polishing apparatus (E.A. Fischione twin jet model) using a solution consisting of 20% perchloric acid and 80% methanol. The foils were examined in a JEOL 100 CX microscope operated at 100 kV.

4.5 Mechanical Tests

4.5.1 Tensile Tests

Tensile tests on different steel specimens were carried out using samples with the geometry sketched in Figure 4.2. An extensometer of 2.54 cm gage length was used for measurement of elongation. All the tensile tests were done an an Instron tensile testing machine using a crosshead speed of .0254 cm/min. The load vs. elongation curves were recorded for the entire period of deformation until fracture. Sectional areas were obtained from diameter measurements. Calibrations were performed at regular intervals to check the accuracy of the machine. Calibration curves were constructed and the error in the load values were estimated. These errors were found to be within ± 0.1 %.

Load elongation curves were digitized and the digitized data were used to plot the necessary curves as follows:

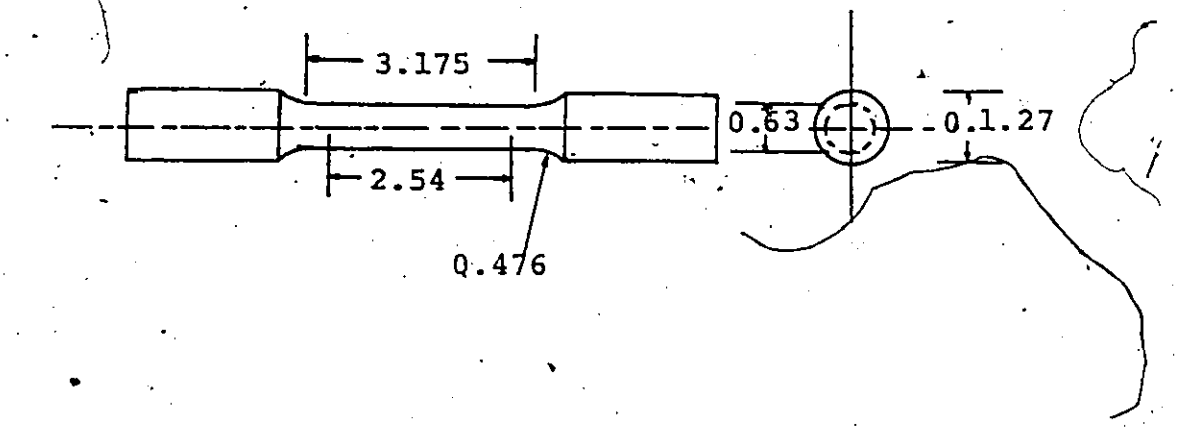

Figure 4.2 Specimen for the tensile test (All dimensions are in centimeters)

1) true stress vs. true strain;

2) log true stress vs. log true strain;

3) work hardening rate vs. strain;

4) log ($d\sigma/d\varepsilon$) vs. log ε;

5) log ($d\sigma/d\varepsilon$) vs. log σ.

These plots were used to draw conclusions about the deformation behaviour of dual phase steels at different strain levels. A detailed discussion on the use of these plots for studying the strain hardening behaviour of dual phase steels is presented in Chapter 6.

Computer programs needed to compute and plot the above-mentioned parameters were developed (Appendix III). An example of each of these plots is shown in Figures 4.3-4.7.

4.5.2 Bauschinger Tests

Specimens with the geometry sketched in Figure 4.8 were utilized. In order to reduce bending stresses, the load alignment fixture shown in Figure 4.9 was borrowed from Dr. R. Sowerby of McMaster University. The specimens were properly aligned in the grips prior to testing in the following manner: the lower threads of Specimen A were firmly screwed onto the lower assembly CD using vise grips. The upper threads on the specimen were then screwed into the upper assembly B as shown in Figure 4.9. The bottom chamber was then placed in the appropriate position on the cross-head beam and bolted down lightly. The beam was then moved slowly upward until the lower grip bell D attached to the bottom of the specimen, was properly placed inside the

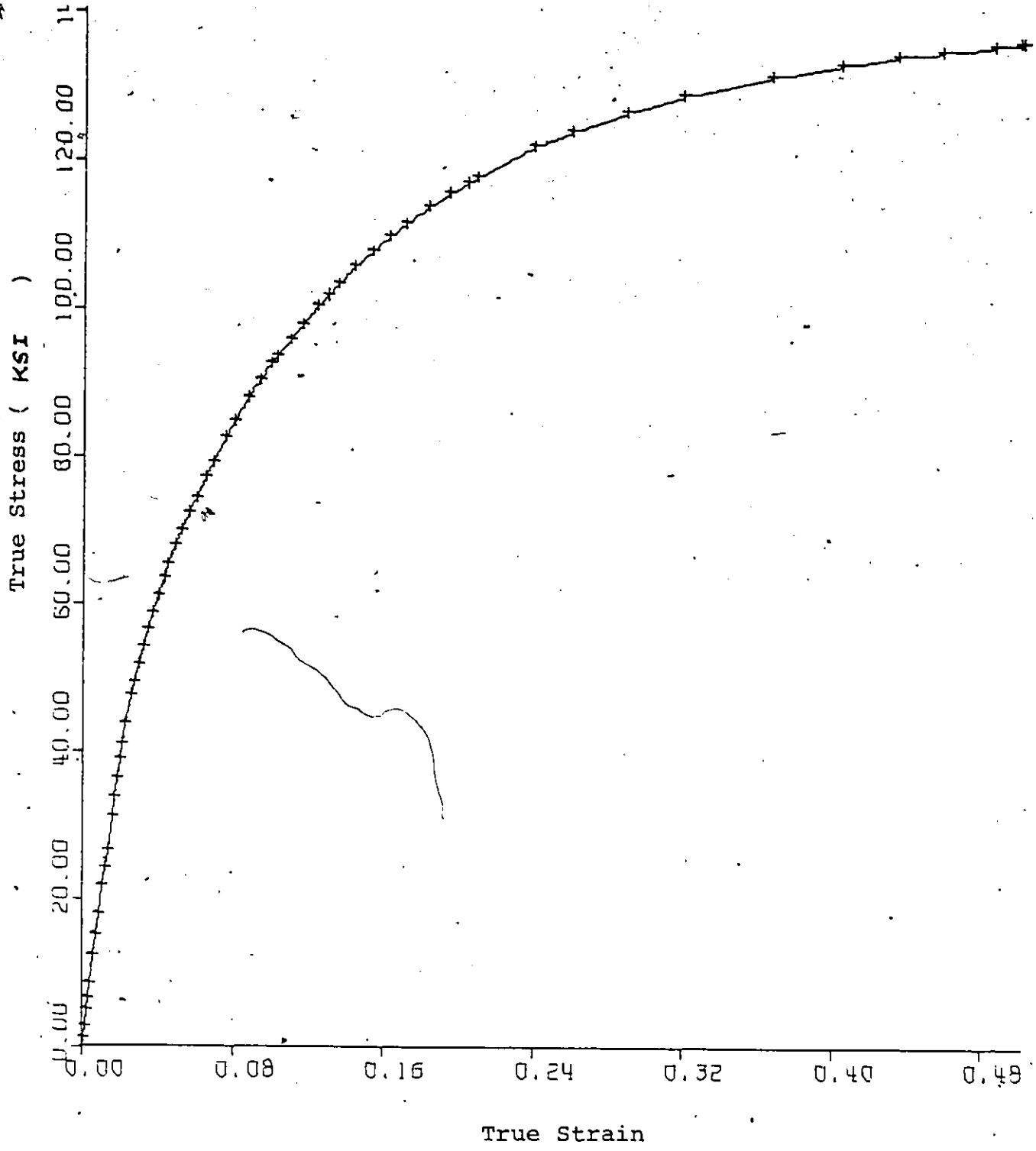

Figure 4.3 Computer generated plot of the true stress-true strain curve of a dual phase from the digitized load-displacement data.

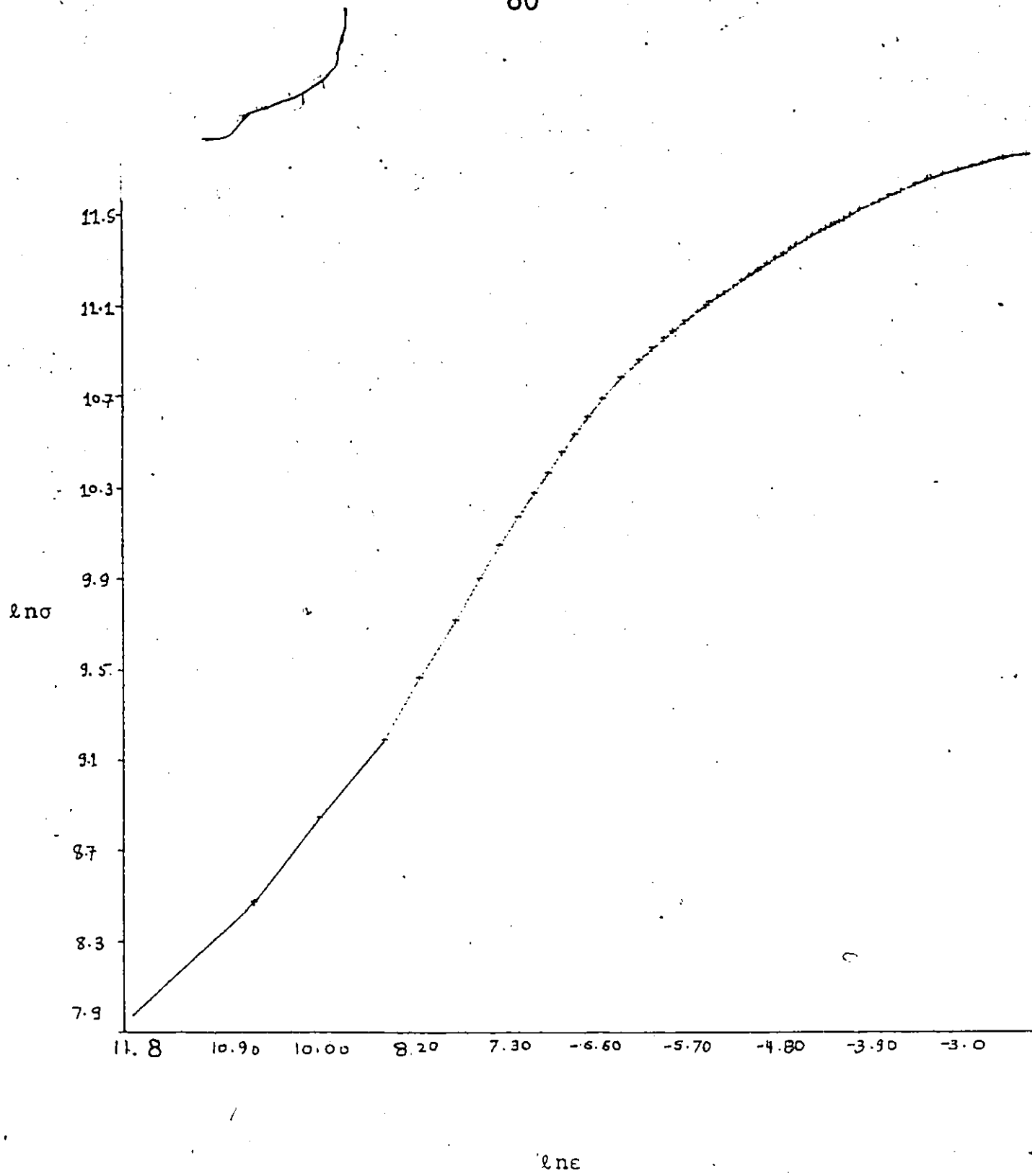

Figure 4.4 Computer generated plot of the ℓn stress vs. ℓn strain from the digitized load-displacement data.

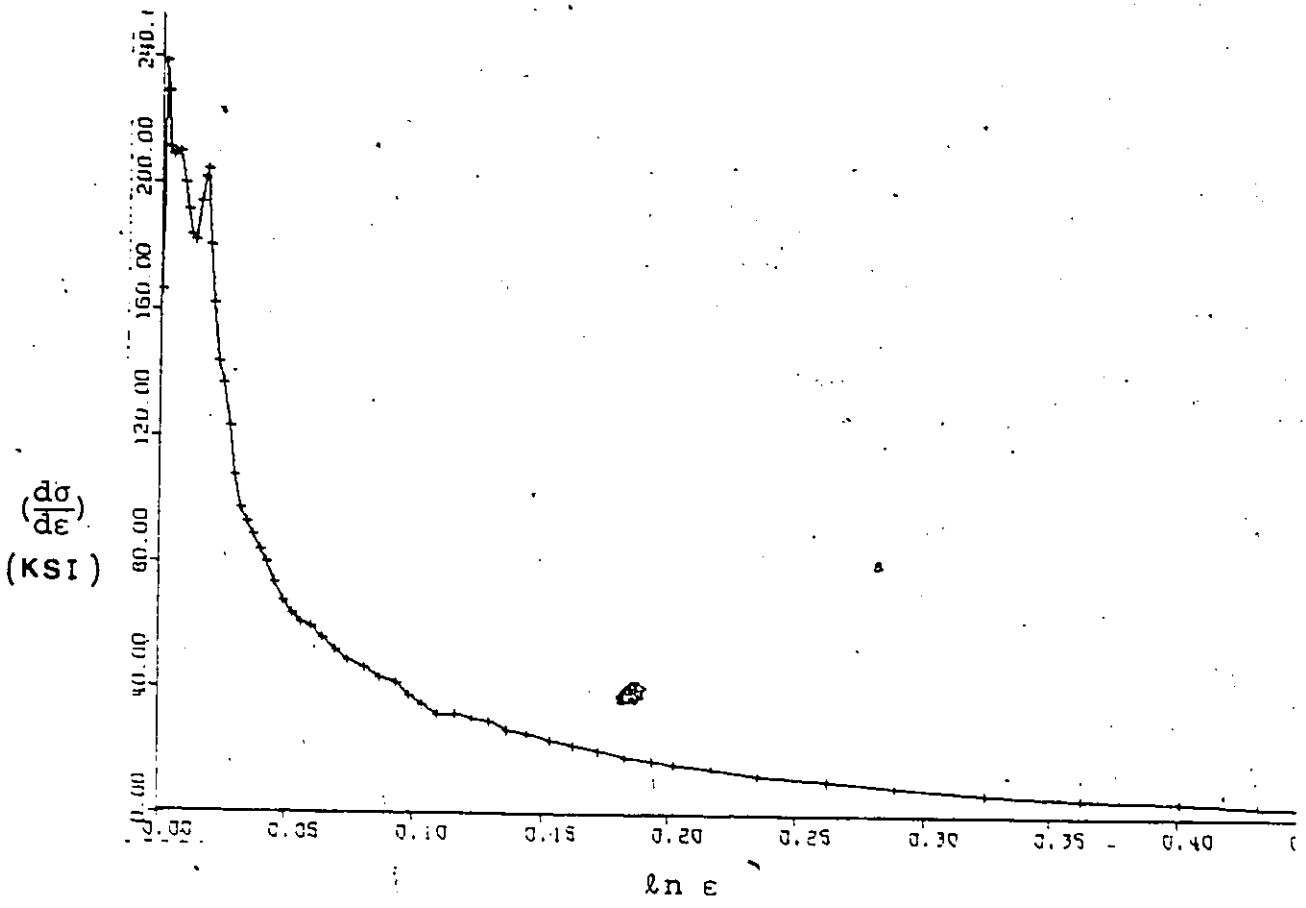

Figure 4.5 Computer generated plot of the work hardening rate vs. strain from the digitized load-displacement data.

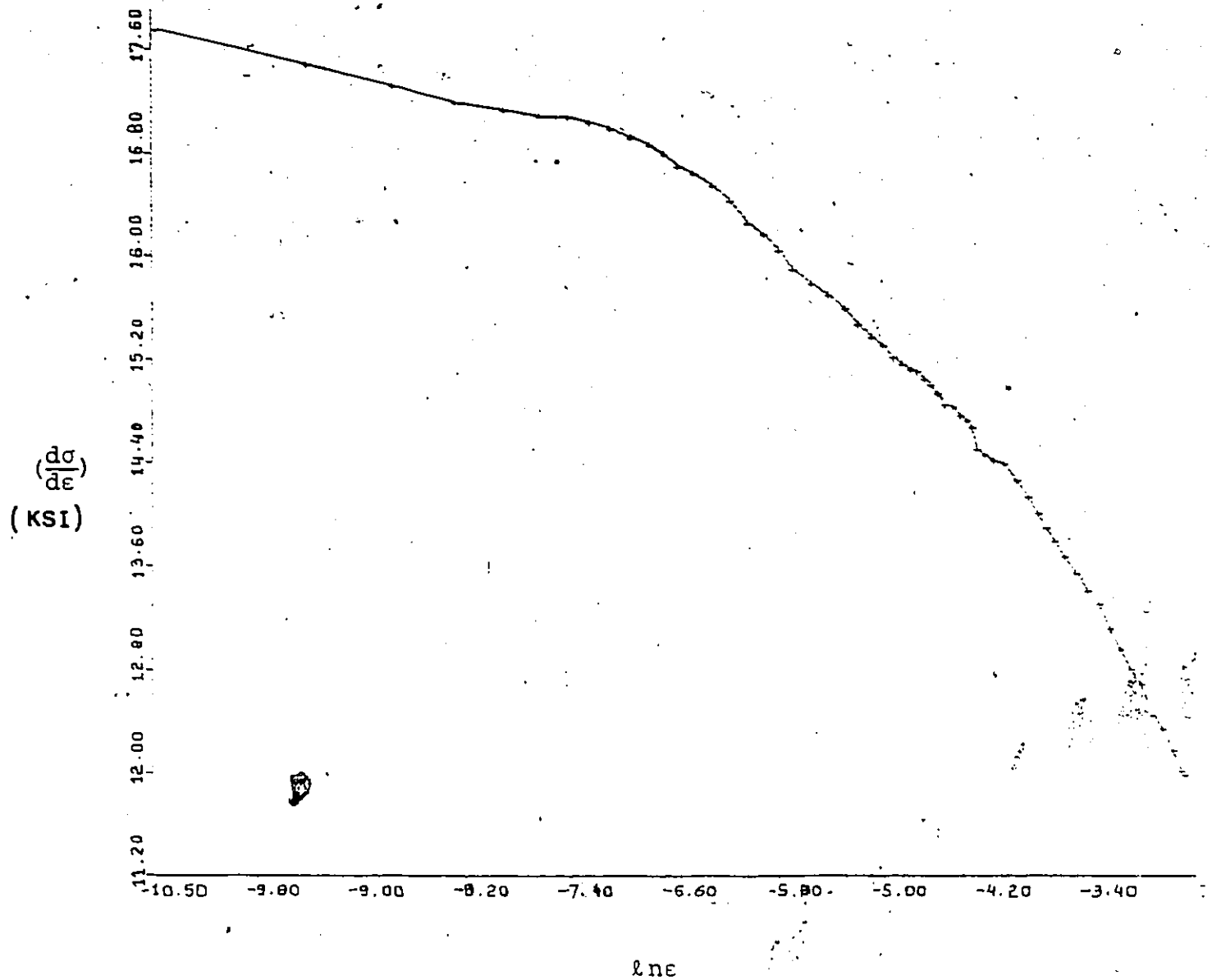

Figure 4.6 Computer generated plot of $\ell n(d\sigma/d\varepsilon)$ vs. $\ell n\varepsilon$ from the load-displacement data.

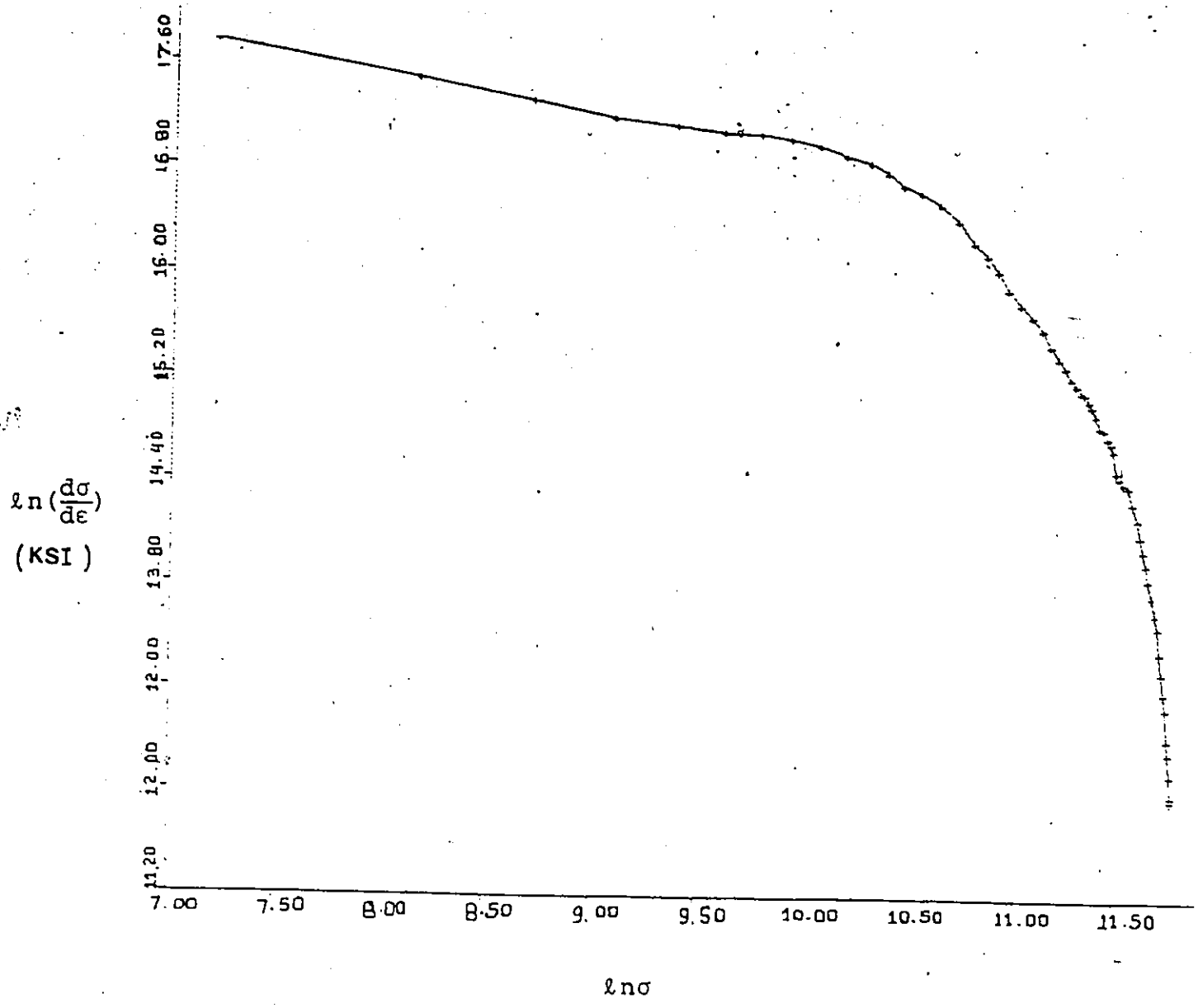

Figure 4.7 Computer generated plot of $\ln(d\sigma/d\varepsilon)$ vs. $\ln\sigma$ from the load-displacement data.

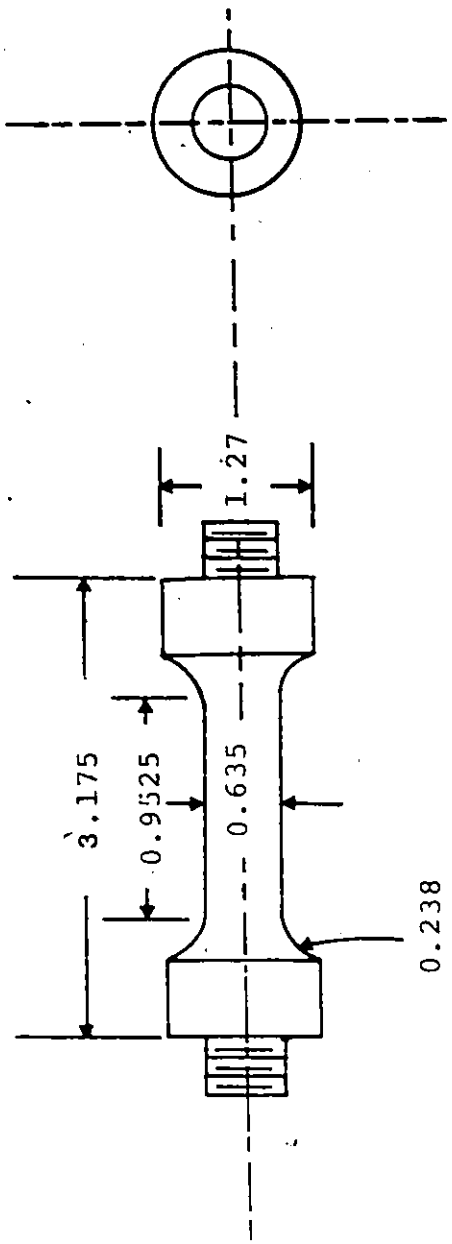

Figure 4.8 Specimen of the Bauschinger test. (All dimensions in centimetres).

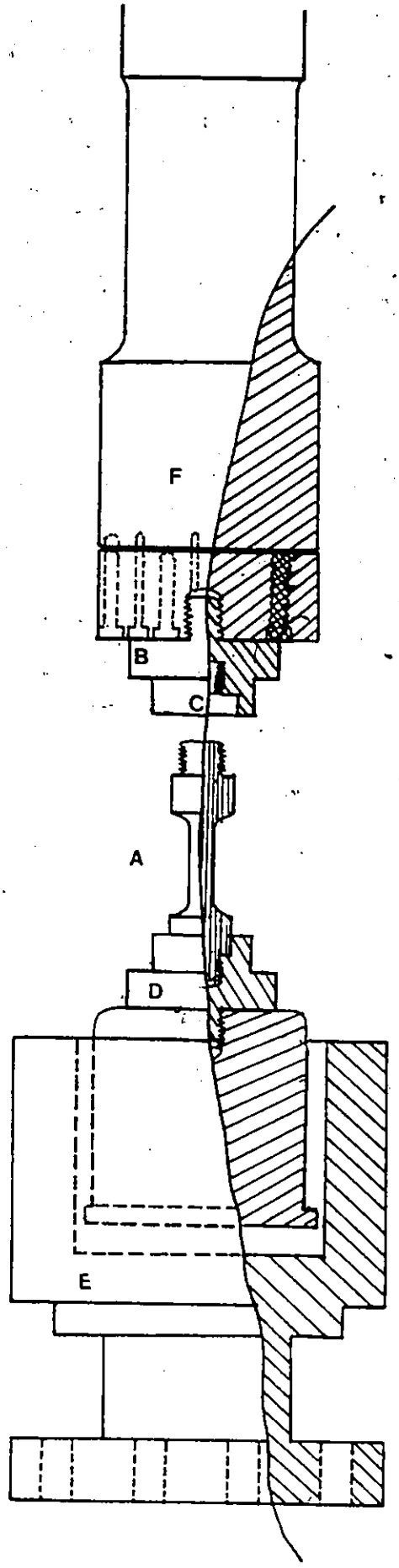

Figure 4.9 Load-alignment fixture used for conducting Bauschinger (push-pull) tests.

bottom chamber E. During this alignment procedure, the screws on the bottom chamber were tightened and the beam was moved up and down by about 5 cm until the bell did not rub against the chamber. If the bell did rub, then the upper grip was tilted relative to the upper loading rod F using the six screws in the upper assembly B to set the axis of the specimen accurately parallel to the direction of the Instron crosshead motion. Then the lower chamber E was again centered on the lower bell D and the clearance (0.5 mm) between them checked by the rub test described above. The lower chamber E was then lowered about 30 cm below the bell D and small pieces of Woods metal (a low melting point alloy of Pb, Sn, Sb, Bi) were then placed inside the bottom chamber E and the chamber was heated for a few minutes, with propane torches, until the Woods metal was molten. The beam was once again moved up to insert the middle assembly D into the molten metal chamber. Care was taken to move the beam slowly and not to compress the specimen accidently during this process. The load measurement system was turned on during the entire specimen mounting procedure so that any load felt by the specimen was recorded. During the time in which the Woods metal was freezing, the beam was adjusted slightly so that the specimen was not subjected to any substantial load. The specimen was cooled with water while the Woods metal was freezing to avoid any annealing of the specimen during freezing process. The specimen was kept cool to the touch ($<40^{\circ}C$). The Instron crosshead position was

adjusted periodically during the freezing and cooling period to compensate for differential contraction or expansion of the system.

The Bauschinger tests were performed at a crosshead speed of .0254 cm/min. The elongation was measured using a 0.95 cm. extensometer attached to the gage length, and the load-extension and load-compression graphs were obtained. Calibrations were done at regular intervals to check the accuracy of the machine. The probable error was estimated from the calibration plots and was found to be within ±0.125%.

Experimental graphs were digitized and converted into true stress-true strain curves from which other necessary curves and parameters were determined. The procedure for obtaining final Bauschinger plots for the measurement of the permanent softening parameter is presented in the beginning of Chapter 7.

CHAPTER 5

Results and Discussion of Tensile Tests

5.1 Results

In this chapter, the experimental results of simple tension tests are divided into three sections dealing with:

a) the isothermal heat treatment variables such as austenitizing temperature, austenitizing time, reaction temperature, reaction time and their correlation with the resulting microstructure;

b) the microstructural parameters such as ferrite grain size, volume fraction of martensite and their correlation with tensile properties;

c) the effect of tempering treatment on tensile properties.

Chapter 6 will discuss methods for more sophisticated analysis of tensile test curves. Chapter 7 presents results for uniaxial compression tests and Bauschinger tests.

5.1.1 Isothermal Heat Treatment Variables and Micro-Structure

In the as-received condition the microstructure of the steel bar comprised of pearlite in a polygonal ferrite matrix is shown in Figure 5.1.

Dual phase ferrite-martensite structures were obtained by isothermal transformation and also by inter-critically annealing. The isothermally annealed specimens were heated in the single phase austenite range of 850 to 980^{o}C for 0.5 to 20 minutes. They were subsequently

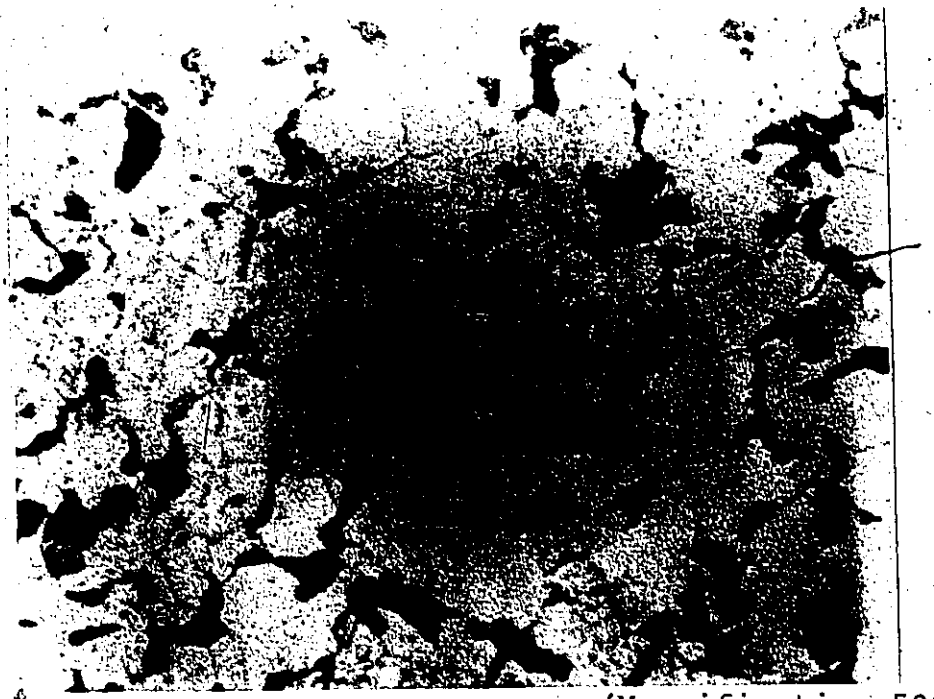

(Magnification 500 X)

Figure 5.1 Microstructure of the as received 1020 plain carbon steel showing free ferrite and pearlite.

reacted in the temperature range of 650°C to 724°C in the two phase ferrite-austenite phase field, for isothermal reaction times in the range of 1 to 60 minutes. The specimens were then water quenched. Thus a wide range of austenitizing and reaction times were utilized to obtain dual phase steels with varying ferrite grain size and martensitic content. An optical micrograph of an isothermally annealed dual phase steel is shown in Figure 5.2. The results of quantitative metallography along with the heat treatment variables are shown in Table 5.1.

The data in Table 5.1 was statistically analyzed using linear modelling and the results are presented in Tables 5.2 and 5.3. These tables represent respectively, the results of linear regression analysis of ferrite grain sizes and martensite volume fractions as a function of heat treatment variables; namely, austenitizing temperature, austenitizing time, reaction temperature, and reaction time. The following empirical equations were obtained by the linear regression analysis of the data:

$$FGS = 6.36 + 0.002A_{Temp} + 0.1A_{Time} - 0.0017R_{Temp} + 0.01R_{Time} \quad (5.1)$$

$$V_M = -59.5 + 0.05A_{Temp} - 0.4A_{Time} + 0.08R_{Temp} - 0.15R_{Time} \quad (5.2)$$

The results in Table 5.1 indicate that the ferrite grain size remained virtually constant for a wide range of heat treatment variables. The coefficients in Equation(5.1) also indicate the same trend. Amongst all the

Table 5.1

Heat Treatment of Tensile Specimens

Specimen	$A_{Temp.}$ (^{o}C)	A_{Time} (min.)	$R_{Temp.}$ (^{o}C)	R_{Time} (min.)	FGS (μm)	$V_{Mart.}$ (%)
3A	971.0	0.50	703.5	4.0	7.756	43.82
3B	939.5	0.50	699.5	4.58	7.827	47.43
3D	850.0	3.0	705.0	4.0	7.420	36.71
3E	856.0	20.0	704.5	4.0	9.9175	35.43
3H	882.0	4.0	656.0	4.0	7.069	33.68
3I	899.0	4.0	677.0	2.0	7.742	33.68
3J	908.0	8.0	680.5	4.0	7.0506	39.16
3L	902.0	2.0	707.0	4.0	8.2009	50.81
3P	893.0	4.0	697.5	30.0	9.0337	38.11
4A	976.5	3.0	704.5	4.0	8.594	39.97
4B	939.5	3.0	699.5	4.58	7.358	36.48
4C	854.5	1.33	706.3	4.0	8.2407	39.70
4D	853.6	8.5	706.0	4.0	7.1480	31.81
4E	818.0	3.0	701.5	4.0	8.0015	33.10
4G	880.0	4.0	856.0	2.0	7.2229	51.28
4K	900.0	2.0	705.0	2.0	6.7973	46.52
4L	898.0	2.0	707.0	4.0	8.4373	43.70
4M	904.5	1.0	710.0	1.0	6.212	51.39
4N	901.5	8.0	710.0	2.0	8.740	39.87
7A	890.0	4.0	699.0	60.0	7.807	30.88
7C	909.0	4.0	722.5	4.0	7.9719	42.54
7E	902.0	4.0	719.3	8.0	7.9750	39.76
7F	902.0	4.0	722.5	16.0	8.8348	38.57

Table 5.2

Linear Modelling of Ferrite Grain Size as a Function of Austenitizing Temperature, Austenitizing Time, Reaction Temperature and Reaction Time

$$FGS(\mu m) = 6.363 + 0.0025A_T + 0.10206A_{Time} - 0.0017R_{Temp.} + 0.0114R_{Time}$$

Specimen No.	Observed FGS (μm)	Predicted FGS (μm)	Residual (Difference)	Low 95% Confidence Limit for Mean	Upper 95% Confidence Limit for Mean
1	7.756	7.691	0.064	6.928	8.454
2	7.827	7.625	0.201	7.068	8.182
3	7.420	7.638	-0.218	7.015	8.261
4	9.917	9.399	0.518	8.041	10.756
5	7.969	7.908	0.060	7.251	8.564
6	7.742	7.891	-0.149	7.405	8.378
7	7.050	8.341	-1.291	7.770	8.913
8	8.200	7.664	0.535	7.267	8.061
9	9.033	8.162	0.870	7.489	8.834
10	8.594	7.960	0.633	7.144	8.776
11	7.358	7.881	-0.523	7.361	8.402
12	8.240	7.476	0.763	6.811	8.141
13	7.148	8.210	-1.062	7.631	8.789
14	8.001	7.563	0.437	6.663	8.463
15	7.222	7.529	-0.307	6.074	8.985
16	6.797	7.639	-0.842	7.221	8.058
17	8.437	7.654	0.782	7.253	8.055
18	6.212	7.528	-1.316	7.061	7.995
19	8.740	8.250	0.489	7.748	8.752
20	7.807	8.496	0.689	7.086	9.906
21	7.071	7.860	0.110	7.473	8.246
22	7.975	7.894	0.080	7.542	8.245
23	8.834	7.980	0.853	7.552	8.408

Note - Austenitizing temperatures (A_{temp}) and Reaction temperatures (R_{temp}) are in degree centigrade. Austenitizing times (A_{Time}) and Reaction times (R_{time}) are in minutes.

Table 5.3

Linear Modelling of Volume Fraction of Martensite as a Function of Austenitizing Temperature, Austenitizing Time, Reaction Temperature and Reaction Time

$$V_m = -59.518 + 0.048A_{Temp.} - 0.431A_{Time} + 0.083R_{Temp.} - 0.155R_{Time}$$

Specimen No.	Observed V_m(%)	Predicted V_m	Difference Between Observed & Predicted FGS	Low 95% Confidence Limit for Mean	Upper 95% Confidence Limit for Mean
1	43.820	45.574	-1.754	41.10	50.048
2	47.430	43.618	3.811	40.351	46.885
3	36.710	38.736	-2/026	35.084	42.388
4	35.43	31.655	3.774	23.696	39.615
5	33.68	35.772	-2.092	31.924	39.621
6	33.68	38.662	-4.982	35.810	41.514
7	39.16	37.356	1.803	34.007	40.706
8	50.81	41.863	8.946	39.537	44.190
9	38.11	35.736	2.373	31.791	39.681
10	39.97	44.847	-4.877	40.063	49.631
11	36.48	42.540	-6.060	39.487	45.593
12	39.70	39.784	-0.084	35.886	43.682
13	31.81	36.623	-4.813	33.228	40.018
14	33.10	36.888	-3.788	31.612	42.165
15	51.28	52.675	-1.395	44.141	62.210
16	46.52	41.910	4.609	39.457	44.362
17	43.70	41.669	2.030	39.317	40.021
18	51.39	43.132	8.257	40.392	45.872
19	39.87	39.812	0.057	36.868	42.756
20	30.88	31.060	-0.180	22.794	39.326
21	42.54	42.635	-0.095	40.368	44.901
22	39.76	41.407	1.647	39.348	43.465
23	38.57	40.432	-1.862	37.923	42.942

A_{temp}, R_{temp} in ^{o}C; R_{temp}, R_{time} in minutes.

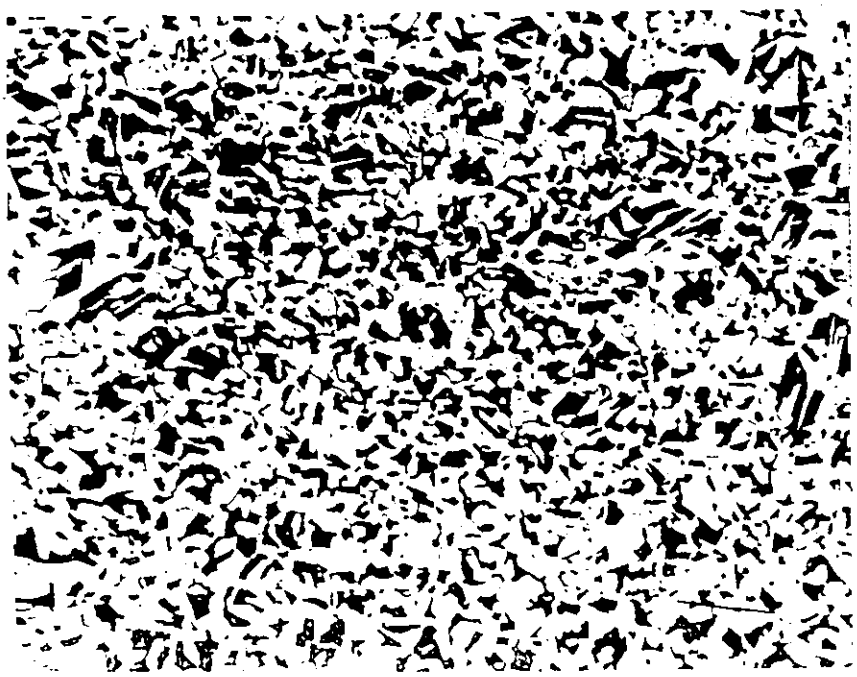

(Magnification 200X)

Figure 5.2 Optical micrograph of an isothermally reacted dual phase steel.

heat treatment variables, austenitizing temperature was found to be the most effective in controlling the ferrite grain size as indicated by Equation 5.1 which predicts a larger ferrite grain size with higher austenitizing temperatures.

The average size of the martensite islands as well as their volume fraction, as expected, increased with increasing isothermal reaction temperature and shorter reaction times as indicated in Table 5.1 and Equation 5.2. The size of the martensite islands is determined by the amount and distribution of unreacted austenite at the end of the reaction period. Between reaction temperature and reaction time, the former was more effective in controlling the volume fraction of martensite. The effect of isothermal reaction time on the volume fraction of martensite is shown in Figure 5.3.

Some pearlite was observed in specimens with isothermal reaction times in excess of 8 minutes as shown in Figure 5.4. In all such cases, the pearlite was consistently observed to be formed at the outer edges of martensite grains.

Rod-like banding of the martensite was observed in the longitudinal direction in almost all the specimens. The microstructure of one of the banded specimens is shown in Figure 5.5.

Dislocations were observed at the ferrite martensite interface (Figure 5.6) in TEM foils. These dislocations form in the ferrite during the austenite to martensite

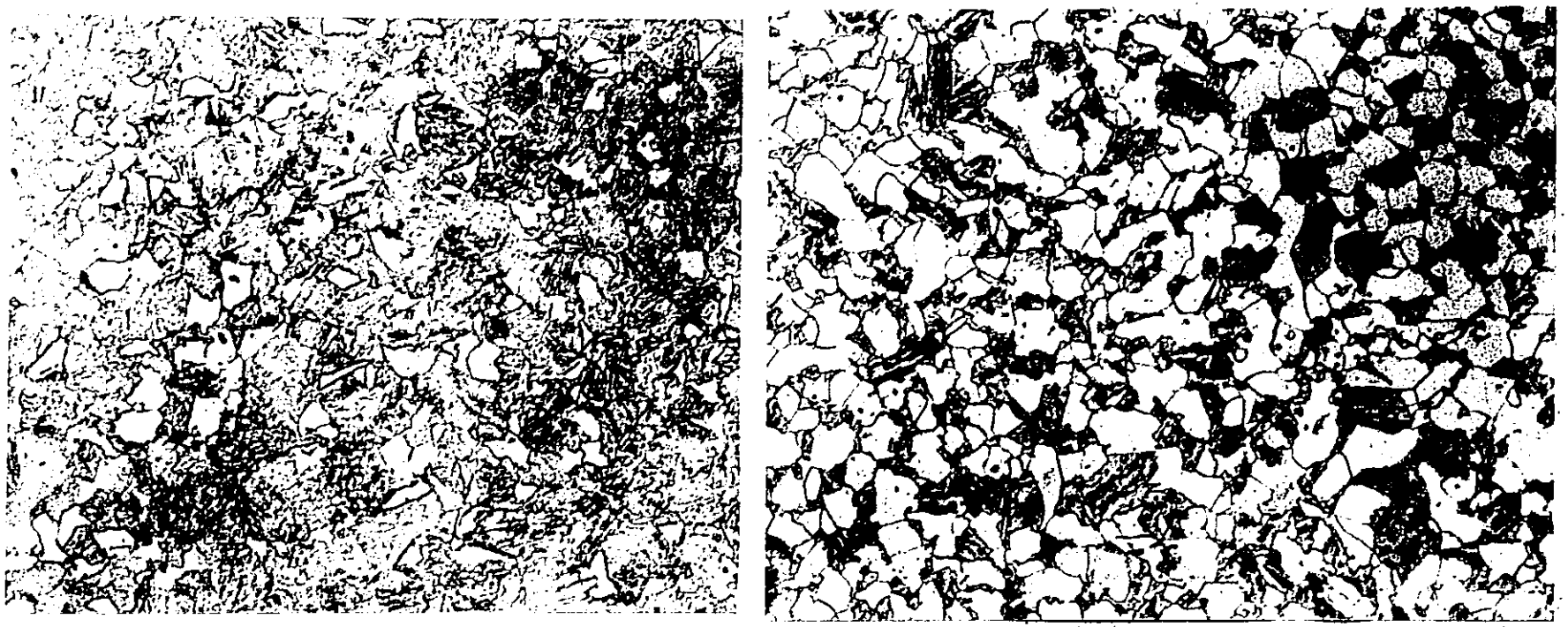

(a) Specimen 7B,
R_{Time} = 1 minute;
V_M = 73.67%

(b) Specimen 7C,
R_{Time} = 4 minutes;
V_M = 42.54%

Figure 5.3 Optical micrographs showing the effect of reaction time on the volume fraction of martensite in an isothermally reacted dual phase steel(Magnification 400X).

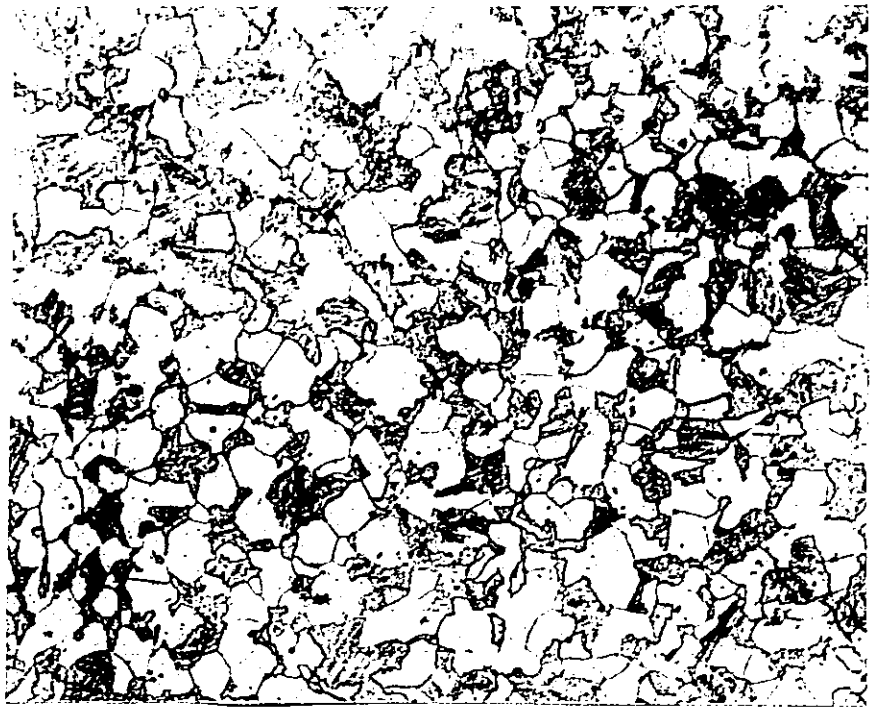

(c) Specimen 7D
R_{Time} = 6 minutes;
V_M = 40.49%

(d) Specimen 7E
R_{Time} = 8 minutes;
V_M = 39.76%

Figure 5.3 Optical micrographs showing the effect of reaction time on the volume fraction of martensite in an isothermally reacted dual phase steel (Magnification 400X).

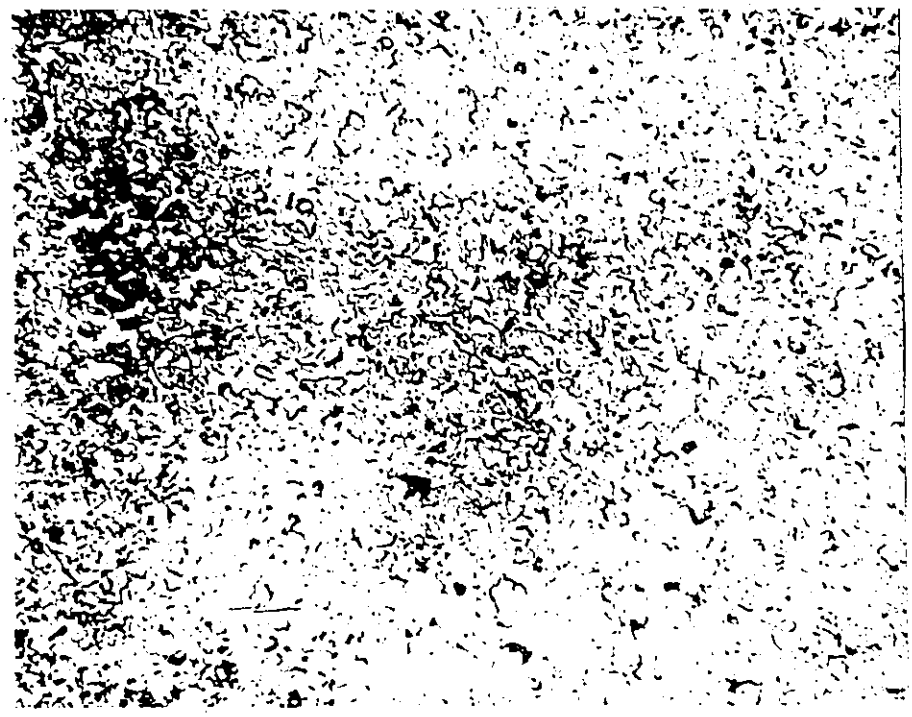

(a) Magnification 100x.

(b) Magnification 1000x.

Figure 5.4 Optical micrographs of an isothermally reacted dual phase steel for a reaction time of 30 minutes at 697°C (specimen 3P).

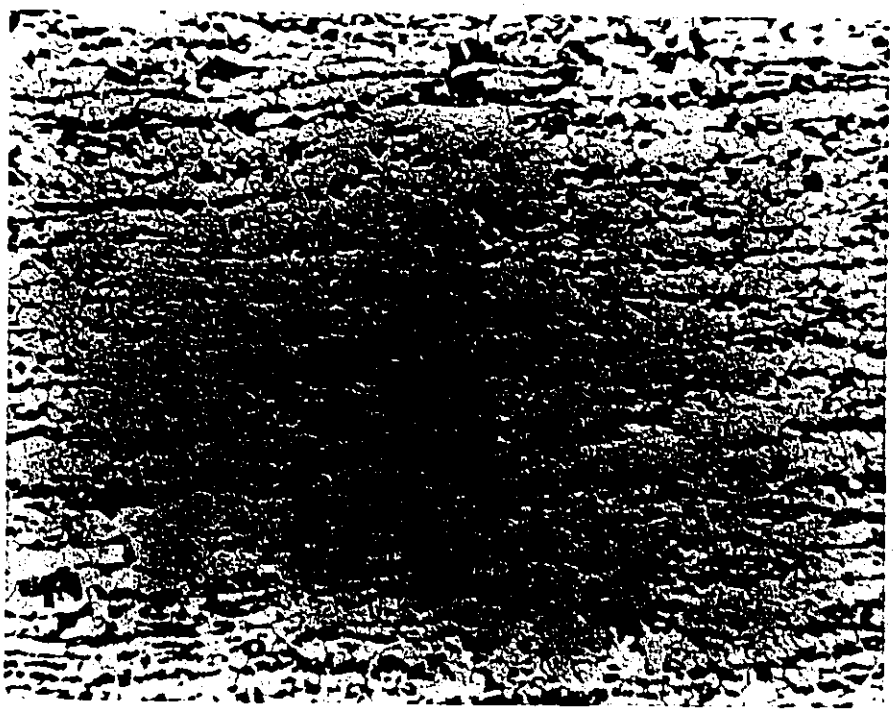

Figure 5.5 Optical micrograph from the longitudinal section of an isothermally reacted dual phase steel showing ferrite and martensite bands(Magnification 200X).

(a) Magnification 75000X

(b) Magnification 100000X

Figure 5.6 Transmission electron micrographs of an isothermally reacted dual phase steel showing a high dislocation density at the ferrite martensite interface.

reaction whose expansion causes plastic deformation of the surrounding ferrite.

5.1.2 Microstructure and Tensile Properties

Tensile tests were done to correlate the ferrite grain size and the volume fraction of martensite with ultimate tensile strength, uniform elongation and strain hardening properties. All the dual phase specimens showed continuous yielding, (i.e., no yield drop), which is typical of such structures. The results of tensile tests are presented in Table 5.4, which represents the volume fraction of martensite, ultimate tensile strength, uniform stress, and uniform strain of different specimens. A range of tensile properties were obtained for volume fractions of martensite ranging from 30 to 50%.

Once again linear regression analysis was used to analyze the relationships between microstructural parameters and tensile properties. Since ferrite grain sizes were relatively constant for most specimens (6-9μ), they were not included in the regression analysis. The results of such an analysis for UTS as a function of volume fraction of martensite is shown in Table 5.5. The results can also be expressed in terms of the following empirical equation:

$$UTS(MPa) = 723.9 + 5.09\ V_M \qquad (5.3)$$

The experimental as well as empirical plot of ultimate tensile strength as a function of volume fraction of martensite is shown in Figure 5.7. Figure 5.8a shows true

Table 5.4

Tensile Properties of Isothermally Transformed Dual Phase Steels

Specimen	$V_{Mart.}$ (%)	UTS (MPa)	εu (Uniform Strain)	Su (Uniform Stress)
3A	43.82	994.95	0.050	990.85
3B	47.43	987.14	0.051	983.11
3D	36.71	965.90	0.054	944.32
3E	35.43	935.25	0.078	956.89
3H	33.68	867.74	-----	------
3I	33.68	956.16	0.061	958.71
3J	39.16	853.53	0.049	885.43
3L	50.81	1056.5	0.024	1051.42
3P	38.11	915.69	-----	------
4A	39.97	943.87	0.059	949.88
4B	36.48	910.15	0.044	899.90
4C	39.70	911.91	0.034	891.95
4D	31.81	869.42	0.072	887.51
4E	33.10	877.77	0.066	887.25
4G	51.28	813.23	0.083	838.48
4K	46.52	974.25	0.05-	974.15
4L	43.70	930.97	0.062	939.08
4M	51.39	1020.20	0.029	1024.43
4N	39.87	933.21	0.047	------
7A	30.88	808.00	-----	------
7C	42.54	937.12	-----	------
7E	39.76	943.09	-----	------
7F	38.57	954.50	-----	------

Table 5.5

Linear Modelling of UTS as a Function of V_m

$$UTS(MPa) = 723.901 + 5.096\ V_m$$

Specimen No.	Observed UTS(MPa)	Predicted UTS(MPa)	Difference Between Observed & Predicted Values	Lower 95% Confidence Limit for Mean	Upper 95% Confidence Limit for Mean
1	994.95	947.211	47.738	920.04	974.38
2	987.14	965.60	21.531	929.21	1002.00
3	965.90	910.97	54.921	884.09	937.85
4	935.25	904.45	30.794	874.78	934.12
5	867.74	895.53	-27.797	861.26	929.81
6	956.16	895.53	60.622	861.26	929.81
7	853.53	923.46	-69.933	899.85	947.07
8	1056.50	982.83	73.666	935.65	1030.01
9	915.69	918.11	- 2.423	893.49	942.73
10	943.87	927.59	16.278	904.30	950.87
11	910.15	909.80	0.343	882.46	937.14
12	911.91	926.21	-14.305	902.86	949.56
13	869.42	886.00	-16.587	846.12	925.89
14	877.77	892.58	-14.811	856.62	928.53
15	813.23	985.22	-171.998	936.45	1033.99
16	974.25	960.70	13.278	927.20	994.73
17	930.97	946.60	- 15.630	919.66	973.53
18	1020.20	985.78	34.410	936.64	1034.93
19	933.21	927.08	6.127	903.77	950.38
20	808.00	881.26	-73.268	838.41	924.12
21	937.12	940.688	- 3.568	915.70	965.66
22	943.09	926.521	16.568	903.19	949.85
23	954.50	920.457	34.042	896.35	944.55

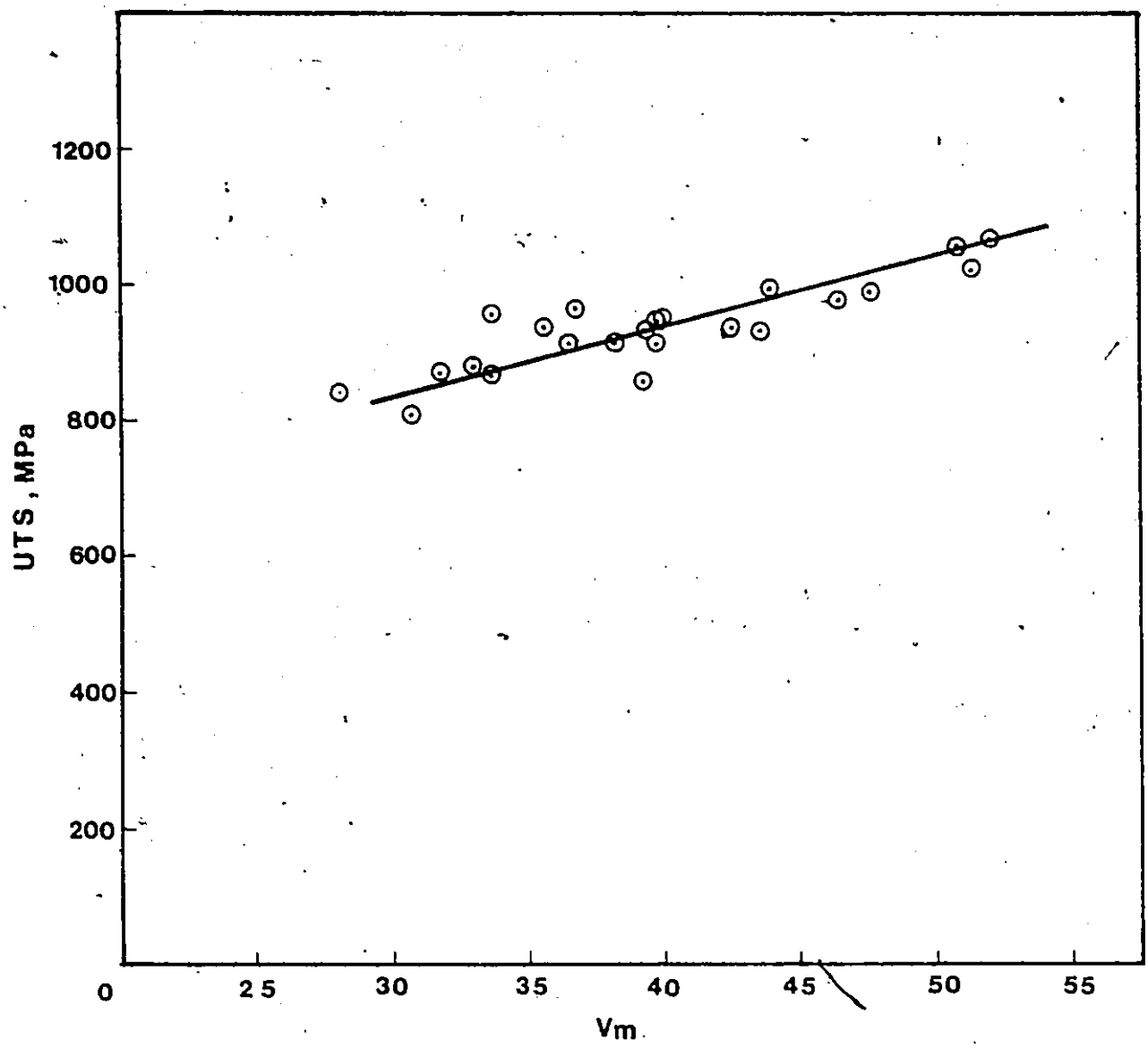

Figure 5.7 Ultimate tensile strength as a function of the volume fraction of martensite (V_m) in isothermally reacted dual phase steels. The straight line drawn in the figure corresponds to the empirical equation: UTS(MPa) = 723.9 + 5.09 V_m.

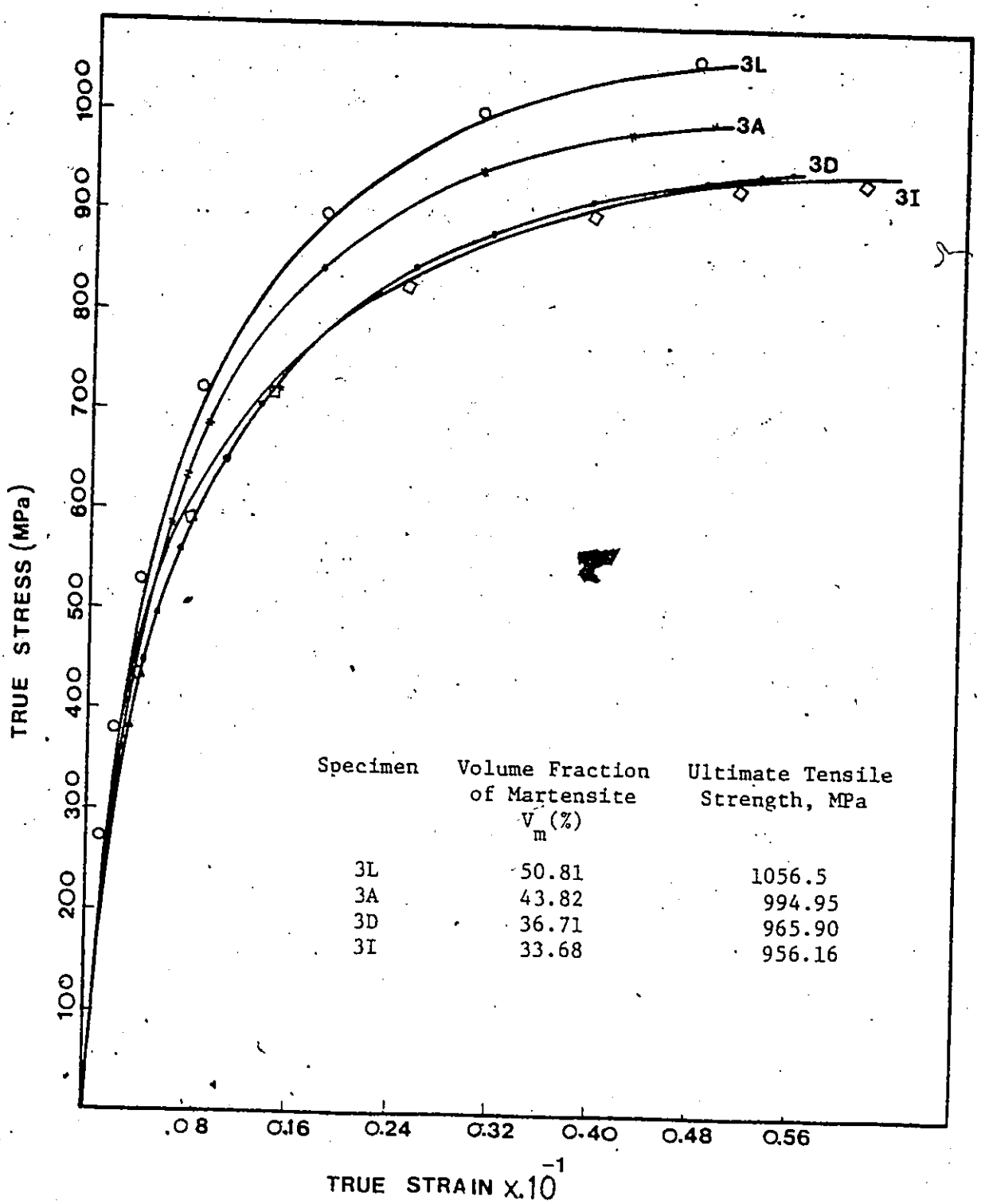

Specimen	Volume Fraction of Martensite V_m(%)	Ultimate Tensile Strength, MPa
3L	50.81	1056.5
3A	43.82	994.95
3D	36.71	965.90
3I	33.68	956.16

Figure 5.8(a) True stress - true strain curves of isothermally reacted dual phase steels for different martensitic contents.

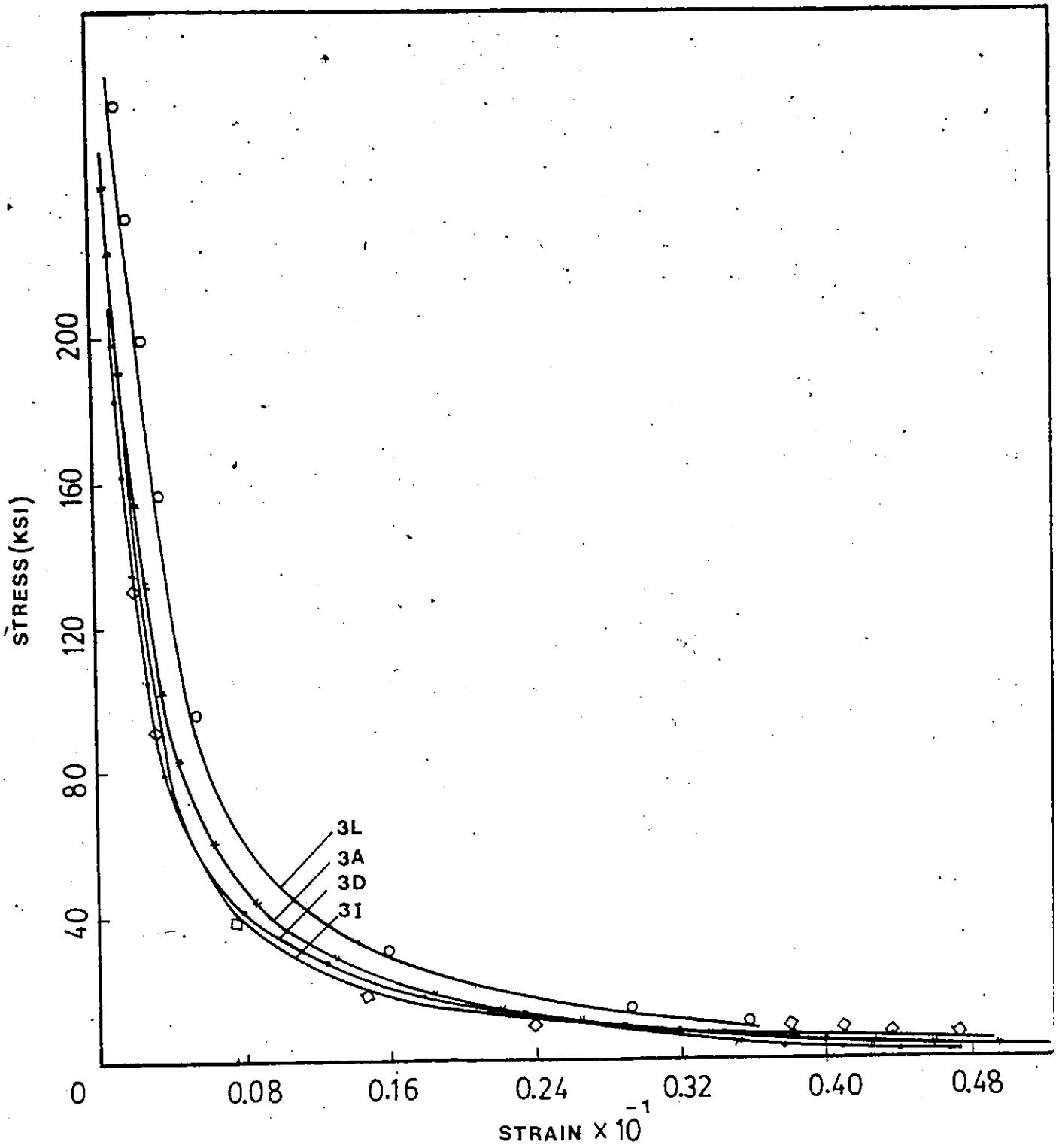

Figure 5.8(b) Work hardening rate vs strain curves of isothermally reacted dual phase steels for different martensitic contents.

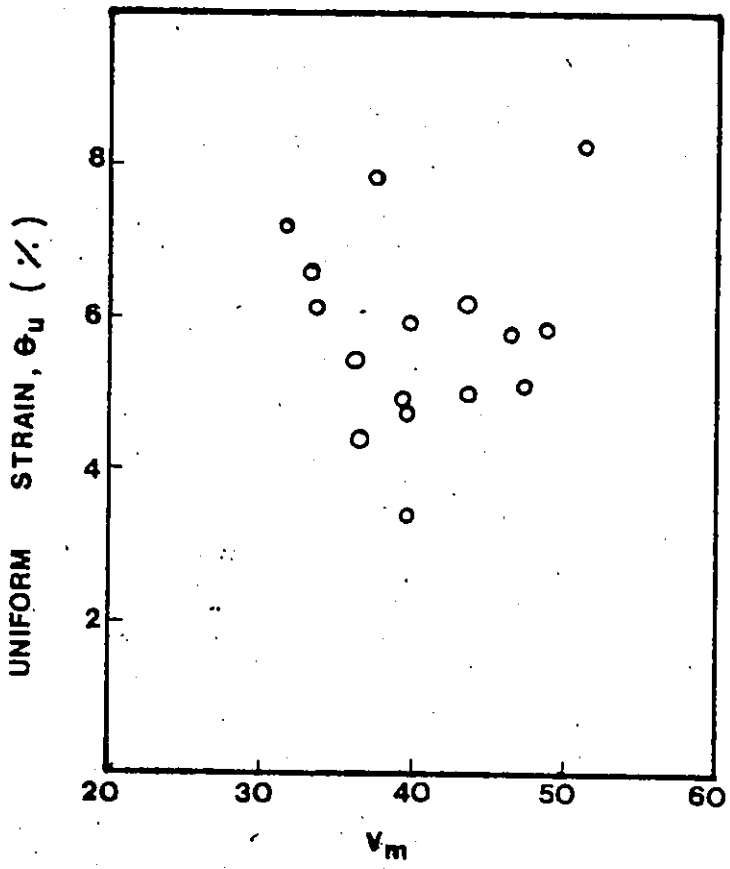

Figure 5.8(c) Uniform strain vs volume fraction of martensite for different isothermally reacted dual phase steels.

stress-true strain curves of 4 tensile specimens with varying martensite contents and ultimate tensile strengths. Figure 5.8b presents the work hardening vs. true strain curves of the same specimens. As evident from these figures, increasing the volume fraction of martensite produced both increasing levels of strength and high work hardening rates.

The uniform strain, ε_u, for each specimen was measured from the Considere Criterion. The uniform strain as a function of martensite content was also analyzed by linear regression analysis. The results as presented in Figure 5.8c, show a large scatter so that there is no apparent simple dependence on the martensite content. The decrease in ε_u with increasing flow stress (and UTS) is shown in Figure 5.9 for specimens 4L and 4D.

Fracture surfaces of specimens were observed at high magnifications (>500X), after tensile testing, by scanning electron microscopy. Figure 5.10 shows a composite picture of the surface of a specimen containing 22% martensite. Examination of a number of fracture surfaces indicated that the fracture initiation takes place at the martensite particles or at the inclusions. Scanning electron micrographs from polished longitudinal sections

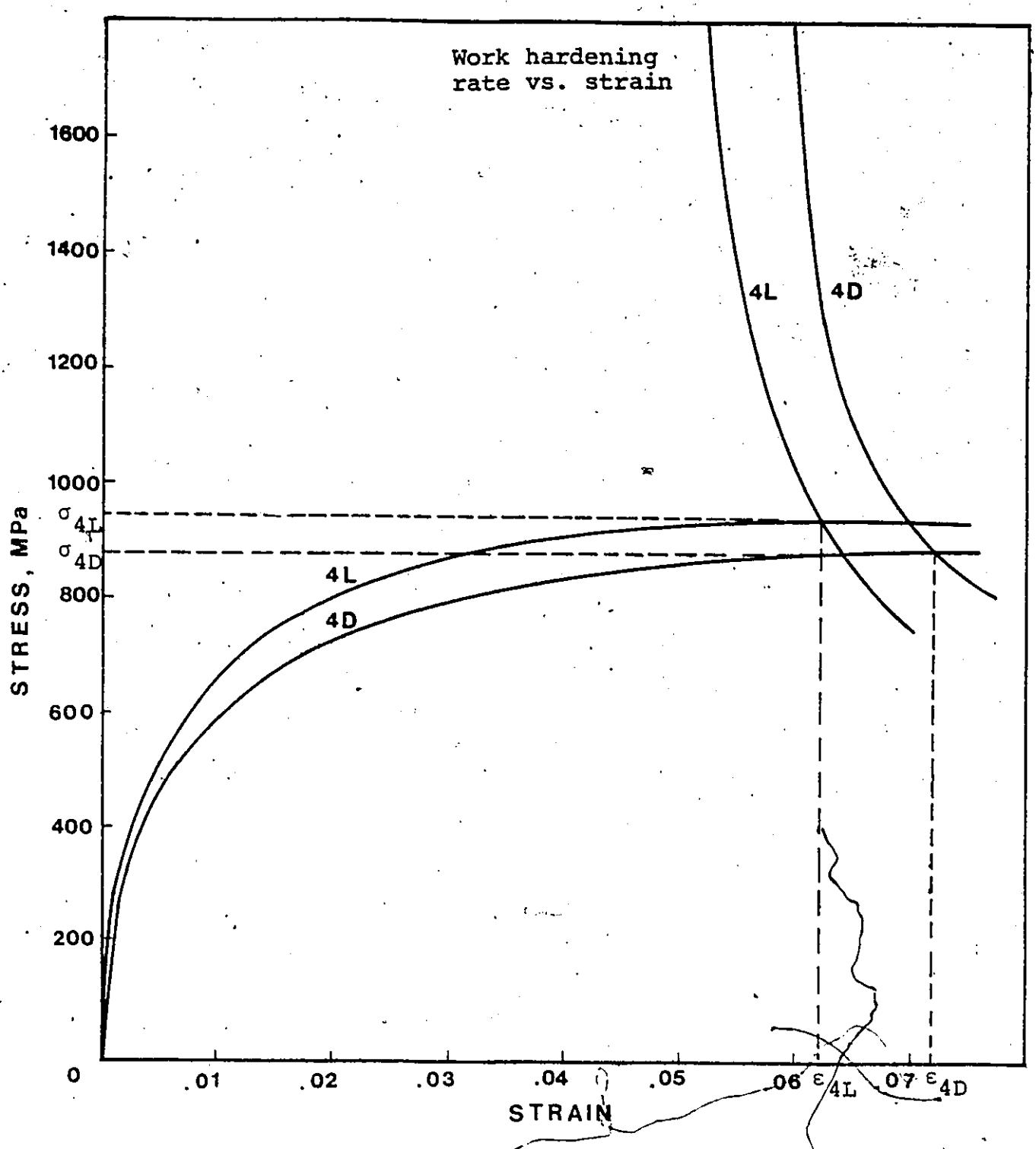

Figure 5.9 A decrease in uniform strain, ε_u, with an increase in flow stress (or UTS) for specimens 4L and 4D.

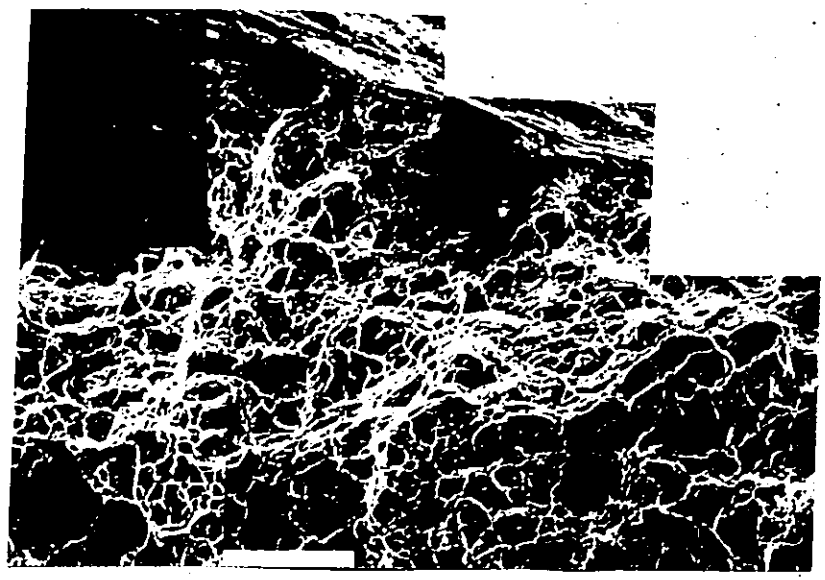

Figure 5.10 Composite picture of the fracture surface of an isothermally reacted dual phase specimen (Mag 315X)

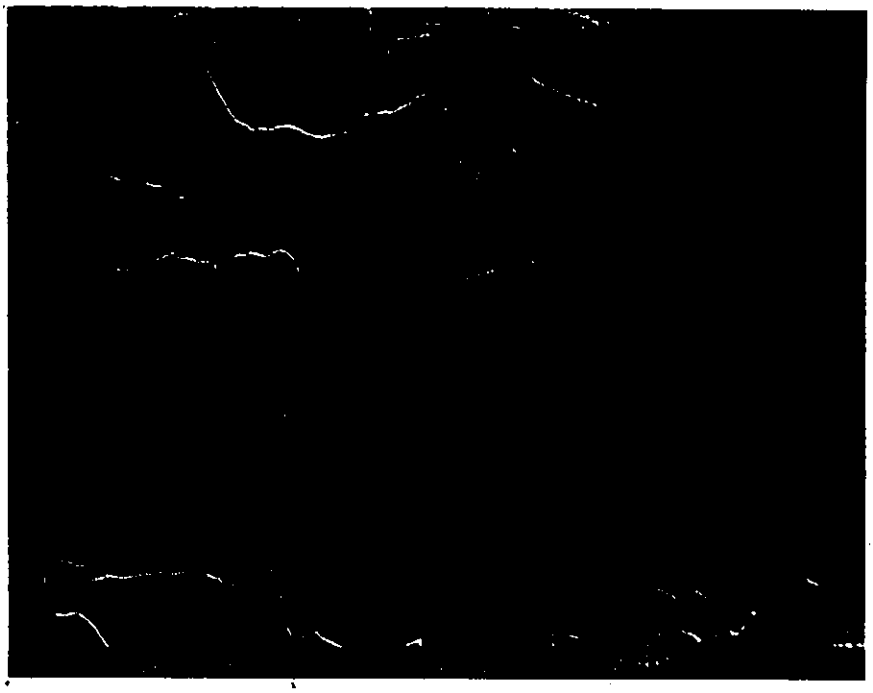

(a) Magnification 640x.

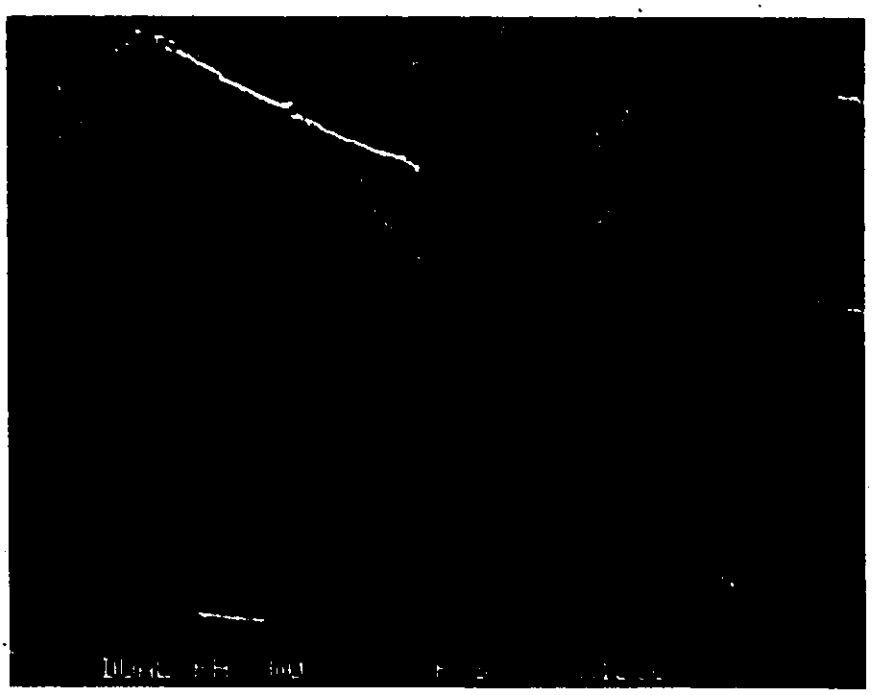

(b) Magnification 1250x.

Figure 5.11 Nucleation and growth of voids near fracture surface. (a) decohesion of ferrite-martensite interface, (b) cracking of the martensite phase.

showed void nucleation and growth below the fracture surface, occurring preferentially at ferrite-martensite interfaces as shown in Figure 5.11. Martensite cracking was also observed in big martensite particles. Isolated cleavage of ferrite grains was also seen, but these cracks may well be initiated at martensite interfaces above or below the plane of observation.

5.1.3 Effect of Tempering

In this section the results of the effect of tempering on the strength and ductility of dual phase steels are presented.

Some separate tests done on these steels indicated that the as-quenched steels would have poor formability in a heading type of process. Therefore it was hoped that a tempering process could be found that would retain good mechanical strength but improve the ductility.

Six sets of two dual phase steel specimens were produced by isothermal transformation. As-received specimens were each austenitized at about 870°C (± 5) for 4 minutes. They were then isothermally transformed at about 686°C (± 4) for 4 minutes and water quenched to obtain the necessary dual phase structures.

Pairs of specimens were tempered at either 240°C, 300°C, 360°C, 440°C or 510°C for an hour and air cooled. The last pair was kept at room temperature. The details of the heat treatment including tempering treatment are given in Table 5.6. Microstructures of specimens in the as-quenched

Table 5.6

Heat Treatment for Studies on Tempering of Isothermally Reacted Dual Phase Steels

Specimen Name	H/T for Obtaining F-M Structure				Tempering Treatment	
	Austenitizing Temperature $A_{Temp.}$ (^{o}C)	Austenitizing Time (min.) A_{Time} ±5 sec	Reaction Temperature $R_{Temp.}$ (^{o}C)	Reaction Time (min.) R_{Time} ± 5 sec	Tempering Temperature $T_{Temp.}$ (^{o}C)	Tempering Time (hr.) T_{Time} (± 3min)
10D	861.6	5	690	4	300± 3	1
10H	855.3	4	682.3	4	300±3	1
10E	860.3	4	689.3	4	360± 3	1
10K	868.0	4	686.0	4	360±3	1
10C	861.6	5	690	4	440± 4	1
10L	873.2	4	685	4	440±4	1
10B	877.5	4	688	4	510± 2	1
10G	862	4.41	685	4	510± 2	1
10I	857.0	4	680.5	4	240± 5	1
10ϕ'	877.0	4	684.3	4	240±5	1
10J	858.0	4	683.3	4	30^{o}C (RT)	-
10M	873.0	4	684.0	4	30^{o}C (RT)	-

condition and after tempering at 240°C, 360°C and 510°C are shown in Figure 5.12.

The results of the tensile tests are presented in Tables 5.7 and 5.8. Table 5.7 represents specimen names, tempering temperatures, initial, uniform and neck diameters and area of cross-sections. Table 5.8 shows the different tensile properties, namely: yield strength, yield point, ultimate tensile strength, uniform stress, true fracture stress and strain, and strain hardening exponent. Different parameters from these tables are plotted in Figures 5.13-5.15. Figure 5.13 shows true stress-true strain curves of specimens tempered at different temperatures. Tempering at 240°C and above resulted in a return of discontinuous yielding, an increase in flow stress from 0.5 percent strain to the necking strain. Flow stress curves in the initial stages for all the tempered specimens were higher than the untempered specimens. Figure 5.14 shows a change in ultimate tensile strength, yield strength and uniform stress with tempering temperature for all the tempered specimens. The ultimate tensile strength and uniform stress decreased continuously with increasing tempering temperature. A decrease in UTS of about 200 MPa was observed for a tempering temperature of 510°C. The yield strength above 240°C was essentially constant. For an undetermined tempering temperature below 240°C, the yield process changes from continuous to discontinuous yielding.

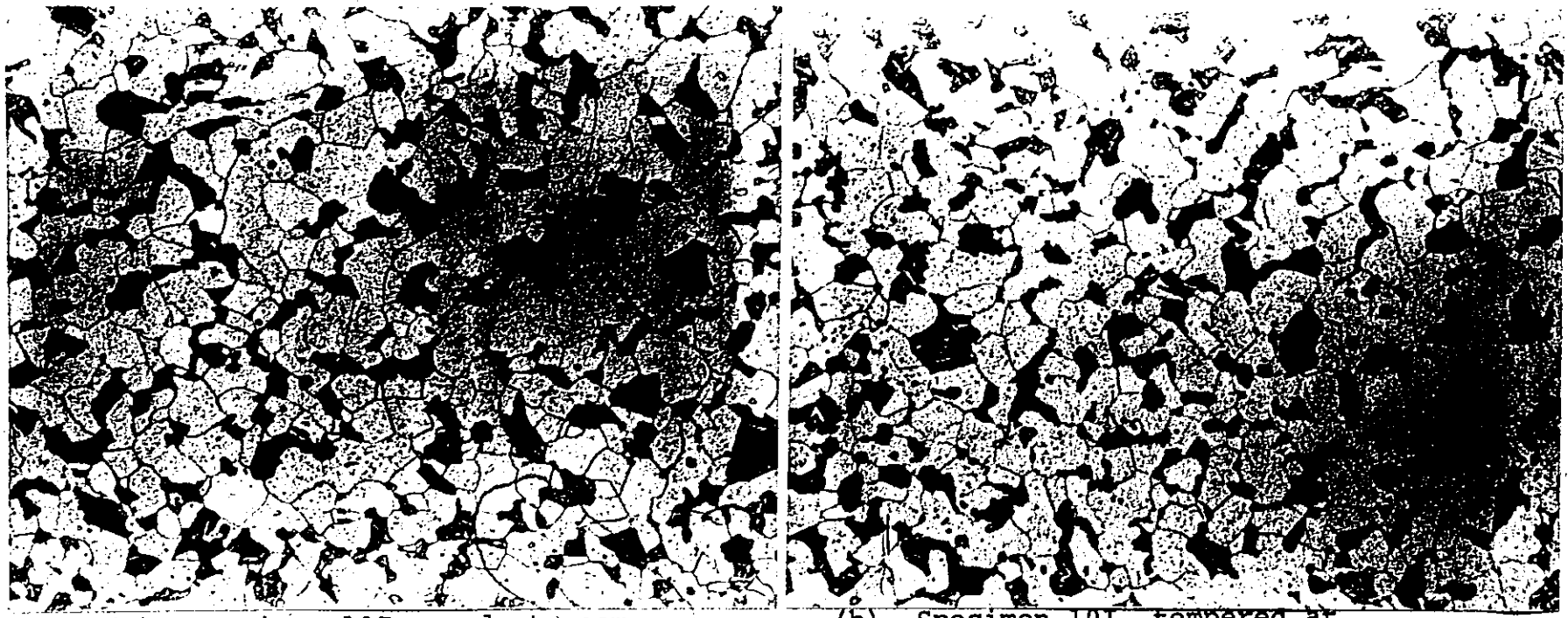

(a) Specimen 10J, aged at room temperature.

(b) Specimen 10I, tempered at 240°C for 1 hour.

Figure 5.12 Optical micrographs of tempered dual phase specimens. (Magnification 500X).

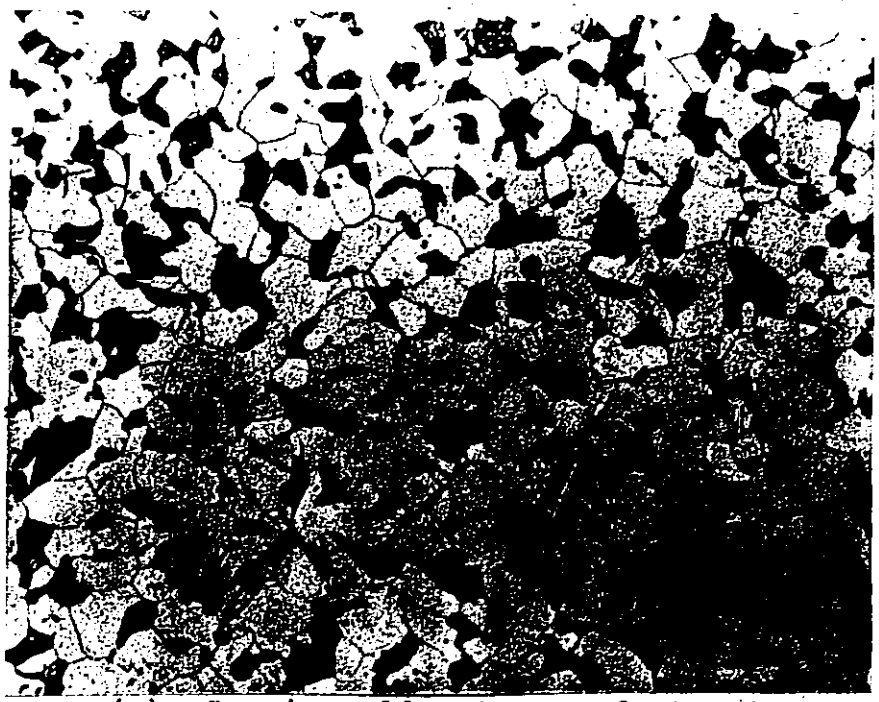

(c) Specimen 10E, tempered at 360°C for 1 hour.

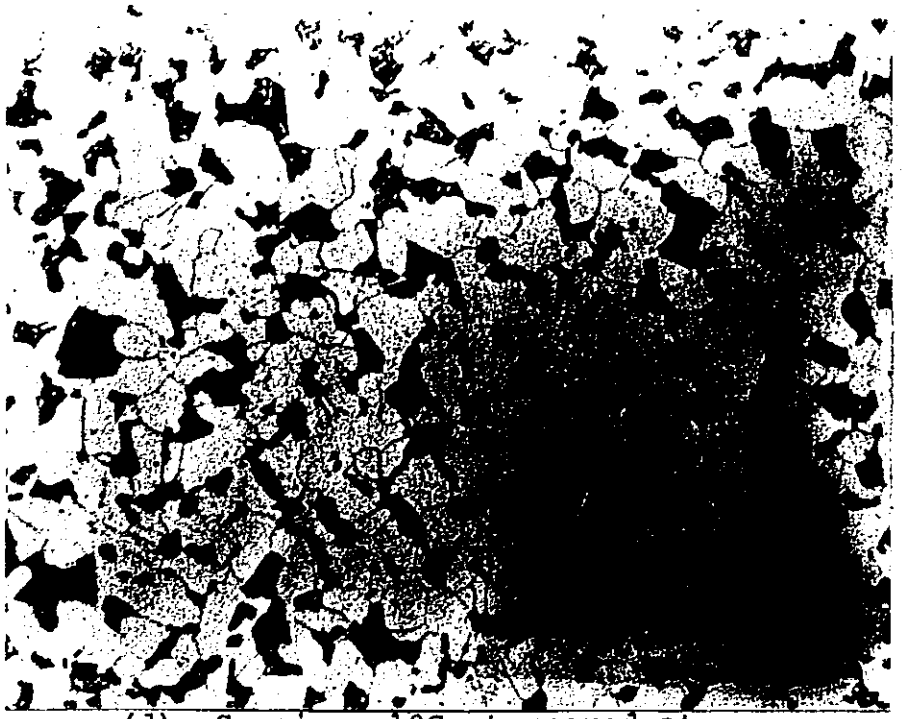

(d) Specimen 10G, tempered at 510°C for 1 hour.

Figure 5.12 Optical micrographs of tempered dual phase specimens. (Magnification 500X).

Table 5.7

Specimen Dimensions During Tensile Testing of Tempered Dual Phase Specimens

Specimen Name	Tempering Temp. (^{o}C)	Initial Diameter (d_o) m	Initial Area (A_o) m^2	Uniform Diameter (d_u) m	Uniform Area (A_u) m^2	Neck Diameter (d_n) m	Neck Area (A_n) m^2	A_o/A_n	$\Delta\ell$ m^2
10B	510	6.40	32.15	6.08	29.01	4.29	14.44	2.228	0.00317
10G	510	6.35	31.65	5.99	28.16	4.26	14.24	2.219	0.00259
10C	440	6.42	32.35	6.13	29.49	4.39	15.12	2.139	0.00266
10L	440	6.42	32.35	6.32	31.35	4.36	14.92	2.165	0.00213
10E	360	6.49	33.06	16.28	30.95	4.87	18.61	1.774	0.00254
10K	360	6.45	32.65	6.16	29.78	4.85	18.46	1.771	0.00259
10D	300	6.49	33.06	6.27	30.86	4.77	17.86	1.850	0.00274
10H	300	6.31	31.25	6.11	29.30	4.59	16.53	1.885	0.00254
10I	240	6.32	31.35	6.15	29.69	4.97	19.39	1.614	0.00228
10O	240	6.38	31.95	6.18	29.98	4.92	19.00	1.679	0.00266
10J	30	6.32	31.35	6.22	30.27	5.13	20.65	1.522	2.00218
10M	30	6.44	32.55	6.28	30.95	5.38	22.72	1.434	0.00238

Table 5.8

Tensile Properties of Tempered Specimens

Specimen Name	Yield Strength σ_u (MPa)	Yield Point Stress σ_{yp} (MPa)	UTS (MPa)	Uniform Stress σ_u (MPa)	True Fracture Stress σ_{fr} (MPa)	True Fracture Strain ϵ_{fr}	n in Equation $\sigma = k\epsilon^n$
10B	458.50	475.82	598.53	662.75	1029.54	0.801	0.167
10G	448.45	476.51	590.05	663.40	989.01	0.797	0.160
10C	470.23	479.82	622.39	682.43	1044.09	0.760	0.143
10L	435.83	466.03	597.57	617.84	1032.51	0.772	0.133
10E	456.45	480.64	664.58	709.04	997.69	0.573	0.140
10K	461.82	475.41	665.54	729.31	993.70	0.572	0.133
10P	429.63	456.45	684.71	733.84	1075.36	0.615	0.127
10H	412.19	454.24	660.99	704.49	1023.48	0.634	0.133
10I	468.58	468.58	707.87	704.49	1012.24	0.479	0.150
10O	430.59	450.04	694.50	740.69	1012.17	0.518	0.150
10J	370.96	---	777.22	803.97	1074.49	0.420	0.237
10M	326.84	---	769.50	808.80	1019.48	0.360	0.200

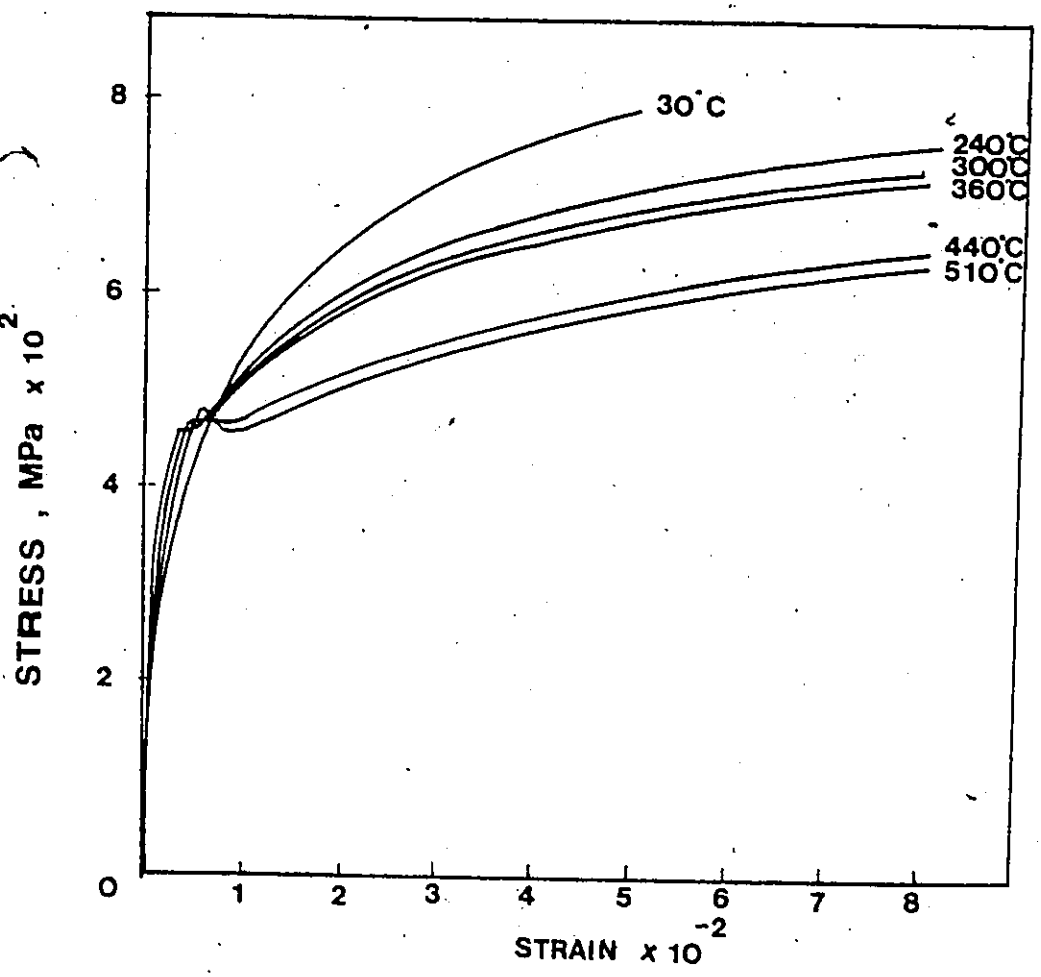

Figure 5.13 Stress-strain curves of tempered dual phase specimens.

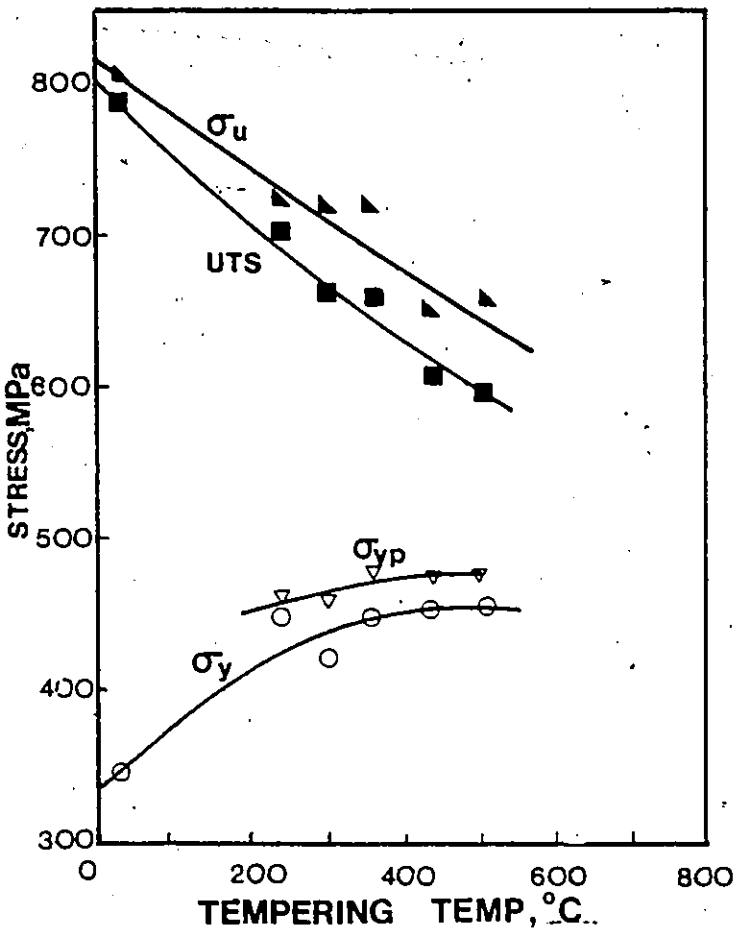

Figure 5.14 Effect of tempering temperature on ultimate tensile strength, yield strength, yield point and uniform stress of dual phase steels.

Figure 5.15a is a plot of true fracture strain and true fracture stress versus tempering temperature. The true strain at fracture increased continuously from .360 at 240°C to .801 at 510°C. The stress at fracture, however, remained nearly constant in the range of 975 to 1075 MPa, with no discernible trend with respect to tempering temperature.

Figure 5.15b shows values of the strain hardening exponent, n, as a function of tempering temperature. The decrease appears to reach a minimum value at about 300°C although the data are insufficient to prove that this is so.

5.2 Discussion

Prior to embarking on a discussion of the data obtained from tensile tests, it is of value to compare the isothermal reaction (IR) treatment procedure with the intercritical annealing (IA) process commonly used for obtaining dual phase structures. Although the transformation of austenite by isothermal transformation is similar in metallographic appearance to the transformation of austenite after intercritical annealing, three features make the former unique.

1) Intercritically annealed dual phase steel contains two types of ferrite; isothermally reacted steels contain only one;

2) The growth and distribution of phases in the isothermally reacted specimens are controlled essentially by kinetic rather than the thermodynamic considerations.

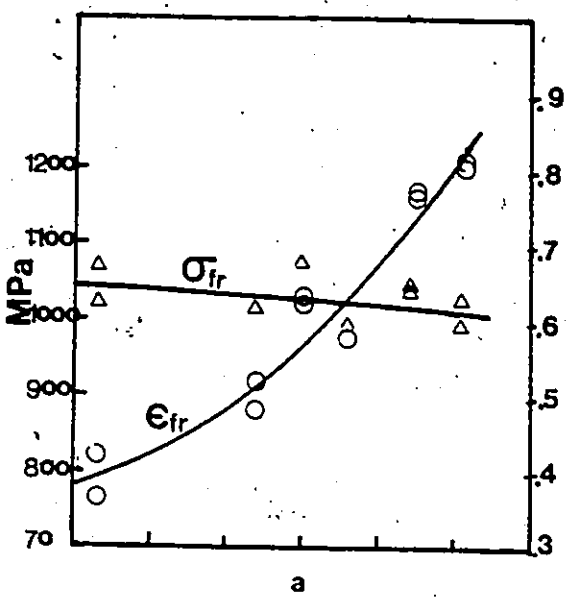

a

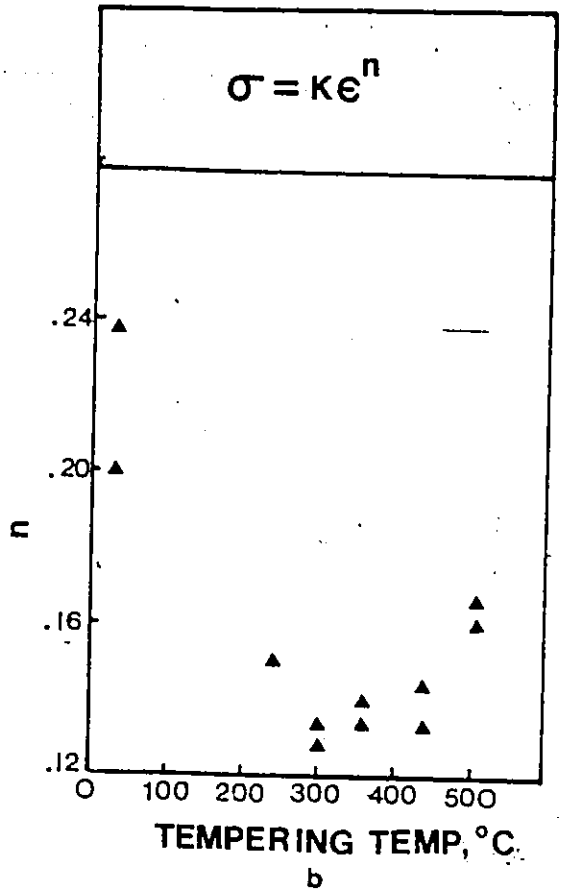

b

Figure 5.15a Effect of tempering temperature on the true fracture stress and strain of dual phase steels.

Figure 5.15b Effect of tempering temperature on the strength hardening exponent, n.

As a result, the carbon distribution in the martensite of the isothermally transformed steel is probably not uniform.

3) The long term anneal in the IA process produces martensite at the ferrite grain boundaries.

5.2.1 Ferrite Differences in IR and IA Structures

In the IA treatment there are two types of ferrite, the room temperature or the retained ferrite which is stable in the $\alpha+\nu$ region, and the ferrite formed by the epitaxial growth into austenite on cooling. TEM observations (30) have shown that there is no structural interface or boundary between the retained and epitaxial ferrite, and provides evidence for epitaxiality of ferrite with the retained ferrite acting as a substrate. TEM observation have also shown that precipitates are present in the retained ferrite during inter-critical annealing whilst the epitaxial ferrite is precipitate free. This reflects the differences in thermal history and composition between the two types of ferrite. Thus the work hardening behaviour of two types of ferrite will be different and this is expected to influence the work hardening behaviour of IA dual phase steels.

In the isothermally reacted steels, all of the ferrite is freshly formed from the austenite, and in plain carbon steels, it is expected that the ferrite will be free of precipitates.

5.2.2 Kinetic vs. Thermodynamic Partitioning

The process by which Bain originally determined isothermal transformation diagrams was essentially the same as

that used to produce dual phase steels in the present study. The specimens were quenched from single phase austenite to a temperature near to or below the eutectoid transformation line on the equilibrium Fe-C diagram. Thus the nucleation and growth of ferrite occurred in austenite which was highly unstable. A significant feature of this transformation was that a large amount of ferrite was formed from austenite in a short time resulting in a fine ferrite grain size. No isothermal transformation diagram was available for the steel used in the present study. However, the 1019 IT diagram, shown earlier in Figure 3.2 is similar in form but the higher Mn content in the 1018 steel will shift the ferrite start and pearlite start curves to the right.

It was observed that transformation products such as pearlite and bainite were suppressed up to a reaction time of about 8 minutes at 670°C. Longer reaction times led to the formation of pearlite, the amount of which increased with reaction time.

A microstructure of the specimen held for 30 minutes at a temperature of 697°C is shown in Figure 5.4. As evident in this figure, pearlite was observed at the outer edges of the martensite. A possible explanation is that the reaction results in a non-uniform distribution of carbon in the austenite. It has been independently observed that the austenite-ferrite reaction is controlled by carbon diffusion in the austenite (22). The center of the austenite grains would therefore be expected to contain a lower carbon level

and hence would transform to martensite at a higher martensite start temperature than the edges. The outer edges of austenite grains, being high in carbon and having therefore a lower M_s temperature, have more time to transform to pearlite during quenching. They also have shorter pearlite start times at equivalent temperatures.

5.2.3 Effect of the Reaction Path on Martensite Morphology

Another important difference between isothermally reacted and intercritically annealed dual phase specimens, as mentioned by other workers (31-33) is the morphology of martensite particles (previously discussed in Chapter 3). However, their results on different martensitic morphologies are in conflict. Kunio et al (31) and Suzuki et al (32) obtained a 'ferrite enclosed martensite' type and a 'martensite enclosed ferrite' type structure from isothermal and intercritical annealing treatments, respectively. On the other hand, Thomas and Koo (33) have observed exactly opposite results for the above-mentioned heat treatments. In addition, the relative strengths and ductilities obtained from the two microstructures are also in conflict.

In the present studies, a more connected martensite morphology was observed for intercritically annealed steels upto martsitic contents of 35% as shown in Figure 5.16. At large martensitic contents, however, a coarser and more connected martensite morphology was visible in both isothermally reacted and intercritically annealed specimens. Martensite

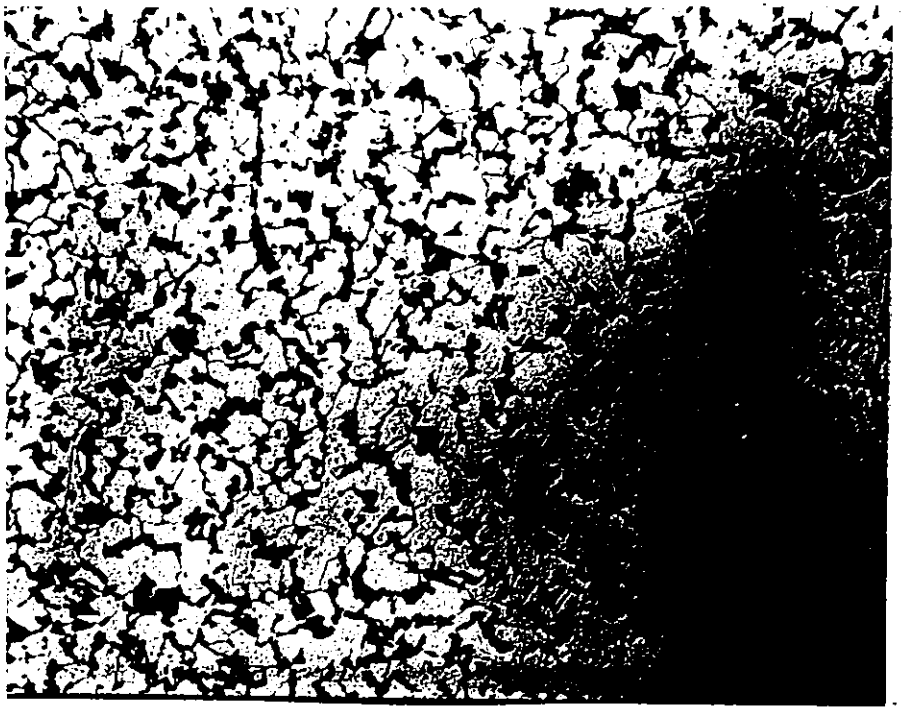

(a) Intercritically annealed specimen. Temp. 736°C; Time-30 minutes; V_M=26.41%; Magnification = 200x.

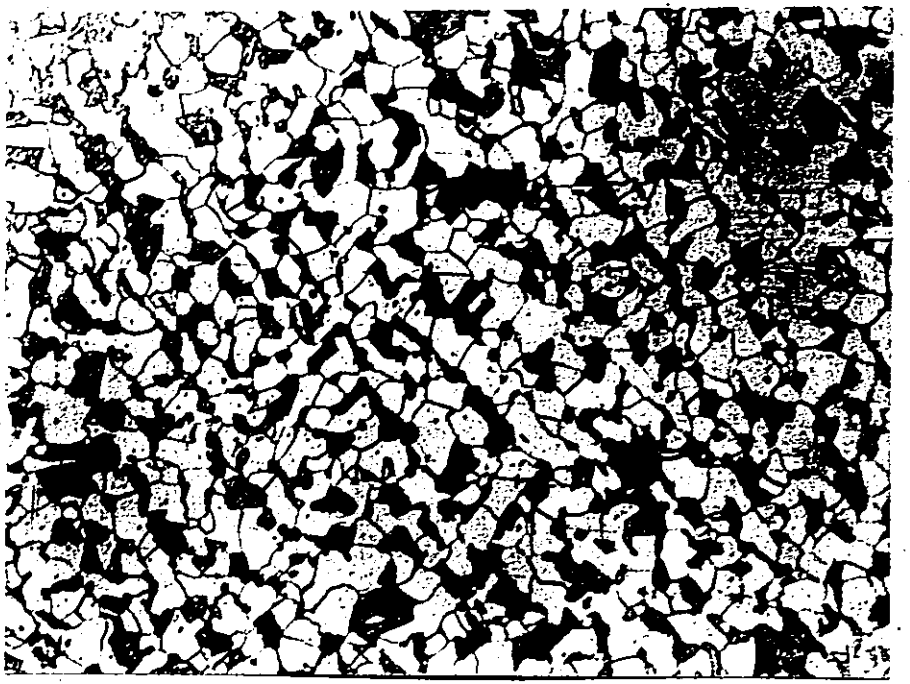

(b) Isothermally Reacted Specimen Reaction Temperature 676°C; Time-4 minutes; V_M = 28.20%; Magnification = 200x.

Figure 5.16 Martensite morphology at low martensitic contents in intercritically annealed and isothermally reacted dual phase specimens.

bands in the longitudinal direction were observed. The apparent conflict in observation between Thomas et al and other workers may have to do with the length of time the specimens are held in the intercritical region. Thomas et al do not give this information, but it takes some time for the austenite to form along the ferrite boundaries, and it appears that Thomas et al may not be holding long enough to develop this morphology.

5.2.4 Comparison of Present Results with Previously Published Studies

5.2.4.1 Effect of Processing Variables on Microstructure

Among the microstructural features that may influence the mechanical properties of dual phase steels are ferrite grain size, ferrite strength, solid solution alloy additions, and dispersed phase strengthening. With the ferrite grain size and solid solution strengthening being maintained at relatively constant levels in the present study, the focus was on the amount and the nature of the martensite second phase.

An analysis of the microstructural features of isothermally reacted dual phase steel specimens showed that the polygonal ferrite grain size remained small and virtually constant (6-9μ). This was due to relatively lower austenitizing temperatures and short austenitizing times which inhibit excessive austenite grain growth. The average size and volume fraction of the martensite islands, increased with

increasing isothermal reaction temperature and decreasing isothermal reaction times. This was due to a large amount of austenite prior to martensitic transformation. The effect of isothermal reaction time was more pronounced in controlling the volume fraction of martensite (Equation 5.2 and Table 5.3). This reflects the important role played by reaction time in controlling the kinetics of austenite-ferrite reaction.

5.2.4.2 Structure-Tensile Properties

The results of tensile tests indicate an increasing level of strength and work hardening rate and a decreasing uniform elongation with increasing volume fraction of martensite in agreement with other workers. Figure 5.17 is a summarized plot of UTS vs. volume fraction of martensite for a number of plain C and other alloyed intercritically annealed dual phase steels (our results are presented by a dotted line in the figure). A higher ultimate tensile strength was observed up to martensite contents of 35%. A rather large scatter in the present results indicate that there may be other factors governing the UTS of dual phase steels in addition to martensite content. There is some controversy over the question of whether the carbon content of the martensite significantly affects the strength of the ferrite-martensite composite (89,90). A number of workers have thus explained their results in terms of a nonlinear variation of UTS with martensite content incorporating the effects of the carbon content of martensite. Other alloy contents also influence

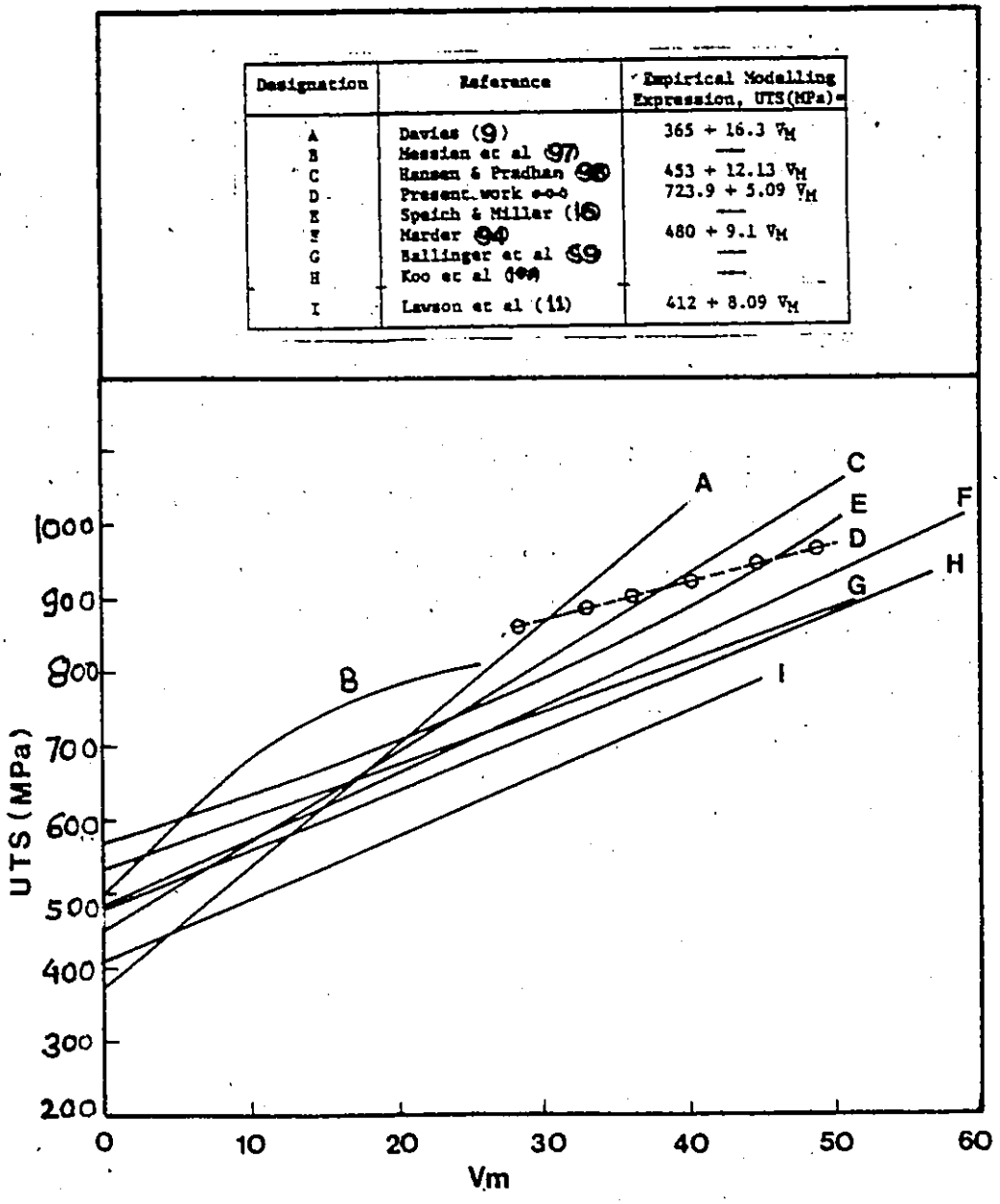

Figure 5.17 UTS as a function of volume fraction of martensite for different dual phase steels. The dotted line represents present results for isothermally reacted dual phase steel. The scatter ion in the present data as shown earlier in Figure 5.7.

the carbon content of martensite (91). Since the present studies have been limited to a single alloy system and one level of carbon, a variation in carbon content of the martensite with a change in martensite content is inevitable. This could very well explain the scatter in the plots of UTS vs. volume fraction of martensite.

Several other investigators have developed linear regression equations specifically relating the tensile strength of dual phase steels to the volume fraction of martensite. The replotted coefficients for martensite range from about 9 to 16 MPa/1% martensite as shown in Figure 5.17. No obvious trends are noted in these studies with regard to a limited range of martensite volume fraction influencing the magnitude of this coefficient. The fact that the constants differed from equation to equation can be attributed to variations in ferrite grain size, solid solution strengthening and ferrite interstitial content.

Figures 5.18 and 5.19 are plots of uniform elongation vs. volume fraction of martensite and uniform (total elongation) vs. UTS respectively for a number of steels. Present results represented by dotted lines indicate low elongation values compared to other workers. This may be due to a number of reasons as follows:

1) Effect of Specimen Shape

In all but one of the previous studies on dual phase steels, thin sheet tensile specimens (2.0 mm or less) have been used compared with the 6.3mmround specimens used in

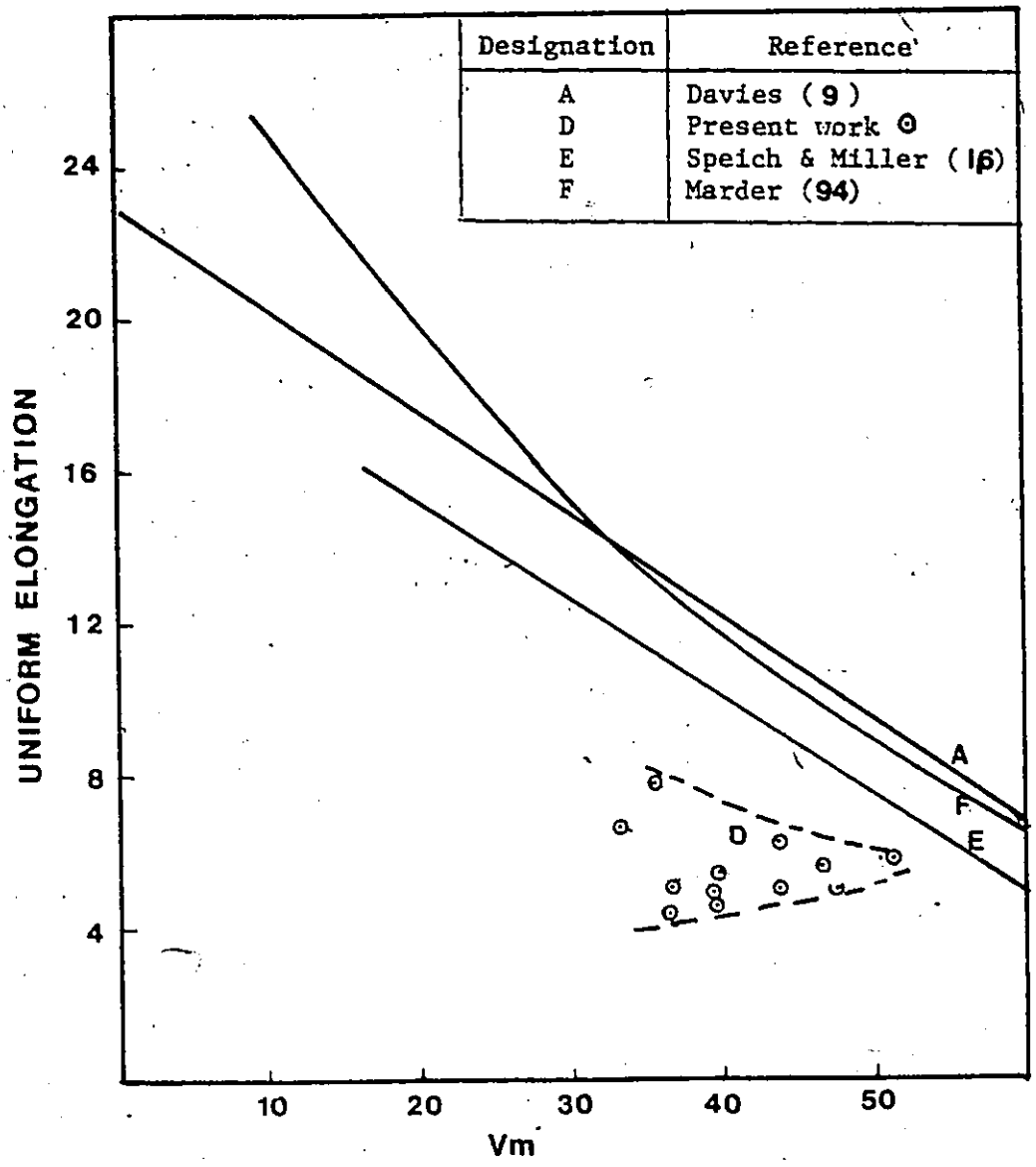

Figure 5.1 Uniform elongation as a function of martensite content for different dual phase steels.

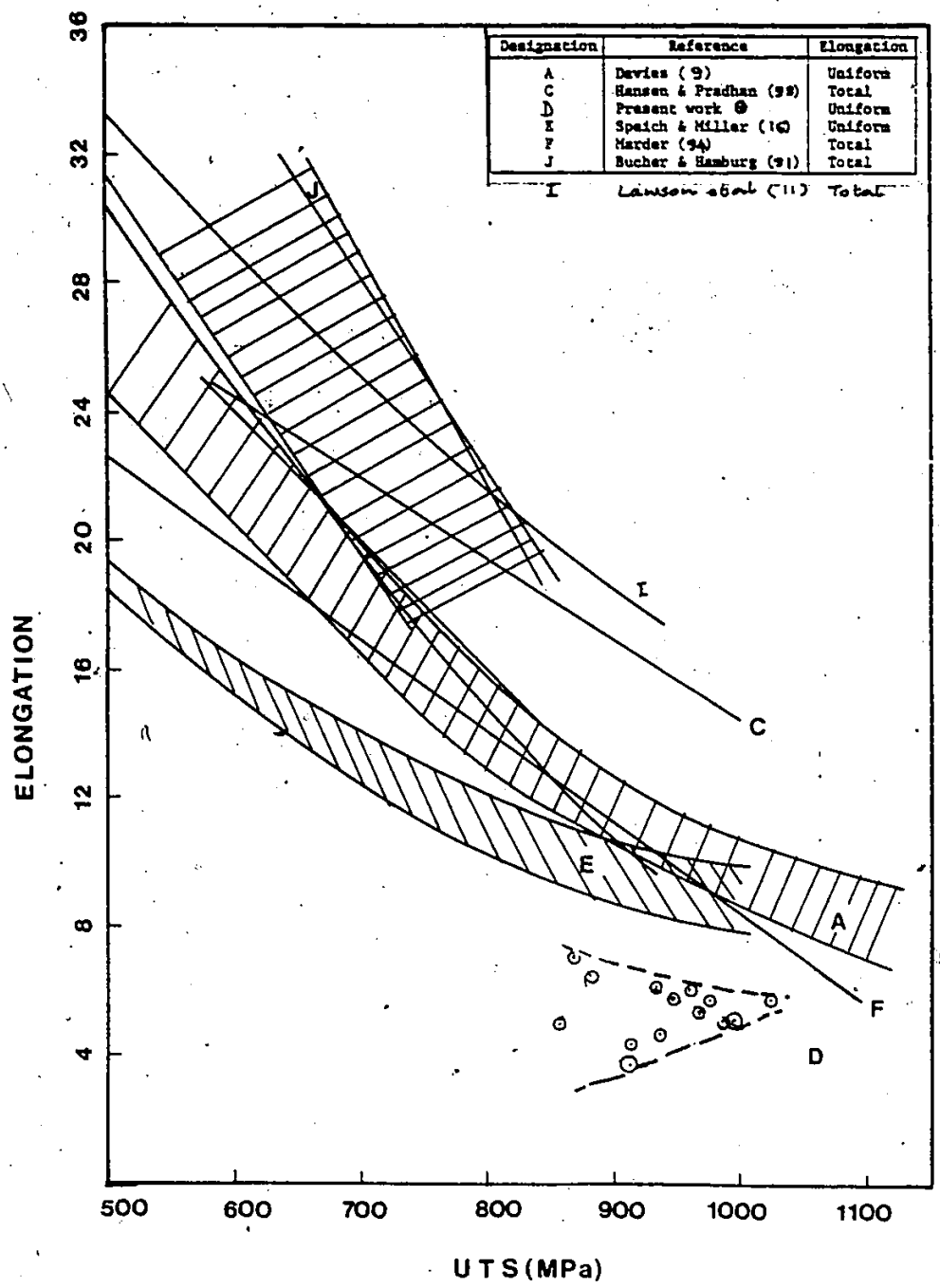

Figure 5.19 Total and uniform elongation as a function of UTS for different dual phase steels.

the present study. Sheet specimens have a strong crystallographic texture from the rolling process. When a textured dual phase sheet steel specimen of rectangular cross-section (width much greater than its thickness) is pulled by tension forces applied along the length, the cross-sectional strain is not isotropic. The measure of this is the "r" value, which is the ratio of the strain in width direction to the strain in the thickness direction. The strain in the thickness direction is less than the strain in the width direction. As a result, the fracture is delayed and a large total elongation is obtained. Specimens cut from hot rolled round bars have rotational symmetry along the tensile axis and the cross-sectional strain is isotropic. There is a more equiaxed strain distribution at the neck and a large stress triaxiality at the neck results. This leads to an early fracture and a lower post-uniform elongation is obtained.

Our results of lower elongation values for round specimens compared to sheet specimens are in agreement with recently reported results (92) for round specimens.

The most general conclusion that can be drawn is that geometrically similar specimens develop geometrically similar necked regions. According to Barba's law, the total elongation to fracture for geometrically similar specimens can be expressed as:

$$e_f = \frac{\sqrt{A_o}}{L_o} e_u$$

It is, however, generally recognized that in order to compare elongation measurements of different-sized speci-

mens, the specimens must be geometrically similar. The above equation shows that critical geometrical factor for which similitude must be maintained is $L_o/\omega_o t_o$* for sheet specimens and L_o/D_o for round bars. Thus from the corresponding values of L_o, ω_o, t_o or D_o for the two different specimen shapes, it is not possible to compare our elongation results with those of other workers. Furthermore, the dimensional details of the specimens of other workers are not always available, making comparisons impossible.

2) Alloy Content

The ductility of dual phase steels has been known to improve by alloying elements such as Si, V, Mo and Mn (90, 93). Si has been found to have the largest effect on ductility. Between the 0.5%Si steel and 1.0%Si steels, there exists an increase in elongation of 5% for the same tensile strength (90). The addition of 1%Si creates a gap between the ferrite and bainite transformations in the TTT diagram. Si inhibits carbide formation at the ferrite-martensite interface in dual phase steels produced by intercritical annealing (93). These carbides are thought to help in the decohesion of ferrite-martensite interface during deformation, thereby decreasing the ductility. In microalloyed dual phase steels containing V,Nb, etc., nitrides, carbides and carbonitrides precipitate in retained ferrite during intercritical annealing (93). The precipitate free epitaxial ferrite has been shown to increase elongation with a moderate decline in strength.

*L_o, ω_o, t_o and D_o represent initial length, width, thickness and diameters respectively,

3) Banded Structures

Rod-like banding was observed in the axial direction in almost all the specimens in the present study. It has been reported that martensite cracking is greatest when the carbon content is high and when the martensite content is large enough to create martensite bands seriously affecting the tensile ductility in dual phase steels (94). Increasing the percentage of martensite shortens the ferrite ligaments separating the martensite particles so that smaller total plastic strains are required to rupture them. Martensite cracking was observed in the present specimens as mentioned earlier.

4) Presence of Inclusions

A rather large number of inclusions were observed in the commercial plain carbon steel used in the present study. It is important to mention here that in all the published research on dual phase steels a high purity steel has been selected as the starting material and no attempt has been made to study the effect of non-metallic inclusions on the loss of ductility in dual phase steels. For a long time, inclusions have been associated with reducing ductility and fatigue failure in steels and it is unfortunate that a study in this direction for commercially produced dual phase steels is lacking. It is expected that a number of factors such as size, shape, chemistry, density, distribution and volume fraction of non-metallic inclusions would determine the criticality of inclusions as crack initiators.

5) Retained Austenite

It has been reported (95) that there is an improved uniform elongation with the increase of retained austenite content. This has been explained in terms of transformation induced increase in work hardening rate which, on the basis of Considère criterion, delays the onset of necking. Others (95) find a small amount of retained austenite (~2-4%) by water quenching as compared to (~6-7%) by air cooling from austenite, so, a corresponding decrease in uniform elongation is expected in the present results.

5.2.4.3 Effect of Tempering

The effects of tempering treatment on mechanical properties of isothermally reacted dual phase steels were presented earlier in Figures 5.13 to 16. The general trend of the changes in yield strength, tensile strength, elongation etc. with tempering temperature was the same as the intercritically annealed dual phase steels. The tempering behaviour of the latter has been described earlier in literature review. Briefly, the tempering reactions in dual phase steels are a combination of those effects expected for each of the individual phases. Thus, in the martensite phase we expect to have the decomposition of martensite, precipitation of carbides and the transformation of the retained austenite (96). Similarly, in the ferrite phase we expect to have carbon segregation to dislocations in the ferrite and precipitation of carbides. In addition, there are synergistic effects that can be attributed to the presence of both

phases. For instance, the formation of martensite generates residual stresses and a high dislocation density in the ferrite, especially near the martensite/ferrite interface. Carbon segregation to these dislocations, and the elimination of the residual stresses by the volume contraction of the martensite phase during tempering, is an important part of the tempering process.

A significant drop of about 200 MPa in UTS, observed in the present study, can be attributed to the fact that no precipitation of alloy carbides is expected in the ferrite of plain C steels. In the tempering of alloy steels, precipitation of alloy carbides leads to secondary hardening Even a very small addition of .01% to .09 %V, to low carbon carbon steels, on tempering leads to a coherent precipitation of V_4C_3 in the matrix as well as on dislocations. The true fracture stress remained virtually constant and apparently corresponds to the stress required for decohesion of ferrite-tempered martensite interface.

Since no electron microscopy on thin films or x-ray work was conducted to observe true microscopic changes during tempering process in the present study, it is not known if there are any significant differences in tempering behaviour of isothermally reacted and intercritically annealed specimens.

CHAPTER 6

Empirical Modelling of Stress-Strain Curves of Dual Phase Steels

This chapter is divided into three sections. In the first section, a review of well-known empirical equations used for describing stress-strain curves of dual phase steels and other materials is presented. In the second section, the results of the analysis of deformation behaviour of dual phase steels based on these established empirical stress-strain relationships are described. In the third section, the results of empirical modelling of isothermally transformed dual-phase steels based on Voce's equation and a newly proposed equation are described. A discussion of the results is presented in the last section.

6.1 Review of Previous Work on Modelling of σ-ε Curves of Dual Phase Steels

In general, the deformation behaviour of a multiphase microstructure is characterized by the deformation of each phase plus the interaction between the phases. In dual phase steels, the deformation behaviour is expected to be dependent on the deformation of ferrite, of martensite, and on the compatibility between the phases. Furthermore, the observed behaviour should depend on the relative strength and volume fraction of each phase. For example, for a constant volume fraction of martensite, as the carbon content in martensite is increased, it is anticipated that the strain distribution between the ferrite and martensite will change, thus altering

both the initial yielding and the strain hardening rate at low strains.

Stress-strain curves and the deformation behaviour of metals are frequently described by means of mathematical expressions. In past investigations (11 ,101,102), distinct stages in the deformation behaviour of dual phase steels have been revealed through the analysis of stress-strain curves. The stress-strain curves have been analyzed by four common constitutive equations: the Hollomon (103), the Voce (104), the Ludwik (105) and the modified Swift (106) equations. In the following sections each of these equations and its usefulness for dual phase steels will be discussed separately. A new equation is proposed, which appears to be useful over a larger range of prestrain, in the last section.

The mathematical expressions which have been most widely used to describe the strain hardening behaviour of iron and steel in uniaxial deformation are:

$$\text{Hollomon's equation:} \quad \sigma = k\varepsilon_p^n \tag{6.1}$$

$$\text{Ludwik's equation:} \quad \sigma = \sigma_o + k'\varepsilon_p^{n'} \tag{6.2}$$

where σ and ε_p are true stress and true plastic strain, and the other parameters are empirical constants. The constants n and k in Equation (6.1) are determined by constructing a log σ vs. log ε_p plot. Equation (6.1) has been used to describe the stress-strain behaviour of dual phase steels (21,22) in which it is assumed that a single n value described the strain hardening behaviour. The results of Ramos

et al (10) as well as our results indicate that the log σ vs. log ε_p plots are clearly not linear and a single value of n in Equation (6.1) does not adequately describe the behaviour of dual phase steels.

Monteiro et al (107) have shown that a convenient method for delineating stages in strain hardening is by the application of Jaoul (108)-Crussard (109) analysis to Equation (6.2). In this analysis, log $(d\sigma/d\varepsilon)$ is plotted vs. log ε. Ramos et al (101), Lawson et al (11) and Cribb et al (102) have studied this possibility for dual phase steels. Cribb and Rigsbee (101) have expressed their results in terms of 3 stage deformation mechanism for dual phase steels. They attribute the 3 stages to:

1) Homogeneous deformation of ferrite matrix produced by mobile dislocation/residual stresses surrounding the martensite particles;

2) Constrained deformation of the ferrite caused by the presence of rigid martensite and transformation of retained austenite to martensite;

3) Formation of dislocation cell structures governed by dynamic recovery and cross-slip and by eventual yielding of the martensite phase.

Both Hollomon's equation and Ludwik's equation analyzed either by plotting log σ vs. log ε_p or log$(d\sigma/d\varepsilon)$ vs. log ε_p, have been criticized by ReedHill et al (111). They point out the drawbacks of using ε_p as the independent variable. According to them, parameters such as n, k and

σ_o, determined by plotting log ε_p, tend to be imprecise because the slope of a $\ell n(d\sigma/d\varepsilon_p)$ (or log σ) vs. log ε_p curve depends on where one locates the strain origin. This is important because variations in structure due to uncertainties involved in the manufacture of a metal may be considered as equivalent to adding unknown amounts of prestrain. They demonstrate this problem by comparing Joaul-Crussard plots for specimens which were prestrained compared with specimens which were not.

Reed Hill (111) has presented a modified approach to Jaoul-Crussard plot for analyzing different stages of deformation, based on the modified Swift equation:

$$\varepsilon_p = \varepsilon_o + c\sigma^m \qquad (6.3)$$

In this analysis $\ell n(d\sigma/d\varepsilon)$ is plotted vs. $\ell n\sigma$. The advantage of this approach is that both the instantaneous values of stress σ and the strain hardening rate $d\sigma/d\varepsilon$ depend only on the current arrangement of dislocations and their barriers. Cribb et al (102) and Lawson et al (11) have used this equation, as well, to express their results and find a three-stage strain hardening behaviour in dual phase steels.

Voce (104) in 1948 proposed the following exponential constitutive equation as a simple form of an approach to a saturation stress,

$$\sigma = \sigma_s - (\sigma_s - \sigma_o)\exp(-\varepsilon/\varepsilon_c) \qquad (6.4)$$

where σ_s is the saturation stress, σ_o is a characteristic

stress (related to the yield stress) and ε_c is a characteristic strain for the material. This equation has also been applied by Lawson et al (11) for the case of dual phase steels. The equation is very flexible so a very good fit is achieved at high strain levels (<3%). But Lawson et al found that Voce's equation did not provide an appropriate description of the stress-strain behaviour for the low strain region. Voce himself, in his critical analysis of the equation, has expressed its limitation at low strains (and stresses).

In contrast to Hollomon, Ludwik and Swift's equations, however, the Voce equation has been found to provide the best fit for 2¼Cr-1Mo steel (112), deformed Cu (113) and Al (114). Use of the Voce equation is further supported by the criticism of ReedHill et al (111) regarding plotting ε_p logarithmically for the case of Hollomon's and Ludwik's equations, mentioned earlier. In its strain hardening form, it does not directly rely on ε. (see Table 6.1).

Figure 6.1 indicates schematically the common methods used to evaluate the stress-strain behaviour of materials, as discussed earlier. In Table 6.1, the four constitutive equations and the corresponding strain hardening equations are presented. The derivations are given in Appendix (II).

In the present work, the applicability of all the four equations mentioned earlier, was studied for predicting different stages in the present dual phase steel specimens tested in uniaxial tension.

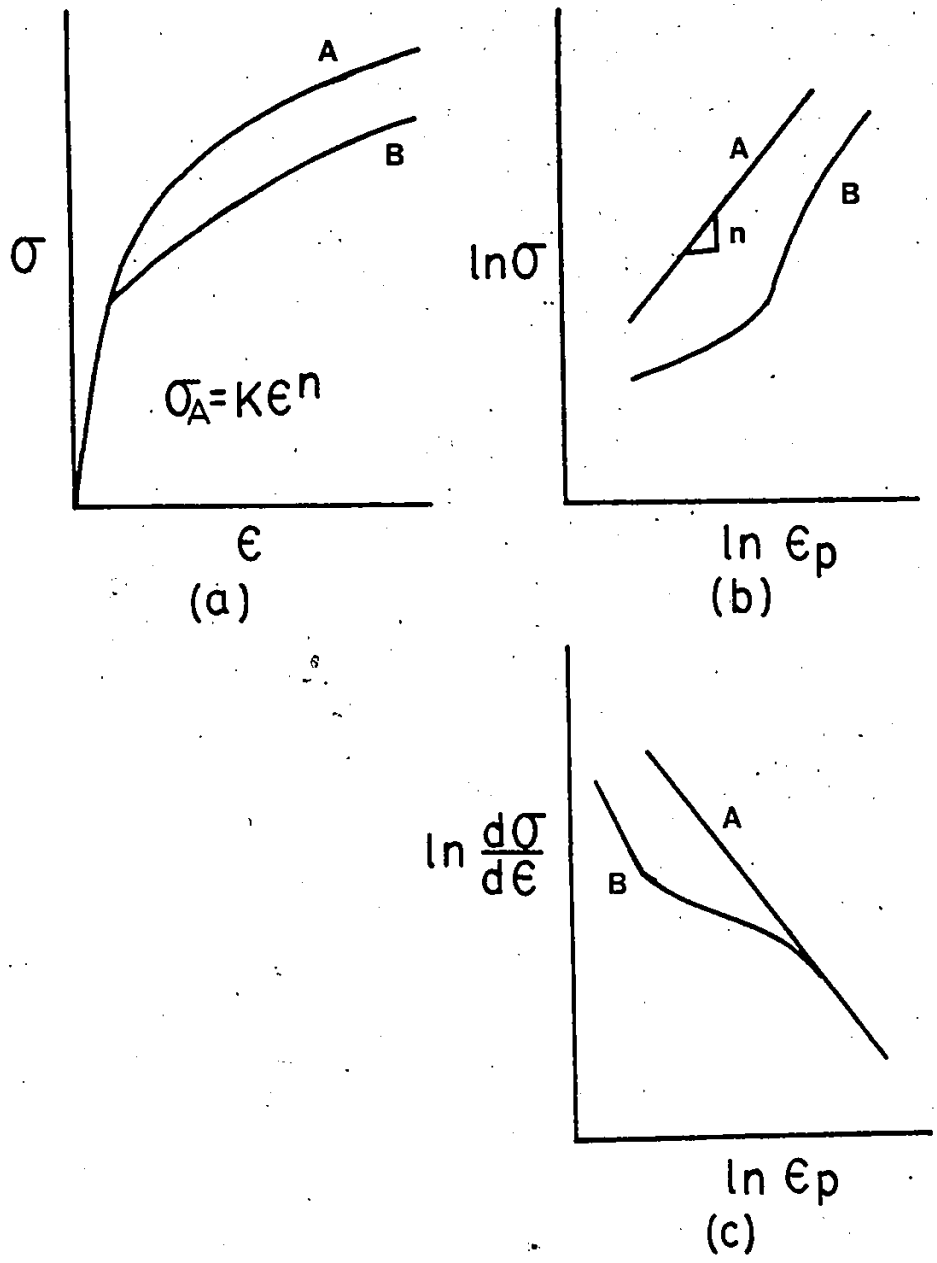

Figure 6.1 Schematics showing the common plots used to evaluate strain-hardening behaviour. (a) stress-strain curves (b) $\ell n\sigma$ vs. $\ell n\varepsilon_p$, (c) $\ell n(d\sigma/d\varepsilon)$ vs. $\ell n\varepsilon_p$ (Jaoul-Crussard plot).

Table 6.1

Constitutive and Analytic Equations Used for Analysis of Strain Hardening Behaviour

Name of Equation	Constitutive Equation	Strain Hardening Equation
Hollomon (103)	$\sigma = k\ \varepsilon_p^n$	$\ell n\sigma = \ell n\ k + n\ell n\varepsilon_p$
Ludwik (105)	$\sigma = \sigma_o + k'\varepsilon_p^{n'}$	$\ell n\ \frac{d\sigma}{d\varepsilon_p} = \ell n(n'k') + (n-1)\ell n\varepsilon_p$
Modified Swift (106)	$\varepsilon_p = \varepsilon_o + c\sigma^m$	$\ell n\ \frac{d\sigma}{d\varepsilon_p} = (1-m)\ell n\sigma - \ell n(cm)$
Voce (104)	$\sigma = \sigma_s - (\sigma_s - \sigma_o)\exp(-\varepsilon/\varepsilon_c)$	$\sigma = \sigma_s + \varepsilon_c(\frac{d\sigma}{d\varepsilon})$

As mentioned later, in the results, all these equations were found to be insufficient to describe the entire stress-strain curves. Voce's equation, however, showed the best fit with the experimental data after a certain initial prestrain.

A new equation, proposed by Watt (110), which predicts the forward flow curves to a reasonable degree of accuracy has been studied in the present work. The proposed equation is based on a differential equation of the following form:

$$\frac{dy}{dx} = A - kx$$

where y and x represent $\ell n\sigma$ and $\ell n\varepsilon$, respectively. This equation will be discussed in detail in Section 6.3.

6.2 Analysis of Deformation Behaviour Using Established Empirical σ-ε Relationships

6.2.1 Results

The following empirical σ-ε relationships were studied:

1. Hollomon Equation $\sigma = k\varepsilon_p^n$
2. Ludwik Equation $\sigma = \sigma_o + k'\varepsilon_p^n$
3. Modified Swift Equation $\varepsilon_p = \varepsilon_o + c\sigma^m$

where σ and ε are true stresses and true plastic strains and σ_σ, ε_o, k, k', n, n', c and m are empirical constants.

For the present analysis, true stress-true strain curves available from the previous tensile tests were utilized. True stress-true strain curves of specimens representing a wide range of ultimate tensile strengths and volume fractions of martensite were carefully selected.

For each specimen about 100 pairs of load-displacement values were used. True stress-true strain plots were converted into $\ell n\sigma$ vs. $\ell n\varepsilon$, $\ell n(d\sigma/d\varepsilon)$ vs. $\ell n\varepsilon$ and $\ell n(d\sigma/d\varepsilon)$ vs. $\ell n\sigma$ plots, using appropriate computer programs, to determine the values of different constants in Hollomon, Ludwik and modified Swift equations respectively. Values of different constants were obtained from the slopes and intercepts of these plots as described in Appendix (II). These constants have been utilized to yield information about deformation mechanisms in materials. Figures 6.2, 6.3, 6.4 and 6.5 represent σ vs. ε, $\ell n\sigma$ vs. $\ell n\varepsilon$, $\ell n(d\sigma/d\varepsilon)$ vs. $\ell n\varepsilon$ and $\ell n(d\sigma/d\varepsilon)$ vs. $\ell n\sigma$ plots respectively of 4 tensile specimens of widely differing martensitic volume fractions and ultimate tensile strengths (Table 6.2). Figure 6.3 shows a $\ell n\sigma$ vs. $\ell n\varepsilon$ plot and is based on Holloman's equation. A continuous change in log σ with log ε is observed for all the 4 specimens. Figure 6.4, referred to as Jaoul-Crussard plot and based on Ludwik's equation, shows a decrease in $\ell n(d\sigma/d\varepsilon)$ with $\ell n\varepsilon$ in an irregular manner. A similar decrease in $\ell n(d\sigma/d\varepsilon)$ with $\ell n\sigma$ can be observed in Figure 6.5 which is an analytical form of the modified Swift equation (106).

In order to study the deformation behaviour of dual phase steels, an attempt was made to carefully define linear regions in each curve, while ignoring local short term fluctuations which might result from inherent errors or transition states from one deformation mehcanism to another. Straight lines passing through the maximum number of

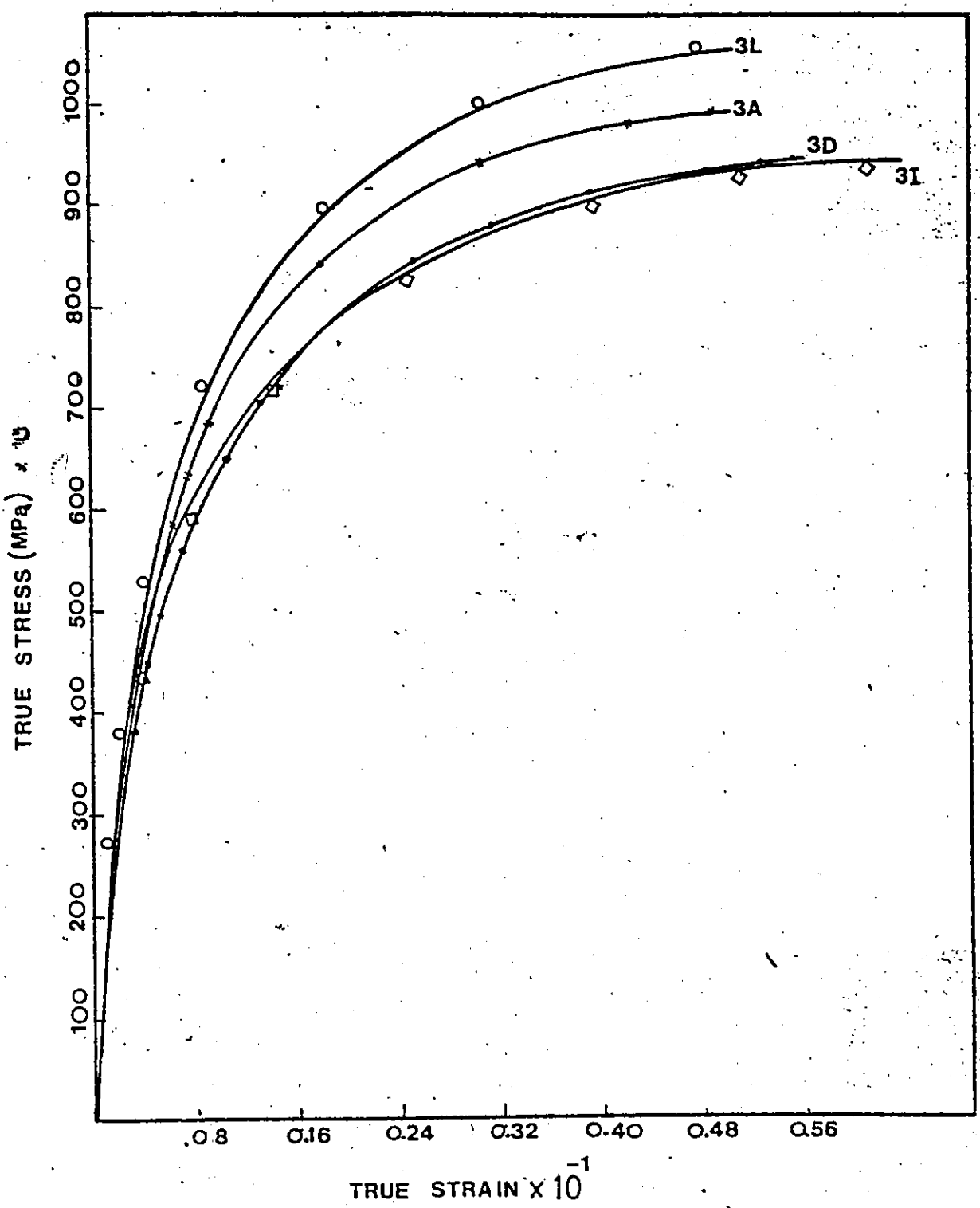

Figure 6.2 True stress - true strain curves of isothermally reacted dual phase steels for different martensitic contents.

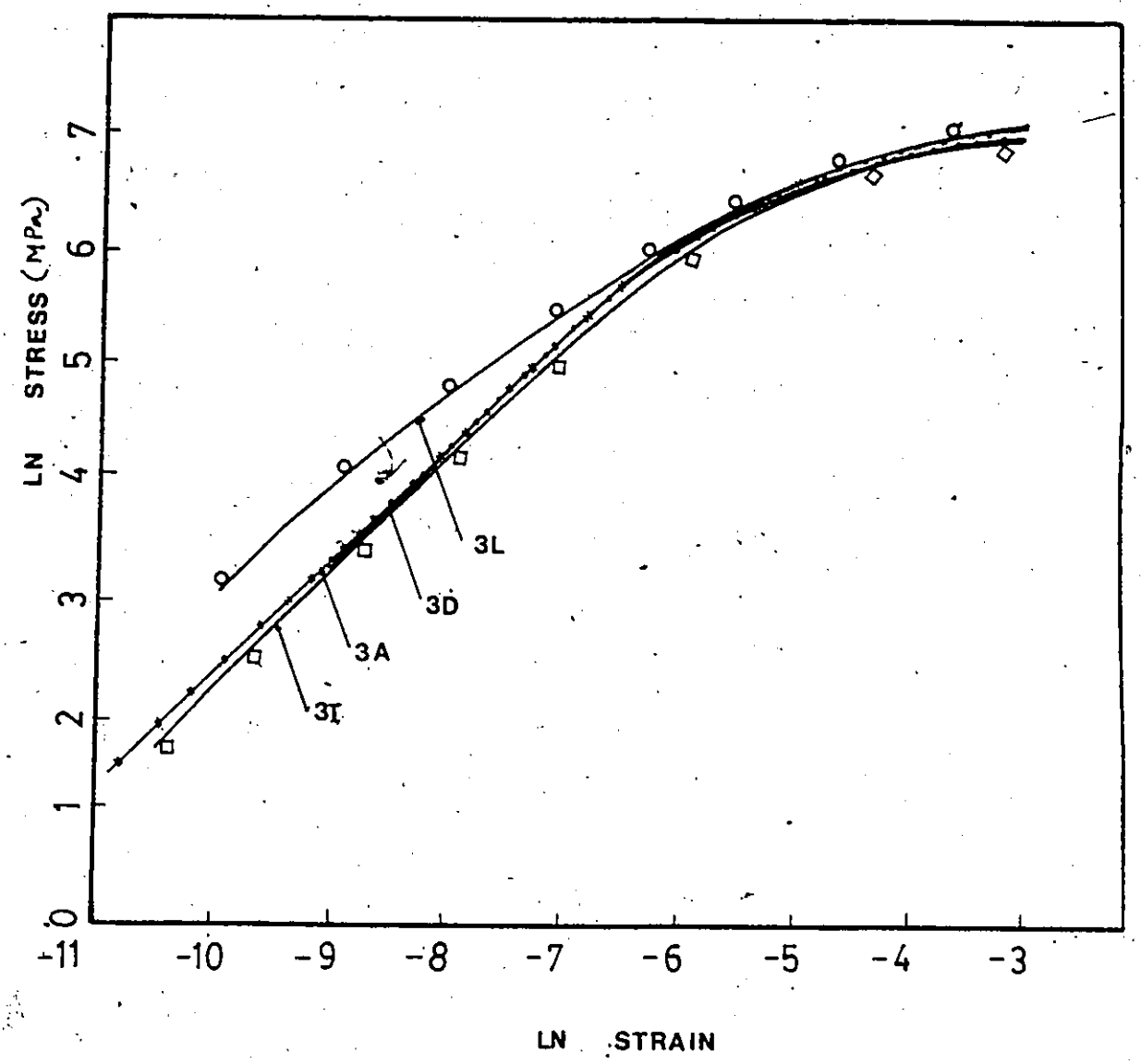

Figure 6.3 ℓn stress vs. ℓn strain curves of specimens 3A, 3D, 3I and 3L. A strain of 0.0025 has a logarith of -6.

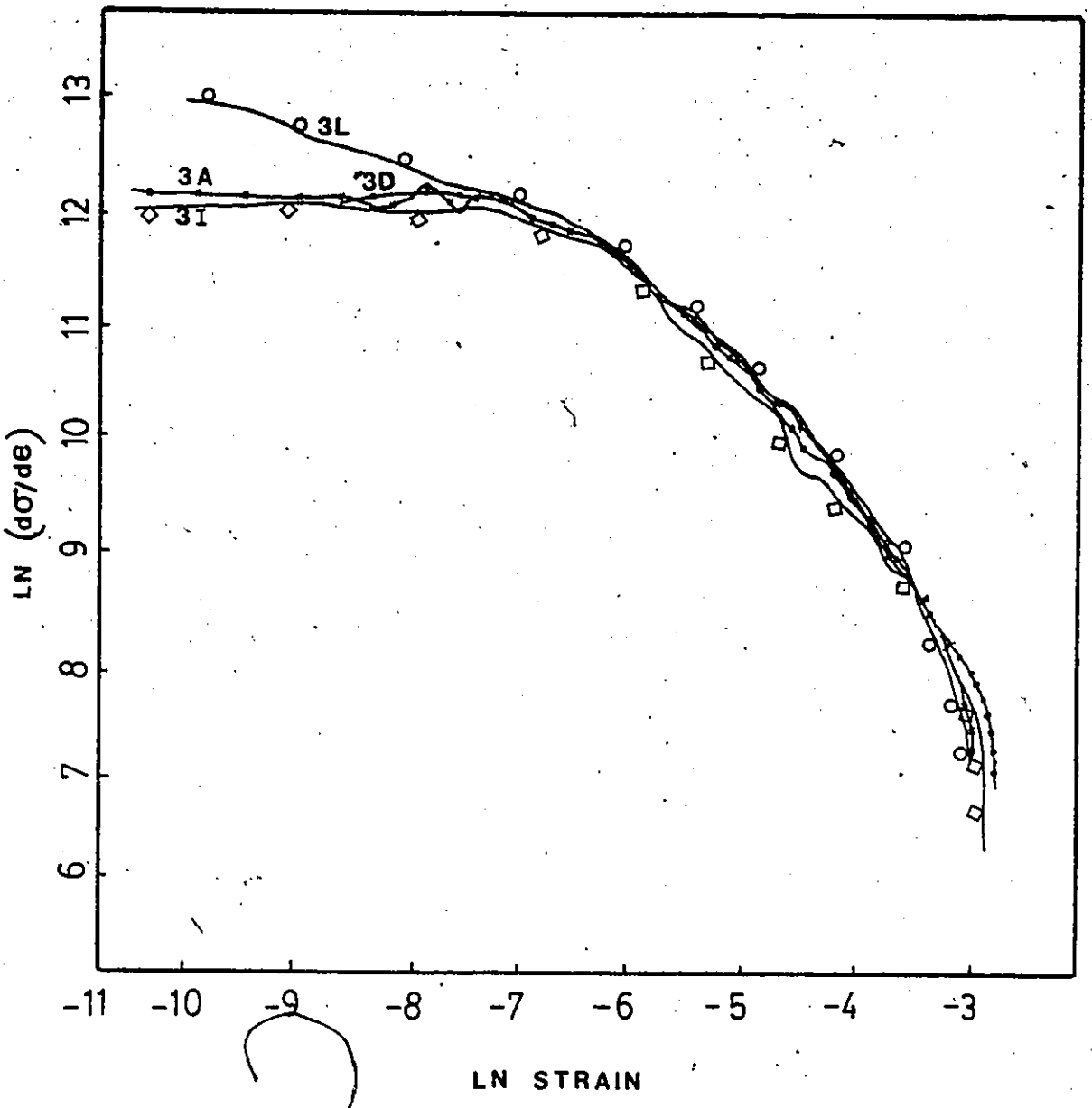

Figure 6.4 $\ell n(d\sigma/d\varepsilon)$ vs. $\ell n\varepsilon$ (Jaoul-Crussard plot) of specimens 3A, 3D, 3I and 3L.

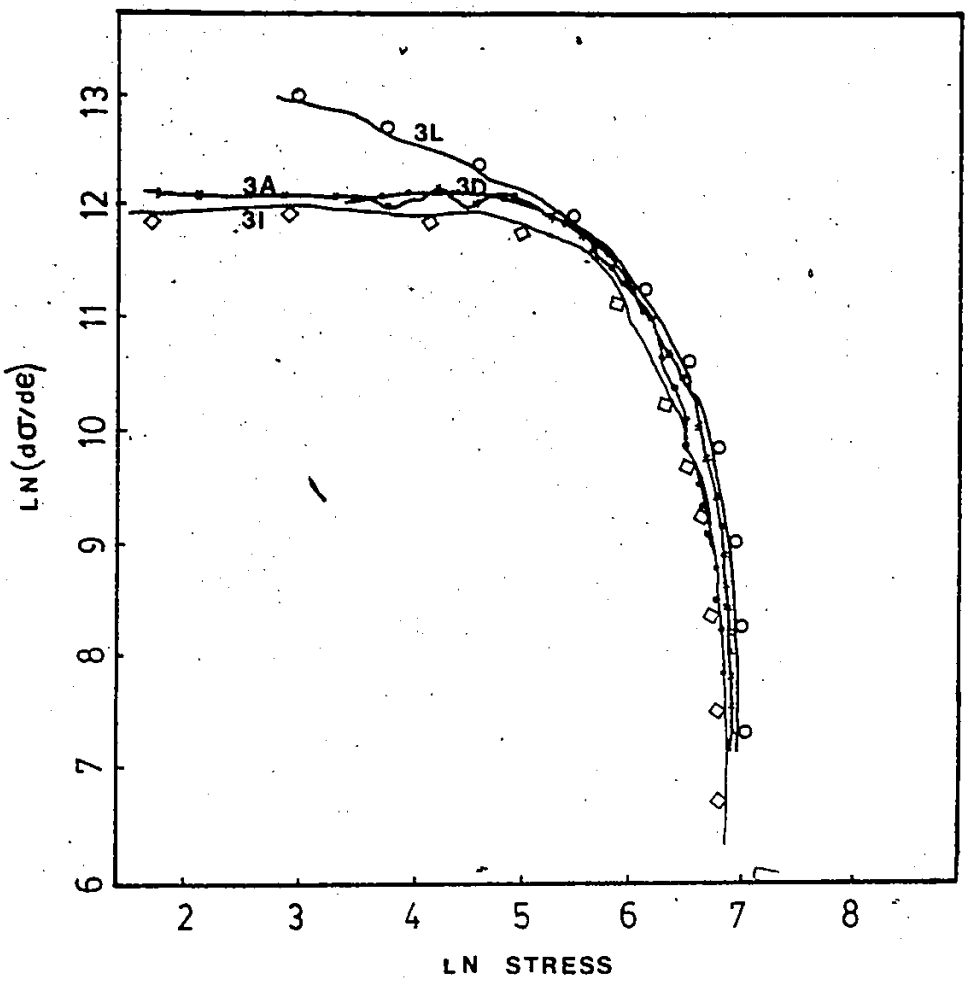

Figure 6.5 ℓn(dσ/dε) vs. ℓn stress curves of specimens 3A, 3D, 3I and 3L.

Table 6.2

The Ferrite Grain Size, Martensitic Content and Ultimate Tensile Strength of Specimens 3A,3D,3I and 3L

Specimen	Ferrite Grain Size (μm)	$V_{Mart.}$ (%)	UTS (Mpa)
3A	7.756	43.82	994.95
3D	7.420	36.71	965.90
3I	7.742	33.68	956.16
3L	8.2009	50.81	1056.5

points on the curve were drawn as shown in Figure 6.6 which represents a Jaoul-Crussard plot of one of the specimens (4F). Each linear region in the figure represents a particular value of the constants σ_o, k' and n and thus can be considered as a deformation stage representing a particular deformation mechanism. From the slope of each linear region or deformation stage in $\ell n(d\sigma/d\varepsilon)$ vs. $\ell n\varepsilon$ curves the values of constant n' were computed. Similarly, from the slope of each stage in $\ell n\sigma$ vs. $\ell n\varepsilon$ and $\ell n(d\sigma/d\varepsilon)$ vs. $\ell n\sigma$ curves, the values of n and m respectively were computed for each deformation stage in a curve. The values of these constants, namely n', n and m obtained from the slope of each stage in $\ell n(d\sigma/d\varepsilon)$ vs. $\ell n\varepsilon$, $\ell n\sigma$ vs. $\ell n\varepsilon$ and $\ell n(d\sigma/d\varepsilon)$ vs. $\ell n\sigma$ plots are shown in Table 6.3 and are plotted as a function of volume fraction of martensite in Figures 6.7, 6.8 and 6.9 respectively. Only 4 stages have been shown in Figures 6.8 and 6.9. A wide scatter in the values of these constants for each stage and from specimen to specimen was observed.

6.2.2 Discussion

In this section a discussion of the analysis of tensile tests based on Hollomon's Ludwik's and modified Swift empirical equations, to characterize the work hardening behaviour of isothermally transformed dual phase steels will be presented. Hollomon's equation ($\sigma=k\varepsilon_p^n$) assumes that the strain hardening behaviour can be described by a single value of n. Present results (Figure 6.3) show logarithmic

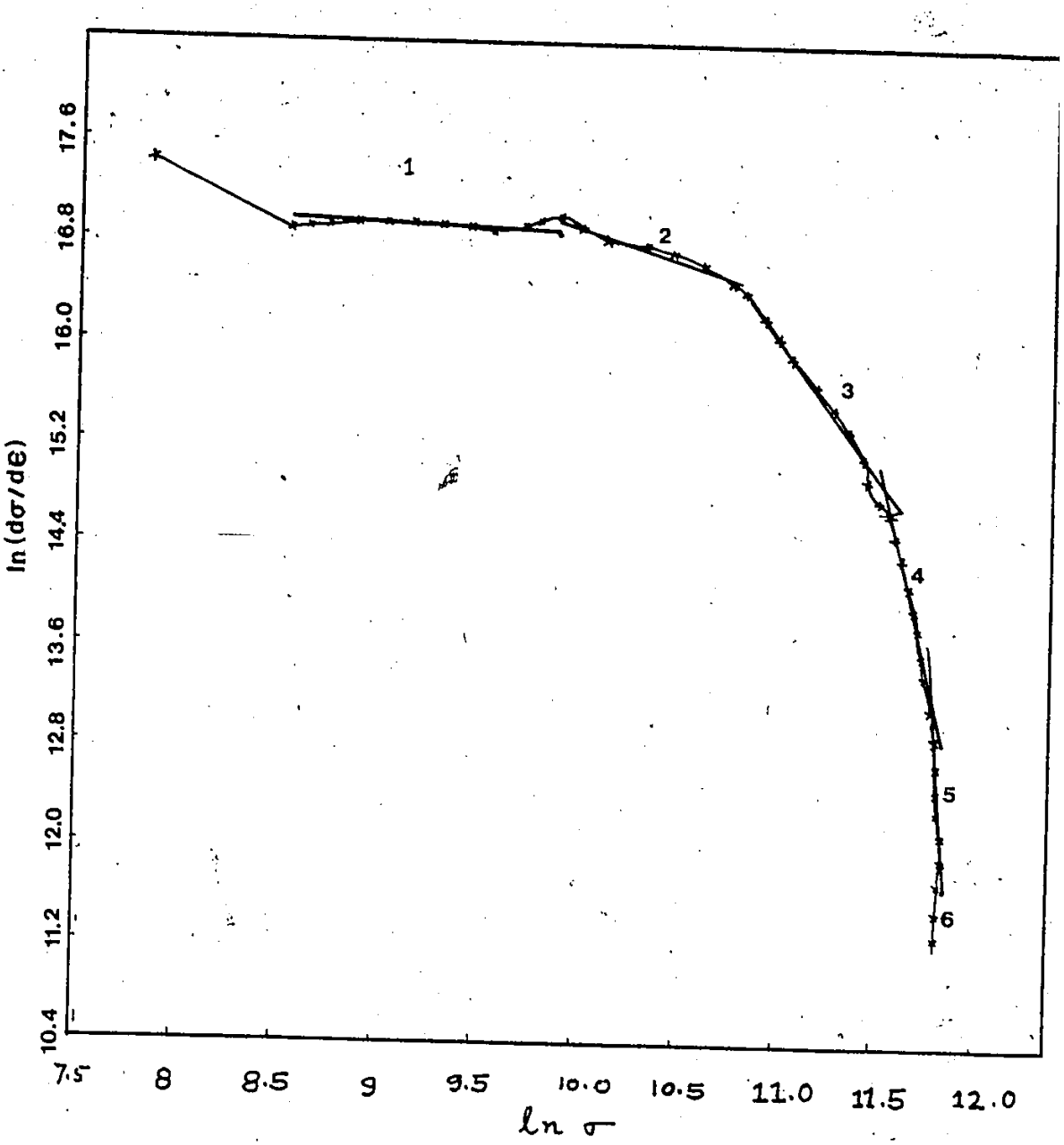

Figure 6.6 $\ln(d\sigma/d\varepsilon)$ vs. $\ln \sigma$ plot for specimen 4F.

Table 6.3

The values of different constants in Hollomon(n), Ludvik(n'), and modified Swift(m) Equation

Stages Number	Specimen Name	Strain Interval	n'	m	n
FIRST	4D	0.000156-0.000421	0.934	1.083	0.631
	4E	0.000233-0.000532	0.835	1.176	0.837
	4B	0.000135-0.000357	1.133	0.863	1.048
	4K	0.000140-0.000344	0.777	1.303	0.799
	4M	0.000149-0.000861	0.686	1.439	0.668
SECOND	4D	0.000731-0.001268	0.421	1.762	0.737
	4E	0.001018-0.00203	0.369	1.481	0.682
	4B	0.001640-0.009132	0.581	1.366	1.015
	4K	0.000432-0.001571	0.604	1.538	0.711
	4M	0.001331-0.001969	0.237	2.144	0.674
THIRD	4D	0.00153 -0.0136	-0.004	3.496	0.358
	4E	0.0025 -0.0131	0.063	3.173	0.513
	4B	0.0016 -0.0091	-0.018	2.904	0.620
	4K	0.0024 -0.0038	-0.101	3.279	0.388
	4M	0.0021 -0.0072	0.001	3.365	0.417
FOURTH	4D	0.018 -0.031	-0.225	5.882	0.256
	4E	0.013 -0.025	-0.611	8.273	0.358
	4B	0.013 -0.025	-0.471	6.502	0.275
	4K	0.006 -0.010	-0.214	4.857	0.316
	4M	0.010 -0.030	-0.681	10.903	0.181
FIFTH	4D	0.046 -0.058	-1.100	12.905	0.159
	4E	0.033 -0.048	-0.980	8.273	0.195
	4B	0.026 -0.039	-2.036	6.502	0.195
	4K	0.013 -0.028	-0.281	6.465	0.237
	4M	0.035 -0.055	-1.075	22.051	0.101
SIXTH	4D	0.059 -0.072	-2.937	39.462	0.0562
	4E	0.053 -0.067	-1.224	81.285	0.0874
	4B	0.040 -0.043	-6.058	150.94	0.0513
	4K	0.049 -0.059	-2.487	38.46	0.0858
	4M	0.057 -0.06	-5.769	143.81	0.0324

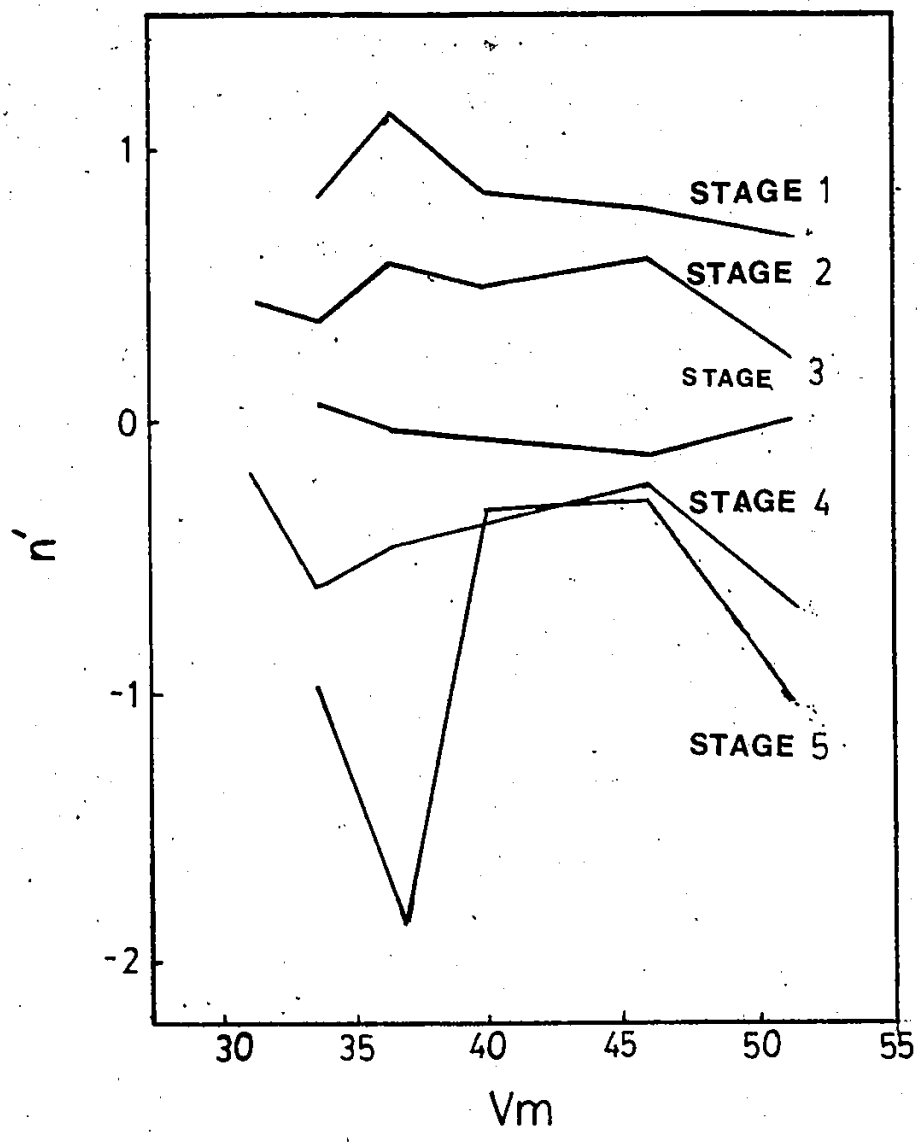

Figure 6.7 Using the Ludwik equation and the $\ell n(d\sigma/d\varepsilon_p)$ vs. $\ell n\varepsilon$ plots, this figure represents a lack of correlation between work hardening parameter n, and the volume fraction of martensite.

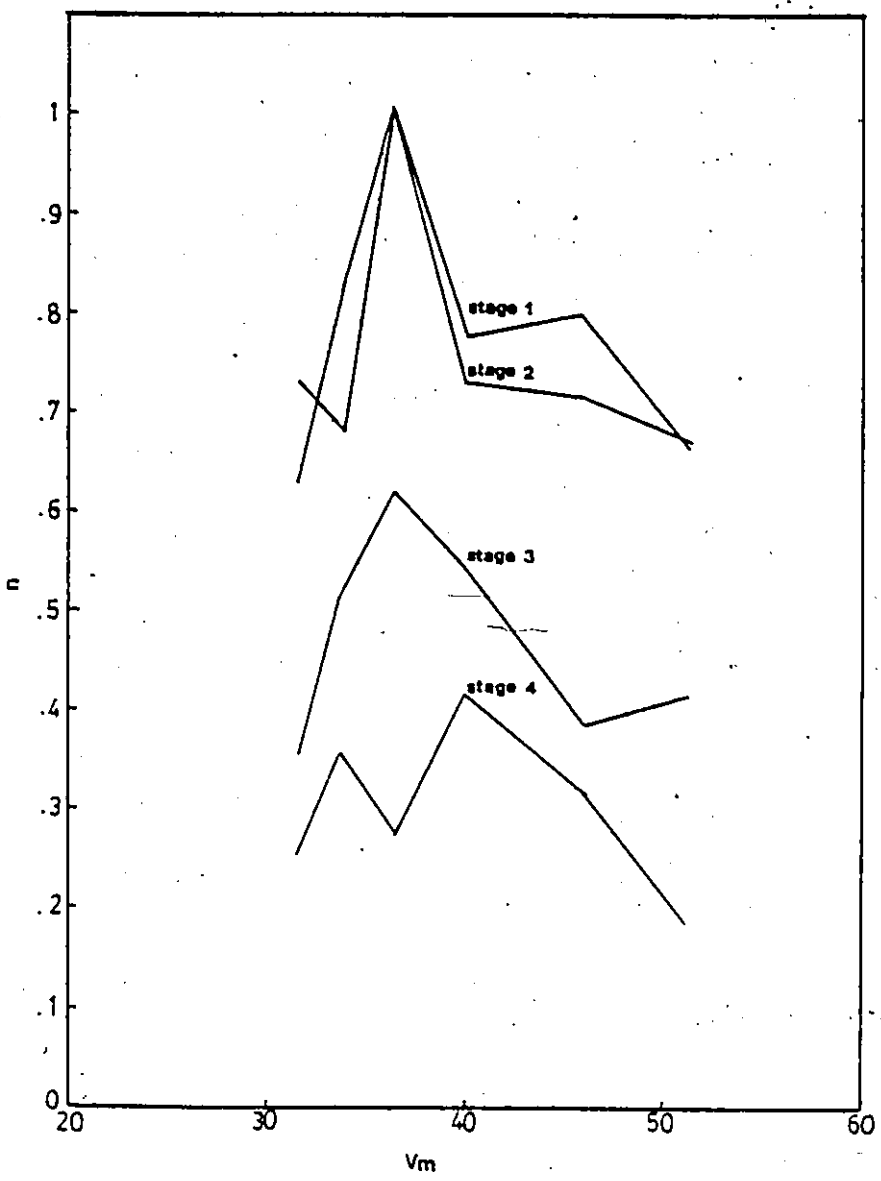

Figure 6.8 Using the Hollomon equation and the $\ell n(d\sigma/d\varepsilon)$ vs. $\ell n\sigma$ plots, this figure represents a lack of correlation between work hardening parameter m and the volume fraction of martensite.

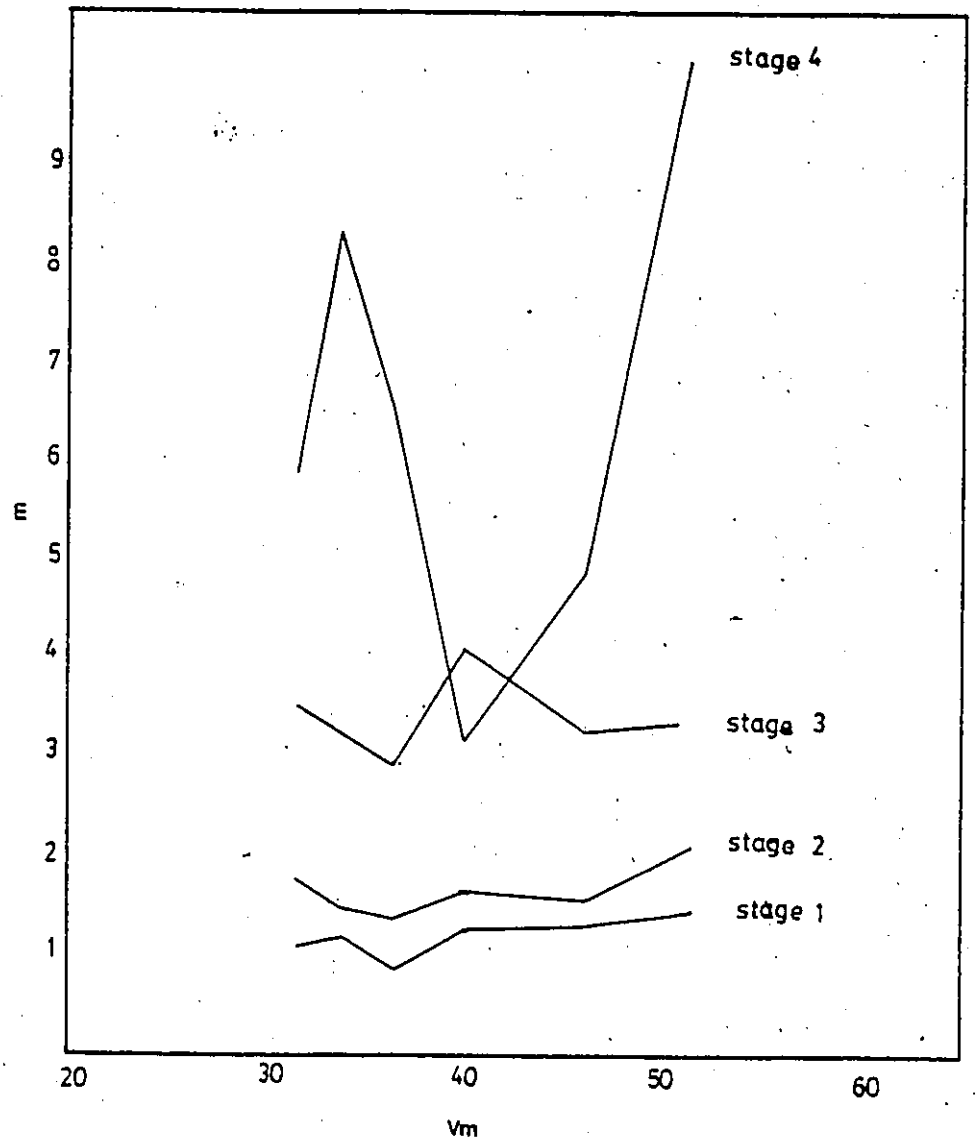

Figure 6.9 Using the Swift equation and the $\ell n\sigma$ vs. $\ell n\varepsilon$ plots, this figure represents a lack of correlation between work hardening parameter n, and the volume fraction of martensite.

plots of σ versus ε for the different dual phase steels. These plots demonstrate, however, that a unique strain hardening parameter, n, does not describe the deformation behaviour of dual phase steels at any level of strain. This is in agreement with the results of other workers (11, 92) for intercritically annealed dual phase steels.

The work hardening processes in dual phase steels, based on Ludwik's and modified Swift's equation, have been explained in terms of three stages (102, 11, 16). According to Cribb et al (102) in the first stage (<0.5%) strain, a rapid work hardening is present because of the elimination of residual stresses and the rapid buildup of back stresses in the ferrite caused by the plastic incompatibility of the two phases. In the second stage (0.5 to 4% strain), the work hardening rate of the ferrite is reduced as the plastic flow of the ferrite is constrained by the hard, undeforming martensite particles. Finally in the third stage (4 to 18% strain), dislocation cell structures are formed and further deformation in the ferrite is governed by dynamic recovery and cross-slip and eventual yielding of the martensite phase. Each of these stages have been shown to provide linear regions in $\ell n(d\sigma/d\varepsilon)$ vs. $\ell n\varepsilon$ and $\ell n(d\sigma/d\varepsilon)$ vs. $\ell n\sigma$ plots. Three stages of deformation have similarly been reported for other two phase dispersion hardening systems (115-117)

In the present studies, more than 3 linear regions were observed. In some specimens (Figure 6.6) as many as 6 linear regions can be separated on Jaoul-Crussard plots

which are based on Ludwik's equation. These plots, in general, showed several linear regions of varying slopes in the initial part of the curve and threafter a continuous nonlinear change in these plots was observed. Thus much of the data towards the end of Jaoul-Crussard plots did not show a sharp transition between different stages. The presence of additional stages in the present study indicates that the strain hardening of dual phase steels may be more complex than the three stage deformation described by other workers. Each stage for deformation of dual phase steels, as described by other workers will now be considered separately. According to Cribb et al (102) a general yielding of ferrite grains takes place during Stage I. All ferrite grains deform and the mean free path of the dislocations in ferrite is equal to the ferrite grain size. The hard martensite phase provides a ready supply of dislocations. It seems from their description of the first stage that the strain hardening rate in this stage would entirely depend upon the ferrite grain size and the mobile dislocation density in the ferrite and it would correspond to a linear region in Jaoul-Crussard plots. This description ignores completely the non-uniformity of both the varying levels of residual stress and of dislocation density in ferrite. The variation of dislocation density and of residual stress in the ferrite depends on a number of factors such as volume fraction of martensite, morphology of ferrite-martensite interface, size and distribution of martensite particles, and ferrite grain size. This description also ignores

interaction of dislocations with various precipitates (alloy carbides, carbonitrides, etc.) which are commonly observed in ferrite as well as the effects of solid solution strengthening of ferrite. It is expected that all these additional factors will influence the strength and work hardening rate of dual phase steels in the initial stages. It is therefore reasonable to assume that initial deformation of ferrite may not behave as a linear region on Jaoul-Crussard plots or there may be more than one linear region corresponding to strains at which different processes are activated. Stage II has been associated with strong interaction between the deforming ferrite and the rigid martensite particles leading to a high dislocation density in the ferrite and the transformation of retained austenite to martensite. Clearly, this stage depends upon the volume fraction, morphology and carbon content of the martensite and the strains at which this stage initiates is liable to change according to these variables. In addition, the transformation of retained austenite to martensite would start at a particular strain and at a characteristic rate different from the buildup of dislocations in ferrite. Thus these processes, referred to as Stage II, cannot be explained in terms of a single linear region. Finally, Stage III has been attributed to the formation of cell structures, cross-slip and dynamic recovery processes, to the initiation and growth of voids at the ferrite-martensite interface and within the martensite, and to the yielding of martensite. All these processes are fairly

complex and it is not reasonable to represent them by a single linear region and associate them with discrete deformation mechanisms. As mentioned earlier in this discussion, no linear regions were observed in the last stage, in the present study, and instead a continuous non-linear decrease in the slope was observed in Jaoul-Crussard plots.

Although much of the data (Figure 6.4, 6.5) did not show sharp transitions between different linear regions, in an effort to compare our results with the results of other workers, lines passing through maximum number of points were carefully drawn and the entire $\ell n\sigma$ vs. $\ell n\varepsilon$, $\ell n(d\sigma/d\varepsilon)$ vs. $\ell n\varepsilon$ and $\ell n(d\sigma/d\varepsilon)$ vs. $\ell n\sigma$ plots were divided into 6 linear regions for each specimen. This was done to evaluate coefficients n, n' and m in the Holloman, Ludwik and modified Swift equations, in a manner analogous to other workers (11, 102) as described earlier. These coefficients were found to vary widely from one linear region to another and also from specimen to specimen, and no particular trend was noticeable (Figure 6.4, 6.5). A straightforward correlation of n, n' and m vs. martensite content as done by Cribb and Rigsbee, could not be duplicated here due to a wide scatter in the coefficients. No changes in microstructure, which correlate with changes in these coefficients, have been observed by any of the workers (11, 101, 102).

These results, thus cast some serious doubts as to the applicability of empirical equations and their analytical functions in delineating different deformation mechanisms

in dual phase steels. The processes involved during deformation are so varied and complex that a single set of parameters cannot consistently describe the deformation behaviour of dual phase steels even over a limited plastic strain range.

In summary, the lack of a linear region on a $\ell n\sigma$ vs. $\ell n\varepsilon$ plot disqualified the Hollomon equation as a valid description of the present data. The plots of $\ell n(d\sigma/d\varepsilon)$ vs. $\ell n\varepsilon$ or $\ell n\sigma$ did not show a few linear regions with common slopes from specimen to specimen, and hence the popular analysis based on Ludwik's or Swift's equations were also not satisfactory. It was not clear if these curves showed a substantial number (>5) of linear regions or if they showed a continuous curvature with some minor fluctuations. In either case, the conclusion was that the Jaoul-Crussard type analysis was not particularly helpful for our specimens.

6.3 Results of Empirical Modelling of σ-ε Curves Based on Voce's Equation and the New Logarithmic Equation

To overcome the difficulties with the poor fit with the Hollomon, Ludwik and Swift equations, a new empirical equation for describing stress-strain curves of dual phase steels has been developed:

$$\sigma = c_o \varepsilon^{A-(k/2)\ell n\varepsilon}$$

where σ, ε are true stresses and true strains and c_o, A and k are constants.

This equation is similar, in essence, to the other three equations mentioned in the previous section as they

all represent parabolic functions. It differs from Hollomon and Ludwik's equation in that it has an additional $\ell n\varepsilon$ term as an exponent of strain to take into account a decreased work hardening rate at larger strains. The proposed equation is based on a simple linear differential equation of the following form:

$$\frac{dy}{dx} = A-kx$$

where y and x represent $\ell n\sigma$ and $\ell n\varepsilon$ respectively. On integration of the above equation, we have,

$$y = -\frac{k}{2}x^2 + Ax + c$$

or, $$\ell n\sigma = -\frac{k}{2}(\ell n\varepsilon)^2 + A\ell n\varepsilon + c$$

and, $$\sigma = c_o \varepsilon^{A-(k/2)\ell n\varepsilon}$$

The values of constants k, A and c can be obtained from the slope of $(d\ell n\sigma/d\ell n\varepsilon)$ vs. $\ell n\varepsilon$ plots (Figure 6.10) in the final stages or by nonlinear curve fitting techniques. Subsequently, in this thesis, this equation will be referred to as the log method.

The Voce equation was also studied for empirical modelling of stress-stress curves. The Voce equation can be expressed as:

$$\sigma = \sigma_s-(\sigma_s-\sigma_o)\exp(-\varepsilon/\varepsilon_c)$$

where σ and ε are true stresses and true strains and σ_s, σ_o and ε_c are constants.

The values of different constants namely, σ_s, σ_o and

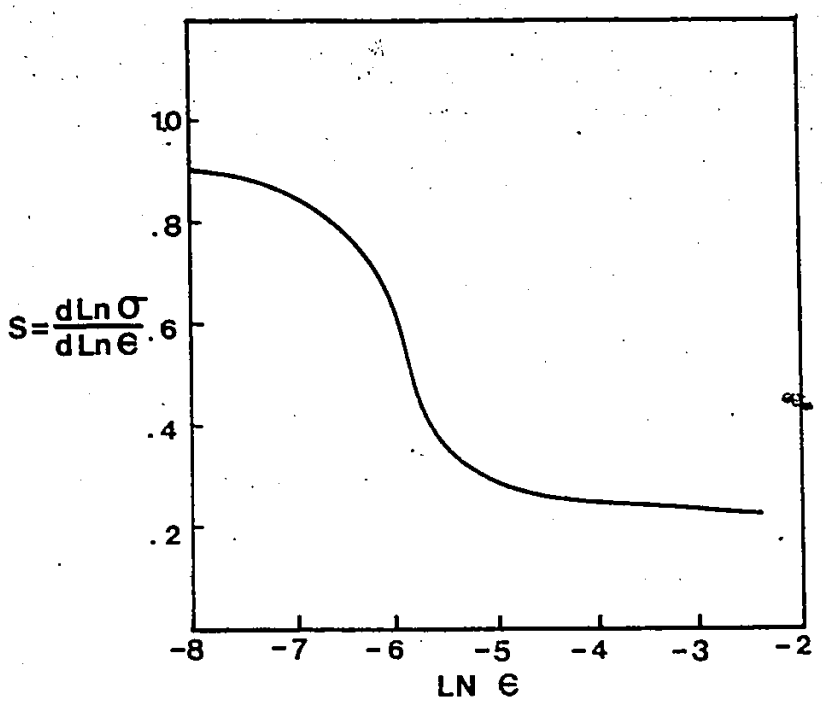

Figure 6.10 Schematic diagram showing a plot of ($d\ell n\sigma/d\ell n\varepsilon$) vs. $\ell n\varepsilon$ for determining constants k, A, c in the log methods. At $\ell n\varepsilon = -5, \varepsilon=0.0067$ and at $\ell n\varepsilon = -23, \varepsilon=0.10$.

ε_c in Voce's equations and k, A and c in the log method were determined by nonlinear fitting techniques (Appendix III).

Both the Voce equation and the log method provided a very good fit to the data, as measured by the least mean square deviation. The Voce equation did not fit as well at low strain levels.

In the present study of the Bauschinger effect, the permanent softening parameter was chosen to be the most representative measure of the Bauschinger effect. The permanent softening parameter is the stress difference between the extrapolated forward prestrain curve and the symmetrically inverted reverse flow curve (Figure 3.13). This procedure requires an accurate extrapolation of the prestrain curve beyond its experimentally measured strain limit. Hence, the following procedure was developed to test the applicability of each of the two equations for data extrapolation procedures.

Initially, curve fitting using each of the above mentioned equations was attempted in a selected strain interval in the early part of the curve (.005 to .01 and .01 to .03) and the values of the constants were determined. These constants were then used to extrapolate the remaining flow stress curve. For example, in the case of specimens B13F, B14I, the entire strain region extends up to .05 and 0.64. Curve fitting parameters were found in the strain interval of .005 to .01 and .01 to .03 and the remaining part of

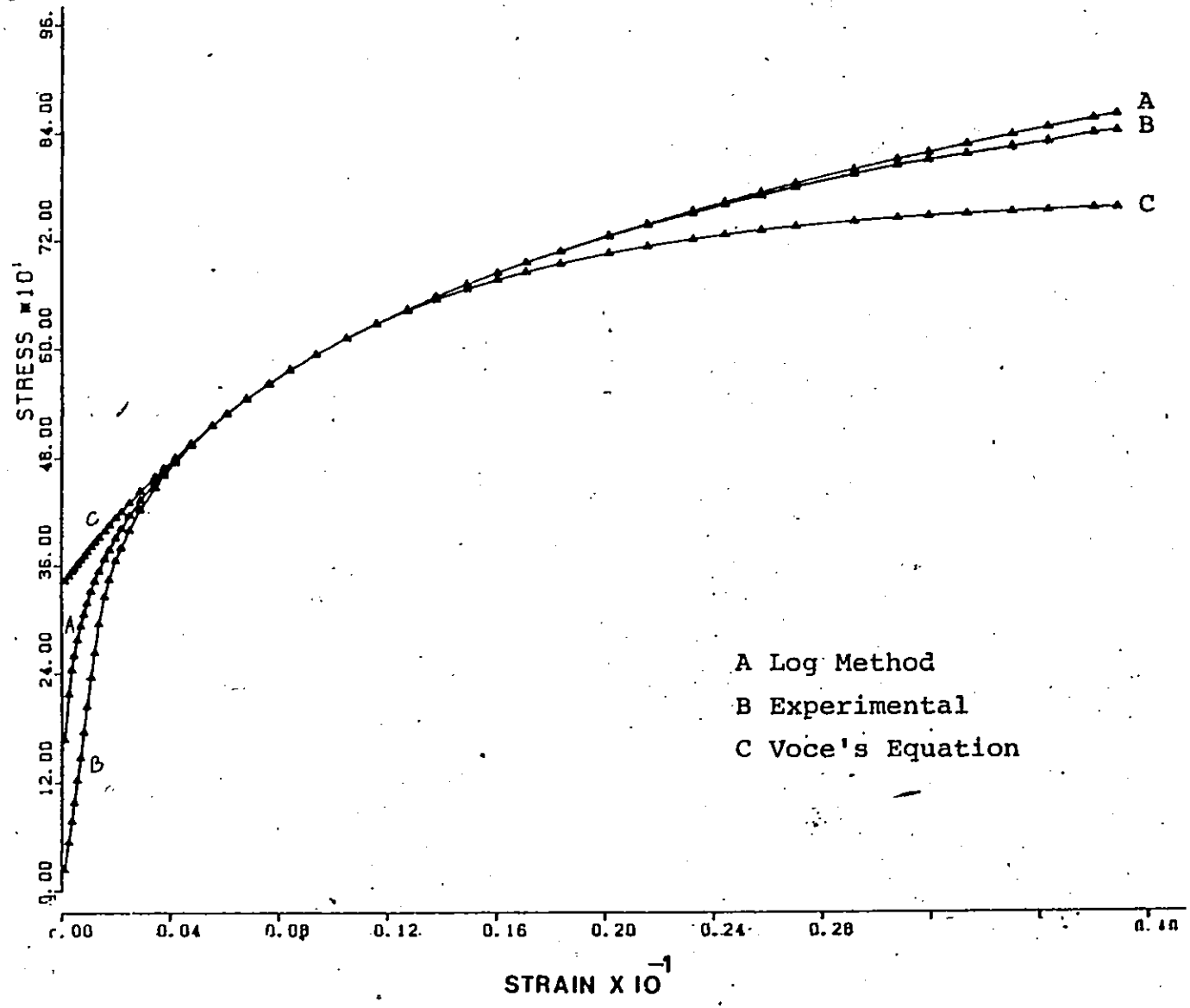

Figure 6.11 Experimental curve for specimen B13F and the extrapolated curves using the Voce's equation and the log method. The curve fitting strain interval is 0.005-0.01.

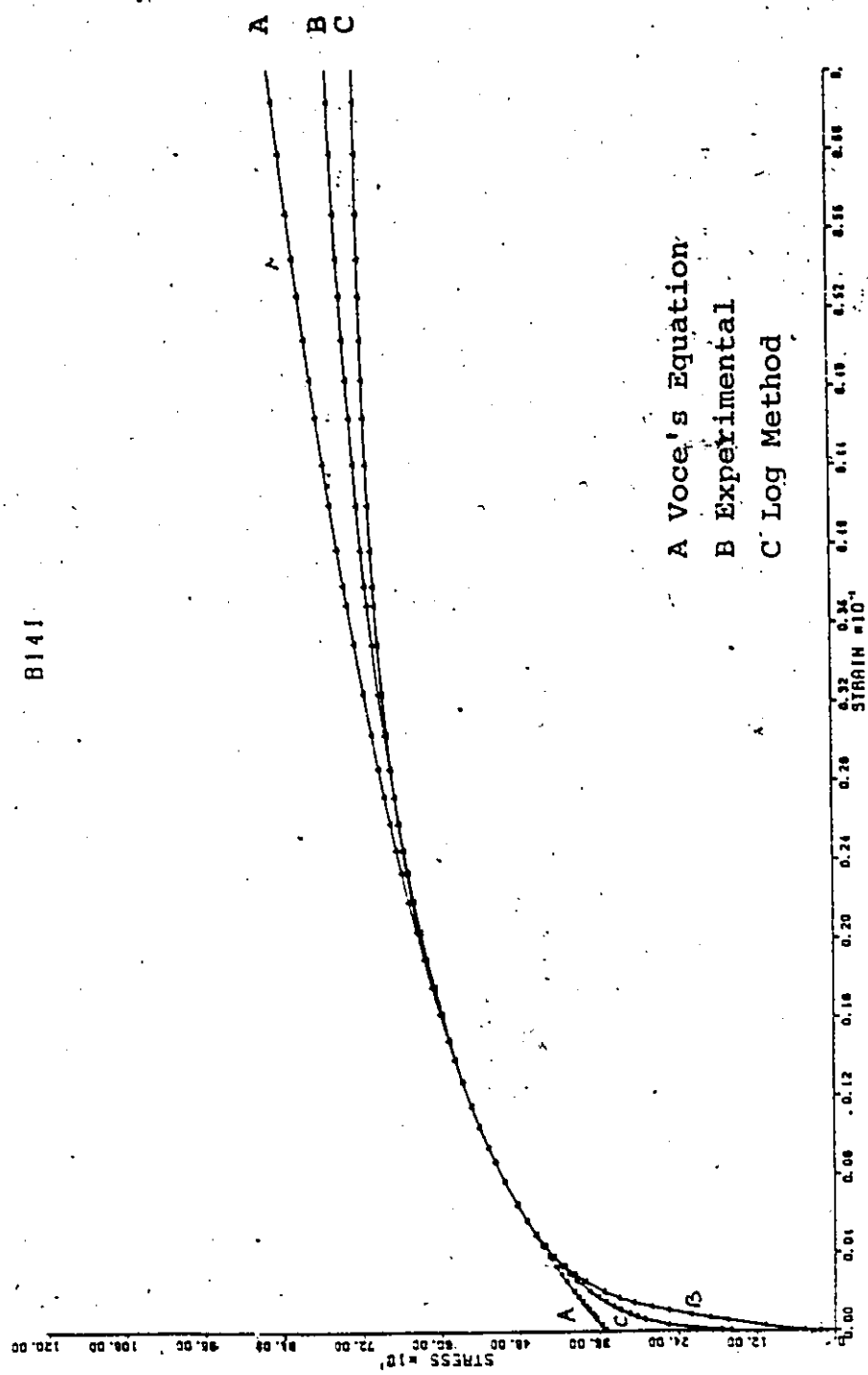

Figure 6.12 Experimental curve for specimen B14I and the extrapolated curves using the Voce's equation and the log method. The curve fitting strain interval is 0.01 to 0.03.

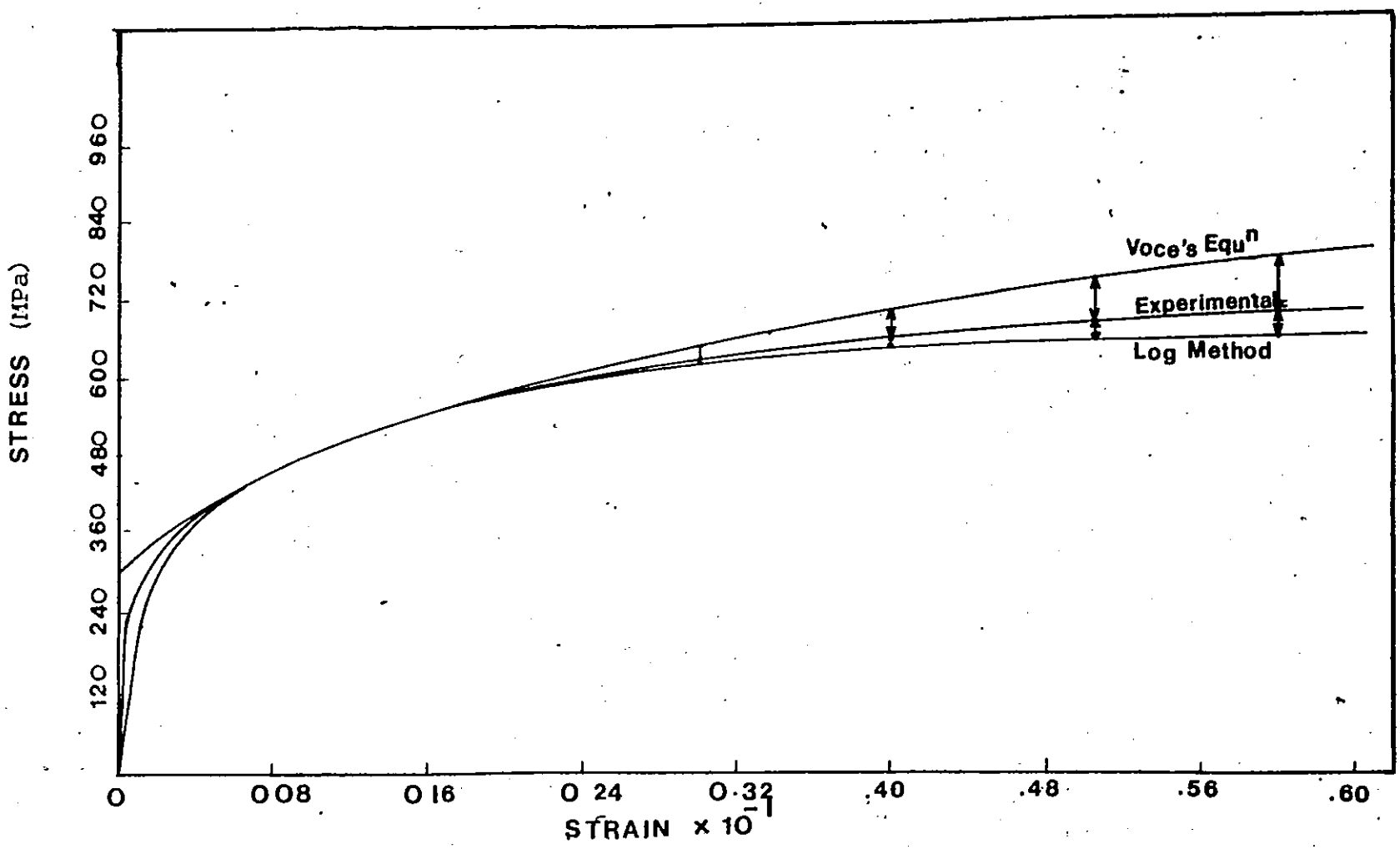

Figure 6.13 Schematic diagram showing the estimation of error in extrapolating experimental curves by the Voce's equation and the log method.

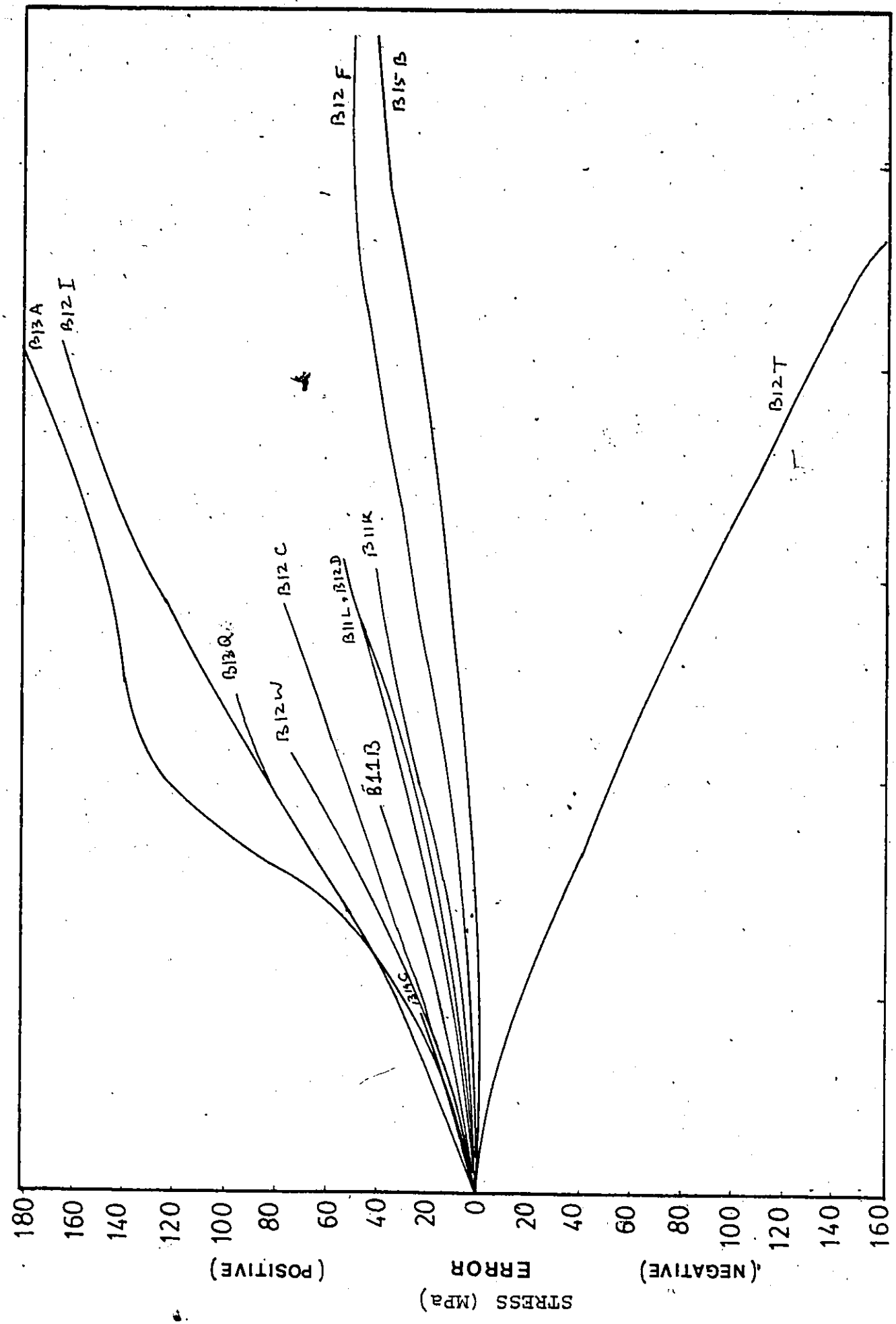

Figure 6.14 Error in extrapolating experimental curves by Voce's equation for curve fitting in the strain interval 0.005 to 0.01.

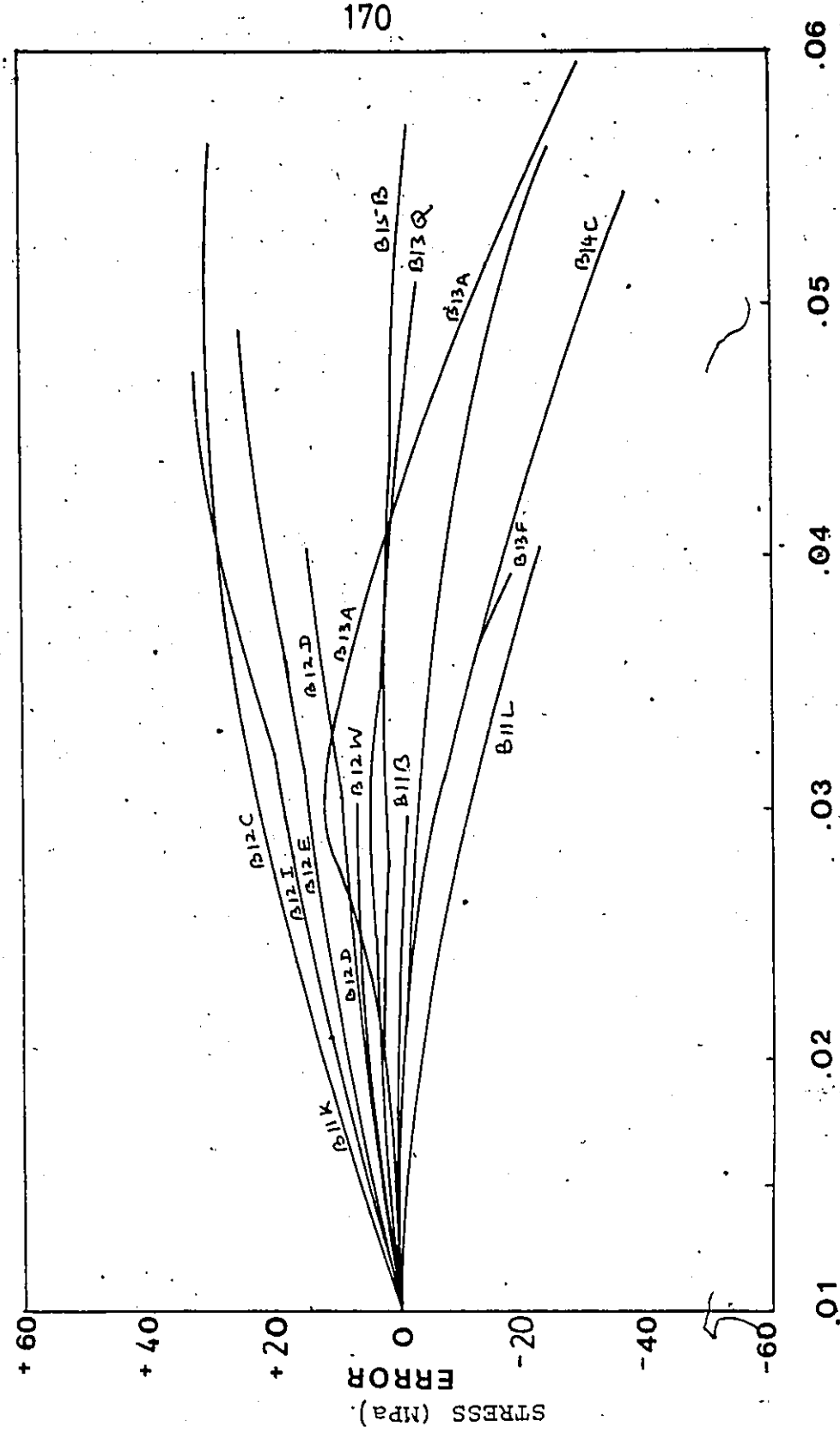

Figure 6.15 Error in extrapolating experimental curves by log method for curve fitting in the strain interval 0.005 to 0.01.

Table 6.4

Curve Fitting in (.005-.01) Strain Interval for Prediction of the Remaining Prestrain Part of Bauschinger Curves

Specimen Name	End of Prestrain	Constants of Log Method			Voce's Constants			Difference by Log Method	Difference by Voce's Equation
		K	A	C	S_I	S_O	$\beta=(1/\varepsilon_c)$		
B11B	.029	0.066451	0.001997	6.940684	676.3962	241.1915	200.2453	- 1.32	37.29
B11K	.046	0.052156	0.025146	7/030735	743.0743	335.3635	50.8146	33.78	58.53
B11L	.040	0.041211	0.095901	7.341964	606.8759	228.1209	120.043	-22.89	39.91
B12C	.037	0.062718	-0.034952	6.738354	634.2848	270.6003	93.5910	28.79	44.37
B12D	.039	0.083051	-0.074510	6.853928	560.3143	175.6721	175.6439	13.81	77.57
B12F	.072	0.030084	0.098110	7.172831	819.009	249.9568	75.7955	- 4.14	48.78
B12T	.077	0.015534	0.208559	7.401125	682.1333	281.6289	97.9473	-45.03	-169.83
B12W	.029	0.053434	0.015596	7.123323	709.7595	332.8340	117.4322	6.84	63.63
B12I	.056	0.054806	0.006996	7.019818	726.3064	301.2190	125.8820	29.63	177.24
B13A	.066	0.031693	0.133461	7.408381	774.4233	309.3953	121.7414	-36.79	210.82
B13Q	.051	0.004205	0.209523	7.376402	---	---	---	- 4.27	---
B14C	.052	-0.042290	0.447069	7.637697	644.6289	275.2549	48.8040	-33.48	17.41
B15B	.057	-0.036767	0.357999	7.123319	626.1833	269.4867	26.3962	- 2.68	32.12
B13F	.038	0.005803	0.237266	7.556628	765.4219	338.7139	96.8180	-18.44	84.83

the curve was extrapolated. The experimental curve and the extrapolated curves using Voce's equation and log method are shown in Figure 6.11 and 6.12 for the two strain intervals.

The differences between the extrapolated and experimental flow stresses were measured, along the extrapolated region, to estimate the accuracy of each of these equations in predicting the flow stress as illustrated in Figure 6.13. The results of such an analysis, for curve fitting in the .005-.01 strain interval, for 12 different specimens, is given in Figure 6.14 and 6.15. The data pertaining to these figures is presented in Table 6.4. These figures represent a plot of the difference between extrapolated and experimental flow stresses (referred to as 'error' in the figures) vs. strain for Voce's equation and log method respectively. As shown in these figures, the errors for both Voce's equation and the log method increase as one moves to higher and higher strains. However, the log method offers a more accurate extrapolation of the flow stress curves as shown in these figures. The variance and the coefficient of variation were determined as 1393.42, 1.2148 and 100.88, 2.1423 for Voce's equation and log method respectively.

Figures 6.16 and 6.17 represent a similar plot of the difference between the extrapolated and experimental flow stresses vs. strains for curve fitting in the strain interval of .01 to .03 by Voce's equation and by the log method. As shown in these figures, the range of errors is much smaller than in the previous case where curve fitting was

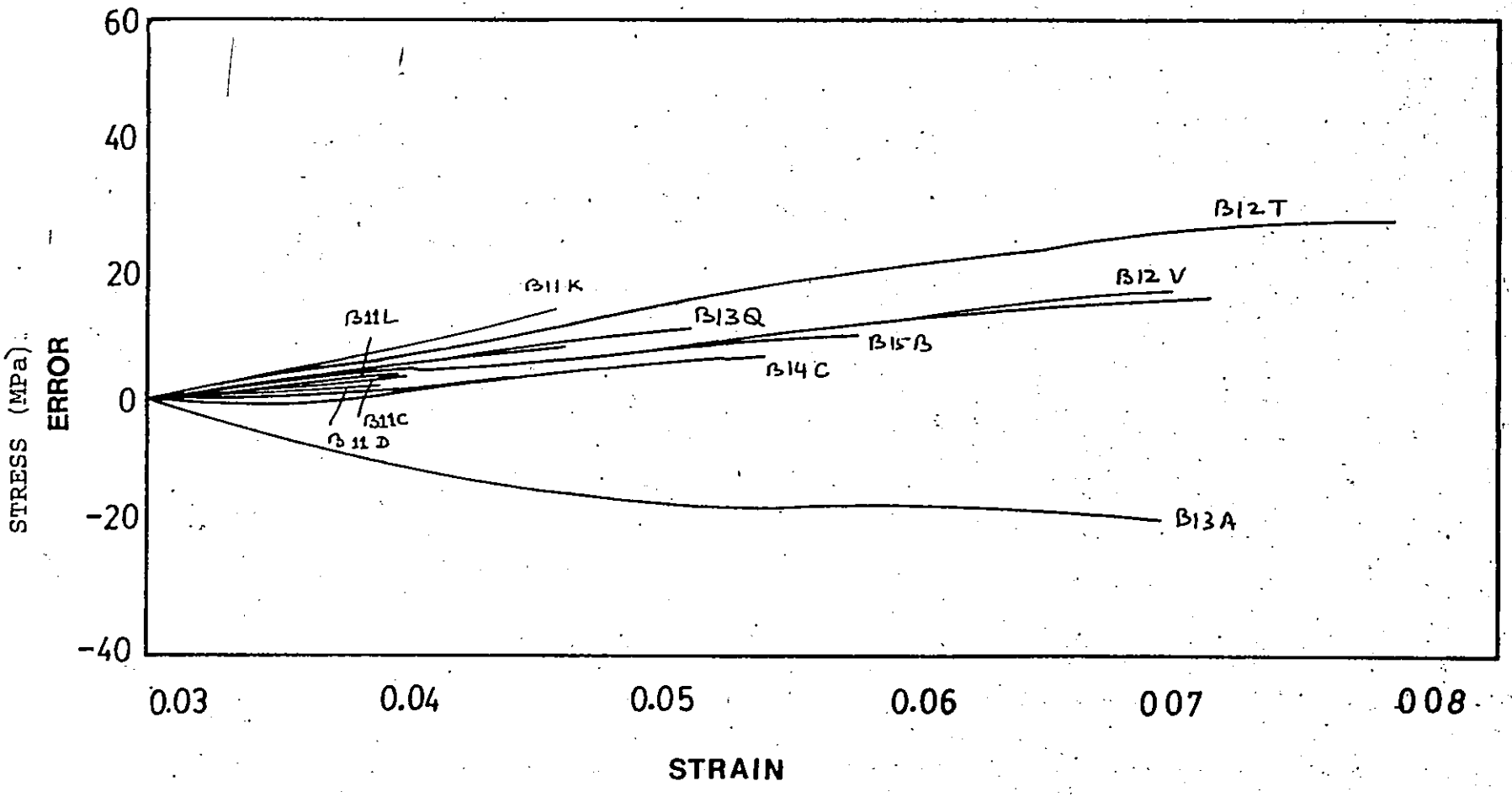

Figure 6.16 Error in extrapolating experimental curves by Voce's equation for curve fitting in the strain interval 0.01-0.03.

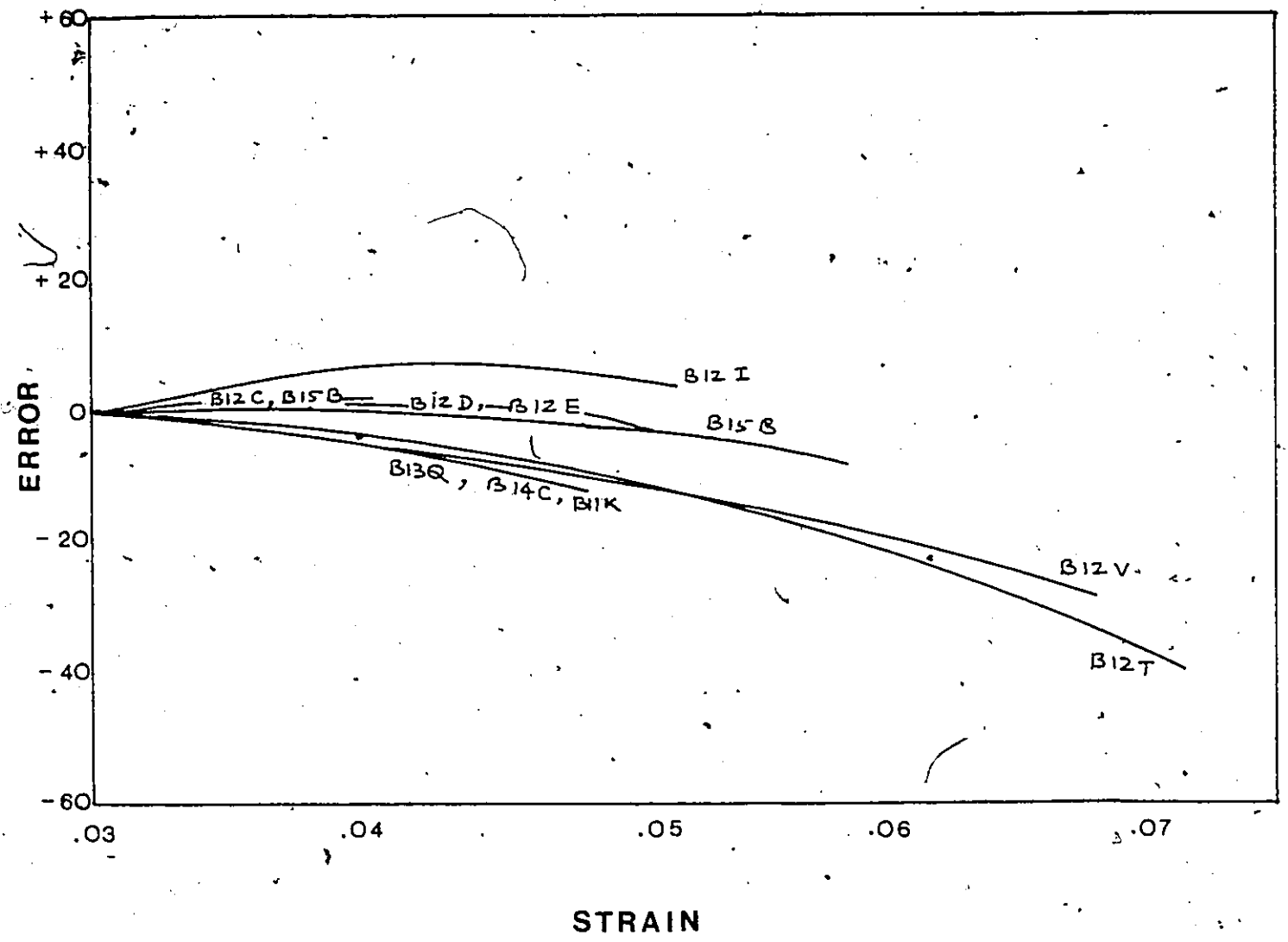

Figure 6.17 Error in extrapolating experimental curves by Log equation for curve fitting in the strain interval 0.01-0.03.

Table 6.5

Curve Fitting in (.005-.03) Strain Interval for Prediction of the Remaining Prestrain Part of Bauschinger Curves

Specimen Name	End of Prestrain	Constants of Log Method			Voce's Constants			Difference by Log Method	Difference by Voce's Equation
		K	A	C	S_I	S_0	$\beta=(1/\varepsilon_c)$		
B11B	.029	0.077875	-0.044834	6.844875	870.4107	395.2180	54.3197	- 0.12	12.25
B11K	.046	0.019752	0.184818	7.419834	615.8142	130.6059	271.7888	-10.25	14.27
B11L	.040	0.057719	0.018835	7.160951	878.6386	365.5954	38.0518	- 5.75	4.54
B12C	.037	0.042199	0.081998	7.055414	778.9958	386.0520	46.3273	- 1.10	6.32
B12D	.039	0.079562	-0.047576	6.939492	891.7482	355.7012	45.2078	0.75	2.12
B12F	.072	0.033204	0.100087	7.213432	1014.0375	411.4578	58.6074	-26.92	17.51
B12T	.077	0.015646	0.203850	7.380347	842.1199	365.9854	43.1733	-41.76	-26.68
B12W	.029	0.039479	0.086049	7.297262	---	---	---	- 3.47	---
B12I	.056	0.059213	0.010463	7.080116	800.2485	400.0508	54.4643	1.17	21.69
B13A	.066	0.026670	0.157662	7.466142	1043.5790	433.0696	40.8099	-47.66	+17.62
B13Q	.051	0.005970	0.209581	7.393724	875.5105	426.8657	42.6662	-12.18	12.18
B14C	.052	-0.017857	0.332513	7.375055	685.3489	303.1145	35.7371	-13.15	6.92
B15B	.057	-0.045373	0.395499	7.204215	551.8459	281.5969	30.5732	- 7.38	10.94
B13F	.038	0.031232	0.128252	7.323212	---	---	---	- 6.94	---

done in .005 to .01 strain interval (Table 6.5). Both the Voce equation and the log method showed very close extrapolations with the experimental curves. The variance and coefficient of variation in extrapolation were determined as 99.222, 1.8676 and 44.2222, -1.2468 for Voce's equation and log method respectively.

A discussion on the accuracy of these two methods will be dealt with in the next chapter on the results and discussion of Bauschinger tests.

CHAPTER 7

Results of Compression Vs. Tension Curves And Bauschinger Tests

This chapter is divided into four sections. In the first section, the results of the application of the proposed stress-strain equation for the extrapolation of prestrain curves of Bauschinger tests will be presented. Also included in this section are the results of heat treatment of Bauschinger specimens to obtain different dual phase microstructures. In the second section, the results on strength-differential observation in different dual phase microstructures will be presented. In the third section, the results of permanent softening as a function of prestrain for different microstructures will be presented. Finally, in the last section, a brief discussion of Bauschinger test results will be presented.

7.1 Measurement of the Permanent Softening Parameter

The degree of plastic incompatibility between the ferrite and martensite phases was estimated from the reverse strain cycles by using the offset of the true stress-true strain curves obtained in tension and compression. The magnitude of permanent softening, σ_{ps}, in an ideal case appears as the difference in flow stress for reverse and forward deformation.

The magnitude of the permanent softening was evaluated

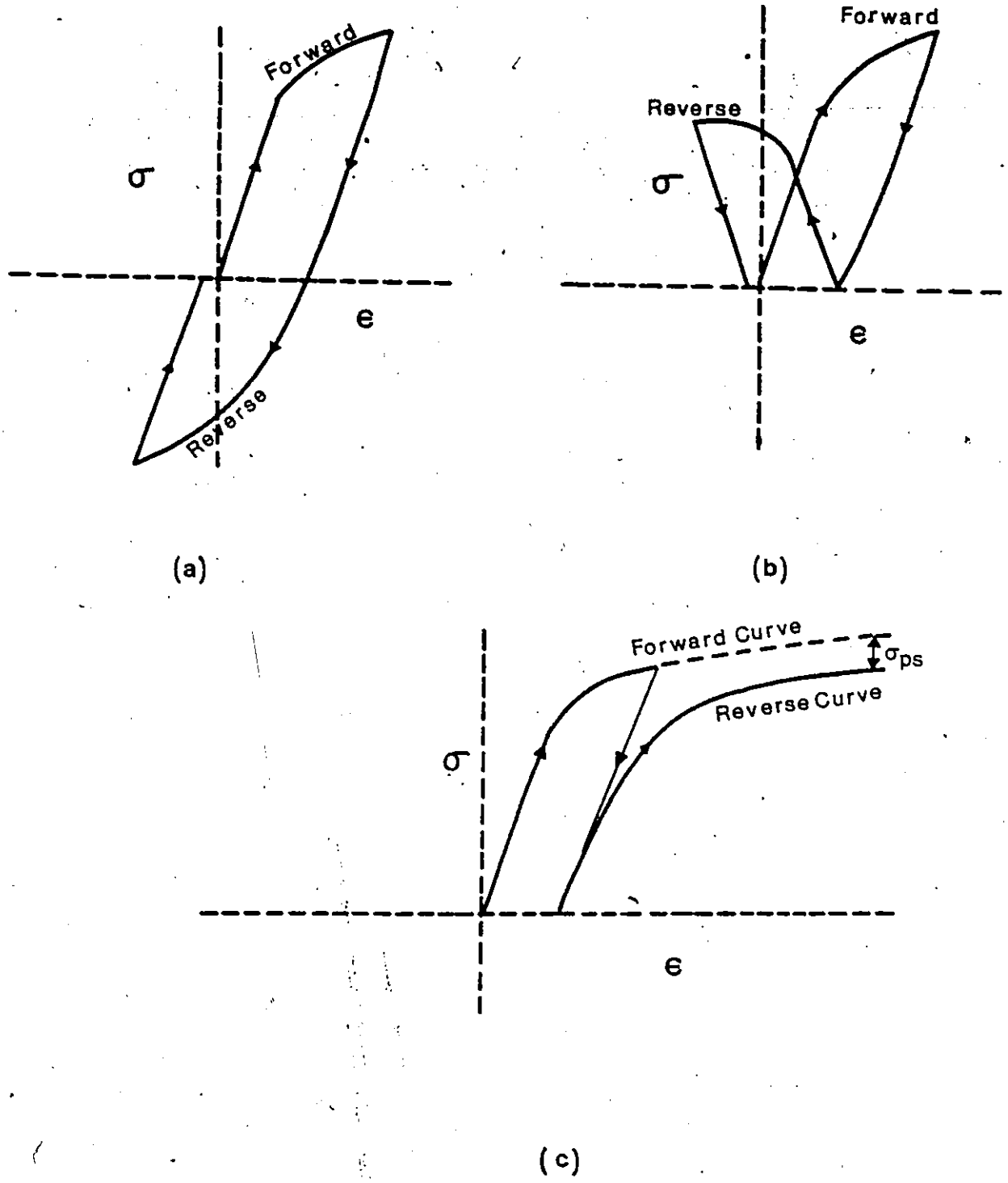

Figure 7.1 Procedure for obtaining final Bauschinger plots for σ_{ps} measurements.

for various tensile and compressive prestrains using separate samples to avoid any problems due to cyclic hardening or softening phenomena. Figure 7.1 illustrates, schematically, how the plots were converted from load-elongation curves to unidirectional true stress-true strain curves for the measurement of the permanent softening parameter on the computer. The dotted line in Figure 7.1(c) indicates the extrapolated part of the curve.

The two equations found most suitable for the extrapolation of stress-strain curves were:

1) Voce's Equation:

$$\sigma = \sigma_I - (\sigma_I - \sigma_o)\exp(-\varepsilon/\varepsilon_c)$$

2) Log Method:

$$\sigma = c_o \varepsilon^{A-(k/2)\ell n\varepsilon}$$

where σ, ε are true stresses and true strains and σ_I, σ_o, ε_c, c_o, A and k are empirical curve-fitting constants.

The log method, as shown in the previous chapter, provided the least error in estimating the flow curves, for both the small prestrain intervals (0.005 to .01) and the large prestrain intervals (.01 to .03). The log method was, therefore, utilized in extrapolating all the Bauschinger curves so that reasonable values of permanent softening parameter, σ_{ps}, could be measured. The results of extrapolation for two specimens with small and large prestrains are illustrated in Figures 7.2 and 7.3 respectively.

Curve fitting was done in the entire prestrain regions

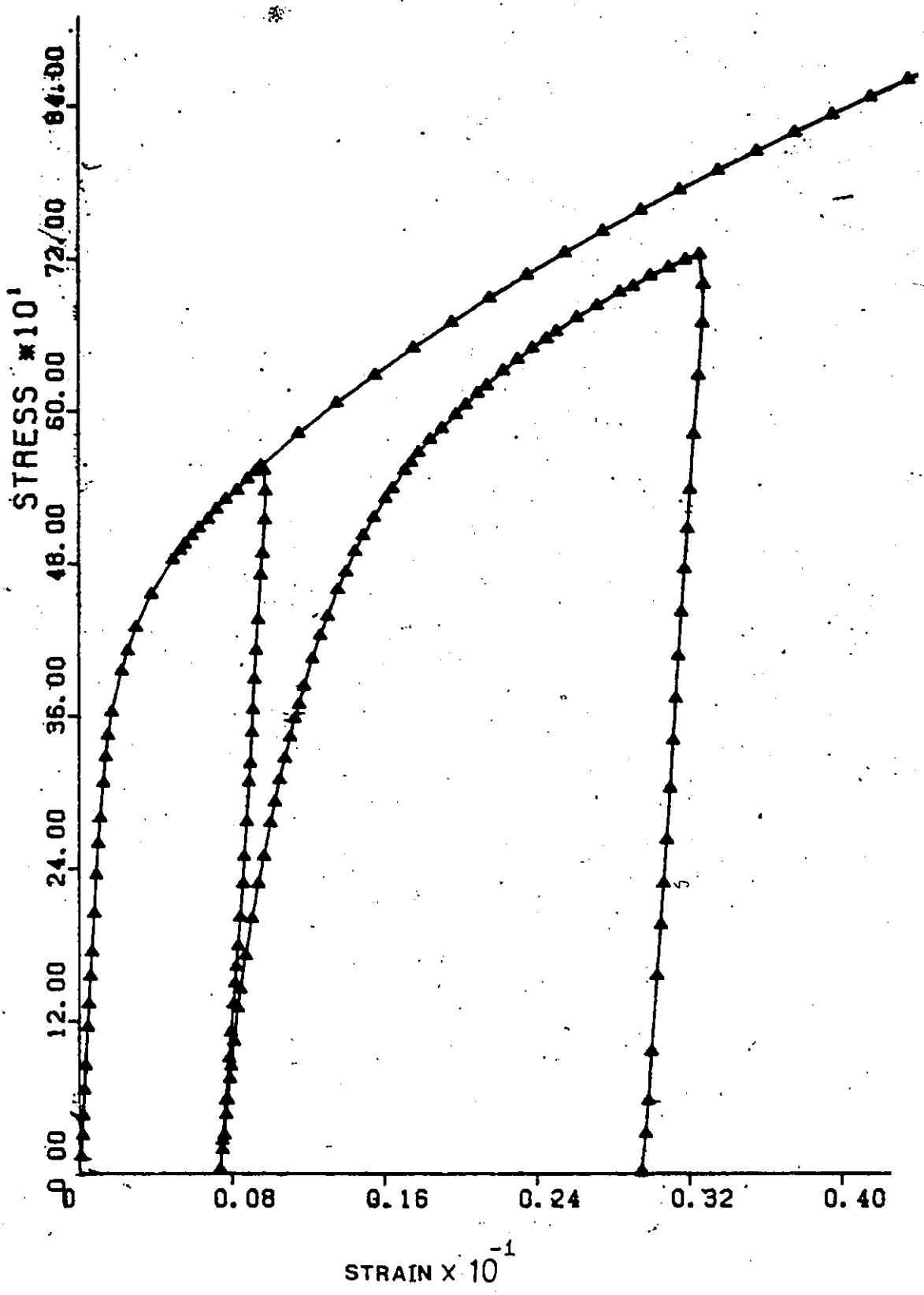

Figure 7.2 Final Bauschinger plot for specimen B11C extrapolated from prestrain 0.0073.

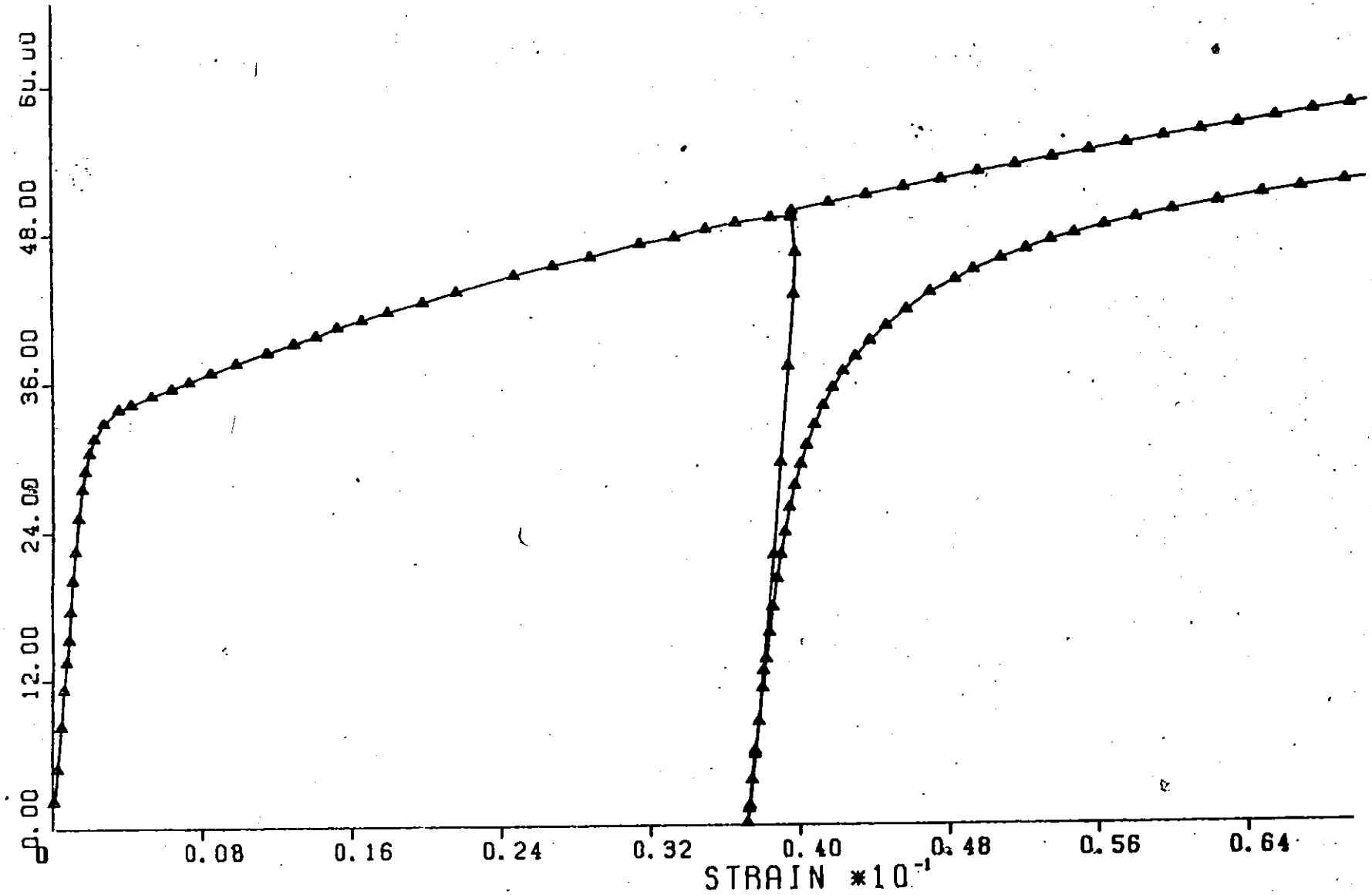

Figure 7.3 Final Bauchinger plot for specimen N14U extrapolated from prestrain 0.038.

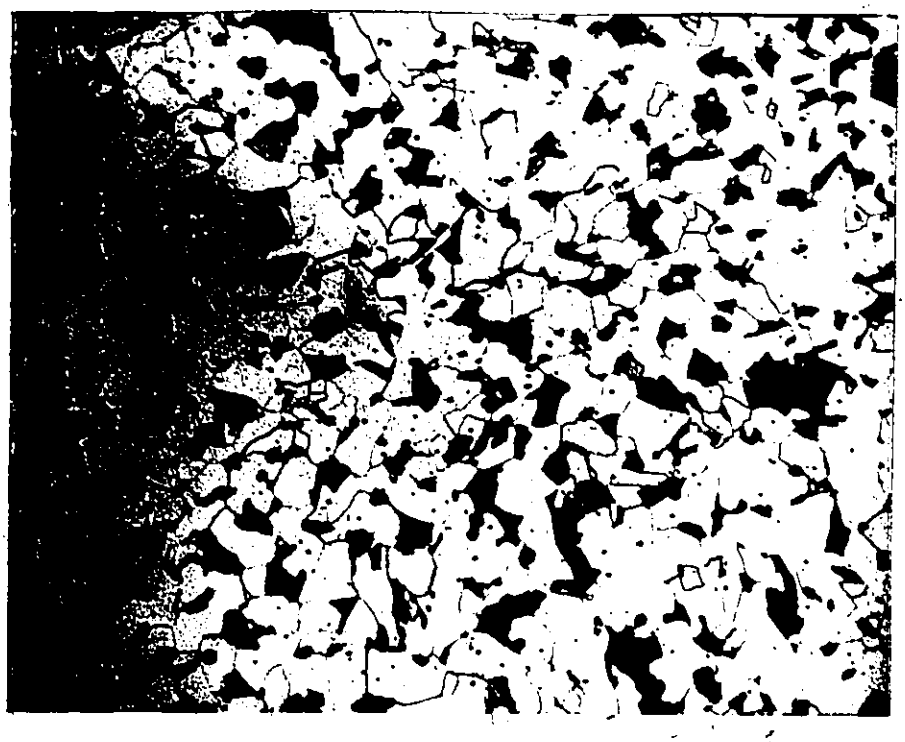

Mag. (150x)

Figure 7.4 Homogenized ferritic-pearlite structure showing large ferrite grain size.

of the specimens in order to determine the best possible values of constants k, A and c. These constants were then utilized for extrapolation purposes. The values of these constants for each specimen, calculated from the prestrain portion of the Bauschinger curves, are shown in Table 7.1.

7.1.1 Heat Treatment of Bauschinger Specimens

Dual phase microstructures in as-received Bauschinger specimens were produced by isothermal reaction or by intercritical annealing methods. This was done to evaluate the effect of heat treatment procedure on the relationship between permanent softening and prestrain.

Banded, isothermally transformed, dual phase Bauschinger specimens were obtained by heating banded ferrite-pearlite specimens in the range of 860°C for 4 minutes. They were subsequently reacted at about 684°C for 4 minutes. The specimens were water quenched from the isothermal transformation temperature.

Unbanded, isothermally transformed dual phase specimens were obtained by homogenizing as-received banded ferrite-pearlite steel bars. This was done by heating steel bars, about 15 cms in length, in vacuum sealed quartz tubes at 1200°C for a week. At the end of this treatment, the specimens from these bars were mounted for optical microscopy. Complete homogenization was achieved during high temperature heating and no banded ferrite-pearlite structure was observed. However, a large ferrite grain size and pearlite interlamellar spacing was observed as shown in Figure 7.4. Bauschinger

Table 7.1

Values of K, A, C in Equation $\sigma=-K/2(\ln\varepsilon)^2+A\ln\varepsilon+C$ From the Prestrain Region of all the Bauschinger Curves for Extrapolation

Specimen No.	Specimen Name	Strain Interval	K	A	C
1	B11A	.005- .026	0.013696	0.141758	7.124813
2	B11C	.005- .007	-0.010508	0.564137	8.177578
3	B11E	.0005- .001	0.586492	-3.161218	-2.334634
4	B11F	.0005- .001	0.459613	-2.236099	0.765052
5	B11G	.0005- .012	0.008475	0.220328	7.516382
6	B11M	.0005- .003	0.201244	-0.811882	4.895278
7	B11N	.0005- .004	0.169960	-0.496724	5.979727
8	B12A	.005- .008	0.043447	0.048012	6.768113
9	B12B	.005- .014	0.008950	0.211227	7.347404
10	B12C	.01 - .034	0.047703	0.059783	7.010843
11	B12G	.0005- .002	0.0033b9	0.257911	7.565844
12	B12H	.0005- .004	0.196709	-0.752928	4.973542
13	B12P	.01 - .032	0.053856	0.031097	6.922381
14	B12R	.01 - .010	0.156131	-0.432082	5.862454
15	B12S	.0005- .004	-0.084004	0.705491	8.628013
16	B12T	.01 - .073	0.078436	-0.038537	6.917442
17	B12U	.0005- .001	0.043447	0.048012	6.768112
18	B13D	.0005- .003	0.218155	-0.857423	4.723278
19	B13K	.005- .013	0.008750	0.208579	7.287540
20	B13O	.005- .024	0.057432	0.028295	7.099655
21	B13F	.001 - .003	0.055130	0.031569	7.128825

...CONTINUED

Table 7.1 (Continued)

Specimen No.	Specimen Name	Strain Interval	K	A	C
22	B13Q	.01 -.048	0.031696	0.106305	7.187890
23	B13E	.0005-.001	0.719653	-3.708869	-3.371407
24	B13L	.0005-.002	0.182900	-0.668172	5.234827
25	B13J	.005-.068	0.027120	0.149126	7.361993
26	B13I	.005-.016	0.005096	0.261553	7.709578
27	B13N	.01 -.021	0.075724	-0.018731	7.201225
28	B13M	.01 -.024	-0.047538	0.481178	8.029243
29	B13H	.01 -.034	0.043132	0.062992	7.139755
30	B14P	.0005-.001	0.019602	0.243313	7.534563
31	B14N	.0005-.001	0.422714	-2.109398	0.627419
32	B14L	.0005-.004	0.139923	-0.523127	5.232955
33	B14O	.005-.016	-0.007476	0.176860	6.823652
34	B14C	.01 -.053	0.023535	0.168578	0.052552
35	B14M	-			
36	B15B	.01 - .055	-0.020912	0.300414	7.021168
37	B14U	.01 -.037	-0.065917	0.457799	7.338066
38	B14S	.01 -.005	0.391758	-1.818963	1.763735
39	B14R	.005-.010	-0.013740	-.296257	7.431665
40	B14D	.005-.024	0.082634	-0.076659	7.002826
41	B14Q	.01 -.031	0.077230	-0.057735	6.863383
42	B15C	.01 -.026	-0.039271	0.369185	7.185304

Table 7.2

Heat Treatment of Bauschinger Specimens

Specimen Type	Average $A_{Temp.}$ (°C)	Average A_{Time} (min)	Average $R_{Temp.}$ (°C)	Average R_{Time} (min)	Average FGS (μm)	Average V_M (%)	Remarks
B11	855.3	4	683.3	4	~7μm	24.5%	Banded, isothermally reacted and aged for about 60 days.
B12 Type I	869.7	4	684.2	4	~7μm		Banded, isothermally reacted and unaged
B12 Type II	860	4	685	4	~7μm	26.6%	Partially Banded Isothermal reacted and unaged.
B13	863.4	4	685.2	4	~7μm	25.1%	Unbanded, isothermally reacted and unaged.
B14	These specimens were intercritically annealed		747.9	20	1) ~7μm 2) ~7μm		Strongly banded, intercritically annealed and unaged 1) dual phase and 2) ferrite-pearlite microstructures

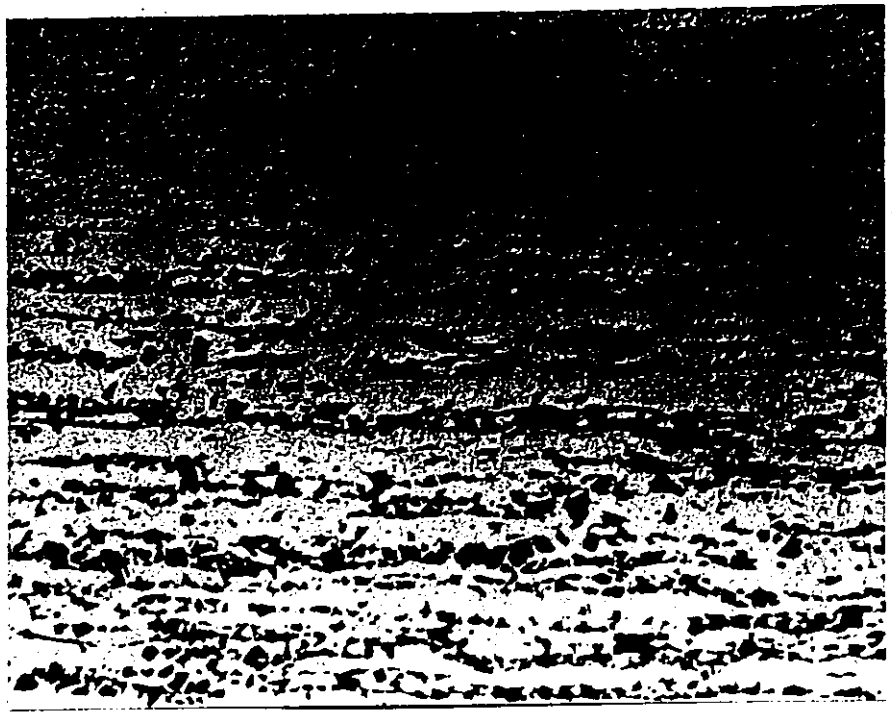

(a) Specimen B12A, Heat Treatment - Isothermal Reaction; Microstructure- Banded and unaged dual phase steel; Magnification - 200x.

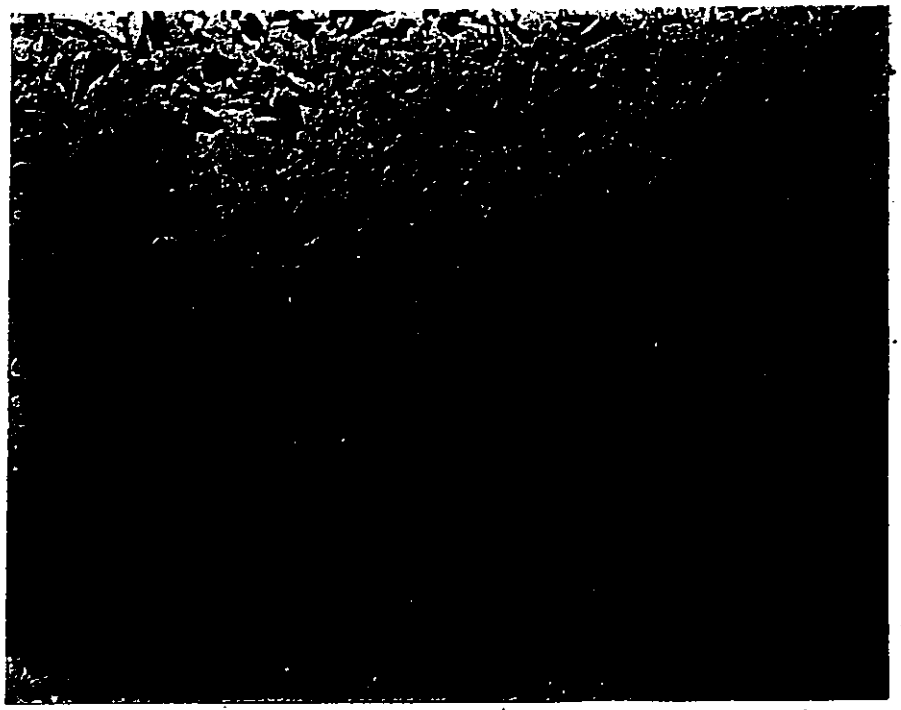

(b) Specimen B12, Heat Treatment - Isothermal Reaction; Microstructure - Banded and aged dual phase steel; Magnification - 200x.

Figure 7.5 Bauschinger specimens with different heat treatments and microstructures.

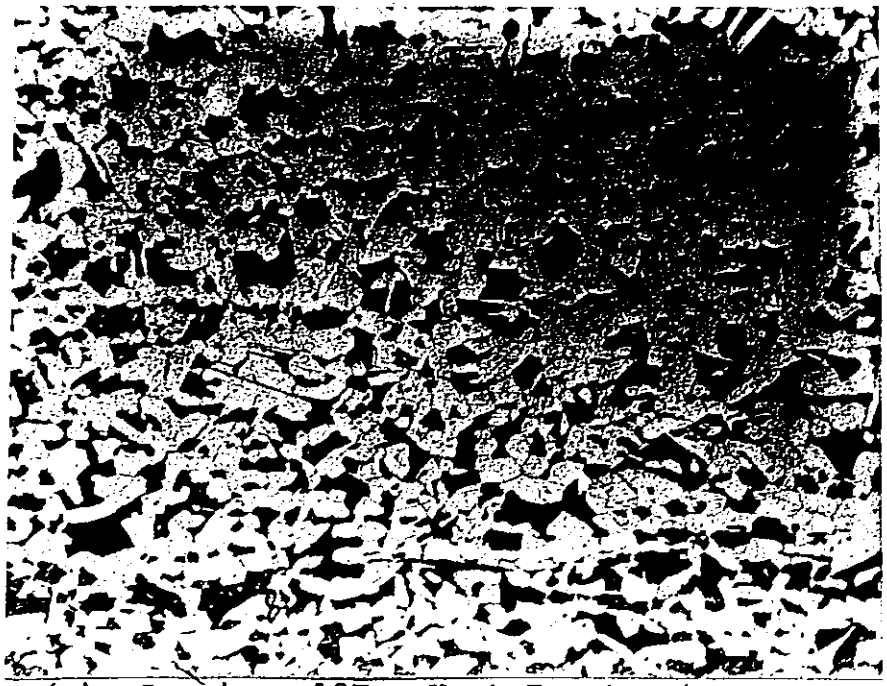

(c) Specimen 12T , Heat Treatment - Isothermal Reaction; Microstructure - Partially banded, dual phase steel; Magnification - 200 x.

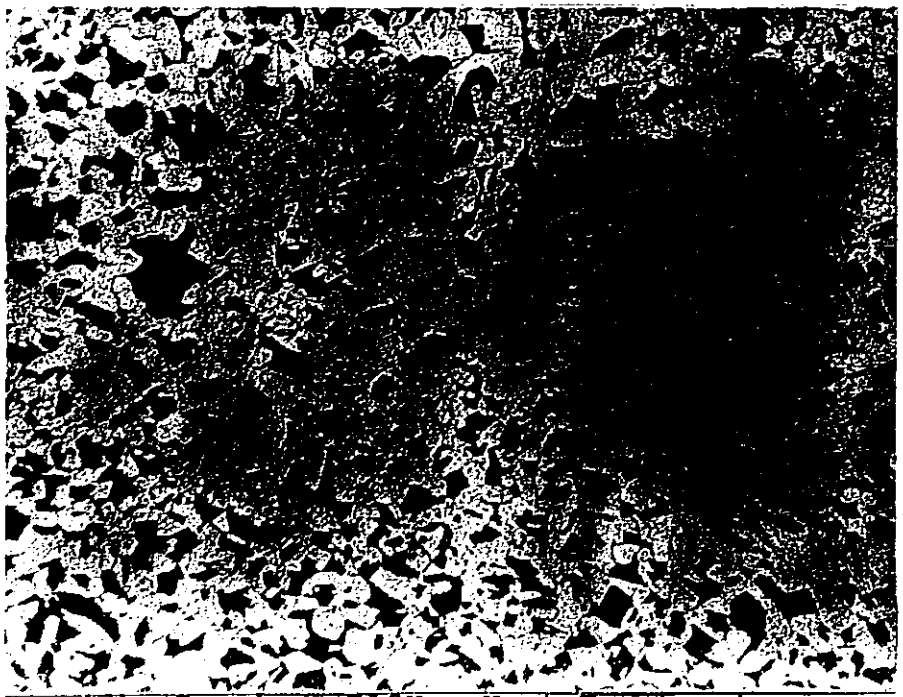

(d) Specimen B13H , Heat Treatment - Isothermal Reaction; Microstructure - Unbanded, dual phase steel; Magnification - 200 x.

Figure 7.5 (Continued).

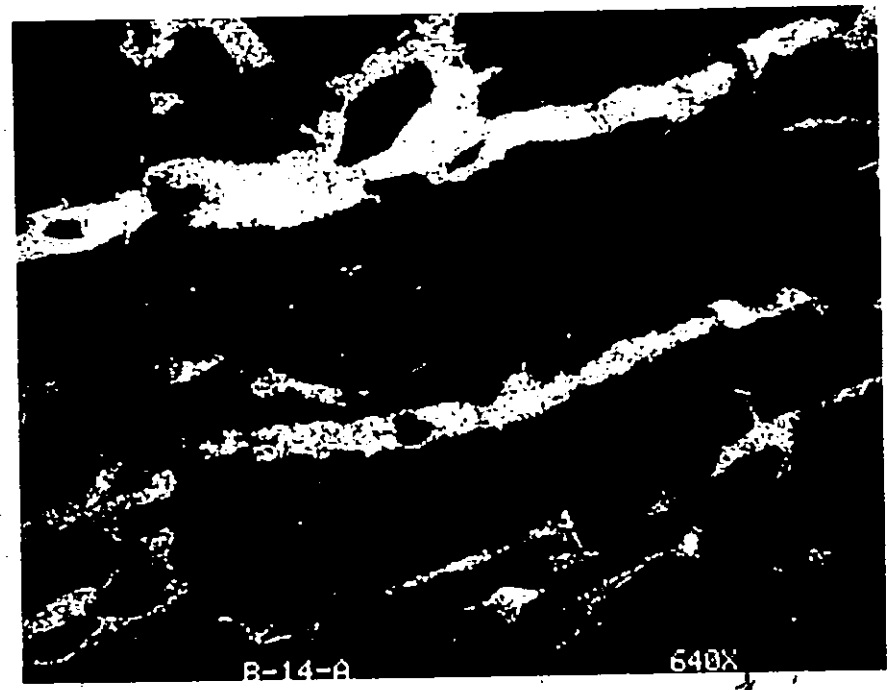

(e) Specimen B15B, Heat Treatment - Intercritical Annealing; Microstructure - Banded ferrite and spherodized pearlite; Magnification - 640x.

(f) Specimen B15B, Heat Treatment - Intercritical Annealing; Microstructure - Banded ferrite and spherodized pearlite; Magnification - 1250x.

Figure 7.5 (Continued)

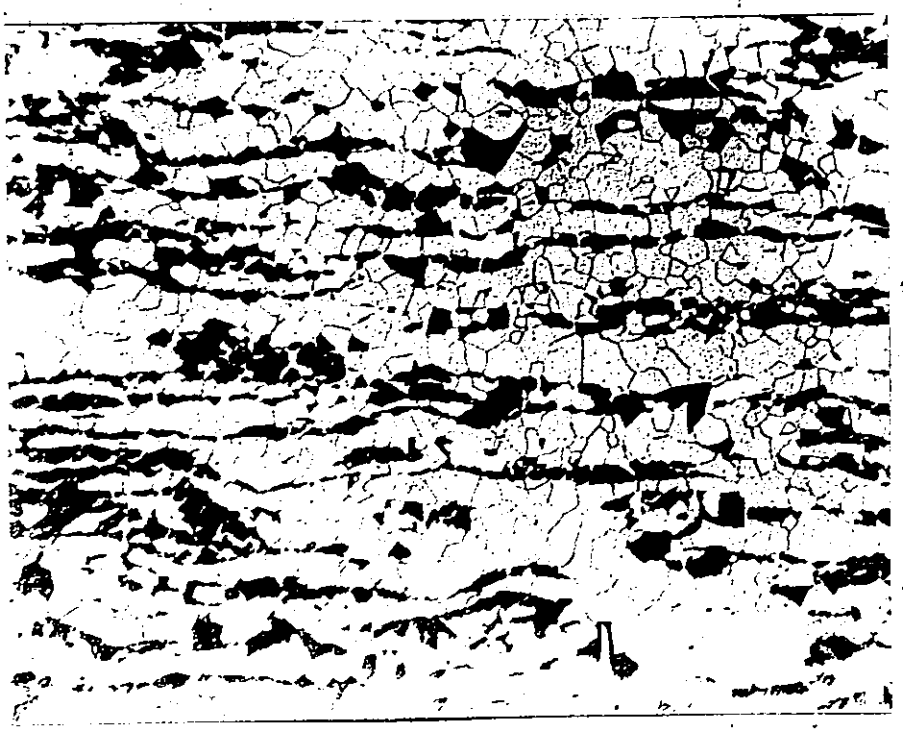

(g) Specimen B14R, Heat Treatment - Intercritical Annealing, Microstructure - Strongly banded, dual phase steel; Magnification - 200x.

Figure 7.5 Continued

specimens, machined from these bars were austenitized at 900°C and quenched to reduce the austenite grain size and obtain a finer ferrite grain size comparable to nonhomogenized specimens.

Banded-intercritically annealed dual phase specimens were obtained by heating the specimens at about 745°C for 20 minutes in the ferrite-austenite range and water quenching. Spherodized carbide or pearlite was observed in some specimens along with the martensite phase. This was due to intercritical annealing temperatures falling slightly below the eutectoid transformation line which could either be due to temperature gradient in the furnace or due to hot salt penetrating the Inconel shield around the thermocouple, giving misleading temperature values. These specimens were, however, utilized for evaluating the B.E. in ferrite-spherodized pearlite microstructures.

The details of heat treatment of Bauschinger specimens are given in Table 7.2. Final microstructures resulting from different heat treatments are shown in Figure 7.5(a-g).

7.2 Strength Differential Observations

In this section the strength-differential effect in dual phase steels is established and various compressive and tensile true stress-strain curves of different dual phase microstructures are presented. This section is arranged into three separate sub-sections dealing with the strength-differential effect in (a) banded, isothermally reacted specimens, (b) unbanded, isothermally reacted specimens, and (c) banded, intercritically annealed specimens.

7.2.1 The S-D Effect in Banded, Isothermally Reacted (BIR) Specimens

Figures 7.6, 7.7 and 7.8 represent the compression and tension σ-ε curves of banded, partially banded, and banded and aged specimens containing the same ferrite grain size and martensitic contents. As shown in these figures, the stress-strain curves in compression lie at higher stress levels for the same plastic strain, compared with tensile curves. Partially banded specimens show slightly lower tensile and compressive flow curves compared to banded specimens, although the gap between tensile and compressive flow curves is substantially the same as for the strongly banded specimens. (Figures 7.6 & 7.7). The effect of aging, shown in Figure 7.8, is clearly to shift both the tensile and compressive curves to higher strength levels.

The relative shift between different compressive and tensile curves was measured by moving the σ-ε curves up and down the elastic modulus line. The average value of the shift in stress between tension and compression curves was thus estimated for banded, partially banded and banded and aged specimens. The data along with the average shift for each of the above-mentioned microstructures is presented in Table 7.3.

7.2.2 S-D Effect in Unbanded-Isothermally Reacted (UBIR) Specimens

Figure 7.9 represents the compression and tension stress-strain curves of UBIR specimens. As shown in the

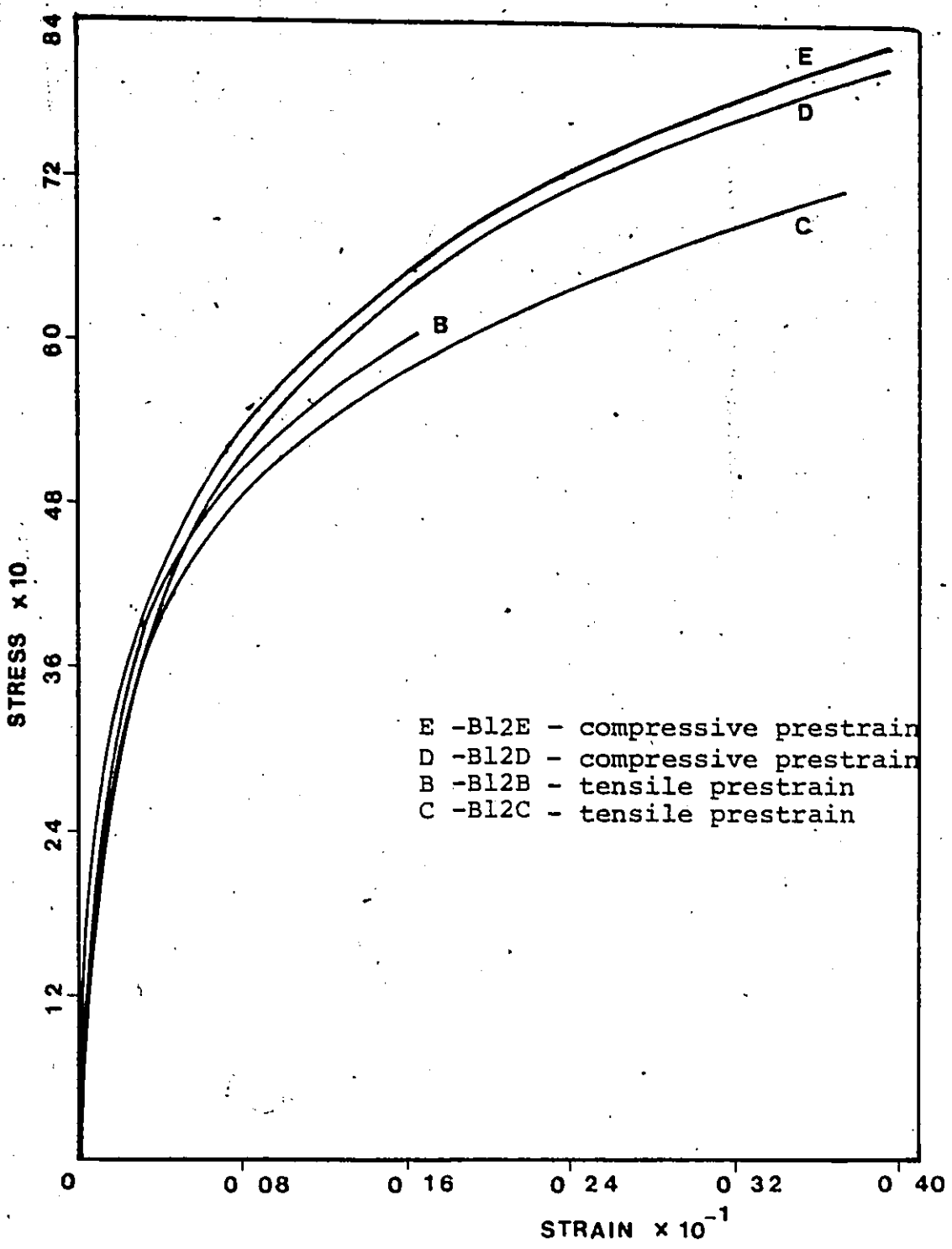

Figure 7.6 Compressive and tensile true stress-true strain curves of banded, unaged and isothermally reacted dual phase (BIR) specimens.

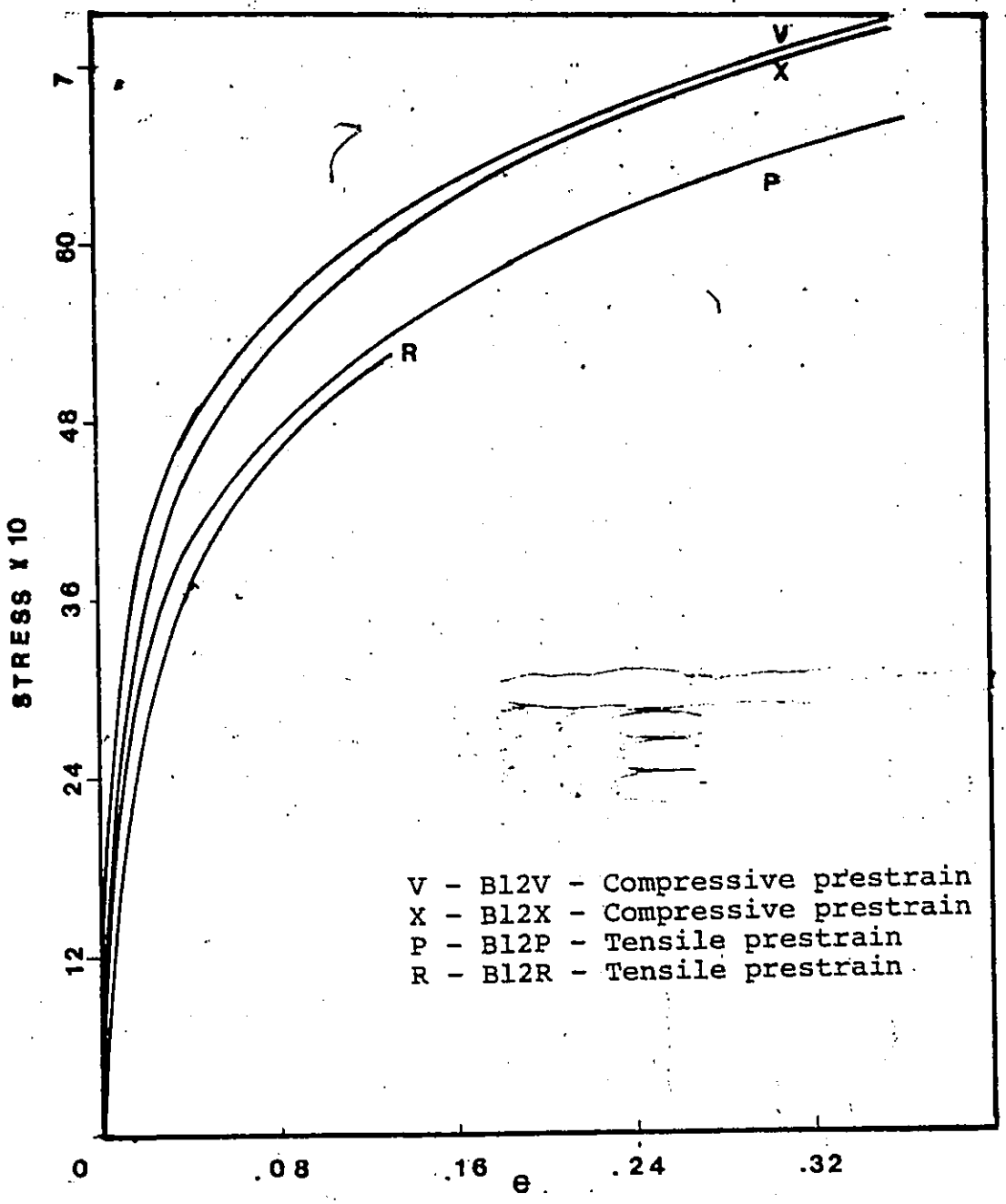

Figure 7.7 Compressive and tensile true stress-true strain curves of partially banded isothermally reacted dual phase (BIR) specimens.

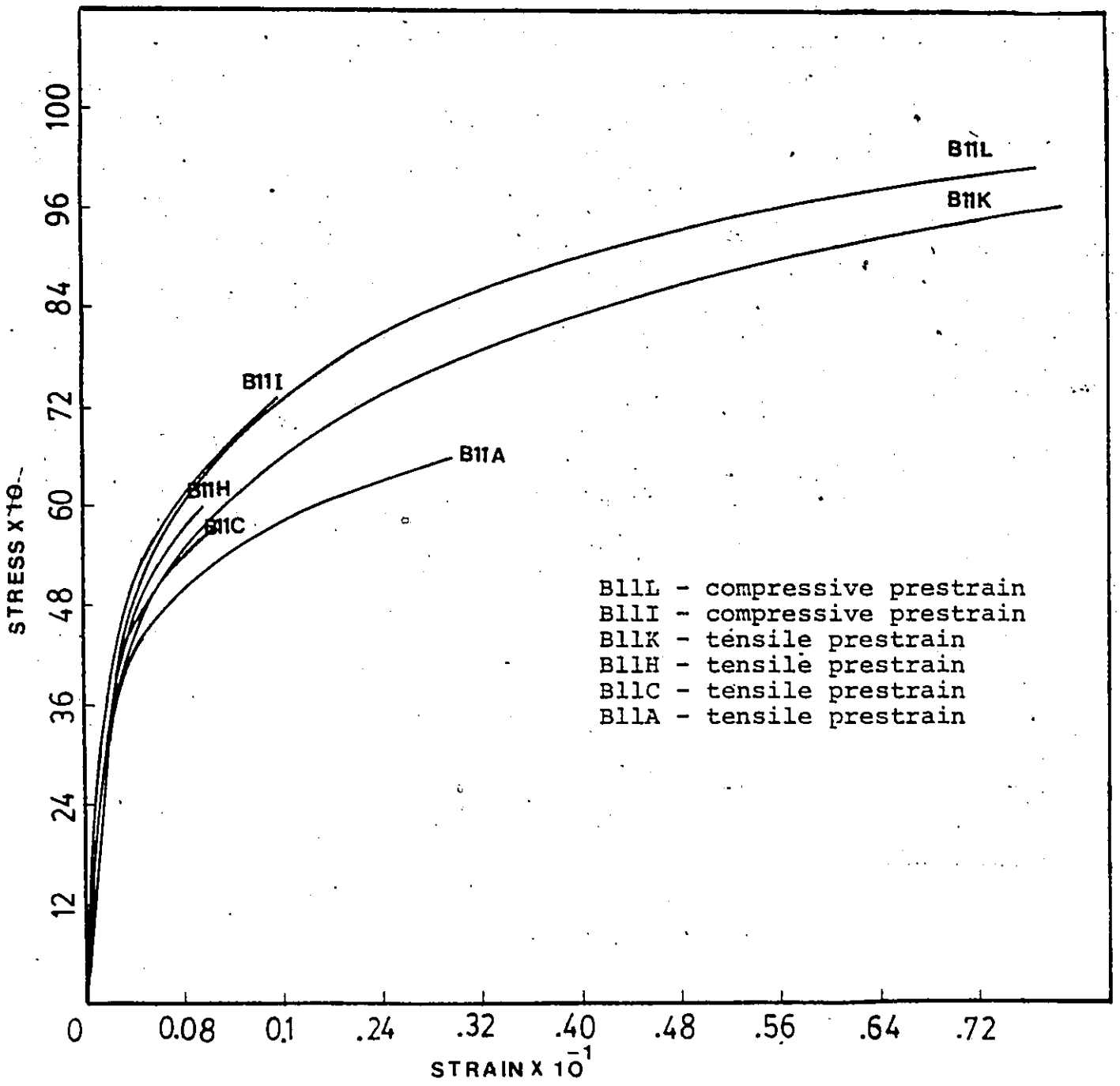

Figure 7.8 Compressive and tensile true stress-true strain curves of banded, aged and isothermally reacted dual phase (BIR) specimens.

Table 7.3

The Shift Between Compressive and Tensile Prestrained σ vs. ε Curves of Different Isothermally Reacted Microstructures

1) Intercritical, partially banded:

	B12V(CT)	B12X(CT)	Average
B12P(TC)	70.86	66.13	68.49
B12R(TC)	84.9	80.20	82.55

Grand Average Shift = 70

2) Banded, isothermal, unaged

	B12E(CT)	B12D(CT)	Average
B12B(TC)	62.13	43.24	52.68
B12C(TC)	100.58	80.78	90.68

Grand Average Shift = 70

3) Banded, isothermal, aged

	B11L(CT)	B11I(CT)	Average
B11K(TC)	59.05	64.0	61.5
B11C(TC)	82.67	84.71	86.39
B11G(TC)	71.32	74.3	72.81
B11A(TC)	190.39	194.82	192.60

Grand Average Shift = 70*

*Omitting B11A

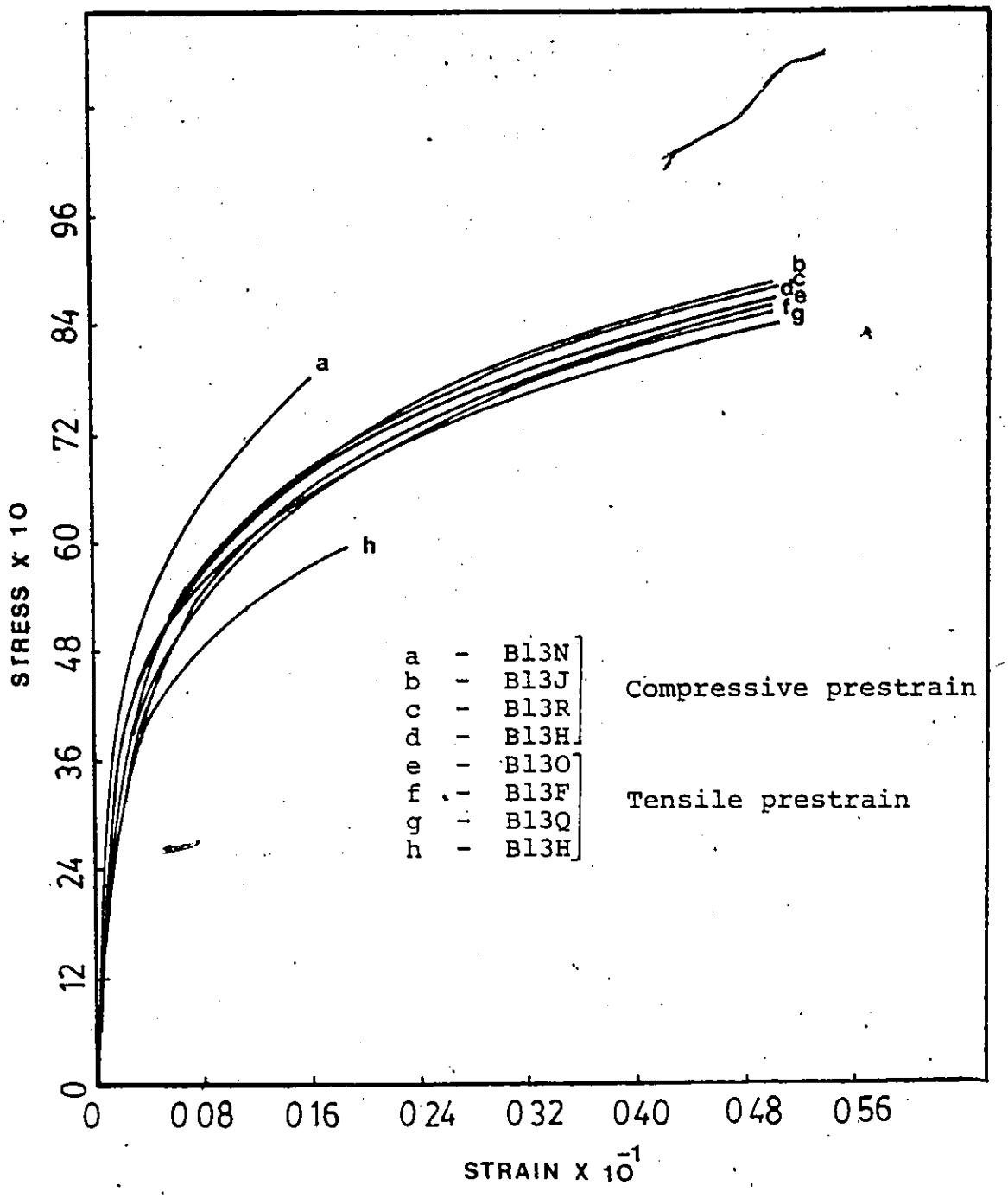

Figure 7.9 Compressive and tensile true stress-true strain curves of unbanded and isothermally reacted (UBIR) specimens.

figure, most σ-ε curves lie within a narrow band with compression curves occupying the upper regions of the band. The specimens, B13N and B13K, as shown in the figure, were found to have σ-ε curves markedly different from the rest of the specimens. Quantitative metallography revealed that specimens B13N and B13K contained respectively a much higher and lower martensite content (29.9% and 19.5%) than the average (25.1%). These specimens were thus not included in the calculations of the average strength differential. The data for the unbanded specimens is presented in Table 7.4.

7.2.3 S-D Effect in Strongly Banded-Intercritically Annealed (SBIA) Specimens

Figure 7.10 represents compression and tension curves of strongly banded-intercritically annealed (SBIA) dual phase specimens. A wide scatter in the compression curves, as shown in the figure, is attributed to variation in martensite contents. The compressive curves, in general, seem to be higher than the tensile curve for the same martensitic content, as shown in Table 7.5 (B14I and B14Q) although the exact shift between the compressive and the tensile curves cannot be determined due to a wide variation in martensitic contents within compressive curves as well as due to unavailability of tensile curves of similar microstructures.

Figure 7.11 represents tensile curves of banded ferrite-spherodized pearlite microstructures. This microstructure was accidently obtained from intercritical annealing treatment as mentioned earlier. These specimens show

Table 7.4

The Shift Between Compressive and Tensile Prestrained vs. Curves of Unbanded, Isothermally Reacted (UBIR) Specimens

Tension Compression Cycles	Compression-Tension Cycles			
Compression / Tension	B13N(CT)	B13M(CT)	B13J(CT)	B13H(CT)
B13O(TC)	174.33	23.62	37.79	9.44
B13F(TC)	181.20	30.50	44.50	15.10
B13Q(TC)	203.0	42.62	55.10	26.30
B13K(TC)	274.0	89.76	110.07	75.50

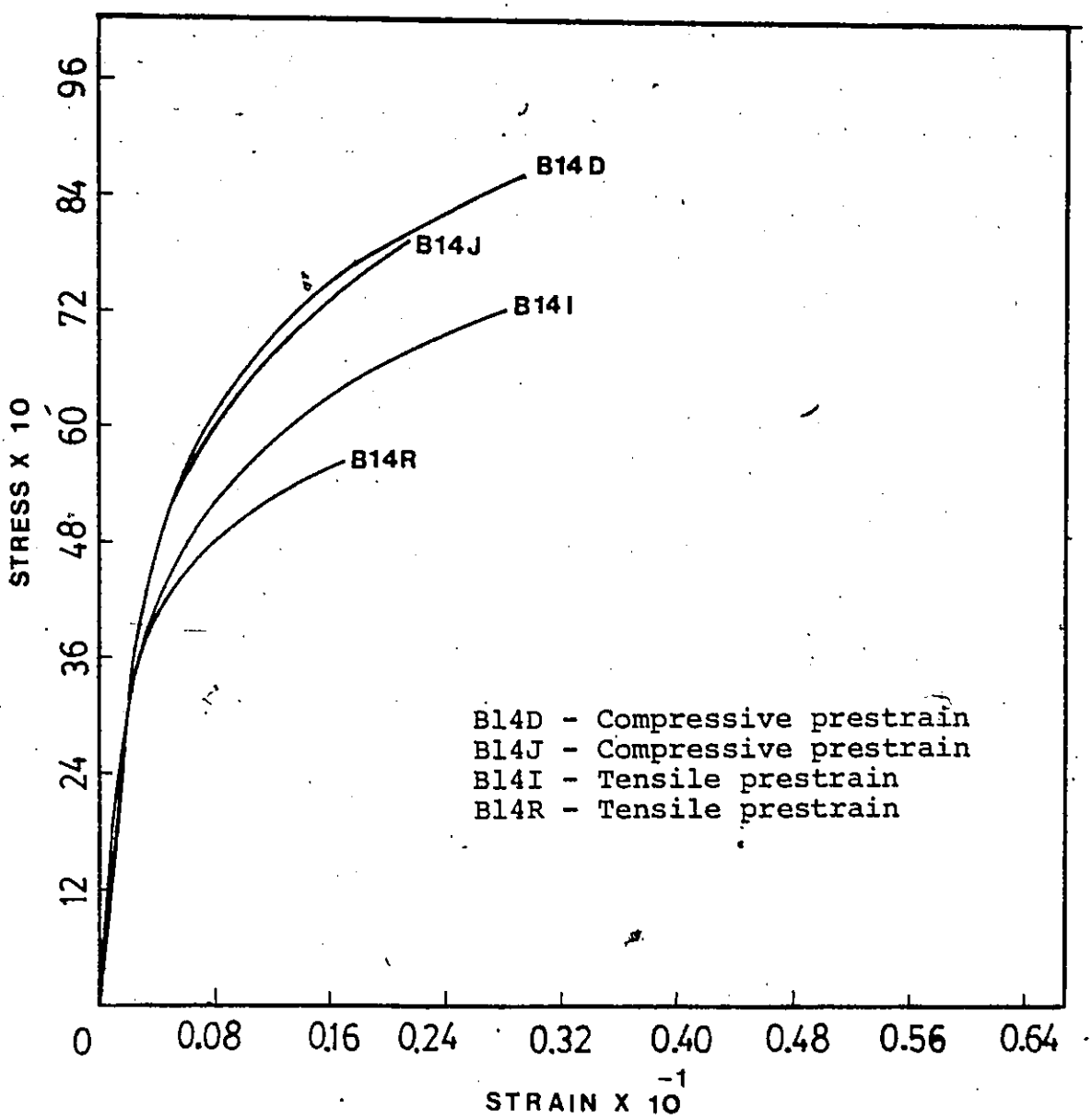

Figure 7.10 Compressive and tensile curves of strongly banded, intercritically annealed (SBIA) dual phase specimens.

Table 7.5

Martensite Contents of Different Strongly Banded Intercritically Annealed (SBIA) Dual Phase Specimens

Specimen Name	Type	%α	%M
B14D	CT	68	32
B14Q	CT	73	27
B14I	TC	72.7	27.3
B14R	CT	76.5	23.5
B14C	CT	78.6	22.4

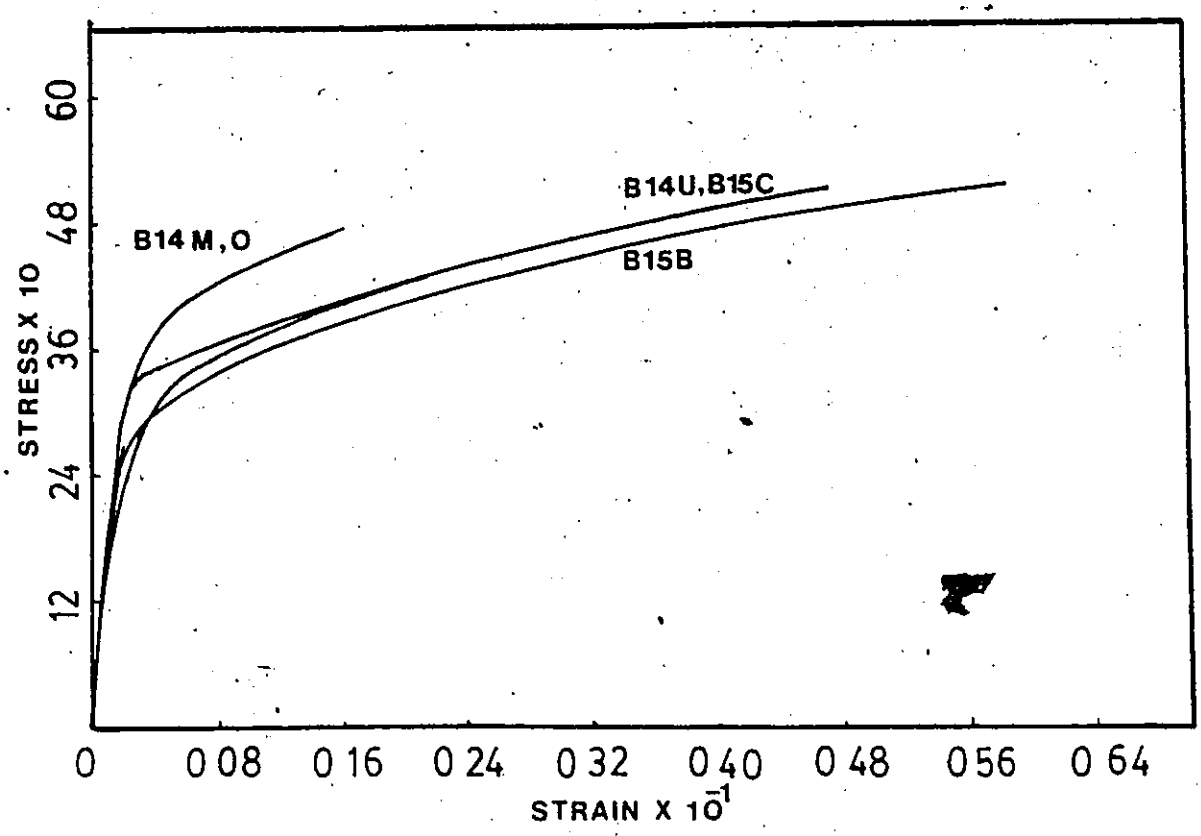

Figure 7.11 Tensile true stress-true strain curves of strongly banded, inter-critically annealed (SBIA) ferritic-pearlitic specimens.

considerably lower tensile flow curves than the dual phase specimens as expected for these microstructures. The values of pearlitic contents of different microstructures are shown in Table 7.6. Some martensite was obtained along with the pearlite phase but the amount of martensite was generally below 5% in these specimens.

7.2.4 Summary of the Strength Differential Results

It appears that a strength differential occurs in dual phase steels. For the isothermally reacted steels, banded, partially banded or banded and aged, this shift was obvious and averaged about 70 MPa. For isothermally reacted, unbanded steels the shift was smaller (25 MPa), but in no case did a compressive stress-strain curve lie below a tensile curve for the same microstructural conditions. Considering the specimen-to-specimen variation, this unviolated segregation may be somewhat fortuitous. Nevertheless, there is no doubt that, even if there was an overlap, the means would be significantly different.

Unfortunately, for the intercritically annealed samples, suitable tensile tests for comparative purposes are lacking. However, when the Bauschinger permanent softening results, to be presented next, are taken into account, it seems that a strength differential in the intercritically annealed specimens is also probable.

Before continuing, however, it is important to take note that the present work represents the first observation of a strength differential effect in a material which contains

Table 7.6

Pearlitic and Martensitic Contents of Ferrite-Spherodized Pearlitic Specimens

Specimen	%α	%P + %M	%M
B14L	76.8	23.19	~15%
B14M	77.16	22.14	~10%
B14N	79.1	20.8	< 5%
B14O	79.1	20.9	< 5%
B14S	78.4	21.6	< 5%
B14T	79.2	20.8	< 5%
B14U	78.2	21.8	~10%

equiaxed free ferrite grains. In fact, the only previous observation of a strength differential in a ferrite-bearing steel was for a Widmanstatten ferrite.

7.3 Permanent Softening Results

The results of permanent softening as a function of prestrain, as measured from final extrapolated Bauschinger plots will now be presented. The results are divided into three separate sections, namely, unbanded-isothermally reacted, strongly banded-intercritically annealed, and banded, isothermally-reacted specimens.

7.3.1 Unbanded-Isothermally Reacted (UBIR) Specimens

The results of Bauschinger tests on these specimens are shown in Table 7.7 and are also presented in Figure 7.12 in the form of two separate curves for tension-compression and compression-tension cycles shown by triangles and squares. The permanent softening parameter, σ_{ps}, increases rapidly with prestrain for both tensile and compressive prestrained specimens. The compressive prestrained curve lies at a significantly higher level indicating a much larger Bauschinger effect. In addition to this, "enhanced Bauschinger effect", the compressive prestrained specimens also show a more rapid increase in σ_{ps} in the initial stages (up to 0.3% prestrain) and a stronger tendency towards saturation than tensile prestrained specimens. In both cases, however, σ_{ps} continued to increase, although at a reduced rate, up to an imposed prestrain of 3.5%.

Table 7.7

Permanent Softening Parameter vs. Prestrain for Unbanded, Isothermally Annealed and Unaged Specimens

Specimen Name	Type T-C/C-T	Prestrain	σ_{ps} (MPa)
B13P	TC	0.002	----
D	TC	0.0035	5.1968
K	TC	0.0131	35.95
"O"	TC	0.0245	50.07
F	TC	0.0345	87.40
Q	TC	0.0482	92.59
E	CT	0.0011	11.81
L	CT	0.0128	79.37
J	CT	0.0685	109.60
I	CT	0.0167	----
M	CT	0.0246	101.57
N	CT	0.021	106.062
H	CT	0.0348	108.6614

TC means Tensile prestrain, compressive reversal.

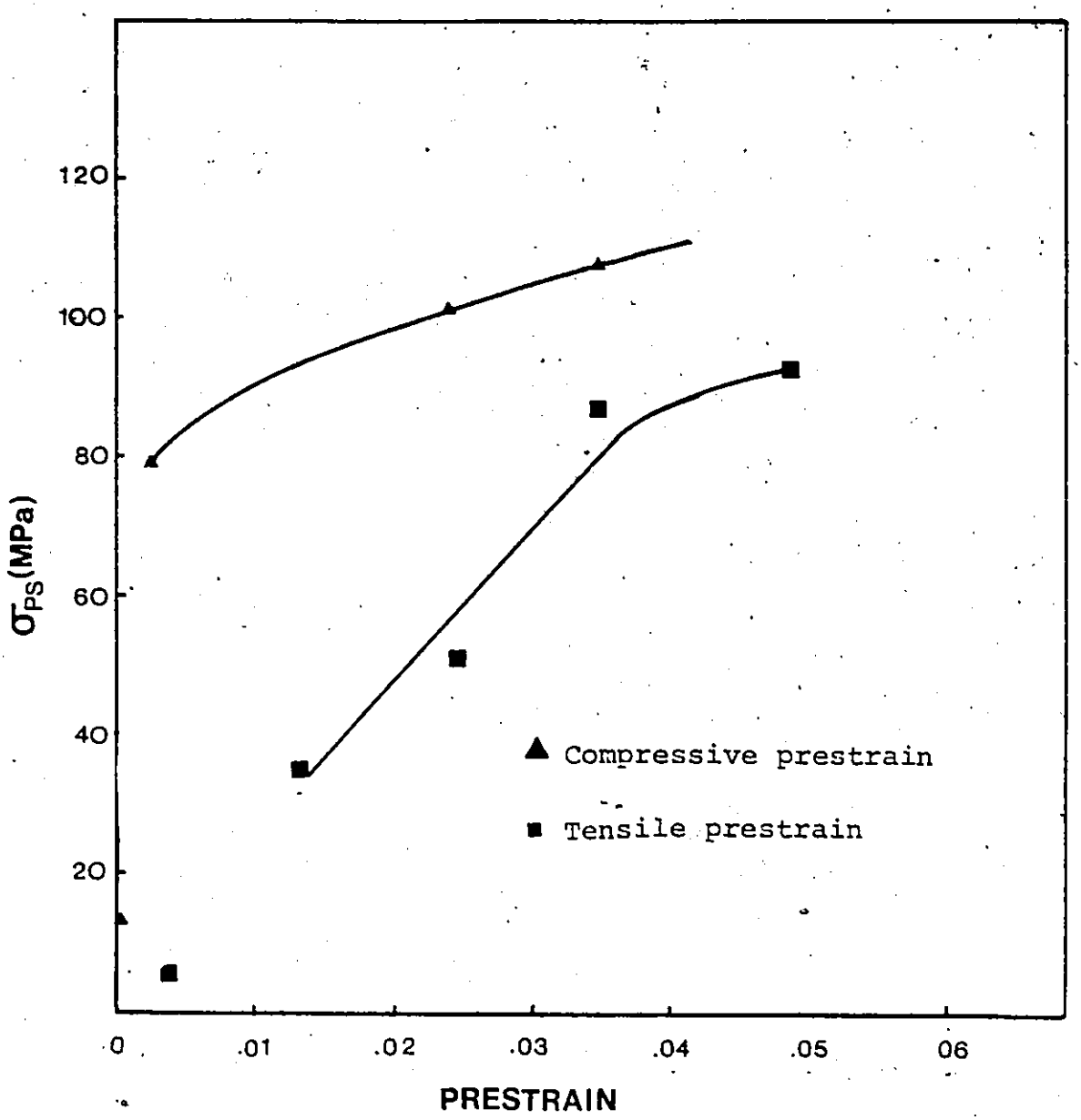

Figure 7.12 Permanent softening parameter vs prestrain for unbanded isothermally reacted(UBIR) specimens.

7.3.2 Strongly Banded-Intercritically Annealed (SBIA) Specimens

The microstructures obtained from the intercritical annealing heat treatment of strongly banded specimens were earlier mentioned as strongly banded intercritically annealed (SBIA) dual phase microstructures and SBIA ferrite-spherodized pearlite microstructures. The results of these two sets of microstructures are shown in Figure 7.13 along with the results of unbanded-isothermally reacted (UBIR) specimens. The data is presented in Table 7.8. The compressive prestrained SBIA dual phase specimens were found to have σ_{ps} vs. prestrain curve slightly lower than the corresponding curve for UBIR specimens, but the SBIA dual phase steel curve was still considerably higher than the tensile prestrained UBIR specimens.

The tensile prestrained ferrite-spherodized pearlite microstructures show much lower values of permanent softening and a stronger tendency towards saturation at higher prestrains (Figure 7.13). The data for the permanent softening parameter vs. prestrain for these microstructures is presented in Table 7.9.

7.3.3 Banded-Isothermally Reacted (BIR) Specimens

In this section only the results of tensile prestrained specimens will be presented. The results of compressive prestrained specimens could not be obtained due to some experimental problems during Bauschinger testing. The experimental curves obtained in compression-tension cycles

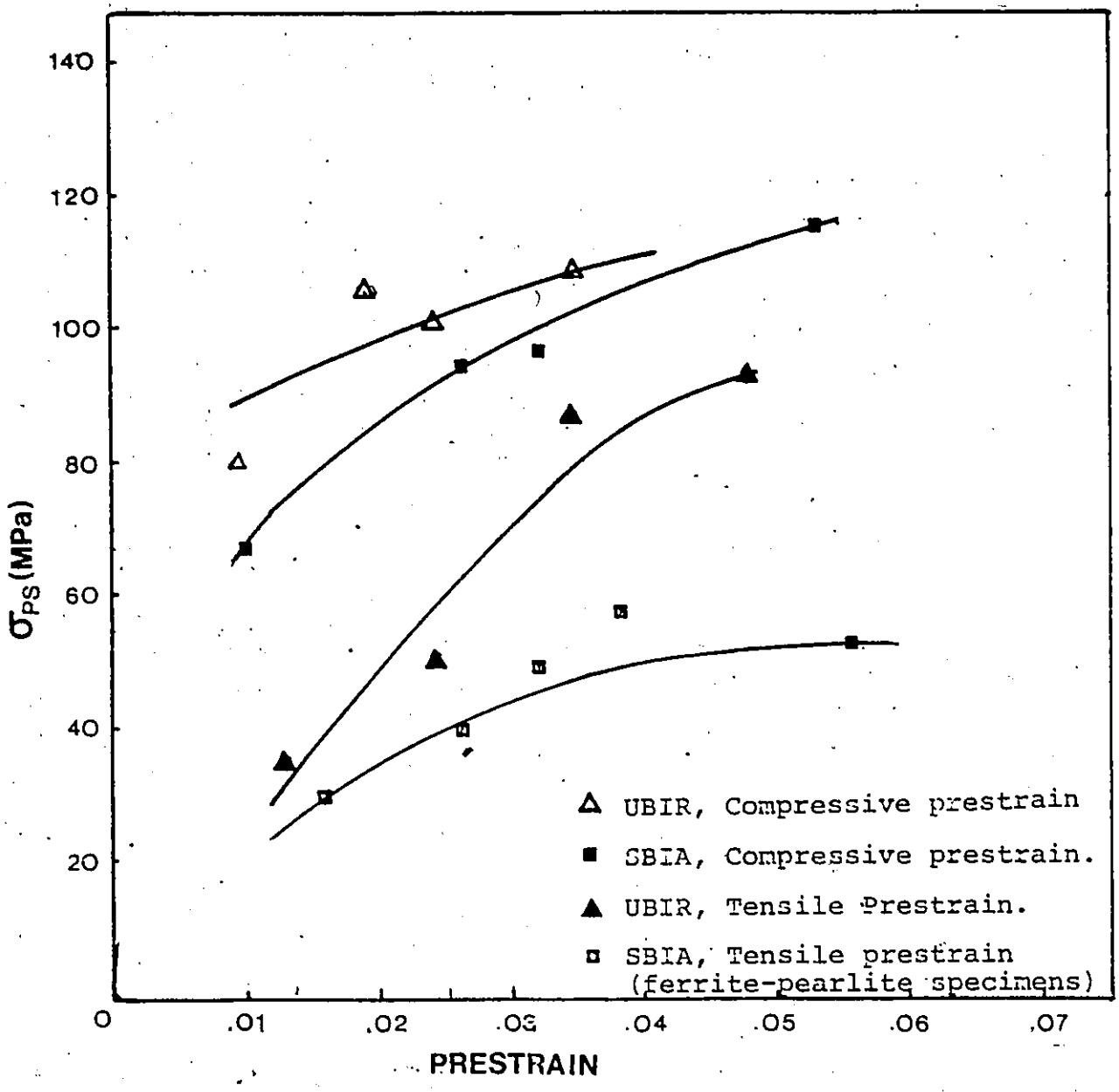

Figure 7.13 σ_{ps} vs. prestrain for (a) unbanded isothermally reacted (UBIR) b) banded intercritically annealed (SBIA) specimens c) banded, isothermally reacted (BIR) specimens.

TABLE 7.8

Permanent Softening Parameter vs. Prestrain For Strongly Banded, Intercritically Annealed Dual Phase Specimens

Specimen Name	Type T-C/C-T	Prestrain	σ_{ps} (MPa)
B14S	CT	0.0052	-
B14R	CT	0.0108	67.5590
B14D	CT	0.0248	94.4881
B14Q	CT	0.0316	95.4330
B14C	CT	0.0535	116.2204

Table 7.9

Permanent Softening Parameter vs. Prestrain For Strongly Banded, Intercritically Annealed And Ferrite-Spherodised Pearlite Specimens

Specimen Name	Type T-C/C-T	Prestrain	σ_{ps} (MPa)
B14P	TC	.0010	-----
N	TC	.0018	-----
L	TC	.0046	-----
"O"	TC	.0161	32.12
C	TC	.0261	38.74
M	TC	.0319	49.60
U	TC	.037	59.05
B	TC	.055	52.91

showed an unusual slope change at zero load after reversal from compressive prestrain. As a result an accurate measurement of the permanent softening values could not be obtained for these specimens. This problem was later remedied.

This section of the thesis is divided into three parts dealing with 1) unaged, 2) aged, and 3) partially banded, unaged specimens.

7.3.3.1 Unaged Specimens

The permanent softening vs. tensile prestrain curves for these specimens is shown in Figure 7.14. At low prestrains, the permanent softening values for these specimens are higher than the corresponding unbanded specimens described earlier. The permanent softening parameter, however, decreases less rapidly and consequently shows lower values compared to unbanded specimens (Figure 7.15).

7.3.3.2 Aged Specimens

These specimens differ from those in the preceding section in that they were strain aged for about 60 days at room temperature prior to testing. The apparent effect of aging on pure tensile and compressive specimens was to increase the ultimate tensile strength and yield strength by about 40 MPa and 160 MPa respectively.

The effect of aging on the permanent softening vs. prestrain curves is shown in Figure 7.14 and the values of σ_{ps} and prestrain are recorded in Table 7.10. The effect of aging was to increase σ_{ps} more rapidly with imposed plastic strain.

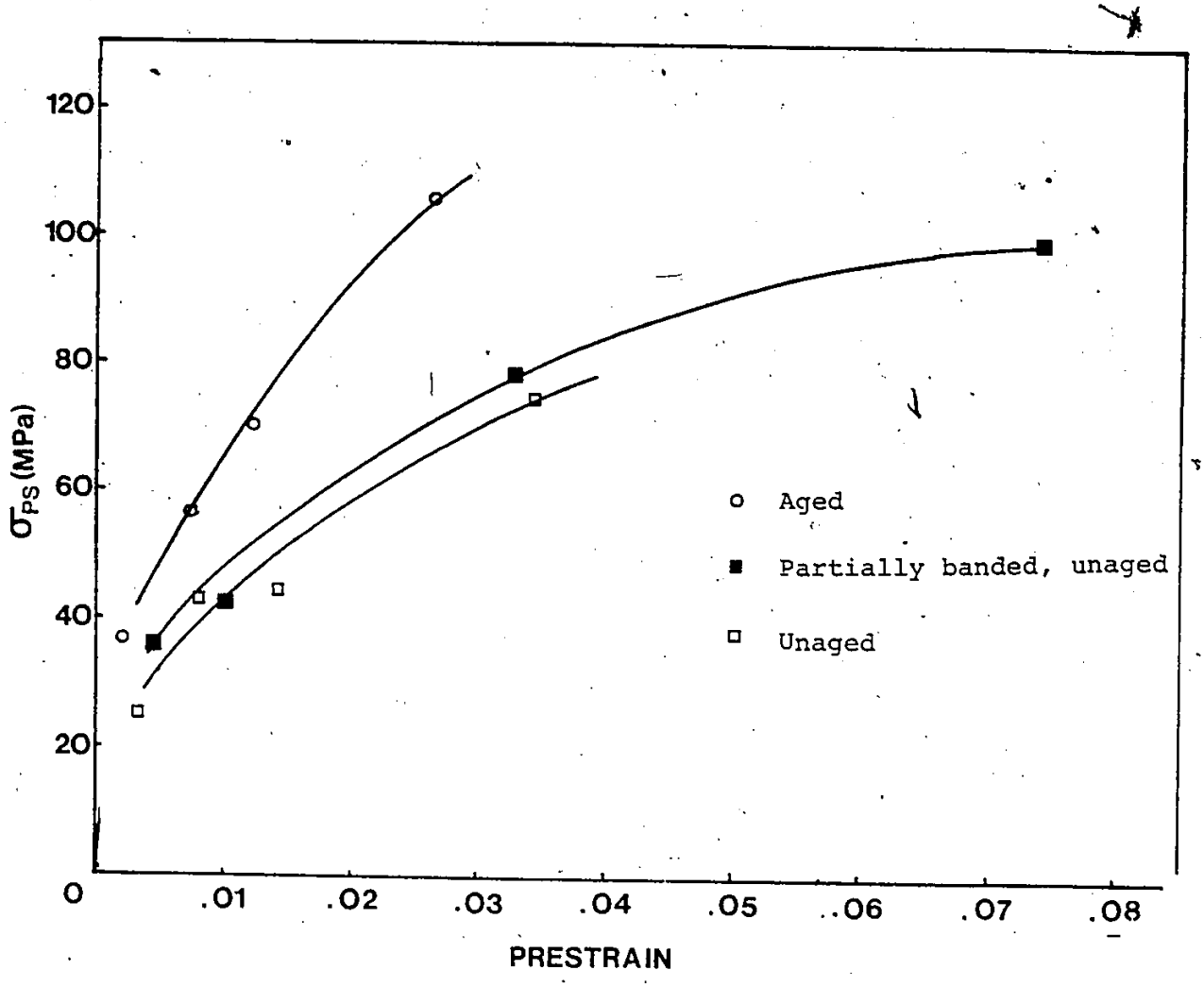

Figure 7.14 σ_{ps} vs. prestrain for banded, isothermally reacted (BIR) specimens. Prestrain is tensile in all cases.

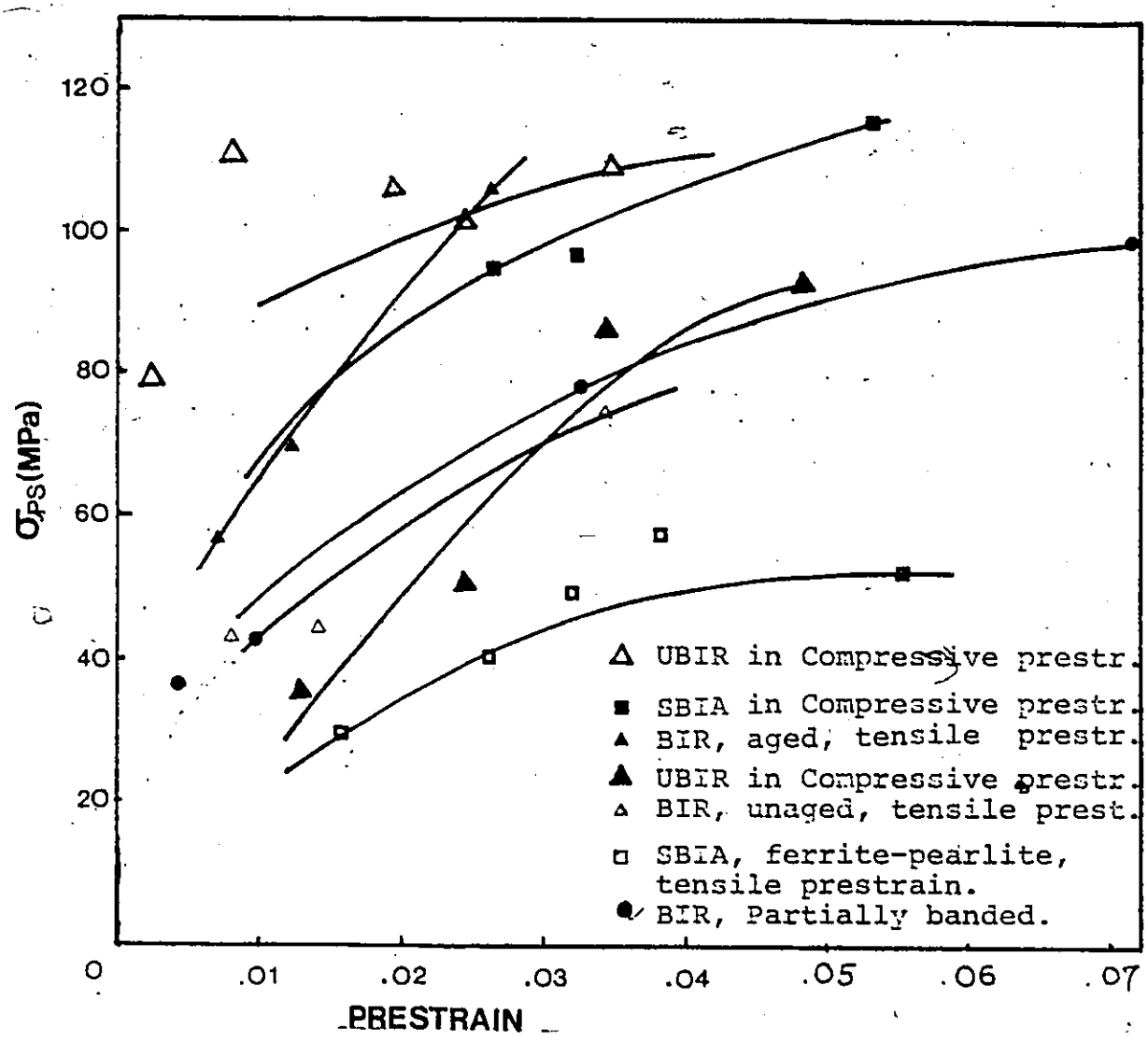

Figure 7.15 Permanent softening parameter vs prestrain for (a) UBIR (b) SBIA (c) BIR specimens.

Table 7.10

Permanent Softening Parameter Vs. Prestrain for 1) Banded, Isothermally Reacted, and Unaged Specimens; 2) Banded, Isothermally Reacted and Aged Specimens

Specimen Name	Banded, Isothermally Reacted and Unaged		Specimen Name	Banded, Isothermally Reacted and Aged	
	σ_{ps} (MPa)	Prestrain		σ_{ps} (MPa)	Prestrain
B12G	25.98	0.00256	B11F	--	0.00136
B12A	43.00	0.0079	B11E	37.62	0.00156
B12B	44.88	0.014	B11M	--	0.0030
B12C	74.68	0.341	B11N	--	0.00219
			B11C	56.69	0.0073
			B11G	69.87	0.0122
			B11A	105.82	0.026

Table 7.11

Permanent Softening Parameter vs. Prestrain For Partially Banded, Intercritically Annealed And Unaged Specimens

Specimen Name	Prestrain	σ_{ps} (MPa)
B12U	.0016	-----
S	.00458	35.45
R	.0105	42.51
P	.0326	79.95
T	.07391	99.21

7.3.3.2 Partially Banded, Unaged Specimens

The results of σ_{ps} vs. tensile prestrain for these specimens are presented in Table 7.11 and are plotted in Figure 7.15 along with banded unaged and banded and aged specimens. As seen in the figure, the permanent softening values are slightly higher than the banded, unaged specimens.

7.3.4 Summary of the Permanent Softening Results

With the exception of the specimens which had been aged, there is a clear separation in the permanent softening values between specimens which had been loaded in compression-tension compared with those that were loaded in tension-compression. As a rough description, the compression prestrain results are about 40 MPa above those of the tensile prestrain values, irrespective of microstructure. A more detailed description must note that the unbanded martensite has a different σ_{ps} functional dependence on prestrain than the banded structures.

The specimens which were aged had much higher permanent softening values than the corresponding unaged specimens (remembering that only tensile prestrains were available). The tensile and compressive curves for the aged specimens were also distinctly higher than the unaged specimens, and thus the higher prestress values are apparently manifested by a larger Bauschinger stress.

7.4 Discussions

The tension-compression and Bauschinger tests have produced two new salient results:

1) There is a strength differential effect such that compressive stress-strain curves of dual phase steels lie above their tensile stress-strain curves.

2) The permanent softening stress observed after a compressive prestrain is larger than that found after a tensile prestrain for these steels.

A descriptive explanation of these results can be developed based on the residual stresses developed during the transformation of austenite to martensite when these steels are heat treated.

It is postulated that the transformation strains produced during the expansion of austenite to martensite in effect prestrain the surrounding ferrite in tension. Figure 7-16 simplifies and exaggerates the effect of such a prestrain to show that it produces the correct general results.

Point O represents the stress-strain origin that would exist for the ferrite in the relaxed state (i.e., one in which the transformation strains were zero). Point A represents the state of stress in the ferrite after the transformation strain has occurred. This is the state that we, as outside observers, take to be datum point for zero stress and strain. The simplified tensile and compression curves drawn in Figure 7.16(a) are drawn so that they are perfectly symmetrical for the true relaxed state at 0. Note that if one puts the stress-strain origin at A, a strength differential is observed.

Figure 7-16(b) shows how this shifted origin modifies

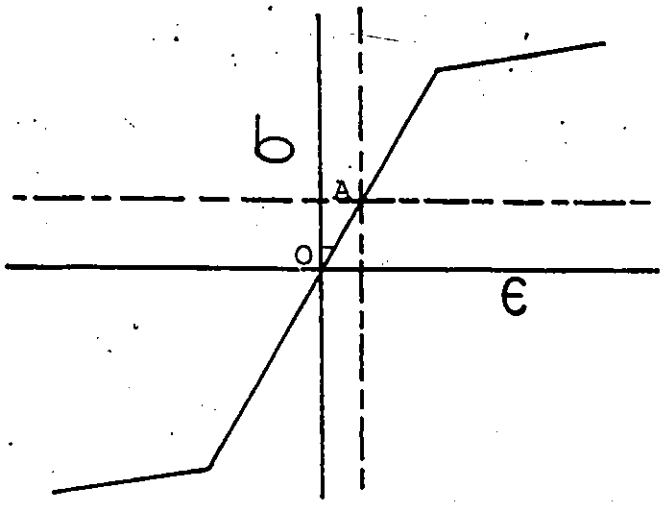

(a)

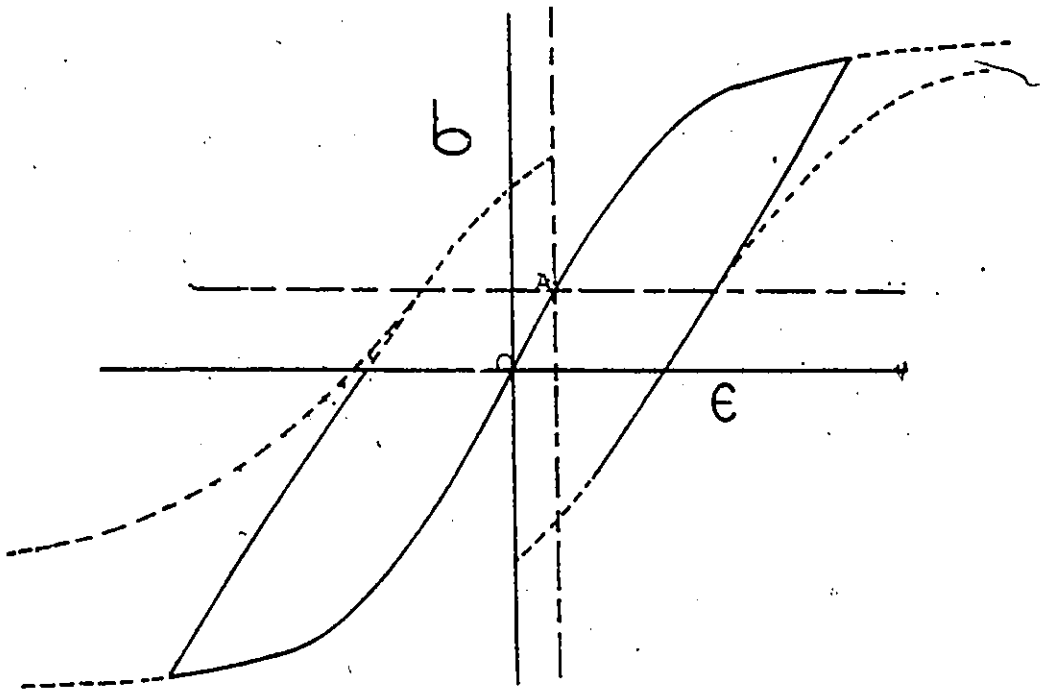

(b)

Figure 7.16 The effect of transformation strains on tensile and compressive deformation of dual phase specimens.

the Bauschinger effect for equal tensile and compressive plastic prestrains. The two curves are once again symmetric about point O, but the stresses (and strain reversals) take place according to the observed origin at A. The results is a much bigger apparent permanent softening for compressive prestrains.

Note that the strength differential stress should be equal to twice the residual stress in the ferrite for this simple model. This is also true for the difference in permanent softening stresses although this is sensitive to the shape of the reverse stress strain curve.

The fact that the prestress has a tensile sign is of interest. A spherical expanding martensite particle creates a state of pure shear around itself as shown in Figure 7.17(a). Thus, for a material subjected to a load in the vertical direction, (through the poles of the particle) it is the material around the equator of the particle which will reach the yield stress first. For the rod-like banded martensite the tensile residual stress fields would be in the coaxial cylinder surrounding the rods (Figure 7.17(b)), and this comprises a substantial volume of material. In compression, the material at the poles would yield first. For the banded material, the residual stresses here would be very high but would not extend over nearly as large a volume. This implies that the yield strengths would be similar or lower but the early strain hardening rates would be substantially higher for the compression specimens. The specimen to specimen variation

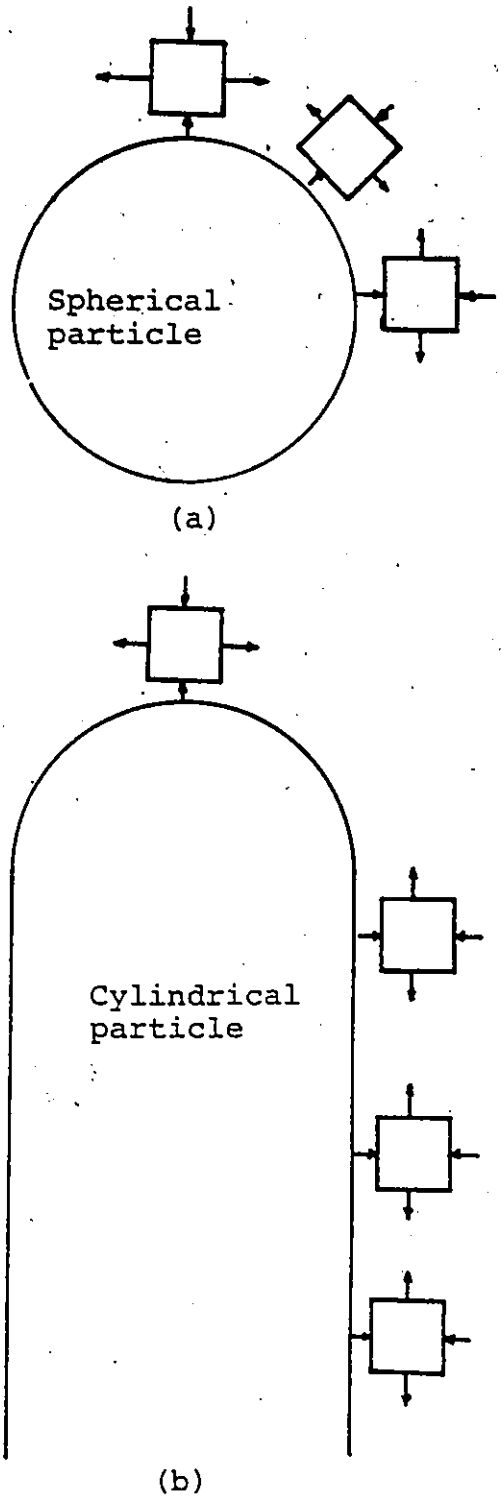

Figure 7.17 Residual stresses around (a) spherical (b) rod-like martensitic particles in dual phase steels.

is such that it is not clear from the stress-curves if this prediction is borne out. This line of reasoning, that tensile and compressive plastic strain take place at different points in the specimen, leads to the conclusion that the compressive as tensile stress strain curves would not be symmetric (as in Figure 7.16(a)). However, this would be true principally during the very early stages of plastic strain. With the onset of general plastic strain in the ferrite, the Brown-Stobbs type of hard particle strain mismatch fields would soon become dominant.

CHAPTER 8

CONCLUSIONS

This study has led to the following conclusions:

1) The isothermal reaction treatment offers a rapid and useful method of producing dual phase ferritic-martensitic microstructures in steel bars, with mechanical properties comparable to intercritically annealed dual phase steels.

2) A more connected martensite morphology is obtained by intercritical annealing treatments up to martensitic contents of about 35%. No apparent differences in martensite morphology are observed at higher martensite contents.

3) Tempering at 240, 300, 360, 440 and 510°C for 1 hour did not improve the strength-uniform elongation combination in isothermally reacted dual phase steels.

4) A unique strain hardening parameter, as defined in the Hollomon, Ludwik and modified Swift equations, does not describe the deformation of dual phase steels at all levels of strain.

5) A new equation to represent the stress-strain curves of dual phase steels has been found to be in good agreement with the experimental data. It can be used for extrapolating prestrain regions of Bauschinger curves from about 1-2% strain to 6-7% with a reasonable degree of accuracy, and this permits an accurate estimation of the permanent softening parameter.

6) A strength-differential exists between the

tensile and compressive curves of dual phase steels. The magnitude of the strength-differential depends upon the microstructure and the type of heat treatment. The magnitude is less for unbanded dual phase steels compared to banded ones.

7) The permanent softening parameter for different microstructures, as measured from the Bauschinger tests, increases rapidly, at first, in the initial stage up to about 2% prestrain and then gradually up to 5 % prestrain. No saturation in permanent softening values is observed up to 5 % prestrain.

8) The permanent softening (or back stress) vs. prestrain curve remains higher for compressive prestrained specimens compared to tensile prestrains. This has been attributed to the transformation stresses arising from austenite to martensite transformation. The residual stress pattern associated with different martensite morphologies determines the extent of such a back stress.

9) Higher permanent softening values have been observed in aged dual phase structures.

CHAPTER 9

Suggestions for Future Work

In an attempt to consolidate and extend the use of the concepts presented in this work, it would be useful to examine the following points.

1) A more comprehensive study of the strength-ductility relationships in isothermally reacted dual phase steels would be required to completely characterize the steel for its commercial production. High purity steels with a range of composition should be studied.

2) A detailed study of the kinetics of the austenite-ferrite reaction and of the formation of dual phase microstructure is of technological importance in the application of isothermally reacted dual phase steels.

3) A study of the carbon distribution within the martensitic grains can lead to some valuable information regarding residual stresses at the ferrite-martensite interfaces as well as in ferrite adjacent to the interface. The back stress is clearly very important and thus it would be useful to determine the cause of this back stress arising from an internal stress due to transformation strain, or from the plastic incompatibility between ferritic and martensitic phases by using careful x-ray methods to investigate the residual stress in the martensite particle.

4) The equation proposed by Watt (110) has shown good agreement with the data on dual phase steels. However, more experiments with other alloy systems as well as pure metals have to be carried out to evaluate its general

applicability.

5) The magnitude of the strength differential needs to be accurately quantified for different dual phase structures. The relationship between the magnitude of the strength-differential and the permanent softening parameter differential would be an interesting study as both seem to depend upon the residual stresses arising from the austenite to martensite transformation. The data for permanent softening vs. prestrain curves of intercritically annealed banded specimens is lacking and needs to be obtained for a more complete discussion of the present results.

It would be of interest to examine the strength differential effect and the permanent softening differential as a function of carbon content, and of martensite content with varying carbon contents in the martensite.

REFERENCES

1. M.S. Rashid, SAE Preprint 770211, (1977).

2. S. Hayami and T. Furukawa, pp. 311-321, in Microalloying '75, Union Carbide Corporation, New York (1977).

3. R.A. Grange, p. 861-876, in "Proceedings of Second International Conference on the Strength of Metals and Alloys," Vol. II, ASM (1970).

4. P.R. Mould, Metals Engineering Quarterly, pp. 22-31, 15, No. 3, (1975).

5. J.Y. Koo and G. Thomas, p. 525, Metallurgical Transactions, Vol. 8A, (1977).

6. Formable HSLA and Dual Phase Steels, A.T. Davenport, ed., TMS-AIME, Warrendale, Pennsylvania (1977).

7. Structure and Properties of Dual Phase Steels, R.A. Kot and J.W. Morris, eds., TMS-AIME, Warrendale, Pennsylvania, (1979).

8. Fundamentals of Dual Phase Steels, R.A. Kot and B.L. Bramfit, eds., TMS-AIME, Warrendale, Pennsylvania (1981).

9. R.G. Davies, pp. 671-679, Metallurgical Transactions A, 9A, (1978).

10. G.R. Speich and R.L. Miller, pp., 145-182, reference 7.

11. R.D. Lawson, D.K. Matlock, and G. Krauss, pp. 347-381, reference 8.

12. J.M. Rigsbee and P.J. VanderArend, pp. 56-86, reference 6.

13. A.R. Marder, pp. 145-160, reference 8.

14. R.G. Davies, pp. 25-39, reference 7.

15. Hsun Hu, pp. 109-125, reference 7.

16. G.R. Speich and R.L.Miller, pp. 3-45, reference 8.

17. C.I. Garcia and A.J. DeArdo, pp. 40-61, reference 7.

18. P. Wycliff, G.R. Purdy and J.D. Embury, pp. 59-83, reference 8.

19. U.R. Lenel, pp. 471-474, Scripta Metallurgica, Vol. 17 1983.

20. F.C. Hull, F.C. Colton and R.F. Mehl, p. 150, Trans. AIME, 185 (1942).

21. M.H. Richman, D.A. Thomas, M. Cohen, p. 816, Vol. 7, Acta Metallurgica (1959).

22. K. Mazanek and J. Cadek, p. 212, Rev. Met., 501 (1958).

23. P. Krahe, K.P. Kinsman, and H.I. Aaronson, p. 1109, Vol. 20, Acta Metallurgica (1972).

24. C.A. Dube, Ph.D. Thesis, Carnegie Inst. of Technology, 1948.

25. F.C. Frank, p. 201, Proc. Roy. Soc. (London), 586 (1956).

26. C. Zener, J. Applied Physics, 20, 950 (1949).

27. V.J. Danilov and J.A. Kristal, Problems in Metallography and Physics of Metals, 1949.

28. R.D. Lawson, D.K. Matlock, and G. Krauss, p. 71-87, Metallography, 13 (1980).

29. G.S. Huppi, D.K. Matlock and G. Krauss, p. 1239-43, Scripta Metallurgica, 14 (1980).

30. D.A. Korzekwa, D.K. Matlock, and G. Krauss, pp. 2061-2064, Metallurgical Transactions, Vol. 13A, Nov. (1982).

31. T. Kunio, M. Shimizu, K. Yamada and H. Suzuki, pp. 411-417, Engineering Fracture Mechanics, Vol. 7, (1975).

32. H. Suzuki and A.J. McEvily, pp. 475-481, Metallurgical Transactions, Vol. 10A, 1979.

33. G. Thomas and J.Y. Koo, p. 183, reference 7.

34. M.S. Rashid and B.V.N. Rao, pp. 249-264, Reference 8.

35. R.G. Davies, pp. 265-277, reference 8.

36. G.R. Speich and R.L. Miller, pp. 279-304, reference 8.

37. J. Bauschinger, columns 289-348, Zivilingenieur, Vol. 27, (1881).

38. R. Sowerby, D.K. Uko and Y. Tomita, pp. 43-58, Materials Science and Engineering, 41 (1979).

39. E. Orowan, in "Internal Stresses and Fatigue of Metals," p. 59, eds. Rass Weiler and Grube, Amsterdam, Elsevier (1966).

40. J.C. Fischer, E.W. Hart and R.H. Pry, Acta Metallurgica, 1, 336 (1953).

41. K. Tanaka, K. Narita and T. Mori, p. 1185, Acta Metallurgica (1971).

42. L.M. Brown and W.M. Stobbs, p. 1185, Phil. Mag., 23, (1971).

43. L.M. Brown and W.M. Stobbs, p. 1201, Phil. Mag., 23 (1971).

44. W.M. Stobbs, p. 1073, Phil. Mag., 27 (1973).

45. J.D. Atkinson, L.M. Brown and W.M. Stobbs, p. 1247, Phil. Mag. 30, (1974).

46. L.M. Brown and W.M. Stobbs, p. 351, Phil. Mag., 34 (1976).

47. M.F. Ashby, pp. 399-424, Phil. Mag., 21 (1970).

48. P.B. Hirsch and F.J. Humphreys, pp. 45-92, Proc. Roy. Soc., A318 (1970).

49. F.J. Humphreys and P.B. Hirsch, pp. 373-390, Phil. Mag. 34 (1976).

50. R.L. Woolley, pp. 597-618, Phil. Mag., 44 (1953).

51. S.N. Buckley and K.M. Entwistle, pp. 352-361, Acta Metallurgica, 4 (1956).

52. S. Kamakura, p. 426-436, Bulletin of JSME, Vol. 11, No. 45 (1968).

53. W. Junische, E. Stolte and J. Kagler, p. 117, Tech. Mitt. Krupp, Forschungsber, 23(4) (1965).

54. N. Ibrahim and J.D. Embury, p. 147, Materials Science and Engineering, 19 (1975).

55. E.H. Edwards and J. Washburn, pp. 1239-1242, Trans. AIME, 200 (1954).

56. A. Abel and H. Muir, p. 489, Phil. Mag. 26 (1972).

57. McClintock and A.S. Argon in "Mechanical Behaviour of Materials," p. , McGraw Hill, New York (1968).

58. D.V. Wilson, pp. 807-814, Acta Metallurgica, 13(7) (1965).

59. D.V. Wilson and Y.A. Konnan, p. 617, Acta Metallurgica, 12 (1964).

60. R.J. Asaro, p. 206, in "Workhardening in Tension and Fatigue," AIME (New York), (1977).

61. L.M. Brown, p. 127, Scripta Metallurgica, 11 (1977).

62. T. Kishi and I. Gokyu, pp. 390-392, Metallurgical Transactions, 4 (1973).

63. T. Kishi and T. Tanabe, pp. 303-315, J. Mech. Phys. Solids, 21 (1973).

64. S.P. Gupta and S.P. Kodali, p. 111, Scripta Metallurgica, 10 (1976).

65. G.D. Moan and J.D. Embury, pp. 925-928, Scripta Metallurgica, 11 (1977).

66. T.C. Harrison, R.T. Weiner and G.D. Fearnehough, p. 334, JISI, 210 (1972).

67. R.M. Jamieson and J.E. Hood, p. 209, JISI, 46 (1971).

68. R.V. Milligan, W.H. Koo and T.E. Davidson, p. 480, Trans. ASME (1966).

69. J.M. Moyer and G.S. Ansell, pp. 178-191, Met. Trans. 6A (1975).

70. D.S. Dabkowski and G.R. Speich, pp. 284-312, in Proc. Mechanical Working and Steel Processing Conference, XV, AIME, New York (1977).

71. M. Hillert, pp. 67-89, Jerkontorets Annaler, 141 (1957).

72. J. Gerbase, J.D. Embury and R.M. Hobbs, pp. 118-144, reference 7.

73. D. Tseng and F.H. Vitovec, p. 3-9-411, reference 8.

74. A. Goel, R.K. Ray and G.S. Murty, pp. 375-380, Scripta Metallurgica, 17 (1983).

75. J.D. Embury and J.L. Duncan, pp. 333-345, reference 8.

76. W.C. Leslie and R.J. Sober, p. 459, Trans. ASM, 60 (1967).

77. D. Kalish and M. Cohen, p. 353, Trans. ASM, 62 (1969).

78. J.P. Hirth and Morris Cohen, p. 3, Met. Trans., 1, (1970).

79. G.C. Rauch and W.C. Leslie, p. 373, Met. Trans. 3, (1972).

80. R. Chait, p. 365, Met. Trans., 3 (1972).

81. R. Chait, p. 351, Scripta Metallurgica, 7 (1973).

82. W.A. Spitzig, R.J. Sober and O. Richmond, p. 885, Acta Metallurgica, 23 (1975).

83. W.A. Spitzig, R.J. Sober and O. Richmond, p. , Acta Metallurgica, (1976).

84. G.C. Rauch, R.L. Daga, S.V. Radcliffe, R.J. Sober and W.C. Leslie, p. 2279, Met. Trans. A, 6a (1975).

85. C.A. Pampillo, L.A. Davis and J.C.M. Li, p. 765, Scripta Metallurgica, 6 (1972).

86. F.B. Fletcher, M. Cohen, and J.P. Hirth, p. 905, Met. Trans. A, 5A (1974).

87. S.V. Radcliffe and W.C. Leslie (reported by G.C. Rauch and W.C. Leslie), p. 21, J. Met., 27A (1969).

88. T. Gladman and F.B. Pickering, BISPA, Ref. MG/CONF/23/63.

89. K. Nakoaka, K. Araki and K. Kurihara, p. 126, reference 6.

90. T. Kato, K. Hashiguchi, I. Takahashi, T. Irie, and N. Ohashi, p. 199, reference 8.

91. J.H. Bucher and E.G. Hamburg, SAE paper, 770164, (1977).

92. A.M. Sarosiek, Thesis, M.I.T. (1982).

93. A.R. Marder and B.L. Bramfitt, p. 242, reference 7.

94. A.R. Marder, p. 86, Met. Trans. A, 13A (1982).

95. T. Furukawa, H. Morikawa, H. Takechi and K. Koyama, p. 281, reference 7.

96. G.R. Specih and W.C. Leslie, p. 1073, Met. Trans., 3, (1972).

97. P. Messien, J.C. Herman, T. Greday, p. 161, reference 8.

98. S.S. Hansen and R.R. Pradhan, p. 113, reference 8.

99. N.J. Balinger and T. Gladman, p. , Metal Science, (1982).

100. J.Y. Koo and G. Thomas, p. 852, Met. Trans. 11A (1980).

101. L.F. Ramos, D.K. Matlock and G. Krauss, p. 259, Met. Trans. A, 10A (1979).

102. W.R. Cribb and J.M. Rigsbee, p. 91, reference 7.

103. J.H. Hollomon, p. 268, Trans. AIME, 162 (1945).

104. E. Voce, p. 537, Journal of the Institute of Metals, 74 (1948).

105. P. Ludwik, p. 32, "Elements der Technoligischen Mechanik," Julius Spinger, Berlin (1909).

106. H.W. Swift, p. 1, J. Mech. Phys. Solids, 1 (1952).

107. S.N. Monteiro, p. 2947, Met. Trans., 2 (1971).

108. B. Jaoul, p. 95, Journal of the Mechanics and Physics of Solids, 5 (1957).

109. C. Crussard, p. 697, Rev. Met., 10 (1953).

110. D.F. Watt, Private Communication.

111. R.E. ReedHill, W.R. Cribb, and S.N. Monteiro, p. 2665, Met. Trans. A, 4 (1973).

112. R.L. Kluch and T.L. Hebble, p. 118, Trans. of ASME, Journal of Pressure Vessel Technology (1976).

113. H.J. Kleemola and M.A. Niemen, p. 1863, Met. Trans., 5 (1974).

114. D.J. Lloyd and D. Kenny, p. 639, Acta Met., 28 (1980).

115. E. Macherrauch, p. 60, Z. Metallkunde (1964).

116. Ch. Schwink and W. Vorbrugg, p. 729, Phys. Stat. Sol. 8 (1965).

117. D. Krause and E. Gottler, p. 485, Phys. Stat. Sol. 8, (1965).

118. J.Morrow and G.Tither, p.16. J.Metals, 30(3), (1978)

APPENDIX I

ESTIMATION OF ERRORS IN THE MEASUREMENT OF TRUE STRESS AND TRUE STRAIN

1. True Stress

True stress is expressed as

$$\sigma = P/A \quad \text{----------(1)}$$

Where σ = true stress
A = instantenous area of cross-section of the specimen
P = load

The above equation can be written in a more general form as

$$\sigma = f(P,A) \quad \text{----------(2)}$$

for which the variance in the measurement of σ can be expressed by the law of propagation of errors as

$$S_\sigma^2 = \left(\frac{\partial \sigma}{\partial P}\right) S_p^2 + \left(\frac{\partial \sigma}{\partial A}\right) S_A^2 \quad \text{----------(3)}$$

where S_σ^2 is the variance in the measurement of stress;
S_p^2 is the variance in the measurement of load;
and S_A is the variance in the measurement of area.

On substituting in equation (2) the values of partial derivatives $(\partial\sigma/\partial P)$ and $(\partial\sigma/\partial A)$ as $1/A$ and $-1/A^2$ respectively we obtain,

$$S_\sigma^2 = \left(\frac{1}{A}\right)^2 S_p^2 + \left(\frac{1}{A}\right)^2 S_A^2$$

$$S_\sigma^2 = \left(\frac{1}{A}\right)^2 S_p^2 + \frac{P^2}{A^4} S_A^2 \quad \text{----------(4)}$$

For typical values of,

A=0.04364 inches(diameter 0.2358); S_A=0.001 inches
P=1000 lbs ; S_p=10 lbs

the standard deviation in stress is

S_σ=0.572 KSi.

and so the standard deviation of the error in measuring the stress stress is 0.572 Ksi giving a 95% confidence limits at $\pm$ 0.112 KSi.

2. True Strain

True strain is expressed as

$$\epsilon = \ln (\ln/l_0) \text{ ----------(5)}$$

Where l_0 is the original length of the specimen and l_1 is the instantaneous length and thus equal to the sum of the original length and the displacement for tensile tests,ie.,

$$l_1 = l_0 + D \text{ ----------(6)}$$

Where D is displacement and can be expressed as

D = distance along the displacement axis on the chart (D_{chart}) X Extensometer factor.
Substituting the value of D in equation (6) we obtain

$$l_1 = l_0 + D_{chart} \text{ X Ext}$$

Following the same procedure for the determination of variance as in the case of stress we obtain the variance in the measurement of l_1 as

$$S_{l_1}^2 = \left(\frac{\partial l_1}{\partial l_0}\right)^2 S_{l_0}^2 + \left(\frac{\partial l_1}{\partial D_{chart}}\right)^2 S_{D_{chart}}^2 + \left(\frac{\partial l_1}{\partial Ext}\right)^2 S_{Ext}^2$$
$$\text{----------(7)}$$

Where $\frac{\partial l_1}{\partial l_0}=1$, $\frac{\partial l_1}{\partial chart}=0$ for a fixed chart distance and $\frac{\partial l_1}{\partial Ext}= D_{chart}$

Substituting the values in equation (7) we get

$$S_{l_1}^2 = S_{l_0}^2 + (D_{chart})^2 S_{Ext}^2 \quad \text{----------(8)}$$

For typical values of ,

l_0 = 1 inch; S_{l_0} = 0.001 inches; D_{chart}= 2 inches

Ext = 0.001(for range 1); and $S_{Ext}= 10^{-6}$

The variance in l_1 is

$$S_{l_1} = 0.001 \quad \text{----------(9)}$$

Similarly, the variance in the measurement of strain can be expressed as

$$S_\epsilon^2 = \left(\frac{\partial \epsilon}{\partial l_1}\right)^2 S_{l_1}^2 + \left(\frac{\partial \epsilon}{\partial l_0}\right)^2 S_{l_0}^2$$

or

$$S_\epsilon^2 = \left(\frac{1}{l_1}\right)^2 S_{l_1}^2 + \left(\frac{1}{l_0}\right)^2 S_{l_0}^2 \quad \text{----------(10)}$$

For typical values of

l_1= 1.002 inches; S_{l_1} = 0.001(from equation (9))

and l_0= 1 inch; S_{l_0}= 0.001 inches

The standard deviation in stress is

$$S_\epsilon = 1.414X10^{-3} \quad \text{----------(11)}$$

and so the standard deviation of the error in measuring the strain is 0.0001414 giving 95% confidence limits at $\pm$ 0.277 $X10^{-3}$.

In the case of Bauschinger tests the initial length of the specimen, l_0 was 0.375 inches, $S_{l_0} = 1.875X10^{-3}$, Ext=0.00125 and $S_{Ext} = 1.25X10^{-6}$. These values(for D_{chart}=2) give

$$S_{l_1} = 1.87X10^{-3}$$

and S_ϵ (for l_1=0.3775)= $7.028X10^{-3}$

and so the standard deviation of the error in measuring the strain in Bauschinger tests is 0.0007028 giving 95% confidence limits at $\pm$ 1.164×10^{-3}.

Appendix II

Analytical Functions From Empirical σ-ε Relationships

1. Hollomon's Equation

This equation is expressed as:

$$\sigma = k\varepsilon_p^n \qquad \text{(I)}$$

where σ and ε_p are true stress and strain and k and n are material constants. Taking the logarithm of Equation 1, we obtain:

$$\ell n\sigma = \ell nk + n\ell n\varepsilon_p$$

which is the analytical form of Hollomon's equation as shown in Figure AII.1.

2. Ludwik's Equation

This equation is expressed as:

$$\sigma = \sigma_o + k\varepsilon_p^n \qquad \text{(II)}$$

where σ, k, n, ε_p have been defined earlier and σ_o is an additional constant referred to as frictional stress. Taking the derivative of Equation II, we obtain:

$$\frac{d\sigma}{d\varepsilon_p} = 0 + k'n'\varepsilon_p^{n'-1}$$

or,

$$\ell n \frac{d\sigma}{d\varepsilon_p} = \ell n(n'k') + (n'-1)\ell n\varepsilon_p$$

This is an analytical form of Ludwik's equation as described in Figure AII.2.

3. Modified Swift Equation

This equation is generally expressed as:

$$\varepsilon = \varepsilon_o + c\sigma^m \qquad \text{(III)}$$

Differentiating the above equation, we obtain:

$$\frac{d\varepsilon}{d\sigma} = 0 + cm\sigma^{m-1}$$

or, $$\frac{d\sigma}{d\varepsilon} = \frac{\sigma^{1-m}}{cm}$$

or, $$\ell n \frac{d\sigma}{d\varepsilon} = (1-m)\ell n\sigma - \ell n\, cm$$

This is an analytical form of Modified Swift Equation as described in Figure AII.3.

4. Voce's Equation

This equation is generally expressed as:

$$\sigma = \sigma_s - (\sigma_s - \sigma_o)\exp(-\frac{\varepsilon}{\varepsilon_c}) \qquad \text{(IV)}$$

Differentiating the above equation, we obtain:

$$\frac{d\sigma}{d\varepsilon} = (\frac{\sigma_o - \sigma_s}{\varepsilon_c})\exp(-\frac{\varepsilon}{\varepsilon_c})$$

or, $$\varepsilon_c \frac{d\sigma}{d\varepsilon} = (\sigma_o - \sigma_s)\exp(-\frac{\varepsilon}{\varepsilon_c})$$

or, $$\varepsilon_c \frac{d\sigma}{d\varepsilon} = \sigma - \sigma_s$$

or, $$\sigma = \sigma_s + \varepsilon_c \frac{d\sigma}{d\varepsilon}$$

This is the analytical form of the Voce equation as shown in Figure AII.4.

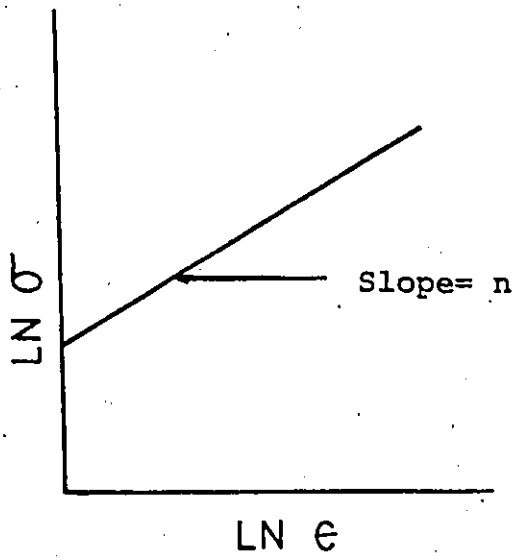

Figure AII.1 Ln Stress vs ln Strain

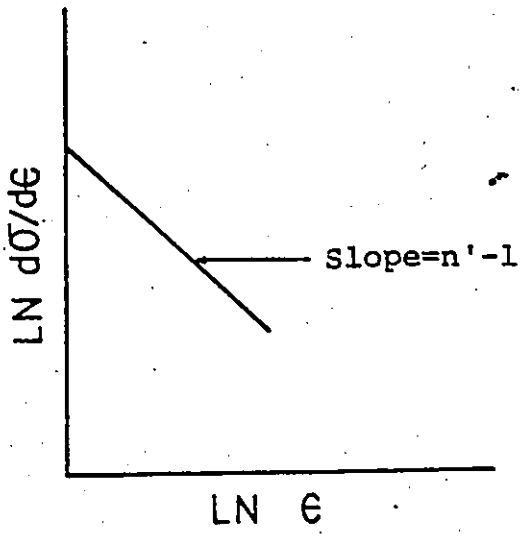

Figure AII.2 Ln(dσ/dϵ) vs ln Strain

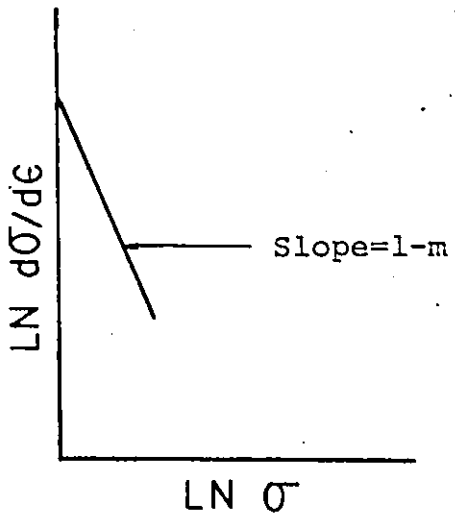

Figure AII.3 Ln(dσ/dϵ) vs ln Stress

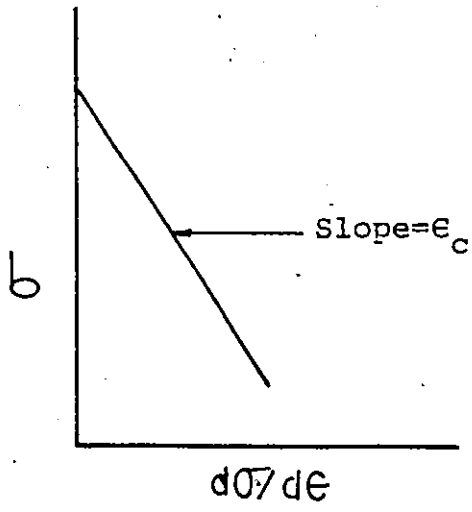

Figure AII.4 Stress vs dσ/dϵ

APPENDIX III

Fortran Computer Programs

The following computer programs, developed for the present work, are enclosed in a serial order.

1. Calculation of mean ferrite grain size from digitized data.
2. General linear modelling.
3. Calculation and plotting of true stress vs. true strain curves and work hardening rate vs. true strain curves of tensile specimens from load vs. displacement values.
4. Calculation and plotting of $\ell n\sigma$ vs. $\ell n\varepsilon$ values.
5. Calculation and plotting of $\ell n(d\sigma/d\varepsilon)$ vs. true stress and $\ell n(d\sigma/d\varepsilon)$ vs. true strain values.
6. Calculation and plotting of 'unflopped' Bauschinger true stress-true strain curves from load vs. displacement Bauschinger curves (unflopped curve on an ordinary plotting paper is enclosed).
7. Calculation and plotting of 'flopped' Bauschinger true stress-true strain curves.
8. Nonlinear curve fitting for evaluating different constants in Voce's and proposed equation with output.
9. Evaluation of the difference between calculated stress values using above equations and experimental values and plotting of experimental and theoretical curves.
10. Calculation and plotting of $d\ell n\sigma/d\ell n\varepsilon$ vs. $\ell n\varepsilon$ curves for prestrain regions of Bauschinger curves for checking linearity.

11. Calculation and plotting of complete 'flopped' Bauschinger σ vs. ε curves, including extrapolated part using Voce's proposed equations for permanent softening measurement.

Appendix III.1

```
      $ JOB WATFIV XXXXXXXXXX MUKESH JAIN
 1            REAL LEN, LEN 1
 2            IPIC1=1
 3            LEN1=0.0
 4            ICTR=1
 5   15       READ 10, IPIC, LEN
 6   10       FORMAT (I2,2X,F4.3)
 7    5       IF(IPIC.EQ.IPIC1)THEN
 8            LEN1=LEN1+LEN
 9            ICTR=ICTR+1
10            GO TO 15
11            ELSE
12            AVG=LEN1/ICTR
13            PRINT,IPIC1,LEN1,AVG
14            IF(IPIC.EQ.99)THEN
15            STOP
16            ELSE
17            ENDIF
18            ICTR=0
19            LEN1=0
20            IPIC1=IPIC
21            GO TO 5
22            ENDIF
23            END
```

APPENDIXIII.2

General Linear Modelling

GLM PROCEDURE

The GLM procedure analyzes General Linear Models, hence the name GLM. Although GLM is a regression procedure, it handles classification variables -those that name discrete levels - as well as continous variables, which measure quatities. Thus GLM can be used for many different analyses:

- simple regression
- multiple regression
- analysis of variance, especially for unbalanced data.
- analysis of covariance
- response surface models
- weighted regression
- polynomial regression
- partial correlations
- multivariate analysis of variance
- others.

Multiple Regression:

In multiple regression, the value of a dependent variable(or response variable) are described or predicted in terms of one or more independent or explanatory variables. The statements

```
PROC GLM
MODEL dependent variable = independent variables;
```

could be used to describe a multiple regression model in GLM.

The GLM printout is organized into four sections:

- overall analysis of variance table.
- miscellaneous statistics.
- results of special tests.
- report on the parameter estimates.

1. Analysis of Variance table: The overall analysis of variantable breaks down the total sum of squares for the dependent variable into the portion attributed to the model, and the portion attributed to error.

   The mean square term is the sum of squares divided by the degrees of freedom(DF). The mean square for error (MS(ERROR)) is an estimate of σ^2, the variance of true residuals.

2. F VALUE This value is the ratio produced by deviding MS(MODEL) by MS(ERROR). It tests how well the model as a whole accounts for the dependent variable's behavior. If the significance probability, lebelled PR>F, is small ,it indicates significance.

3. R-SQUARE: R^2 measures how much variation in the dependent variable can be accounted for by the model. R^2 , which can range from 0 to 1, is the ratio of the sum of squares for the model devided by the sum of the squares for the corrected total. In general, the larger the value of R^2 , the better the model's fit.

4. C.V. : This measure is the coefficient of variation,

and is often used to describe the amount of variation in the population. It is equal to the standard deviation of the dependent variable, devided by the mean, times 100. The coefficient of variation is often a preferred measure because it is unitless.

5 STD DEV : This is the standard deviation of the dependent variable. It is equal to the square root of the square root of MS(ERROR).

6 dep MEAN : This is the mean of the dependent variable.

Appendix III.3

```
      DIMENSION P(150), D(150),DISP(150),XLTH(150),XLRT(150)
      DIMENSION TRSTN(84),AREA(150),XLOAD(150),TRSTS(84)
      DIMENSION XLNSTS(150),XLNSTR(150),ASTRS(150),ASTRN(150)
      DIMENSION STSTS(84),STSTN(84),SW(84)
      DATA STSTN/84*0.0/
      DATA SW/84*0.0/
      INTEGER R,Q
      CALL PLOTID('MUKESH        JAIN','R12700S602')
      CALL NLIMIT(1000.)
      AMOVE=-1.0
      READ 5,NOSPC
    5 FORMAT(2X,I2)
      DO 3 I=1,NOSPC
      READ 6,NAME
    6 FORMAT(2X,I2)
      PRINT 7,NAME
    7 FORMAT(2X,I2)
      GAGLH=1.00
      XLOFR=500.0
      EXTFR=0.0
      READ 8,DIAMO
    8 FORMAT(2X,F6.4)
      READ 9,NOPTS
    9 FORMAT(2X,I2)
      DO 1 N=1,NOPTS
      READ 10,IND,P(N),D(N),FAC
   10 FORMAT(I1,1X,F5.3,1X,F6.3,1X,F8.6)
      IF(IND.EQ.6) XLOFR=1000.0
      IF(IND.EQ.5) EXTFR=FAC
      DISP(N)=D(N)*EXTFR
      XLTH(N)=GAGLH+DISP(N)
      XLRT(N)=XLTH(N)/GAGLH
      TRSTN(N)=ALOG(XLRT(N))
      PI=3.141593
      AREAO=PI*DIAMO*DIAMO/4.0
      AREA(N)=AREAO/XLRT(N)
      XLOAD(N)=P(N)*XLOFR
      TRSTS(N)=XLOAD(N)/AREA(N)
      ASTRS(N)= ABS(TRSTS(N))
      ASTRN(N)=ABS(TRSTN(N))
      XLNSTS(N)=ALOG(ASTRS(N))
      XLNSTR(N)=ALOG(ASTRN(N))
      PRINT 11,P(N),D(N),TRSTS(N),TRSTN(N)
   11 FORMAT(2F10.3,5X,F10.2,5X,F10.7)
    1 CONTINUE
      N=NOPTS
      K=NOPTS+2
      CALL CALCO2(TRSTN,TRSTS,K,AMOVE,10.,10.,0.0,0.0,0.0,0.0,0.0,1,-1,2)
      DO 4 N=1,NOPTS
      R=N-1
      Q=N+1
      IF(N.EQ.1) GO TO 2
      IF(N.EQ.NOPTS) GO TO 15
      GO TO 14
    2 STSTS(N)=TRSTS(N)
      STSTN(N)=TRSTN(N)
      SW(N)=STSTS(N)/STSTN(N)
      GO TO 16
   14 STSTS(N)=(TRSTS(R)+TRSTS(N)+TRSTS(Q))/3
      STSTN(N)=(TRSTN(R)+TRSTN(N)+TRSTN(Q))/3
      SW(N)=(STSTS(N)-STSTS(R))/(STSTN(N)-STSTN(R))
      GO TO 16
   15 STSTS(N)=(TRSTS(R)+TRSTS(N))/2
      STSTN(N)=(TRSTN(R)+TRSTN(N))/2
      SW(N)=(STSTS(N)-STSTS(R))/(STSTN(N)-STSTN(R))
   16 PRINT 12,STSTS(N),STSTN(N),SW(N)
   12 FORMAT (10X,F10.2,5X,F10.7,5X,F14.2)
      J=NOPTS+2
    4 CONTINUE
      CALL CALCO2(STSTN,SW,J, 10.,10.0,10.0,0.0,0.0,0.0,0.0,0.0,0.0,1,-1,2)
      AMOVE=10.
    3 CONTINUE
      CALL PLTEND(10.)
      STOP
      END
```

Appendix III.4

```
      DIMENSION P(200), D(200)
      DIMENSION TRSTN(200),TRSTS(200),ASTRS(200),ASTRN(20(
      DIMENSION XLNSTS(200),XLNSTR(200)
      CALL PLOTID('MUKESH      JAIN','R12700S602')
      CALL NLIMIT(1000.)
      AMOVE=-1.0
      READ 5,NOSPC
5     FORMAT(3X,I2)
      DO 9 I=1,NOSPC
      READ 6,NAME
6     FORMAT(3X,I2)
      PRINT 11,NAME
11    FORMAT(3X,I2)
      READ 10,NOPTS
10    FORMAT(3X,I3)
      R=0.0
      DO 1 N=1,NOPTS
      READ 2,M,P(N),D(N),TRSTS(N),TRSTN(N)
2     FORMAT(I1,5X,F6.3,1X,F6.3,2X,F9.2,1X,F10.7)
      IF(M.EQ.0) GO TO 7
      IF(M.EQ.1) GO TO 3
      IF(M.EQ.2) GO TO 4
3     R=TRSTN(N)
      GO TO 7
4     TRSTN(N)=(R-TRSTN(N))
7     PRINT 12,N,P(N),D(N),TRSTS(N),TRSTN(N)
12    FORMAT(1H0,I1,5X,F6.3,1X,F6.3,2X,F9.2,1X,F10.7)
      ASTRS(N)=ABS(TRSTS(N))
      ASTRN(N)=ABS(TRSTN(N))
      XLNSTS(N)=ALOG(ASTRS(N))
      XLNSTR(N)=ALOG(ASTRN(N))
      PRINT 14,XLNSTR(N),XLNSTS(N)
14    FORMAT(1H0,3X,F15.7,5X,F15.7)
1     CONTINUE
      J=N+2
      CALL CALCO2(XLNSTR,XLNSTS,J,AMOVE,15.,10.,-8.,5.,10,
      AMOVE=15.
9     CONTINUE
      CALL PLTEND(15.)
      STOP
      END
```

Appendix III.5

```
      DIMENSION P(150), D(150),DISP(150),XLTH(150),XLRT(150)
      DIMENSION TRSTN(84),AREA(150),XLOAD(150),TRSTS(84)
      DIMENSION XLNSTS(150),XLNSTR(150),ASTRS(150),ASTRN(150)
      DIMENSION STSTS(84),STSTN(84),SW(84)
      DIMENSION XSTSTS(150),XSTSTN(150),XSW(150)
      DATA STSTN/84*0.0/
      DATA SW/84*0.0/
      INTEGER R,Q
      CALL PLOTS(53.0,-9)
      AMOVE=-1.0
      READ 5,NOSPC
    5 FORMAT(2X,I2)
      DO 3 I=1,NOSPC
      READ 6,NAME
    6 FORMAT(2X,I2)
      PRINT 7,NAME
    7 FORMAT(2X,I2)
      GAGLH=1.00
      XLOFR=500.0
      EXTFR=0.0
      READ 8,DIAMO
    8 FORMAT(2X,F6.4)
      READ 9,NOPTS
    9 FORMAT(2X,I2)
      DO 1 N=1,NOPTS
      READ 10,IND,P(N),D(N),FAC
   10 FORMAT(I1,1X,F5.3,1X,F6.3,1X,F8.6)
      IF(IND.EQ.6) XLOFR=1000.0
      IF(IND.EQ.5) EXTFR=FAC
      DISP(N)=D(N)*EXTFR
      XLTH(N)=GAGLH+DISP(N)
      XLRT(N)=XLTH(N)/GAGLH
      TRSTN(N)=ALOG(XLRT(N))
      PI=3.141593
      AREAO=PI*DIAMO*DIAMO/4.0
      AREA(N)=AREAO/XLRT(N)
      XLOAD(N)=P(N)*XLOFR
      TRSTS(N)=XLOAD(N)/AREA(N)
      ASTRS(N)= ABS(TRSTS(N))
      ASTRS(N)=0.006894*ASTRS(N)
      ASTRN(N)=ABS(TRSTN(N))
      PRINT 11,P(N),D(N),ASTRS(N),ASTRN(N)
   11 FORMAT(2F10.3,5X,F8.2,5X,F10.7)
    1 CONTINUE
      N=NOPTS
      DO 4 N=1,NOPTS
      R=N-1
      Q=N+1
      IF(N.EQ.1) GO TO 2
      IF(N.EQ.NOPTS) GO TO 15
      GO TO 14
    2 STSTS(N)=ASTRS(N)
      STSTN(N)=ASTRN(N)
      SW(N)=STSTS(N)/STSTN(N)
      GO TO 16
   14 STSTS(N)=(ASTRS(R)+ASTRS(N)+ASTRS(Q))/3
      STSTN(N)=(ASTRN(R)+ASTRN(N)+ASTRN(Q))/3
      SW(N)=(STSTS(N)-STSTS(R))/(STSTN(N)-STSTN(R))
      GO TO 16
   15 STSTS(N)=(ASTRS(R)+ASTRS(N))/2
      STSTN(N)=(ASTRN(R)+ASTRN(N))/2
      SW(N)=(STSTS(N)-STSTS(R))/(STSTN(N)-STSTN(R))
   16 XSTSTS(N)=ALOG(STSTS(N))
      XSTSTN(N)=ALOG(STSTN(N))
      XSW(N)=ALOG(SW(N))
      PRINT 12,XSTSTS(N),XSTSTN(N),XSW(N)
   12 FORMAT (10X,F10.2,5X,F10.7,5X,F14.2)
      J=NOPTS+2
      K=NOPTS+2
    4 CONTINUE
      CALL ZPLOT2(XSTSTN,XSW,K,AMOVE,15.,10.,-13.,1.,13.,-1.
      CALL ZPLOT2(XSTSTS,XSW,J,15.,15.,10.,-3.,1.,13.,-1.,1.
      AMOVE=15.
    3 CONTINUE
      CALL PLOT(15.0,0.0,999)
      STOP
      END
```

Appendix III.6

```
      DIMENSION P(250), D(250),DISP(250),XLTH(250),XLRT(250)
      DIMENSION TRSTN(250),AREA(250),XLOAD(250),TRSTS(250)
      DIMENSION XLNSTS(250),XLNSTR(250),ASTRS(250),ASTRN(250
      INTEGER R,Q
      CALL PLOTID('MUKESH       JAIN','R12700S602')
      CALL NLIMIT(1000.)
      AMOVE=-1.0
      READ 5,NOSPC
5     FORMAT(2X,I2)
      DO 3 I=1,NOSPC
      READ 6,NAME
6     FORMAT(2X,I2)
      PRINT 7,NAME
7     FORMAT(2X,I2)
      READ 2,GAGLH
2     FORMAT(2X,F5.3)
      XLDFR=1000.0
      EXTFR=0.0
      READ 8,DIAMO
8     FORMAT(2X,F6.4)
      READ 9,NOPTS
9     FORMAT(2X,I3)
      DO 1 N=1,NOPTS
      READ 10,D(N),P(N),FAC,IND
10    FORMAT(F7.3,1X,F5.3,1X,F8.6,1X,I1)
      IF(IND.EQ.6) XLDFR=2000.0
      IF(IND.EQ.5) EXTFR=FAC
      IF(IND.EQ.4) XLDFR=1000.0
      DISP(N)=D(N)*EXTFR
      XLTH(N)=GAGLH+DISP(N)
      XLRT(N)=XLTH(N)/GAGLH
      TRSTN(N)=ALOG(XLRT(N))
      PI=3.141593
      AREAO=PI*DIAMO*DIAMO/4.0
      AREA(N)=AREAO/XLRT(N)
      XLOAD(N)=P(N)*XLDFR
      TRSTS(N)=XLOAD(N)/AREA(N)
      ASTRS(N)= ABS(TRSTS(N))
      ASTRN(N)=ABS(TRSTN(N))
      XLNSTS(N)=ALOG(ASTRS(N))
      XLNSTR(N)=ALOG(ASTRN(N))
      PRINT 11,N,P(N),D(N),TRSTS(N),TRSTN(N)
11    FORMAT(1H0,I3,5X,2F10.3,5X,F10.2,5X,F10.7)
1     CONTINUE
      N=NOPTS
      K=NOPTS+2
      CALL CALCO2(TRSTN,TRSTS,K,AMOVE,10.,10.,0.0,0.0,0.0,0.0,0.
      AMOVE=10.
3     CONTINUE
      CALL PLTEND(10.)
      STOP
      END
```

Appendix III.7

```
      DIMENSION P(250), D(250)
      DIMENSION TRSTN(250),TRSTS(250)
      CALL PLOTID('MUKESH       JAIN','R12700S602')
      CALL NLIMIT(1000.)
      AMOVE=-1.0
      READ 5,NOSPC
5     FORMAT(2X,I2)
      DO 9 I=1,NOSPC
      READ 6,NAME
6     FORMAT(2X,I2)
      PRINT 11,NAME
11    FORMAT(2X,I2)
      READ 10,NOPTS
10    FORMAT(2X,I3)
      R=0.0
      DO 1 N=1,NOPTS
      READ 2,M,P(N),D(N),TRSTS(N),TRSTN(N)
2     FORMAT(5X,I1,6X,F6.3,4X,F6.3,6X,F9.2,5X,F10.7)
      IF(M.EQ.0) GO TO 7
      IF(M.EQ.1) GO TO 3
      IF(M.EQ.2) GO TO 4
3     R=TRSTN(N)
      GO TO 7
4     TRSTN(N)=R+(R-TRSTN(N))
7     PRINT 12,P(N),D(N),TRSTS(N),TRSTN(N)
12    FORMAT(1H0,F5.3,4X,F6.3,6X,F9.2,5X,F10.7)
1     CONTINUE
      J=N+2
      CALL CALCO2(TRSTN,TRSTS,J,AMOVE,10.,10.,0.0,0.0,0.0,0.0,0.(
      AMOVE=10.
9     CONTINUE
      CALL PLTEND(10.)
      STOP
      END
```

Appendix III.8

```
1          S A S   L O G     OS SAS 82.3          VS2/MVS JOB WMEGA2   STEP SAS823   PROC

NOTE: THE JOB WMEGA2 HAS BEEN RUN UNDER RELEASE 82.3 OF SAS AT THE UNIVERSITY OF WINDSOR (06509001).

NOTE: CPUID    VERSION = 00  SERIAL = 010126  MODEL = 3031 .

NOTE: NO OPTIONS SPECIFIED.

1              DATA;
2              INPUT SS ST;
3              CARDS;

NOTE: DATA SET WORK.DATA1 HAS 15 OBSERVATIONS AND 2 VARIABLES. 651 OBS/TRK.
NOTE: THE DATA STATEMENT USED 0.15 SECONDS AND 204K.

19             TITLE SS=EXP((-K/2)*(LOG(ST)**2)+(A*LOG(ST))+C);
20             PROC NLIN BEST=20 PLOT METHOD=MARQUARDT;
21             PARAMETERS K=.01 TO .05 A=.01 TO .5 BY .01 C=.1 TO 1 BY .1;
22             P=(-K/2)*(LOG(ST)**2);
23             Q=A*LOG(ST);
24             MODEL SS=EXP(P+Q+C);
25             DER.K=(-SS/2)*(LOG(ST)**2);
26             DER.A=SS*LOG(ST);
27             DER.C=SS;
28             OUTPUT PREDICTED=PY RESIDUAL=RY;

NOTE: DATA SET WORK.DATA2 HAS 15 OBSERVATIONS AND 4 VARIABLES. 361 OBS/TRK.
NOTE: THE PROCEDURE NLIN USED 15.25 SECONDS AND 226K AND PRINTED PAGES 1 TO 3.

29             PROC PLOT; PLOT SS*ST='*' /OVERLAY;

NOTE: THE PROCEDURE PLOT USED 0.51 SECONDS AND 212K AND PRINTED PAGE 4.
NOTE: SAS USED 226K MEMORY.

NOTE: SAS INSTITUTE INC.
      SAS CIRCLE
      PO BOX 8000
      CARY, N.C.  27511-8000
```

Appendix III.9

```
      DIMENSION TRSTN(200),TRSTS(200),SLOG(200),DIFF1(200)
      DIMENSION SS(200),ST(200),VSTS(200),DIFF2(200)
      REAL K
      INTEGER O
      CALL PLOTS(53.0,-9)
      AMOVE=-1.0
      READ 15,NOSPC
 15    FORMAT(3X,I2)
      DO 9 M=1,NOSPC
      READ 6,NAME
 6    FORMAT(3X,I2)
      PRINT 11,NAME
 11   FORMAT(3X,I2)
      READ 10,NOPTS
 10   FORMAT(3X,I2)
      DO 13 N=1,NOPTS
      READ 2,TRSTS(N),TRSTN(N)
 2    FORMAT(9X,F6.2,6X,F9.7)
      SS(N)=ALOG(TRSTS(N))
      ST(N)=ALOG(TRSTN(N))
 13   CONTINUE
      READ 34,IP
 34   FORMAT(3X,I1)
      L=1
 5    IF(L.LE.IP)GO TO 33
      GO TO 9
 33   READ 23,K,A,C
      PRINT 23,K,A,C
 23   FORMAT(2X,F9.6,1X,F9.6,1X,F9.6)
      READ 27,SI,SO,B
      PRINT 27,SI,SO,B
 27   FORMAT(1X,F9.4,1X,F9.4,1X,F9.4)
      DO 1 N=1,NOPTS
      SLOG(N)=EXP((-K/2)*((ST(N))**2)+(A*(ST(N)))+C)
      VSTS(N)=SI-((SI-SO)*EXP(-B*TRSTN(N)))
      DIFF1(N)=TRSTS(N)-SLOG(N)
      DIFF2(N)=TRSTS(N)-VSTS(N)
      PRINT 12,TRSTS(N),SLOG(N),VSTS(N),TRSTN(N),DIFF1(N),DIFF2(N)
 12   FORMAT(1H0,1X,F9.2,1X,F8.3,1X,F8.3,1X,F10.7,1X,F5.2,1X,F5.2)
 1    CONTINUE
      L=L+1
      J=NOPTS+2
      CALL ZPLOT2(TRSTN,TRSTS,J,AMOVE,17.,10.,0.,.004,0.,120.,1,-1,2)
      VSTS(NOPTS+1)=TRSTS(NOPTS+1)
      VSTS(NOPTS+2)=TRSTS(NOPTS+2)
      TRSTN(NOPTS+1)=TRSTN(NOPTS+1)
      TRSTN(NOPTS+2)=TRSTN(NOPTS+2)
      CALL ZPLOT2(TRSTN,VSTS,J,0.,17.,10.,0.,0.004,0.,120.,1,-1,2)
      SLOG(NOPTS+1)=VSTS(NOPTS+1)
      SLOG(NOPTS+2)=VSTS(NOPTS+2)
      TRSTN(NOPTS+1)=TRSTN(NOPTS+1)
      TRSTN(NOPTS+2)=TRSTN(NOPTS+2)
      CALL ZPLOT2(TRSTN,SLOG,J,0.,17.,10.,0.,0.004,0.,120.,1,-1,2)
      AMOVE=17.
      GO TO 5
 9    CONTINUE
      CALL PLOT(17.0,0.0,999)
      STOP
      END
```

Appendix III.10

```
      DIMENSION P(200), D(200)
      DIMENSION TRSTN(200),TRSTS(200),ASTRS(200),ASTRN(200)
      DIMENSION XLNSTS(200),XLNSTR(200),S(200)
      CALL PLOTID('MUKESH      JAIN','R12700S602')
      CALL NLIMIT(1000.)
      AMOVE=-1.0
      READ 5,NOSPC
5     FORMAT(3X,I2)
      DO 9 I=1,NOSPC
      READ 6,NAME
6     FORMAT(3X,I2)
      PRINT 11,NAME
11    FORMAT(3X,I2)
      READ 10,NOPTS
10    FORMAT(3X,I3)
      R=0.0
      DO 1 N=1,NOPTS
      READ 2,M,P(N),D(N),TRSTS(N),TRSTN(N)
2     FORMAT(I1,5X,F6.3,1X,F6.3,2X,F9.2,1X,F10.7)
      IF(M.EQ.0) GO TO 7
      IF(M.EQ.1) GO TO 3
      IF(M.EQ.2) GO TO 4
3     R=TRSTN(N)
      GO TO 7
4     TRSTN(N)=(R-TRSTN(N))
7     PRINT 12,N,P(N),D(N),TRSTS(N),TRSTN(N)
12    FORMAT(1H0,I1,5X,F6.3,1X,F6.3,2X,F9.2,1X,F10.7)
      ASTRS(N)=ABS(TRSTS(N))
      ASTRN(N)=ABS(TRSTN(N))
      XLNSTS(N)=ALOG(ASTRS(N))
      XLNSTR(N)=ALOG(ASTRN(N))
      IF(N.EQ.1)GO TO 16
      S(N)=((XLNSTS(N)-XLNSTS(N-1))/(XLNSTR(N)-XLNSTR(N-1)))
16    S(1)=1.2
      PRINT 14,XLNSTR(N),XLNSTS(N),S(N)
14    FORMAT(1H0,3X,F15.7,5X,F15.7,5X,F18.7)
1     CONTINUE
      S(1)=S(2)
      J=N+2
      CALL CALCO2(XLNSTR,S,J,AMOVE,15.,10.,-11.2,.5,0.0,0.2,1
      AMOVE=15.
9     CONTINUE
      CALL PLTEND(15.)
      STOP
      END
```

Appendix III.11

```
      DIMENSION TRSTN(200),TRSTS(200),VSTS(200)
      DIMENSION EPSIL(30),SIGMA(30)
      REAL K
      INTEGER O,S,T
      CALL PLOTS(53,0,-9)
      AMOVE=-1.0
      READ 5,NOSPC
5     FORMAT(3X,I2)
      DO 9 I=1,NOSPC
      READ 6,NAME
6     FORMAT(3X,I2)
      PRINT 11,NAME
11    FORMAT(3X,I2)
      READ 23,K,A,C
      PRINT 23,K,A,C
23    FORMAT(1X,F9.6,1X,F9.6,1X,F9.6)
      READ 10,NOPTS
10    FORMAT(3X,I3)
      R=0.0
      DO 1 N=1,NOPTS
      READ 2,M,TRSTS(N),TRSTN(N)
2     FORMAT(I1,6X,F9.2,F11.7)
      IF(M.EQ.0) GO TO 7
      IF(M.EQ.1) GO TO 3
      IF(M.EQ.2) GO TO 4
3     R=TRSTN(N)
      GO TO 7
4     TRSTN(N)=R+(R-TRSTN(N))
7     TRSTN(N)=ABS(TRSTN(N))
      TRSTS(N)=.0068948*TRSTS(N)
      VSTS(N)=EXP((-K/2)*((ALOG(TRSTN(N)))**2)+(A*ALOG(TRSTN(N)))+C)
      PRINT 12,TRSTS(N),VSTS(N),TRSTN(N)
12    FORMAT(1H0,6X,F9.2,5X,F8.3,5X,F10.7)
1     CONTINUE
      DO 25 T=1,NOPTS
      N=T+1
      S=N-1
      IF(TRSTS(N).LT.TRSTS(S)) GO TO 17
      GO TO 25
17    EPSIL(1)=ABS(TRSTN(S))
      SIGMA(1)=TRSTS(S)
      PRINT 26,SIGMA(1),EPSIL(1)
26    FORMAT(10X,F9.2,5X,F10.7)
      DO 20 L=1,20
      SIGMA(L)=EXP((-K/2)*((ALOG(EPSIL(L)))**2)+(A*ALOG(EPSIL(L)))+C)
      EPSIL(L+1)=EPSIL(L)+0.002
      PRINT 15,SIGMA(L),EPSIL(L)
15    FORMAT(1H0,6X,F9.2,5X,F10.7)
20    CONTINUE
      GO TO 28
25    CONTINUE
28    O=L+2
      J=NOPTS+2
      CALL ZPLOT2(TRSTN,TRSTS,J,AMOVE,17.,10.,0.,.004,0.,120.,1,-1,2)
      SIGMA(L+1)=TRSTS(NOPTS+1)
      SIGMA(L+2)=TRSTS(NOPTS+2)
      EPSIL(L+1)=TRSTN(NOPTS+1)
      EPSIL(L+2)=TRSTN(NOPTS+2)
      CALL ZPLOT2(EPSIL,SIGMA,O,0.,17.,10.,0.,0.004,0.,120.,1,-1,2)
      AMOVE=17.
9     CONTINUE
      CALL PLOT(17.0,0.0,999)
      STOP
      END
```

VITA AUCTORIS

1958	Born in Chhatarpur, India.
1980	Received a Bachelors degree in Engineering (B.E.) from the Indian Institute of Science, Bangalore, India.
1980	Worked as a Junior Research Engineer with R & D Centre for Iron and Steel, Ranchi, India.
1982	Accepted into M.A.Sc. program in Eingeering Materials at the University of Windsor, Canada
1984	Received a M.A.Sc. degree from the University of Windsor.
1984	Accepted into Ph.D. program in Metallurgical Engineering at Queen's University, Canada.